



Sigillum Universitatis Ludovici Maximiliani

Switching on the first light in the Universe

Dissertation der Fakultät für Physik

DISSERTATION OF THE FACULTY OF PHYSICS / DISSERTAZIONE DELLA FACOLTÀ DI FISICA

der Ludwig-Maximilians-Universität München

AT THE LUDWIG MAXIMILIAN UNIVERSITY OF MUNICH / DELL'UNIVERSITÀ LUDWIG MAXIMILIAN DI MONACO

für den Grad des

FOR THE DEGREE OF / PER IL TITOLO DI

Doctor rerum naturalium

vorgelegt von Umberto Maio

PRESENTED BY / PRESENTATA DA

aus Montella, AV (Italy)

FROM / DA

München, 10.10.2008



Sigillum Universitatis Ludovici Maximiliani

1. Gutachter: Prof. Dr. Simon D. M. White

REFeree: / RELATORE:

2. Gutachter: Prof. Dr. Andreas M. Burkert

REFeree: / RELATORE:

Tag der mündlichen Prüfung: 12.12.2008

DATE OF THE ORAL EXAM: / DATA DELL'ESAME ORALE:

Curriculum vitæ et studiorum

Umberto Maio

Personal data

First Name: Umberto
Last name: Maio
Date of birth: 22nd March, 1981
Place of birth: Avellino (Italy)
Citizenship: Italian
Hobbies: Literature, History, Philosophy, reading
Sports: swimming, playing football, cycling, running
Languages: Italian, English, German, Latin

Contacts

✉ *Address:* c/o Max-Planck-Institut für Astrophysik
Karl-Schwarzschild-Straße, 1
D-85748 Garching b. München - M (Germany)
or
via della Libera, 25
83048 Montella, AV (Italy)

☎ *Phone:* +49 (0)89 30 000 2196, +39 (0)827 61275

📱 *Mobile:* +49 (0)176 4714638, +39 (0)328 3826882

@ *E-mail:* maio@mpa-garching.mpg.de, umbertomaio@hotmail.com

Education

2008, 12th December: Ph. D. rer. nat. Ludwig-Maximilians-Universität München
Max-Planck-Institut für Astrophysik (Garching b. München)

2005, 14th July: Laurea in Astronomy,
University of Bologna · Alma Mater Studiorum (Italy)
Faculty of Mathematical, Physical and Natural Sciences
Department of Astronomy
Thesis: *Early structure formation in quintessence models*
Supervisor: Prof. Dr. Lauro Moscardini
Final score: 110 / 110 cum laude
GPA: 29.5 (in 30 point system) and 11 laudes

2000, 21st July: Diploma di Maturità Scientifica,
Liceo Scientifico R. d'Aquino, Montella - AV (Italy)
Final score: 100 / 100

1995 - 2000: Liceo Scientifico R. d'Aquino, Montella - AV (Italy)

1992 - 1995: Scuola Media G. Capone, Montella - AV (Italy)

1987 - 1992: Scuola Elementare G. Palatucci, Montella - AV (Italy)

Research

Subjects: cosmology, cosmic structure formation, gas physics, turbulence
Methods: analytical, numerical and statistical calculations (CFD simulations)

Refereed publications

- ✓ U. Maio, B. Ciardi, N. Yoshida, K. Dolag, L. Tornatore, *The onset of star formation in primordial haloes*, submitted (2008).
- ✓ U. Maio, *Cloud fragmentation and initial mass function from turbulence modeling*, submitted (2008).
- ✓ U. Maio, K. Dolag, B. Ciardi, L. Tornatore, *Metal and molecule cooling in simulations of structure formation*, Mon. Not. R. Astron. Soc., **379**, 963-973 (2007).
- ✓ U. Maio, K. Dolag, M. Meneghetti, L. Moscardini, N. Yoshida, C. Baccigalupi, M. Bartelmann, F. Perrotta, *Early structure formation in quintessence models and its implications for cosmic reionization from first stars*, Mon. Not. R. Astron. Soc., **373**, 869-878 (2006).

Non-refereed publications (proceedings and others)

- ✓ U. Maio, B. Ciardi, K. Dolag, L. Tornatore, N. Yoshida, *Early molecules, star formation and metal pollution*, in press, Paris (2008).
- ✓ U. Maio, B. Ciardi, K. Dolag, L. Tornatore, N. Yoshida, *Onset of star formation and impact on the surroundings*, IAU/CUP Symposium series, in press (2008).
- ✓ U. Maio, B. Ciardi, K. Dolag, L. Tornatore, *Cooling in primordial structure formation*, American Institute of Physics Conf. Proc. **990**, 33 (2008).

Laurea/Master thesis

U. Maio, *Formazione delle prime strutture in modelli cosmologici di quintessenza*, Tesi di Laurea, Alma Mater Studiorum · Università di Bologna (2005). Libro moderno – Monografia – Tesi e dissertazioni – UBO2782561; [2005?]. - VII, 238 p. : ill. ; 30 cm. Tesi ds. di laurea in Astronomia, Università degli studi di Bologna, Facoltà di Scienze matematiche, fisiche e naturali, a.a. 2004/2005.

Umberto Maio

LEARN ALL THE RULES AND
THEN BREAK SOME OF THEM

Nepalese tantra

Contents

Contents	3
Zusammenfassung	13
Abstract	15
Riassunto	17
Introduction	19
Conventions and abbreviations	23
I General overview	25
1 Mathematical description of the Universe	27
1.1 The approach of General Relativity	27
1.1.1 The field equations	28
1.1.2 The geodesics equations	30
1.2 Relativistic cosmology	31
1.2.1 The metric of the Universe from the cosmological principle	32
1.2.2 The Friedmann equations	33
1.2.3 Equation of state, density evolution and temperature evolution	35
1.3 Frequently used cosmological quantities	37
1.3.1 Redshift	37
1.3.2 Density parameters and Friedmann equations	39
1.3.3 Time-redshift relation	41
1.3.4 Distances and expansion of the Universe	42

2	Mathematical description of cosmic structure formation	47
2.1	The global scenario: hot big bang	47
2.2	From primordial fluctuations to structure formation	49
2.2.1	Linear evolution	50
2.2.2	Non-linear evolution	55
2.3	Statistics of structure formation	57
2.4	Dark matter haloes and baryonic structure formation	61
2.4.1	Gas and halo properties	62
2.4.2	Protogalaxies	64
3	Star formation, initial mass function and feedback	69
3.1	First stars and subsequent generations	69
3.2	Stellar system properties	71
3.3	Features of primordial stars	73
3.4	Feedback processes	75
3.4.1	Mechanical feedback	75
3.4.2	Radiative feedback	77
3.4.3	Chemical feedback	77
3.5	Final remark	79
II	Cosmological simulations	81
4	Numerical simulations of early structure formation	83
4.1	Numerical techniques	84
4.1.1	Treatment of gravitation	84
4.1.2	Treatment of fluid-dynamics	86
4.2	The code Gadget	88
4.2.1	Overview	89
4.2.2	Star formation	90
4.2.3	Metal enrichment	92
4.3	Implementation of molecule and metal chemistry	92
4.3.1	Molecules	94
4.3.2	Metals	97

4.3.3	Cooling	99
4.4	Summary	104
5	Tests for star formation, molecule and metal chemistry	105
5.1	Star formation and wind feedback	105
5.2	Redshift evolution of primordial chemical species	112
5.3	Cosmic structure formation from homogeneous initial conditions	114
5.4	Formation and evolution of a cluster	117
5.4.1	Metal fine-structure cooling	118
5.4.2	Adding molecules	121
5.4.3	Star formation and metal pollution history	124
5.5	Summary	127
6	On the onset of star formation	129
6.1	On the onset of star formation events	129
6.2	Threshold for star formation	131
6.3	Simulation set-up	132
6.4	Results	135
6.4.1	Mean-region simulation	135
6.4.2	High-density region simulation	141
6.5	Discussion	144
6.6	Summary	148
7	Early structure formation and critical metallicity	151
7.1	Simulation set-up	151
7.2	Effects of Z_{crit} on SFR	154
7.3	Filling factor and Z_{crit}	159
7.4	Remarks	159
7.5	Summary	160
8	A model for the IMF	163
8.1	Properties of the star forming regions	164
8.2	Turbulence and fragmentation processes	167
8.3	Turbulence and IMF	168

8.3.1	Treatment of turbulence	170
8.3.2	Connection to the IMF	174
8.4	Discussion	178
8.5	Summary	180
9	Conclusions	183
III	Appendices	187
A	Cooling function	189
A.1	Definition of cooling function	189
A.2	Statistical equilibrium of atoms and molecules	189
A.2.1	Collisional rates	190
A.2.2	Radiative rates	193
A.2.3	General expressions	194
B	Star formation rate indicators	197
B.1	Stellar luminosities and star formation	197
B.2	Schmidt law	198
C	Molecular and atomic data	201
C.1	Molecular rates	201
C.2	Metal atomic data	204
D	Entropy	209
E	Gravitational instability and viscous dissipation	211
E.1	Perturbative treatment	211
E.2	Time-scales	214
IV	Bibliography	215

List of Figures

1	Introduction: evolution of cosmological systems	20
1.1	Density parameter evolution (closed, flat, open models)	40
1.2	Density parameter evolution (matter-radiation- Λ model)	41
1.3	Age of the Universe	43
1.4	Measurements of the cosmic expansion rate	45
1.5	Distances	46
2.1	Cosmic microwave background fluctuation map	50
2.2	Density contrast (Λ CDM model)	54
2.3	Spherical “top-hat” model	56
2.4	Matter power spectrum (Λ CDM model)	58
2.5	Mass variance and non-linear scale	59
2.6	Mass functions	61
2.7	H and He cooling	63
2.8	Primordial cooling function (H, He, H ₂ , HD)	66
3.1	IMF comparison	72
3.2	SFR determinations	74
3.3	Scheme of fates of population III stars	76
3.4	Population III SFR	78
4.1	Domain decomposition	86
4.2	SPH technique	88
4.3	Peano-Hilbert curve	89
4.4	Domain decomposition with Peano-Hilbert curve	91
4.5	Rate temperature dependence	95

4.6	Low-temperature cooling functions	101
4.7	Complete cooling function	103
5.1	Schmidt law	107
5.2	Galaxy projection	108
5.3	Galaxy statistics	108
5.4	Galaxy phase diagrams	109
5.5	Galaxy SFR and winds	111
5.6	Primordial abundace evolution	113
5.7	Cosmological temperature maps	115
5.8	Cosmological halo number density	115
5.9	Cosmological gas clumping factor	117
5.10	Cluster projection	119
5.11	Cluster phase diagrams	119
5.12	Cluster maps	122
5.13	Cluster zoom maps	123
5.14	Cluster phase diagrams and abundance distribution	125
5.15	Cluster SFR and metallicity	126
6.1	Cosmological maps	136
6.2	Mean-region phase diagram	137
6.3	Evolution of primordial haloes	139
6.4	Star formation rates	140
6.5	High-density peak phase diagram	143
6.6	H ₂ distribution	145
6.7	Global clumping factors	147
7.1	Maps	153
7.2	Metallicity Maps	153
7.3	SFR comparison	154
7.4	Cosmological metallicity evolution	156
7.5	SFR ratios	157
7.6	Average SFR ratios	158

7.7 Filling factor	160
8.1 Turbulent network in the Large Magellanic Cloud	166
8.2 Cascade process	169
8.3 IMF prediction	178
A.1 Level populations	192
B.1 CO R ratios	199
B.2 Schmidt law	199
C.1 Atomic levels	207

List of Tables

4.1	Set of chemical reactions	93
6.1	Cosmological parameters	134
6.2	Simulation parameters	134
8.1	Measurements of the power spectrum index	173

Zusammenfassung

Sternentstehung (SE) ist ein noch ungelöstes Problem in der Astrophysik. Die Kühlung des Gases ist der hauptsächliche Mechanismus, der zur Kondensation des Gases und danach zur Stern- und Strukturentstehung führt. In einem metallfreien Raum sind H, He, H₂ und HD die wichtigsten verfügbaren Atome und Moleküle, die zur Kühlung beitragen können; Von dem Zeitpunkt an, ab dem das Gas mit Metallen angereichert ist, tragen diese am meisten zur Kühlung bei. Um die SE im frühem Universum zu bestimmen, haben wir in dieser Doktorarbeit die Kühlung durch Feinstrukturübergänge in Metallen berechnet und zusammen mit einem Reaktionsnetzwerk implementiert. Außerdem haben wir die Entwicklung der SE im frühen Universum mit Hilfe von hoch auflösenden, 3D, N-body/Hydrodynamik Simulationen erforscht, unter Berücksichtigung von nichtgleichgewichts- Atom- und Molekülchemie, SE-Vorschriften und Feedbackeffekte. Wir untersuchten auch wie sich die frühe SE verändert, gemäß verschiedener semi-analytischer Ansätze, Kosmologischer Parameter, Anfangsbedingungen und kritischer Metallizitäten (Z_{krit}) für den Übergang von SE aus Gas primordialer, bis hin zu einer mit Metallen angereicherten Zusammensetzung. Unsere wichtigsten Ergebnisse sind: Das H₂-Molekül trägt am meisten zur Kühlung im frühen Universum bei; Eine zusätzliche Kühlung von $\sim 10\% - 20\%$ resultiert von HD-Molekülen in den dichtesten Gebieten des Gases; Kühlung durch Metalle hat speziell bei niederen Temperaturen einen bedeutenden Einfluß auf die Entstehung und Entwicklung von ersten Strukturen; Typische numerische “sub-grid” Modelle liefern nicht die korrekte Kühlung des frühen Gases und sagen vorzeitige SE ($z \sim 30$) vorher; Unter Einbeziehung des Reaktionsnetzwerk finden wir, ausgehend von den gleichen Anfangsbedingungen, ein späteres Einsetzen der SE-Epoche ($z \sim 15$); In seltenen, stark verdichteten Gebieten kann SE sogar ab $z \gtrsim 40$ einsetzen; Aufgrund des sehr kurzen Lebens der ersten Sterne ist die metallfreie SE sogar vernachlässigbar im Vergleich zur gesamten SE-Rate; Sie ist nur für $\Delta z \simeq 1$ (bei $z \sim 16$) relevant; Verunreinigung durch primordiale Metalle bis zu $\sim 10^{-3} Z_{\odot}$ ¹ oder höher verläuft äußerst schnell und ermöglicht einen sehr raschen Übergang zur Standard-SE; Die verschiedenen SE-Raten und Metallanreicherungen für verschiedene Z_{krit} sind gut unterscheidbar und überdecken etwa eine Größenordnung für $Z_{krit}/Z_{\odot} \in [10^{-6}, 10^{-3}]$. Wegen der Relevanz der Ursprünglichen Massenfunktion wird zusätzlich ein analytisches Modell präsentiert, das ihre mögliche Herkunft aus turbulenter Dissipation beschreibt.

¹ Die solare Metallizität ist $Z_{\odot} \simeq 0.02$.

Abstract

Star formation (SF) is still an unsolved problem in astrophysics. Gas cooling is the principal mechanism leading to the condensation of gas and consequently to star and structure formation. In a metal-free environment, the main available coolants are H, He, H₂ and HD; once the gas is enriched with metals, these also become important. In this work, in order to properly determine the SF in the early Universe, we compute fine-structure transition metal cooling and implement and test molecular chemistry. Moreover, we investigate its redshift (z) evolution and compare different modeling running very high-resolution, three-dimensional, N-body/hydrodynamic simulations including non-equilibrium, atomic and molecular chemistry, SF prescriptions and feedback effects. We also study how the primordial SF changes accordingly to different semi-analytical approaches, cosmological parameters, initial set-ups and critical metallicity (Z_{crit}) for the transition from a metal-free SF regime to a standard enriched one.

Our main findings are: the H₂ molecule is the most relevant coolant in early times; inclusion of HD cooling results in a $\sim 10\% - 20\%$ higher gas clumping; metal cooling at low temperatures can have a significant impact on the formation and evolution of first objects; typical numerical “sub-grid” models fail in following the cooling of primordial gas and predict too early SF ($z \sim 30$); considering molecular cooling, we get a postponed epoch ($z \sim 15$) for the same initial conditions; rare, high-density peak can host SF even at $z \gtrsim 40$; metal-free SF regime is completely negligible with respect to the global SF rate, because of the very short first star life-times; it has some relevance only for $\Delta z \simeq 1$ (at $z \sim 16$); primordial pollution up to $\sim 10^{-3} Z_{\odot}$ ¹, or higher, is extremely rapid and allows for a very fast transition to standard SF regimes; the different SF rates and metal enrichment got for different Z_{crit} are well distinguishable and span about one order of magnitude for $Z_{crit}/Z_{\odot} \in [10^{-6}, 10^{-3}]$. Given the importance of the initial stellar mass distribution function, an analytical model describing its possible derivation from turbulent dissipation is presented.

¹ The solar metallicity is $Z_{\odot} \simeq 0.02$.

Riassunto

La formazione stellare (FS) è ancora un problema irrisolto dell’astrofisica. Il raffreddamento del gas è il meccanismo principale che conduce alla condensazione ed, in seguito, alla formazione di stelle e strutture. In assenza di metalli, le specie che raffreddano più efficientemente sono H, He, H₂ e HD; una volta che il gas è stato arricchito di metalli, anch’essi diventano importanti. Nel presente lavoro, al fine di determinare la FS nell’Universo primordiale, calcoliamo il raffreddamento dovuto a transizioni metalliche di struttura fine ed implementiamo e testiamo la chimica molecolare. Inoltre, investighiamo la sua evoluzione in redshift (z) e confrontiamo diversi modelli eseguendo simulazioni N-corpi/idrodinamiche, tridimensionali, ad alta risoluzione che includono chimica al non-equilibrio atomica e molecolare, prescrizioni per la FS ed effetti di auto-regolazione. Studiamo anche il cambiamento della FS a seconda di diversi approcci semianalitici, parametri cosmologici, impostazioni iniziali e metallicità critiche (Z_{crit}) per la transizione da un regime di FS in assenza di metalli ad uno arricchito e standard.

Principalmente, troviamo che: la molecola H₂ rappresenta il modo più rilevante per raffreddare il gas in tempi primordiali; l’inclusione di raffreddamento da HD risulta in una concentrazione di gas più alta del 10% – 20%; il raffreddamento metallico a basse temperature può avere un impatto significativo per la formazione ed evoluzione dei primi oggetti; i tipici modelli numerici “sotto griglia” falliscono nel seguire il raffreddamento di gas primordiale e predicono FS troppo anticipata ($z \sim 30$); considerando il raffreddamento molecolare, otteniamo un’epoca di FS postposta ($z \sim 15$) per le stesse condizioni iniziali; rari picchi ad alta densità possono ospitare FS anche a $z \gtrsim 40$; il regime di FS in assenza di metalli è del tutto trascurabile rispetto al tasso complessivo, a causa dei cortissimi tempi di vita delle prime stelle; esso ha una certa rilevanza solo per $\Delta z \simeq 1$ (a $z \sim 16$); un inquinamento metallico primordiale fino a $\sim 10^{-3} Z_{\odot}$ ¹, o più, avviene in modo estremamente rapido e permette una transizione molto veloce ad un regime di FS standard; i vari tassi di FS e arricchimento metallico per diversi Z_{crit} sono ben distinguibili e ricoprono circa un ordine di grandezza per $Z_{crit}/Z_{\odot} \in [10^{-6}, 10^{-3}]$. Data l’importanza della funzione di distribuzione di massa stellare iniziale, viene presentato un modello per una sua possibile derivazione a partire da dissipazione turbolenta.

¹ La metallicità solare è $Z_{\odot} \simeq 0.02$.

Introduction

Panditur interea domus omnipotentis Olympi

VERGILIUS, AEN., X, 1

One of the greatest challenges for the human mind is the understanding of the *cosmos* we are in. In History, there have been philosophers and scientists who tried to give an explanation of the observable things in many possible ways. Historically, such “world views” (or *Weltanschauungen*) have often influenced the common conception of the Universe, starting from the geocentric Aristotelic-Ptolemaic system (Aristoteles, IVbC; Ptolemy, 150) until the establishment of the heliocentric system (Copernicus, 1543; Galilei, 1610; Kepler, 1619; Galilei, 1623, 1632) and the birth of modern physics based on scientific principles and mathematical description (Newton, 1687; Bernoulli, 1738; D’Alembert, 1743; Kant, 1755; Lagrange, 1788; Poincaré, 1892; Maxwell, 1873; Lamb, 1879; Planck, 1900; Jeans, 1902; Einstein, 1916; Fermi, 1956, etc.).

And sometimes, the very dominant “world view” has influenced the success of certain scientific theories: this is the case for the ancient, Pithagoric, heliocentric vision, overtaken by the Aristotelic one, or, in more recent times, for the very first conception of the Universe as an infinite, evolving system, dating back to the “erethical” monk and philosopher Giordano Bruno (Bruno, 1584), indirectly rehabilitated only in the XX century, with full mathematical support, by the physicist A. Friedmann (Friedmann, 1922) and the astronomer G. Lemaître (Lemaître, 1927).

Nowadays, the emerging picture of an infinite, expanding Universe is accompanied by numerous, complicated, unsolved issues. One of these is the formation and evolution of all the cosmic structures we see today. Indeed, they present an extremely high level of complexity and, in order to address them, it is fundamental to rely on several branches of physics and perform detailed, numerical analyses of the involved variables, with powerful

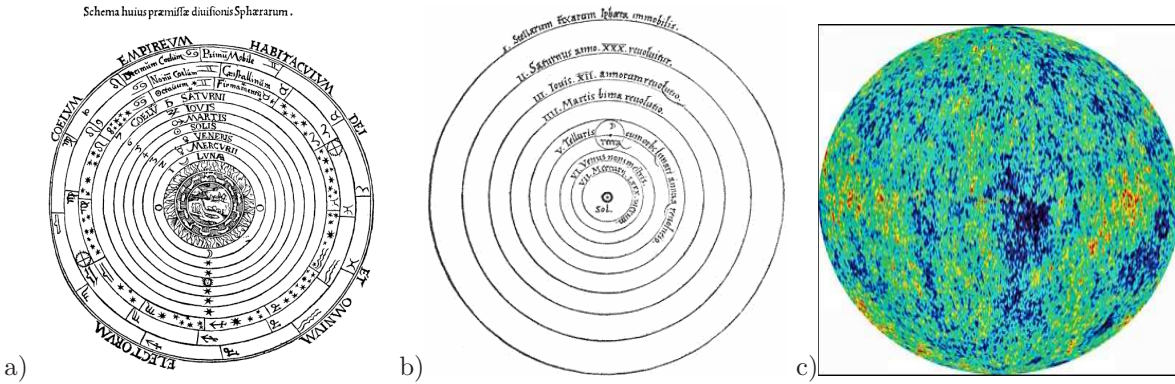


Figure 1: a) Ptolemaic system (Ptolemy, 150) with the Earth in the center and the Moon, the Sun and the planets orbiting around it in circular motion (in order, Earth, Moon, Mercury, Venus, Sun, Mars, Jupiter, Saturn). b) Copernicus’s order of the celestial orbits (Copernicus, 1543, Lib. I, Cap. X). The Sun is in the center; going outwards the circular orbits of the planets (Mercury, Venus, Earth with Moon, Mars, Jupiter, Saturn, Motionless Sphere of Fixed Stars) are traced. c) Bidimensional projective map of the cosmic background temperature fluctuations (Spergel et al., 2007). They correspond to the infinite seeds that grew to become the present-day structures.

means of calculation.

A schematic summary of the different, dominant conceptions of the Universe is given in Figure 1, from the oldest (left panel) to the modern one (right panel).

It efficiently shows how the cosmological scenario has changed during the centuries.

In the present work we will try to stand on the “shoulders” of our great ancestors, but, “looking a bit further” than them, we will also try to give modern justifications to some of the cosmological enigmas we do not understand, yet.

In particular, we will study the main features of cosmic gas and the processes which allow it to condense and form stars, dealing with molecular abundance evolution schemes, calculations of fine-structure transition cooling functions, density threshold models and their implementation in cosmological codes. Such mechanisms, given the amount of computational costs, must necessarily be followed with the help of numerical simulations. Moreover, we will stress the role of chemistry in leading primordial gas cooling and its importance for the formation of the very first objects. Formation of successive generations will be characterized by completely different features, due to the presence of metals spread by previous structures. Therefore, we will also check for the effects of metallicity and its impacts on star formation focusing on the transition from a primordial metal-free regime to a subsequent metal-enriched regime.

The thesis is organized as follows.

After defining our mathematical conventions, we will give a general overview (part I) about the standard approaches to study cosmology (chapter 1), structure formation (chapter 2) and star formation in the Universe (chapter 3).

Then, we will focus on more practical applications in cosmological simulations (part II): we describe the code we have used and the numerical implementation we have done (chapter 4); we discuss the tests we performed in order to test it (chapter 5); we show the resulting implications for the onset of star formation (chapter 6) and the role of metallicity (chapter 7). We conclude presenting a possible derivation of the stellar initial mass function (chapter 8), one of the main observables in astrophysics and one of the fundamental ingredients of our research.

At the end of the work, it is possible to find some appendices (part III) about cooling function (appendix A), star formation rate indicators (appendix B), molecular and atomic data (appendix C), clarifying observations on the definition of entropy (appendix D) and analysis of gravitational instability in viscous environments (appendix E). To finish we give some bibliographic references (part IV).

Conventions, abbreviations and relevant physical quantities

*Quelli che s'innamoran di pratica senza scienza
son come 'l nocchiere ch'entra in navilio senza
timone o bussola, che mai ha certezza dove si vada.*

LEONARDO DA VINCI, SCRITTI LETTERARI

We assume $(+, -, -, -)$ for the the signature of the metric $g^{\mu\nu}$; the components of the Riemann tensor are defined as follows: $R^{\alpha}_{\beta\gamma\delta} = \Gamma^{\alpha}_{\beta\delta,\gamma} - \Gamma^{\alpha}_{\beta\gamma,\delta} + \Gamma^{\alpha}_{s\gamma}\Gamma^s_{\beta\delta} - \Gamma^{\alpha}_{s\delta}\Gamma^s_{\beta\gamma}$, where the Γ s are the Christoffel symbols; in the Einstein equations, the cosmological constant Λ is taken positive, therefore it contributes positively to the energy density and negatively to the pressure.

The speed of light in vacuum is denoted with c ; the sound speed with c_s or v_s ; the expansion parameter, or scale factor, in the FLRW metric and in the Friedmann equations, is indicated with a , the redshift with z .

Regarding the chemical symbols, X stands for the hydrogen mass fraction, Y for the helium mass fraction and Z for the sum of all the mass fractions of the other elements, “metallicity”. As a reference, the solar metallicity, Z_{\odot} , is about 2%.

All the quantities referring to the Sun have the suffix \odot .

Typical distances we deal with are of the order of thousands of *parsec*, *kiloparsec*, kpc, (1 kpc = 10^3 pc), or of millions of *parsec*, *megaparsec*, Mpc, (1 Mpc = 10^6 pc); 1 *parsec*, pc, is defined as the distance at which an observer would see the length Earth-Sun (astronomical unit, *AU*) under the “parallax” angle of one second of arc ($1''$). As $1 AU \simeq 1.49 \cdot 10^{13}$ cm and one radiant $1 \text{ rad} = 206265''$, then $1 \text{ pc} \simeq 3,08567 \cdot 10^{18}$ cm.

An important quantity is the present-day critical density of the Universe: $\rho_{0,cr} = 1.878 \cdot 10^{-29} h^2 \text{ g/cm}^3 = 2.774 \cdot 10^{11} h^2 M_{\odot}/\text{Mpc}^3 = 277.4 h^2 M_{\odot}/\text{kpc}^3$, corresponding to a number density of $n_{0,cr} = \rho_{0,cr}/(\mu m_H) = 1.12 \cdot 10^{-5} \mu^{-1} h^2 \text{ cm}^{-3}$,

where h is the present-day normalized expansion rate of the Universe (about 0.72) and μ the mean molecular weight (about 1.2 for a standard, cosmological, neutral chemical composition having $X = 0.76$, $Y = 0.24$, $Z = 0$).

In the text we have adopted the following mathematical notations for the different kinds of derivatives

$\frac{\partial f}{\partial x^\mu}$ or $\partial_\mu f$ or $f_{,\mu}$	partial derivative of f with respect to the variable x^μ
$\nabla_\mu f$ or $f_{;\mu}$	covariant derivative of f with respect to the variable x^μ
\dot{f}	temporal derivative of f

and the following symbols

\simeq	about equal
\sim	estimate of the magnitude asymptotic behaviour
\approx	approximated
\equiv	equal by definition
\propto	proportional
\rightarrow	react(s) to give
\forall	for all
\in	belong(s)

We remind some important physical and astronomical quantities, in c.g.s. units:

G	gravitational constant	$6.67323 \cdot 10^{-8} \text{ dyn cm}^2 \text{ g}^{-2}$
c	speed of light in vacuum	$2.99792 \cdot 10^{10} \text{ cm s}^{-1}$
\hbar	reduced Planck constant	$1.05457 \cdot 10^{-27} \text{ erg s}$
h	Planck constant	$2\pi\hbar$
k_B	Boltzmann constant	$1.38065 \cdot 10^{-16} \text{ erg K}^{-1}$
N_A	Avogadro number	$6.02214 \cdot 10^{23} \text{ mol}^{-1}$
R	perfect gas constant	$k_B N_A$
σ	Stefan – Boltzmann constant	$5.67040 \cdot 10^{-5} \text{ erg cm}^{-2} \text{ s}^{-1} \text{ K}^{-4}$
σ_r	radiation constant	$4\sigma/c$
m_H	proton mass	$1.67262 \cdot 10^{-24} \text{ g}$
m_e	electron mass	$9.10938 \cdot 10^{-28} \text{ g}$
σ_T	Tomson cross – section	$6.65246 \cdot 10^{-25} \text{ cm}^2$
M_\odot	solar mass	$1.9892 \cdot 10^{33} \text{ g}$
R_\odot	solar radius	$6.9599 \cdot 10^{10} \text{ cm}$
L_\odot	solar luminosity	$3.826 \cdot 10^{33} \text{ erg s}^{-1}$
Z_\odot	solar metallicity	0.02

Part I

General overview

Chapter 1

Mathematical description of the Universe

È dunque l'universo uno, infinito...

BRUNO, DE LA CAUSA, PRINCIPIO ET UNO

We will begin our work discussing the problem of studying the Universe as a whole, in a physical-mathematical context. In particular, we will pay our attention to the principal methods that allow us to describe

I – the space-time on very large (cosmological) scales;

II – the birth and evolution of the cosmic structures “contained” in it.

Gravity will be the main character of such investigations, as it is the only fundamental force dominating the scenario. Therefore, the first issue (discussed in this chapter) will be addressed using Einstein’s theory of General Relativity and the additional assumption of isotropy and homogeneity of the Universe, the cosmological principle (Einstein, 1916, 1917), while the second one will require an approach based on Jeans’s theory of gravitational instability (Jeans, 1902) and on numerical simulations.

For any reference, see Weinberg (1972), Misner et al. (1973), Peebles (1993), Coles and Lucchin (1995), Peacock (1999).

1.1 The approach of General Relativity

The basic idea of Einstein’s theory of gravitation is to look at the interaction among bodies in a geometrical way: each massive body modifies the space-time around it, so that any test particle (either massive or massless) travels along the geodesics in the modified

geometry. In a renowned summarizing motto, *matter tells the space-time how to change and the space-time tells the matter how to move* (Misner et al., 1973).

In this view, the determination of the motion of a test particle in a gravitational field becomes the determination of the metric describing the space-time in which the test particle is moving along the geodesics. The steps to be performed are then:

- given a mass distribution, to determine the metric tensor of the modified space-time geometry;
- computed the metric tensor, to write the equations of motion of a test particle in that geometry.

In the following sections we will address these two points using the standard relativistic formalism. We will adopt Einstein's summation convention, and denote the components of a metric tensor with g_{ij} . By definition, the space-time interval ds will be

$$ds^2 = g_{ij}dx^i dx^j \quad (1.1)$$

with $g_{ij} = g_{ji}$ (symmetry condition of any metric tensor) and g^{ij} the components of the inverse of the metric.

In a 4-dimensional space-time (3-dimensional space plus 1-dimensional time), the number of independent components is 10; often, Roman letters are used for the spatial indices running between 1 and 3 and Greek indices in general when including also the temporal 0th-component. The metrics we deal with are the usual relativistic metrics, so the spatial coordinates have a different sign than the time coordinate and the signature is $(+, -, -, -)$.

1.1.1 The field equations

In order to determine the metric tensor, Einstein proposed the following field equations (Einstein, 1916)

$$G_{\mu\nu} = \kappa T_{\mu\nu} \quad (1.2)$$

where $T_{\mu\nu}$ are the components of the stress-energy tensor describing the distribution of matter, or, better, of the sources of the gravitational field and $G_{\mu\nu}$ are the components of the so-called Einstein tensor, related to the geometry of the space-time.

The stress-energy tensor in 4 dimensions has 16 components, but it is symmetric under reflection of coordinate system (energy does not depend on the sign of the axes), $T_{\mu\nu} = T_{\nu\mu}$,

therefore the independent components are only 10. They are given by the variation of the action S with respect to the metric tensor, times a factor dependent on the speed of light c and on the determinant of the metric g (Landau and Lifshitz, 1975)

$$T_{\mu\nu} = \frac{2c}{\sqrt{-g}} \frac{\delta S}{\delta g^{\mu\nu}} \quad \text{or} \quad T^{\mu\nu} = -\frac{2c}{\sqrt{-g}} \frac{\delta S}{\delta g_{\mu\nu}} \quad (1.3)$$

from which the symmetry is clear. The transition from covariant to contravariant components is done via $g^{\mu\sigma} g_{\sigma\nu} = \delta^\mu_\nu$, implying $\delta g^{\mu\nu} = -g^{\mu\rho} g^{\nu\sigma} \delta g_{\rho\sigma}$. The expression for $G_{\mu\nu}$ is a combination of the Ricci tensor $R_{\mu\nu}$ and the Ricci scalar $\mathcal{R} = g^{\mu\nu} R_{\mu\nu}$:

$$G_{\mu\nu} \equiv R_{\mu\nu} - \frac{1}{2} g_{\mu\nu} \mathcal{R}. \quad (1.4)$$

The Ricci tensor is defined as

$$R_{\mu\nu} = R^\lambda_{\mu\lambda\nu} \quad (1.5)$$

obtained contracting the contravariant component of the Riemann tensor with its second covariant component¹. The components of the Riemann tensor depend on the convention adopted; we define them as:

$$R^\lambda_{\mu\nu\rho} = \Gamma^\lambda_{\mu\rho,\nu} - \Gamma^\lambda_{\mu\nu,\rho} + \Gamma^\lambda_{\sigma\nu} \Gamma^\sigma_{\mu\rho} - \Gamma^\lambda_{\sigma\rho} \Gamma^\sigma_{\mu\nu} \quad (1.6)$$

being

$$\Gamma^\lambda_{\mu\nu} = \frac{1}{2} g^{\lambda\sigma} (g_{\sigma\mu,\nu} + g_{\nu\sigma,\mu} - g_{\mu\nu,\sigma}) \quad (1.7)$$

the Christoffel coefficients and having used the comma for simple derivatives and the semicolon for covariant derivatives². Given these relations, $R_{\mu\nu}$ and $G_{\mu\nu}$ result to be symmetric as well.

The expression (1.2) represents 16 equations of which only 10 are independent, because of the previous symmetry reasons. In virtue of Bianchi's identities ($G^{\mu\nu}{}_{;\nu} = 0$) and the conservation rules ($T^{\mu\nu}{}_{;\nu} = 0$), taking the quadri-divergence of (1.2), we get four identities $0 = 0$, meaning that the problem is well posed.

The constant κ appearing in the field equations (1.2) is calibrated on the Poisson equation

¹ There is only one possible independent contraction.

² For any vector with components V^i , the covariant derivative with respect to the j -th coordinate is

$$V^i{}_{;j} = V^i{}_{,j} + \Gamma^i_{kj} V^k \quad (1.8)$$

and if we consider the covariant derivative for $V_i = g_{ij} V^j$, the plus sign is replaced by a minus sign. For a generic tensor $T^{i_1 i_2 \dots}$ similar rules apply:

$$T^{i_1 i_2 \dots}{}_{j_1 j_2 \dots; k} = T^{i_1 i_2 \dots}{}_{j_1 j_2 \dots, k} + \Gamma^{i_1}{}_{lk} T^{l i_2 \dots}{}_{j_1 j_2 \dots} + \Gamma^{i_2}{}_{lk} T^{i_1 l \dots}{}_{j_1 j_2 \dots} + \dots - \Gamma^l{}_{j_1 k} T^{i_1 i_2 \dots}{}_{l j_2 \dots} - \Gamma^l{}_{j_2 k} T^{i_1 i_2 \dots}{}_{j_1 l \dots} - \dots \quad (1.9)$$

in the classical “static”, “non-relativistic”, “weak field” limit, so that the right Newtonian behaviour at low energies is retrieved. In practice, relations (1.2) are expanded at the first order, and reduced to the only significative relation

$$G_{00} = \kappa T_{00}. \quad (1.10)$$

If we imposes that (1.10) coincides with the Poisson equation

$$\Delta\phi(\mathbf{x}) = 4\pi G\rho(\mathbf{x}) \quad (1.11)$$

where $\phi(\mathbf{x})$ is the gravitational potential and $\rho(\mathbf{x})$ the density distribution at the spatial position \mathbf{x} , this procedure leads to³ $\kappa = 8\pi G/c^4$ and the field equations can be rewritten as

$$R_{\mu\nu} - \frac{1}{2}g_{\mu\nu}\mathcal{R} = \frac{8\pi G}{c^4}T_{\mu\nu}. \quad (1.12)$$

It is now possible to determine $g^{\mu\nu}$ from (1.12), once $T^{\mu\nu}$ is assigned. The addition of a constant term like $\Lambda g_{\mu\nu}$ does not change the conservation laws, as $(\Lambda g^{\mu\nu})_{;\nu} = 0$. The constant Λ is called cosmological constant and was first introduced by Einstein in 1917: long discussions followed and still exist about its physical meaning.

1.1.2 The geodesics equations

The second step is to write down the equations of motion for a test particle moving in a space-time specified by the metric $g^{\mu\nu}$. This is a relatively simple problem, because a test particle falling in a gravitational potential will travel along the geodesics, so the equations of motions are just the equations of the geodesics:

$$\frac{d^2x^\lambda}{d\tau^2} + \Gamma_{\mu\nu}^\lambda \frac{dx^\mu}{d\tau} \frac{dx^\nu}{d\tau} = 0 \quad (1.13)$$

where x^λ are the space-time components of the particle and τ is the variable parameterizing the geodesics, *alias* the proper time. The first term can be seen as the kinematic term, the second one as the potential term arising from the metric hidden in the Christoffel coefficients.

Also these equations lead to the correct classical limit

$$\ddot{x}^i = -\frac{\partial\phi(x)}{\partial x_i} \quad (1.14)$$

³ The expression for κ depends on the conventions: sometimes a c^2 is included in the stress-energy tensor obtaining $\kappa = 8\pi G/c^2$, or the Riemann tensor is defined with the opposite sign getting $\kappa = -8\pi G/c^4$. The value $\kappa = -8\pi G/c^2$ is obtained if the c^2 is included in $T_{\mu\nu}$ and the Riemann tensor is defined with a different sign. In his original work, Einstein used $\kappa = 8\pi G/c^2 \simeq 1.87 \cdot 10^{-27} \text{ dyn s}^2 \text{ g}^{-2}$ (Einstein, 1916). Anyway, for possible notations see also Weinberg (1972); Misner et al. (1973); Landau and Lifshitz (1975).

if we identify the gravitational potential with the perturbation h_{00} of the temporal component of the Minkowskian metric, $\eta_{\mu\nu} = \text{diag}(1, -1, -1, -1)$,

$$\phi(\mathbf{x}) = \frac{c^2}{2}h_{00}(\mathbf{x}) + \text{constant} \quad (1.15)$$

with the “static”, “non-relativistic”, “weak field” conditions

$$g_{\mu\nu} = \eta_{\mu\nu} + h_{\mu\nu} \quad \text{and} \quad |h_{\mu\nu}| \ll 1. \quad (1.16)$$

In practice, in equations (1.13) one expands all the terms up to the first order in $h_{\mu\nu}$, finds three equations binding the accelerations \ddot{x}^i with the gradient of h_{00} and imposes (1.15), in order to get (1.14). The “weak field” condition $|h_{\mu\nu}| \ll 1$ reads then

$$\frac{2|\delta\phi|}{c^2} \equiv \frac{2|\phi(\mathbf{x}_2) - \phi(\mathbf{x}_1)|}{c^2} \ll 1 \quad (1.17)$$

being $\delta\phi$ the difference of potential at two different points \mathbf{x}_1 and \mathbf{x}_2 .

The geodesics equations (1.13) justify the weak equivalence principle on the equality of inertial and gravitational mass, according to which, the motion of a test particle in a gravitational field does not depend on its mass.

Conceptually, the problem is solved: one takes the stress-energy tensor $T^{\mu\nu}$ of the system studied, solves for the metric $g_{\mu\nu}$ in the field equations (1.12) and eventually computes the $\Gamma^\lambda_{\mu\nu}$ and determines the motion of a test particle x^λ via (1.13).

Nonetheless, in reality there are a lot of complications due to the fact that it is not always possible to give appropriate stress-energy tensors to any system, or to solve the field equations and deduce $g_{\mu\nu}$. Even if some exact solutions are known, often further hypotheses or approximations must be introduced. In cosmology we will manage to get a metric tensor adding a *cosmological principle* that will allow us to establish the evolution of the Universe from the field equations themselves.

1.2 Relativistic cosmology

We have seen the two steps on which Einstein’s Relativity is based. We will now apply such concepts to cosmology and build a mathematical model of the Universe. The goal will be reached introducing the

- cosmological principle

from which it will be possible to extract a form for the metric. The first attempts in this regard, trace back to the early decades of the XX century, to Einstein, Friedmann, Lemâitre, Robertson and Walker.

1.2.1 The metric of the Universe from the cosmological principle

General Relativity is a classical field theory and therefore it deals with continuous distributions of gravitational sources. On the other hand, we know well that matter is not distributed in a continuous way, so it is fundamental to point out that the main approximation is to consider the Universe as filled with a “fluid of matter” whose description is feasible in terms of the stress-energy tensor. In addition, it is not possible to know such tensor at each point of the Universe, simply because the Universe is infinite. So, to determine the metric, it is necessary to introduce some additional hypotheses.

The basic assumption is then that the cosmic fluid is spatially isotropic and homogeneous. More precisely,

- *isotropic* with respect to a given point means that its properties are the same in each direction, at that given point;
- *homogeneous* means that it is isotropic with respect to any point.

These two statements constitute the so-called *cosmological principle* or *principle of homogeneity and isotropy of the Universe* and allow a determination of the metric avoiding the field equations.

Let’s consider a reference frame comoving with a locally inertial observer; the coordinates of any event measured by this observer will be called comoving coordinates and the generic space-time interval satisfying the cosmological principle can be written as

$$ds^2 = (cdt)^2 - a^2(t)dl^2, \quad (1.18)$$

being $a(t)$ a scale factor, which takes into account a possible evolution of the metric with time, t (this does not violate the spatial isotropy and homogeneity of the Universe), and dl the infinitesimal, comoving line element, whose form depends on the geometry. Mathematically, it is possible to prove that there are only three forms for the comoving line element satisfying the cosmological principle, corresponding to the only three possible

homogeneous spaces. Namely,

$$ds^2 = (cdt)^2 - a^2(t) \left[\frac{dr^2}{1 - Kr^2} + r^2(d\theta^2 + \sin^2 \theta d\varphi^2) \right] \quad (1.19)$$

where

$$\begin{cases} K = 0 & \text{for flat spaces (Euclidean geometry);} \\ K > 0 & \text{for closed spaces (hyper - spheric geometry);} \\ K < 0 & \text{for open spaces (hyperbolic geometry).} \end{cases} \quad (1.20)$$

The quadratic form (1.19) is known as the ‘‘Friedmann-Lemâitre-Robertson-Walker’’ (FLRW) metric.

It is always possible to re-define simultaneously K and $a(t)$ to reduce the values of the geometric parameter K to $k = 0, +1, -1$, respectively. Moreover, the FLRW metric (1.19) is conformally flat for $K = 0$ and is enough to introduce the conformal time

$$d\tau = \frac{dt}{a(t)}, \quad (1.21)$$

to get immediately, from equation (1.19),

$$ds^2 = a^2(\tau) \left[(cd\tau)^2 - \frac{dr^2}{1 - Kr^2} - r^2(d\theta^2 + \sin^2 \theta d\varphi^2) \right] \quad (1.22)$$

and, for null spatial curvature,

$$ds^2 = a^2(\tau) [(cd\tau)^2 - dr^2 - r^2(d\theta^2 + \sin^2 \theta d\varphi^2)]. \quad (1.23)$$

So far, we have not yet used the field equations, but we have got a metric from the cosmological principle only.

1.2.2 The Friedmann equations

To know how the metric evolves in time we can now use the field equations substituting the expression (1.19) in (1.12) and using the perfect fluid tensor in curved spaces

$$T_{\mu\nu} = (P + \rho c^2)U_\mu U_\nu - P g_{\mu\nu}. \quad (1.24)$$

Here, ρ is the energy density, P the pressure, U_μ the components of the four-velocity, $g_{\mu\nu}$ the components of the metric tensor.

As we said, the relations (1.2) or (1.12) represent 10 independent equations, but we need to know only the evolution of $a(t)$ and, indeed, one finds that

1. the equation relative to the temporal indices

$$G_{00} = \kappa T_{00}$$

gives (“dynamic equation”)

$$\ddot{a} = -\frac{4}{3}\pi G \left(\rho + \frac{3P}{c^2} \right) a \quad (1.25)$$

2. the three equations relative to the spatial indices

$$G_{ii} = \kappa T_{ii}$$

reduce to (“energy equation”)

$$\dot{a}^2 + Kc^2 = \frac{8}{3}\pi G \rho a^2 \quad (1.26)$$

3. the six (independent) equations relative to the mixed indices

$$G_{\mu\nu} = \kappa T_{\mu\nu}, \quad (\mu \neq \nu)$$

are identically zero.

The equations (1.25) and (1.26) are called “Friedmann equations” and describe the dynamical evolution of an isotropic and homogeneous Universe, via $a(t)$: they can be bound to each other adding the usual adiabaticity condition

$$d(\rho c^2 a^3) + P da^3 = 0. \quad (1.27)$$

Therefore, the three equations (1.25), (1.26) and (1.27) form a set of equations of which only two are independent.

In the presence of a cosmological constant, the Friedmann equations result slightly modified as one has to consider an additional term in the field equations

$$G_{\mu\nu} - \Lambda g_{\mu\nu} = \frac{8\pi G}{c^4} T_{\mu\nu} \quad (1.28)$$

or formally to substitute

$$\tilde{T}_{\mu\nu} = T_{\mu\nu} + \frac{c^4}{8\pi G} \Lambda g_{\mu\nu} \equiv T_{\mu\nu} + T_{\mu\nu}^{\Lambda}, \quad (1.29)$$

$$\tilde{\rho} = \rho + \frac{\Lambda c^2}{8\pi G} \equiv \rho + \rho_{\Lambda}, \quad (1.30)$$

$$\tilde{P} = P - \frac{\Lambda c^4}{8\pi G} \equiv P + P_{\Lambda} \quad (1.31)$$

so the following Friedmann equations are obtained:

$$\ddot{a} = -\frac{4}{3}\pi G \left(\rho + \frac{3P}{c^2} \right) a + \frac{\Lambda}{3} c^2 a \quad (1.32)$$

$$\dot{a}^2 + Kc^2 = \frac{8}{3}\pi G \rho a^2 + \frac{\Lambda}{3} c^2 a^2. \quad (1.33)$$

These results are extremely important, because they show that the Universe is expanding with an acceleration different from zero (1.32). In the absence of a cosmological constant the Universe decelerates, but the presence of Λ can make it accelerate or pass from a decelerated phase to an accelerated phase. It is interesting to stress that the geometry of the universe is involved only in the (1.33).

An interesting particular case is the Einstein-de Sitter cosmological model: it is a flat, matter only model, without cosmological constant, $\Lambda = 0$.

1.2.3 Equation of state, density evolution and temperature evolution

To completely close the system and determine the thermodynamical evolution of the Universe we still need an equation of state, a relation between pressure and density. Usually it is parametrized as

$$P = w\rho c^2 \quad (1.34)$$

with w equation of state parameter, related to the cosmic fluid considered. For matter only, a suitable modeling is based on the “dust fluid”, i.e. a perfect, non-relativistic gas of non-interacting particles. Such a fluid has

$$P = nk_B T = \rho c^2 \left(\frac{k_B T}{mc^2} \right) \simeq 0 \quad (1.35)$$

where n is the gas number density, k_B the Boltzmann constant, T the temperature and m the particle mass. Equation (1.35) implies $w = 0$.

For radiation, we know that

$$P = \frac{1}{3}\rho c^2 \quad (1.36)$$

with ρc^2 energy density; therefore $w = 1/3$.

The cosmological constant has instead

$$P = -\rho c^2 \quad (1.37)$$

and $w = -1$, because of the relations (1.30) and (1.31).

Given the equation of state for a certain fluid, the resulting sound speed in that fluid is

$$c_s^2 = \left(\frac{\partial P}{\partial \rho} \right)_S = wc^2; \quad (1.38)$$

the suffix S indicates constant entropy.

The equation of state written as in (1.34) allows us to express in an easy way the evolution of the different components of the cosmic fluid: substituting it in the adiabatic condition (1.27), we obtain

$$\rho(a) = \rho_0 \left(\frac{a}{a_0} \right)^{-3(1+w)} \quad (1.39)$$

where ρ_0 and a_0 are the value of the density and of the expansion parameter at the present day. For this scaling, it is common to find the normalization $a_0 \equiv 1$.

Relation (1.39) leads to $\rho(a) \sim a^{-3}$ for matter, $\rho(a) \sim a^{-4}$ for radiation and $\rho(a) \sim \text{constant}$ for Λ .

Furthermore, simple thermodynamical considerations for the energy density and the equation of state in the adiabatic condition (1.27) lead, for perfect gas, to

$$d \left(\frac{3}{2} n k_B T_m a^3 \right) + n k_B T_m da^3 = 0 \quad (1.40)$$

with n number density evolving as $\sim a^{-3}$, according to (1.39), k_B Boltzmann constant and T_m matter temperature. For radiation at temperature T_r with a black-body spectrum, the differential equation

$$d (\sigma_r T_r^4 a^3) + \frac{1}{3} \sigma_r T_r^4 da^3 = 0 \quad (1.41)$$

holds. In fact, the energy density is the integral over the frequency ν of the spectral energy density

$$u(T_r, \nu) = \frac{8\pi}{c^3} \frac{h\nu^3}{e^{h\nu/k_B T_r} - 1} \quad (1.42)$$

and it is given by $\sigma_r T_r^4$, being σ_r the black-body constant, while the radiation pressure is 1/3 the energy density. A two-fluid – matter and radiation in thermodynamical equilibrium – universe is described by

$$d \left[\left(\frac{3}{2} n k_B T_m + \sigma_r T_r^4 \right) a^3 \right] + \left(n k_B T_m + \frac{1}{3} \sigma_r T_r^4 \right) da^3 = 0. \quad (1.43)$$

Integrating relations (1.40), (1.41) and (1.43), it is easy to retrieve the evolution of matter and radiation temperatures. Indeed, relations (1.40) and (1.41) give

$$T_m = T_{0,m} \left(\frac{a}{a_0} \right)^{-2} \quad (1.44)$$

$$T_r = T_{0,r} \left(\frac{a}{a_0} \right)^{-1} \quad (1.45)$$

respectively. In the early phases, radiation and matter are “hot”, therefore, only in this regime the hypothesis of thermodynamical equilibrium between these two components is reasonable and the equilibrium temperature $T \equiv T_m = T_r$ in (1.43) has a behaviour ruled by

$$\frac{dT}{T} = - \left(\frac{\sigma_{rad} + 1}{\sigma_{rad} + 1/2} \right) \frac{da}{a} \quad (1.46)$$

with σ_{rad} radiation entropy per baryon⁴

$$\sigma_{rad} = \frac{4\sigma_r T_r^3}{3nk_B} = \frac{4\sigma_r T_{0,r}^3}{3n_0 k_B}, \quad (1.47)$$

where n_0 is the matter number density at the present time. As the constant $\sigma_{rad} \gg 1$, the solution is $T \sim a^{-1} \sim T_r$: the plasma is radiation dominated.

1.3 Frequently used cosmological quantities

In this section we will define some important quantities, which are commonly used in cosmology. The most relevant is without any doubt the expansion parameter

$$H \equiv \frac{\dot{a}}{a} \quad (1.48)$$

because it describes the evolution of the Universe, as it is directly related to (1.32) and (1.33). The local value of H is typically referred to as H_0 . Often it is convenient to define the additional adimensional parameter h normalized via $H_0 \equiv 100 h \text{ km/s/Mpc}$. In the following, we will define some more handy quantities.

1.3.1 Redshift

A very useful quantity is the redshift, z , because it is easily measured by observers. It is defined as:

$$z \equiv \frac{\Delta\lambda}{\lambda_{em}} = \frac{\lambda_{obs} - \lambda_{em}}{\lambda_{em}} = \frac{\lambda_{obs}}{\lambda_{em}} - 1 = \frac{\nu_{em}}{\nu_{obs}} - 1 \quad (1.49)$$

where λ_{obs} and λ_{em} are the wavelengths of the radiation observed on Earth and emitted by a certain source, respectively; similarly, ν_{obs} and ν_{em} are the frequencies observed on Earth and emitted by the same source, respectively. Using the standard relativistic relations, the chain of formulæ (1.49) is equivalent to

$$1 + z = \frac{\lambda_{obs}}{\lambda_{em}} = \frac{\nu_{em}}{\nu_{obs}} = \sqrt{\frac{c+v}{c-v}} \stackrel{v \ll c}{\approx} 1 + \frac{v}{c} + \mathcal{O}\left(\frac{v^2}{c^2}\right) \quad (1.50)$$

⁴ This adimensional quantity is basically the entropy of radiation per unit volume, $\sim 4\sigma_r T_r^3/3$, divided by the entropy of gas per unit volume, $\sim nk_B$.

where v is the velocity of the source and c the velocity of the electromagnetic waves. From the latter steps,

$$\frac{v}{c} = \frac{(1+z)^2 - 1}{(1+z)^2 + 1} \quad (1.51)$$

and it follows

$$1 + z_{12} = \frac{1 + z_2}{1 + z_1} \quad (z_1 < z_2) \quad (1.52)$$

where z_{12} is the redshift difference between two points at redshifts z_1 and z_2 . Differentiating relations (1.50), one gets

$$\frac{dz}{1+z} = \frac{dv}{c} \left(1 - \frac{v^2}{c^2}\right)^{-1} \underset{v \ll c}{\approx} \frac{dv}{c} + \mathcal{O}\left(\frac{v^2}{c^2}\right) \quad (1.53)$$

and can interpret dv as the *peculiar velocity* if dz is the shift from the cosmological redshift due to the peculiar motion ($z_{measured} - z_{cosmological}$).

The variable z is moreover bound to the scale factor a . In fact, according to the line element (1.19) we can define the function

$$f(r) \equiv \int_0^r \frac{dr'}{\sqrt{1 - kr'^2}} \quad (r \geq 0) \quad (1.54)$$

and solving the integral

$$f(r) = \begin{cases} \arcsin r & k = 1 \\ r & k = 0 \\ \operatorname{arcsinh} r & k = -1 \end{cases} . \quad (1.55)$$

Because (1.19), for any light signal connecting the origin with a certain point at the coordinate r and at the instant t , along the geodesics ($ds^2 = 0$):

$$\int_0^r \frac{dr'}{\sqrt{1 - kr'^2}} = \int_t^{t_0} \frac{cdt'}{a(t')} \quad (t \leq t_0) \quad (1.56)$$

where t_0 is the arrival time and $t_0 - t$ is the time spent to cover the path $[0, r]$.

In particular, let's consider two different instants t_{em} and $t_{em} + \delta t_{em} > t_{em}$, during which the space-time experiences expansion, while $f(r)$ does not change because it is a function of the comoving coordinate. In this case,

$$f(r) = \int_{t_{em}}^{t_{obs}} \frac{cdt'}{a(t')} = \int_{t_{em} + \delta t_{em}}^{t_{obs} + \delta t_{obs}} \frac{cdt'}{a(t')} \quad (1.57)$$

where t_{obs} and $t_{obs} + \delta t_{obs}$ are the respective arrival times. From (1.57), for small time intervals, it follows that $\delta t_{em}/a_{em} = \delta t_{obs}/a_{obs}$ and therefore, in frequencies and wavelengths:

$$\nu_{em} a_{em} = \nu_{obs} a_{obs} \quad \text{and} \quad a_{em}/\lambda_{em} = a_{obs}/\lambda_{obs}, \quad (1.58)$$

respectively. From a comparison with (1.50), we have

$$1 + z = \frac{a_{obs}}{a_{em}}. \quad (1.59)$$

In virtue of this relation, all the previous equations (Friedmann equations, adiabaticity condition, density or temperature evolution etc.) can be read as a function of z , instead of a .

1.3.2 Density parameters and Friedmann equations

The density for which, in the case $\Lambda = 0$, the Universe is always flat (spatial curvature $K = 0$) is called the critical density:

$$\rho_{cr}(t) \equiv \frac{3H^2(t)}{8\pi G}, \quad (1.60)$$

as one may easily see from equations (1.33) and (1.48). The density parameter for the generic component of cosmic fluid with equation of state parameter w is defined as:

$$\Omega_w(t) \equiv \frac{\rho_w(t)}{\rho_{cr}(t)}, \quad (1.61)$$

and the redshift dependence is given, through equations (1.39) and (1.59), by

$$\rho_w(z) = \rho_{0,w}(1+z)^{3(1+w)}. \quad (1.62)$$

The cosmological constant parameter computed at the present time is:

$$\Omega_{0\Lambda} = \frac{\Lambda c^2}{3H_0^2}, \quad (1.63)$$

because of (1.30).

By differentiating the definition (1.48), the Friedmann equation for \ddot{a} (1.25) is related to H via $\ddot{a} = a(\dot{H} + H^2)$.

With the previous definitions and (1.59), the Friedmann equation (1.26) can be written as

$$H^2(z) = H_0^2 \left[(1 - \Omega_{0,tot})(1+z)^2 + \Omega_{0,m}(1+z)^3 + \Omega_{0,r}(1+z)^4 + \Omega_{0,\Lambda} \right] \equiv H_0^2 E^2(z) \quad (1.64)$$

being $\Omega_{0,tot}$, $\Omega_{0,m}$, $\Omega_{0,r}$ the present-day total, matter and radiation density parameter, respectively.

The quantity $H(z)$ evolves as a power law, according to the dominant component and it is

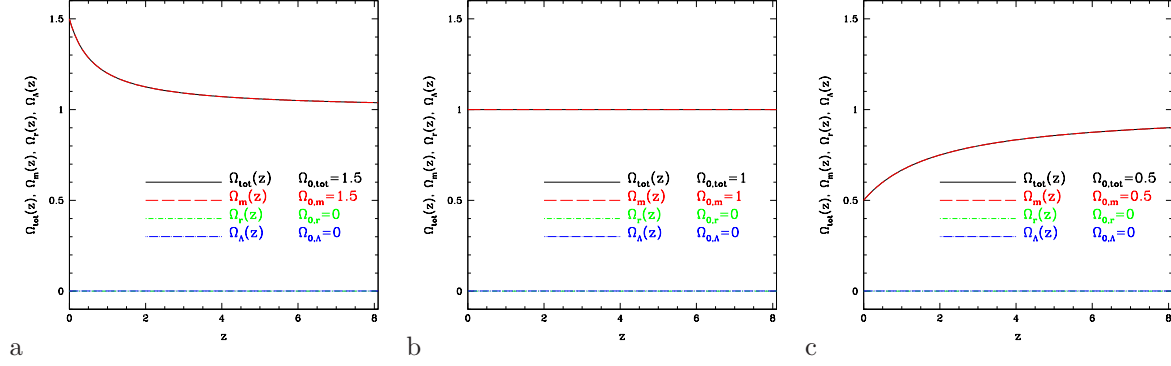


Figure 1.1: Evolution of density parameters in a closed (a), flat (b) and open (c) matter only model with $\Omega_{0,tot} = \Omega_{0,m} = 1.5, 1, 0.5$, respectively. Contributions from radiation and cosmological constant are null.

straightforward to see that, in a matter dominated universe at high redshift, it converges to the Einstein-de Sitter case.

The evolution of ρ_{cr} as a function of z is, by definition,

$$\rho_{cr}(z) = \frac{3H_0^2 E^2(z)}{8\pi G} \equiv \rho_{0,cr} E^2(z). \quad (1.65)$$

For (1.60), (1.61) and (1.65),

$$\Omega_w(z) = \frac{\rho_{0,w}(1+z)^{3(1+w)}}{\rho_{0,cr} E^2(z)} = \frac{\Omega_{0,w}(1+z)^{3(1+w)}}{E^2(z)} \quad (1.66)$$

and, consistently with relation (1.62), we can write

$$\rho_w(z) = \Omega_w(z) \rho_{cr}(z) = \Omega_{0,w} \rho_{0,cr} (1+z)^{3(1+w)}. \quad (1.67)$$

For flat cosmologies, indicating with i the different fluid components, $E^2(z) = \sum_i \Omega_{0,w_i} (1+z)^{3(1+w_i)}$ and

$$\sum_i \Omega_{w_i}(z) = 1 = \sum_i \Omega_{0,w_i} \quad \forall z \geq 0. \quad (1.68)$$

The behaviour of the different density parameters in different cosmologies is shown in Figure 1.1 and in Figure 1.2. In Figure 1.1, we show the evolution of density parameters in a closed (a), flat (b) and open (c) model, with $\Omega_{0,tot} = \Omega_{0,m} = 1.5, 1$ and 0.5 , respectively. In Figure 1.2, we plot the same quantities in a cosmological constant dominated scenario with $\Omega_{0,tot} = 1$, $\Omega_{0,m} = 0.3$, $\Omega_{0,\Lambda} = 0.7$, $\Omega_{0,r} = 0$ (left panel), $\Omega_{0,r} = 10^{-4}$ (right panel).

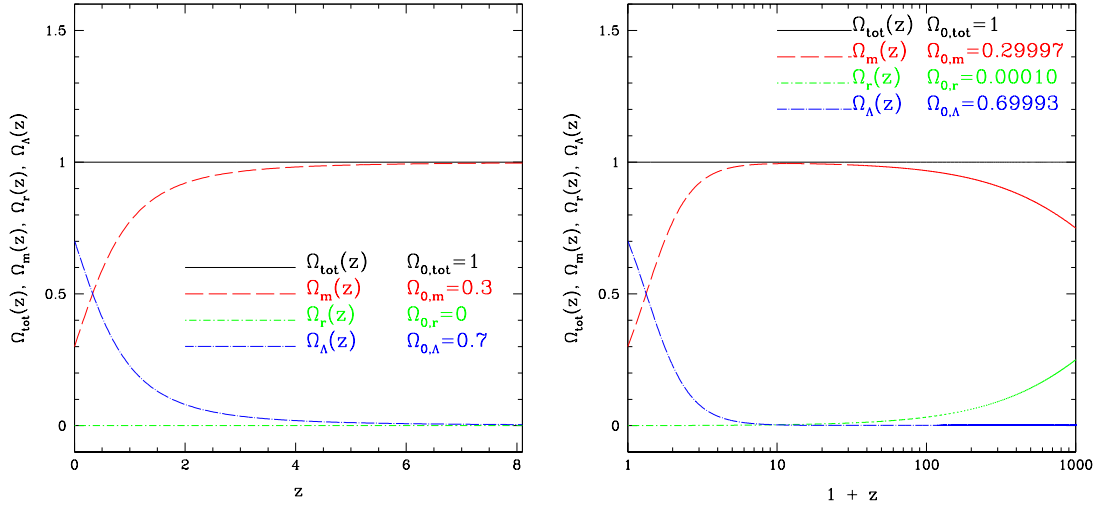


Figure 1.2: Left panel: evolution of density parameters for a cosmological model with $\Omega_{0,tot} = 1$, $\Omega_{0,m} = 0.3$, $\Omega_{0,\Lambda} = 0.7$. Contribution from radiation, $\Omega_{0,r}$, is null. Right panel: as in the left panel, but with a contribution from radiation of 10^{-4} .

1.3.3 Time-redshift relation

Differentiating the definition of redshift (1.59), one gets

$$\frac{\dot{z}}{1+z} = -\frac{\dot{a}}{a} = -H \quad (1.69)$$

and

$$dt = -\frac{dz}{(1+z)H(z)} = -\frac{1}{H_0} \frac{dz}{(1+z)E(z)} = -t_H \frac{dz}{(1+z)E(z)} \quad (1.70)$$

where we have defined

$$t_H \equiv \frac{1}{H_0} \simeq 3.0857 \cdot 10^{17} h^{-1} \text{ s} \simeq 9.7958 h^{-1} \text{ Gyr}. \quad (1.71)$$

The time elapsed between the Big Bang ($z \rightarrow +\infty$) and redshift z is

$$t(z) = \int_z^{+\infty} \frac{dz'}{(1+z')H(z')} = t_H \int_z^{+\infty} \frac{dz'}{(1+z')E(z')}. \quad (1.72)$$

This formula is the time-redshift relation and allows us to link the main observable, z , with the time, t , it corresponds to. The age of the Universe, t_{age} , is obtained by integrating (1.72) from $z = 0$. The look-back time (from ‘now’ up to redshift z) is instead $t_{LB}(z) \equiv t_{age} - t(z)$:

$$t_{LB}(z) = \int_0^{+\infty} \frac{dz'}{(1+z')H(z')} - \int_z^{+\infty} \frac{dz'}{(1+z')H(z')} = \int_0^z \frac{dz'}{(1+z')H(z')} \quad (1.73)$$

and allows us to link the redshift z where a given object is situated with the time needed to a light ray emitted from a source in the origin of coordinates to reach it.

In a flat, matter only cosmology (Einstein-de Sitter model), relation (1.64) for H becomes

$$H(z) = H_0 \sqrt{\Omega_{0,m}} (1+z)^{3/2} \quad (1.74)$$

with $\Omega_{0,m} = \Omega_{0,tot} = 1$. Therefore,

$$t(z) = \frac{2}{3H_0 \sqrt{\Omega_{0,m}}} (1+z)^{-3/2} = \frac{2}{3} t_H (1+z)^{-3/2} \quad (1.75)$$

and

$$t_{age} = \frac{2}{3H_0 \sqrt{\Omega_{0,m}}} = \frac{2}{3} t_H \simeq 9.3 \left(\frac{h}{0.7} \right)^{-1} \text{ Gyr.} \quad (1.76)$$

Because of what discussed in the previous section, it is obvious that any matter dominated cosmology at high redshift behaves as an Einstein-de Sitter model.

In Figure 1.3, the age of the Universe according to different models is shown. The asymptotic convergence to the Einstein-de Sitter case, at large z , is clearly seen.

1.3.4 Distances and expansion of the Universe

The line element (1.19) allows us to define different types of distances. Using the definition for $f(r)$ in (1.54), we can express it in the following way:

$$f(r) = \int_t^{t_0} \frac{cdt'}{a(t')} = \int_a^{a_0} \frac{c da'}{a' \dot{a}'} = \int_a^{a_0} \frac{c}{a'^2} \frac{da'}{H(a')} = \frac{c}{a_0} \int_0^z \frac{dz'}{H(z')} \quad (1.77)$$

with $a \leq a_0$ and $z \geq 0$. It is found then

$$r = f^{-1} \left(\int_0^r \frac{dr'}{\sqrt{1 - kr'^2}} \right) = f^{-1} \left(\frac{c}{a_0} \int_0^z \frac{dz'}{H(z')} \right). \quad (1.78)$$

This has a simple analytical solution for matter only universes, $w = 0$, for any $\Omega_0 = \Omega_{0,m} = \Omega_{0,tot}$ (Mattig's formula):

$$r = \frac{2c}{a_0 H_0} \frac{\Omega_0 z + (\Omega_0 - 2) (\sqrt{\Omega_0 z + 1} - 1)}{\Omega_0^2 (1+z)}. \quad (1.79)$$

There exist also non simple, analytical expressions for universes made of matter, radiation and Λ , too (Dabrowski and Stelmach, 1987, and references therein), but we will not go into details.

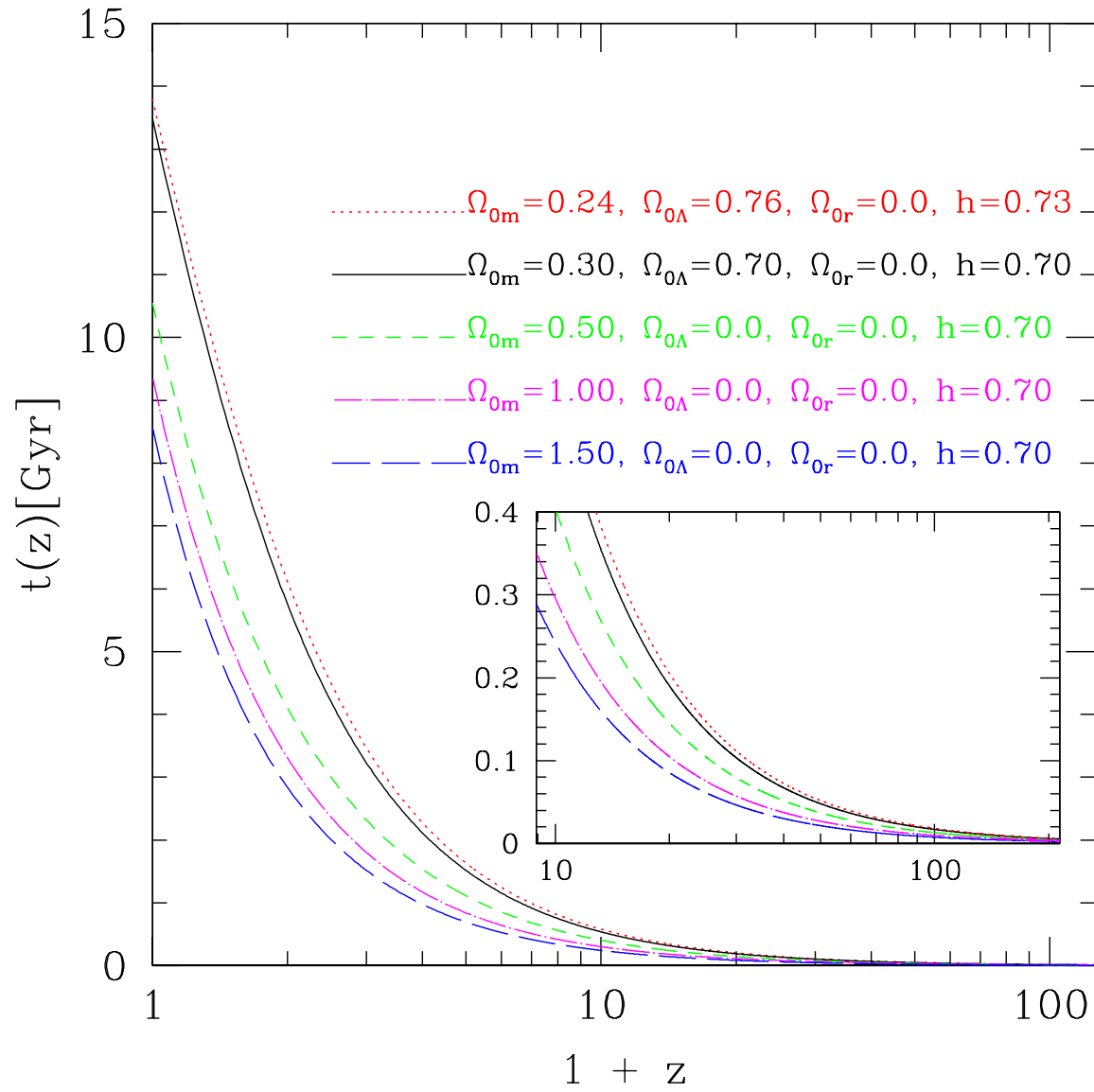


Figure 1.3: The age of the Universe according to different cosmological models, as indicated from the labels, is shown. All the predictions have the same asymptotic behaviour at high z coinciding with the Einstein-de Sitter model (dotted-dashed purple line). The inset is a zoom of $t(z)$ [Gyr], for $1+z \in [9, 200]$.

The proper distance of a point whose radial coordinate with respect to the origin is r (and corresponds to redshift z) is:

$$d_{PR}(r) \equiv a \int_0^r \frac{dr'}{\sqrt{1-kr'^2}} = af(r) = \left(\frac{a}{a_0}\right) a_0 f(r) \quad (1.80)$$

(basically it is the radial distance according to the FLRW metric). Defining

$$D_H \equiv \frac{c}{H_0} \simeq 9.25 \cdot 10^{27} h^{-1} \text{ cm} \simeq 2997.9 h^{-1} \text{ Mpc} \quad (1.81)$$

where c is the speed of light, one has also

$$d_{PR}(z) = \frac{c}{1+z} \int_0^z \frac{dz'}{H(z')} = \frac{D_H}{(1+z)} \int_0^z \frac{dz'}{E(z')} \quad (1.82)$$

or, as a function of a ,

$$d_{PR}(a) = ac \int_a^{a_0} \frac{da'}{\dot{a}'^2 H(a')} = a D_H \int_a^{a_0} \frac{da'}{\dot{a}'^2 E(a')}. \quad (1.83)$$

By definition of proper distance, equation (1.80), and by differentiating with respect to time, one easily finds the velocity-distance relation

$$v = \dot{a}f(r) = \frac{\dot{a}}{a} af(r) = H d_{PR} \quad (1.84)$$

relating the distance of a point with its recession velocity from the observer. This is a clear evidence of the expansion of the Universe, with a rate H_0 which is about 70 km/s/Mpc ($h \simeq 0.7$). Observational determinations of H_0 are quoted in Figure 1.4. The very first data suggested $H_0 \simeq 500$ km/s/Mpc ($h \simeq 5$), more recent data $H_0 \simeq 72$ km/s/Mpc ($h \simeq 0.72$).

The comoving distance is instead defined as the proper distance computed at the present day:

$$d_{com} \equiv d_{PR}(a_0) = a_0 f(r) = c \int_0^z \frac{dz'}{H(z')} = D_H \int_0^z \frac{dz'}{E(z')}. \quad (1.85)$$

By comparing equations (1.82) and (5.4), it is found

$$d_{PR} = \frac{d_{com}}{1+z} \quad (1.86)$$

In a flat, matter only universe,

$$d_{com} = a_0 r = 2D_H \frac{\Omega_0 z + (\Omega_0 - 2) (\sqrt{\Omega_0 z + 1} - 1)}{\Omega_0^2 (1+z)} \quad (1.87)$$

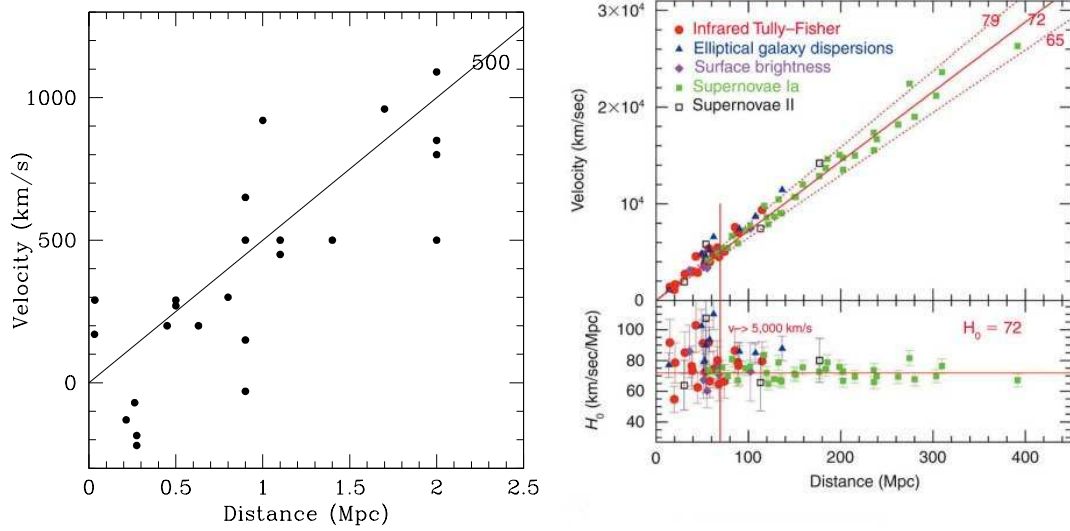


Figure 1.4: Left panel: first measurement of the H_0 parameter using Cepheid method for 24 Nebulae within 2 Mpc distance from Earth; the plot reproduces the data quoted by Hubble (1929); Hubble and Humason (1931): the solid straight line has a slope of 500 km/s/Mpc. The very large scatter due to peculiar motions which dominates over the cosmic expansion over such small distances is evident. It is also clear the presence of blue-shifted points (negative/approaching velocities). Right panel: measures of the local expansion rate H_0 (Freedman et al., 2001) up to 400 Mpc using different techniques (quoted in the labels). Points below ~ 25 Mpc are seriously affected by peculiar motions.

having used Mattig's formula (1.79) and the definition (1.81).

The angular diameter distance is the distance of an object deduced from its transversal dimension (via the transverse part of the FLRW metric). If D is the proper diameter of the source and $d\theta$ the viewing angle, then the (angular diameter) distance is

$$d_A = \frac{D}{d\theta} = ar = \left(\frac{a}{a_0}\right) a_0 r. \quad (1.88)$$

For flat universes, it holds

$$d_A = d_{PR} = \frac{d_{com}}{1+z}. \quad (1.89)$$

The luminosity distance is built to preserve the Euclidean inverse-square law for the flux and is probably one of the most important because this is what very often astronomers measure. The emitted flux of a source radiating an energy dE , in the time interval dt , located at a distance d_L (i.e. at redshift $z > 0$), is

$$f = \frac{dE}{4\pi d_L^2 dt}. \quad (1.90)$$

The observed flux ($a = a_0$, $z = 0$) is

$$f_0 = \frac{dE_0}{4\pi (a_0 r)^2 dt_0}, \quad (1.91)$$

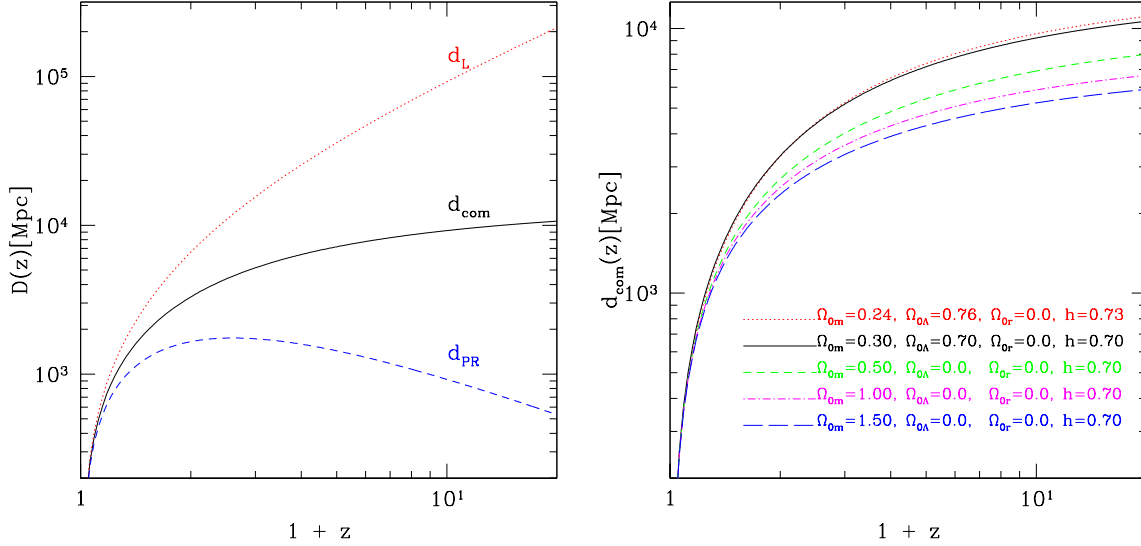


Figure 1.5: Left panel: distances as function of redshift z in a flat universe with cosmological parameters $\Omega_{0,m} = 0.3$, $\Omega_{0,\Lambda} = 0.7$, $\Omega_{0,r} = 0.0$, $h = 0.7$. We show: the proper distance, coinciding with the angular diameter distance (dashed line), the comoving distance (solid line) and the luminosity distance (dotted line). Right panel: comoving distance for different cosmological models, as indicated by the labels.

being r the comoving coordinate of the source in a frame centered with the observer. Including redshift effects, as, for (1.58), $a\nu = \text{constant}$, $dE \sim \nu \sim 1/a \sim (1+z)$ and $dt \sim 1/\nu \sim a \sim 1/(1+z)$. Imposing $f = f_0$, it follows

$$\frac{dE}{4\pi d_L^2 dt} = \frac{dE_0}{4\pi (a_0 r)^2 dt_0} = \frac{dE}{4\pi (a_0 r)^2 dt} \left(\frac{a}{a_0}\right)^2 \quad (1.92)$$

and

$$d_L = \frac{a_0^2}{a} r. \quad (1.93)$$

For flat universes,

$$d_L = (1+z)d_{com} = (1+z)^2 d_{PR}. \quad (1.94)$$

A plot showing the behaviour of the different definitions of distances for a flat, standard cosmology with $\Omega_{0,m} = 0.3$, $\Omega_{0,\Lambda} = 0.7$, $\Omega_{0,r} = 0.0$, $h = 0.7$ is in Figure 1.5 (left panel). The results for the comoving distance in different cosmological models as function of redshift are also plotted (right panel). We stress that the proper (and angular diameter) distance is *decreasing* with redshift, while the comoving and the luminosity distance are always increasing with z . At low redshift, there is no distinction between the different definitions and the different cosmologies adopted.

Chapter 2

Mathematical description of cosmic structure formation

Fiat lux

GENESIS

In this chapter, we will address the main astrophysical problem concerning the “content” of the Universe: structure birth, formation and evolution. We will also give an overview of how it is possible to describe mathematically such processes using linear, perturbative analysis and numerical, non-linear simulations.

The bulk of such investigations will produce results about the cosmological evolution of cosmic structures which are valid in a statistical sense.

2.1 The global scenario: hot big bang

Given the basic equations for cosmic expansion, it is possible to recover the whole history of the expanding Universe and to build the so-called standard cosmological model: the *hot big bang*. In this scenario, the main constituents are radiation and matter that, during the primordial phases, were in thermodynamical equilibrium with a black-body energy spectrum (1.42) and a temperature behaviour dominated by radiation (1.46). Because of such equilibrium, statistically, each atom interacts with one photon and therefore the plasma results ionised: only when the temperature becomes low enough, due to the expansion, recombination will be possible and matter will become neutral.

The radiation spectrum, better known as cosmic microwave background (CMB), is still observable at the present-day at an effective temperature of about 2.725 K.

During the evolution of the Universe, a transition from a radiation dominated to a matter

dominated epoch is expected. More generally, three specific “instants” can be identified: the *equivalence*, *decoupling* and *recombination* time or more commonly redshift.

The *equivalence* redshift, z_{eq} , is the redshift at which the energy density of matter and radiation are equivalent, $\rho_m(z_{eq}) = \rho_r(z_{eq})$. This is given by

$$1 + z_{eq} = \frac{\Omega_{0,m}}{\Omega_{0,r}} \quad (2.1)$$

because of the scalings (1.34) and (1.59). At $z > z_{eq}$ the energy density is dominated by radiation, which scales $\propto (1+z)^4$; at smaller redshift, instead, matter density dominates, as it is $\propto (1+z)^3$, (1.39).

The *decoupling* redshift, z_{dec} , corresponds to the epoch when the temperature of matter equals the temperature of radiation, $T_m(z_{dec}) = T_r(z_{dec})$. According to (1.44), (1.45) and (1.59), it is found

$$1 + z_{dec} = \frac{T_{0,r}}{T_{0,m}}. \quad (2.2)$$

Physically, we expect a decoupling between matter and radiation because, during the cosmic expansion, density and temperature decrease and with them also the interactions between particles and photons are rarer and rarer, until they become irrelevant.

At early times, the behaviour is ruled by radiation and there is the same scaling for the two temperatures, evolving as $(1+z)$, in virtue of (1.46); later on, at $z < z_{dec}$, statistical equilibrium between the two components is broken and the radiation temperature continues decreasing as $(1+z)$, while matter temperature goes as $(1+z)^2$. So, after the decoupling, matter and radiation evolve independently.

The *recombination* redshift is defined by the recombination of 50% of hydrogen atoms, when the global temperature drops below 10^4 K (more likely some thousands Kelvin), as a consequence of the cosmic expansion, and is expected to happen between equivalence and decoupling (when matter and radiation do not interact any more).

Recent data (Hinshaw et al., 2008, five-year WMAP satellite data) suggest that the Universe is flat with a contribution from cosmological constant dominant over the other components: $\Omega_{0,tot} \simeq 1.0$, $\Omega_{0,\Lambda} \simeq 0.74$, $\Omega_{0,m} \simeq 0.26$. Baryonic matter seems to be a negligible part of the whole matter content ($\Omega_{0,b} \simeq 0.04$), which is instead dominated by dark matter (matter interacting only gravitationally). The expansion parameter is estimated $h \simeq 0.72$, matter-radiation equality is expected at $z_{eq} \simeq 3176$ and decoupling at $z_{dec} \simeq 1090.51$ (Hinshaw et al., 2008). These values rule out the flat matter only

Einstein-de Sitter cosmology and are consistent with the so-called Λ CDM standard model, which is defined by the set of parameters $\Omega_{0,tot} = 1.0$, $\Omega_{0,\Lambda} = 0.7$, $\Omega_{0,m} = 0.3$ and $h = 0.7$. The non-zero $\Omega_{0,\Lambda}$ term is probably related to the cosmological constant (Einstein, 1917), but, as proposed by many authors (Ratra and Peebles, 1988; Brax and Martin, 1999; Peebles and Ratra, 2003), can also be connected to other types of unknown “dark energies”, whose effects on structure formation history have been firstly studied by Maio et al. (2006), via numerical simulations, and by Crociani et al. (2008), via analytical calculations.

The existence of non-baryonic matter has been suggested several decades ago and structure formation models based on the growth of primordial gravitational instabilities (Peebles, 1974) were developed since the early works by Gunn and Gott (1972).

2.2 From primordial fluctuations to structure formation

The presence of density/energy disomogeneities capable of growing under gravitational instability is fundamental for structure formation. Nowadays the presence of primordial fluctuations of the order of 10^{-5} the mean density is well established and evident for example in the temperature map of the CMB (Figure 2.1). Probably they were originated in the very early phases of the Universe undergoing an exponential expansion (“inflation”). Afterward quantum fluctuations would have been growing, becoming the actual seeds of structure formation. These original seeds are random events for which a Gaussian probability distribution function (PDF) is usually assumed. In more quantitative terms, one can define the density contrast $\delta(\mathbf{x}, t)$, as a function of the cosmic time and spatial position

$$\delta(\mathbf{x}, t) \equiv \frac{\rho(\mathbf{x}, t) - \rho_b(t)}{\rho_b(t)}, \quad (2.3)$$

being $\rho(\mathbf{x}, t)$ the density at point \mathbf{x} and instant t and $\rho_b(t)$ the background mean density of the Universe at the same cosmic time. Assuming a Gaussian PDF p for the primordial fluctuations δ means imposing

$$p(\delta)d\delta = \frac{1}{\sqrt{2\pi\sigma^2}} \exp\left(-\frac{\delta^2}{2\sigma^2}\right) d\delta. \quad (2.4)$$

The mean value $\langle\delta\rangle$ is null by definition and the variance $\sigma^2 \equiv \langle\delta^2\rangle$. We notice that, according to (2.4), δ can assume values between $-\infty$ and $+\infty$, but in practice it must be

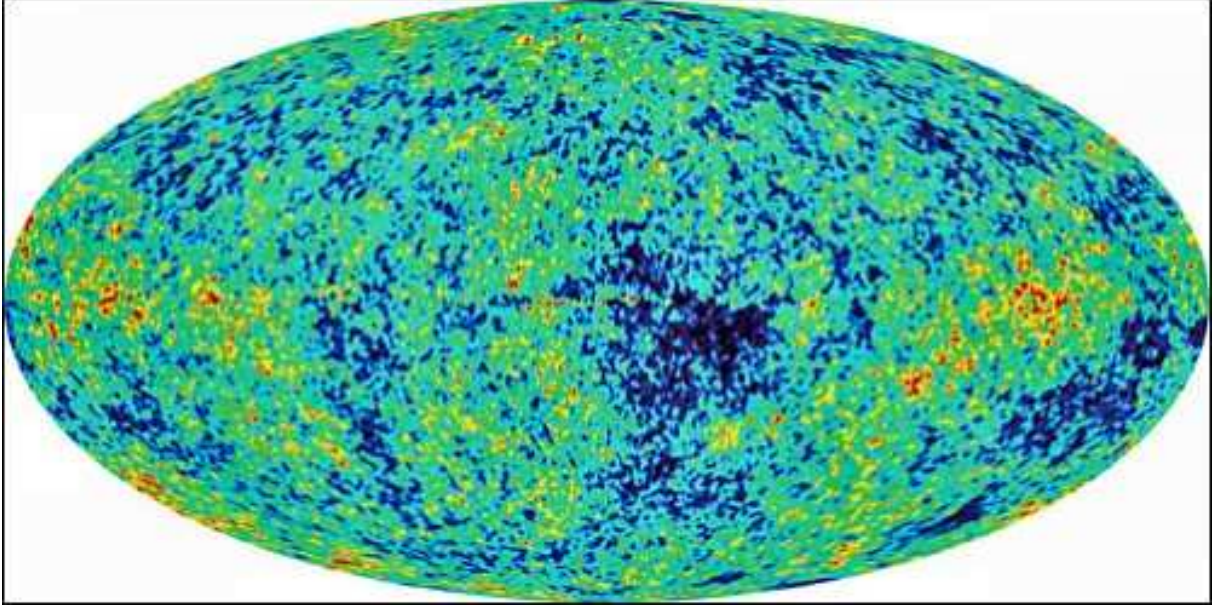


Figure 2.1: Bidimensional projective map $\{(\theta, \phi) \in [-\pi/2, \pi/2] \times [-\pi, \pi]\}$, where ϕ is the galactic longitude and θ the galactic latitude, of the cosmic background temperature fluctuations (from the observations of WMAP NASA satellite Spergel et al., 2007)). The image reveals 13.7 billion year old temperature fluctuations shown as color differences: red warmer, blue colder than the mean temperature of 2.725 Kelvin, in the range ± 200 micro-Kelvin. They correspond to the seeds that grew to become the present-day structures.

$\delta \geq -1$, because of (2.3). The regime of the perturbations is said linear if $|\delta| \ll 1$ and non-linear if $\delta \geq 1$.

When over-densities are present, they can grow only if the gravitational forces are stronger than pressure or dispersion forces. The growth of perturbations is a problem mathematically treated integrating the equations governing the behaviour of the cosmic fluid.

2.2.1 Linear evolution

The classical approach to gravitational instability is to write the equations governing the evolution of a fluid in a gravitational field ϕ , and to expand them in perturbative series assuming that the perturbations are “small” and the change of entropy is negligible.

A fluid is described by its density ρ , pressure P and velocity field \mathbf{u} . The equations ruling its behaviour, in a static space-time, are

- the continuity equation

$$\frac{\partial \rho}{\partial t} + \nabla \cdot (\rho \mathbf{u}) = 0 \quad (2.5)$$

- the Euler equations

$$\frac{\partial \mathbf{u}}{\partial t} + (\mathbf{u} \cdot \nabla) \mathbf{u} = -\frac{\nabla P}{\rho} - \nabla \phi \quad (2.6)$$

- the Poisson equation

$$\nabla^2 \phi = 4\pi G \rho. \quad (2.7)$$

The different quantities can be decomposed in a background average value and a perturbation term as follows

$$\begin{cases} \rho = \rho_b + \delta\rho \equiv \rho_b(1 + \delta) \\ P = P_b + \delta P \\ \mathbf{u} = \delta\mathbf{u} \\ \phi = \phi_b + \delta\phi \end{cases} \quad (2.8)$$

with $|\delta| = |\delta\rho/\rho_b| \ll 1$, $|\delta P/P_b| \ll 1$, $|\delta\phi/\phi_b| \ll 1$ and the velocity identified with the perturbation velocity because we assume the reference frame of the fluid. The linearization of the system leads to the linearized

- continuity equation

$$\frac{\partial \delta\rho}{\partial t} + \rho_b \nabla \cdot (\delta\mathbf{u}) = 0 \quad (2.9)$$

- Euler equations

$$\frac{\partial \delta\mathbf{u}}{\partial t} = -\frac{c_s^2}{\rho_b} \nabla \delta\rho - \nabla \delta\phi \quad (2.10)$$

- Poisson equation

$$\nabla^2 \delta\phi = 4\pi G \delta\rho \quad (2.11)$$

where the sound speed, c_s , at constant entropy S is

$$c_s^2 = \left(\frac{\partial P}{\partial \rho} \right)_S = \frac{\delta P}{\delta \rho}. \quad (2.12)$$

In Fourier space, the system reads

$$\begin{cases} \omega \hat{\delta} - \mathbf{k} \cdot (\hat{\delta}\mathbf{u}) = 0 \\ \omega(\hat{\delta}\mathbf{u}) = \mathbf{k} \left[c_s^2 \hat{\delta} + (\hat{\delta}\phi) \right] \\ -k^2 (\hat{\delta}\phi) = 4\pi G \rho_b \hat{\delta} \end{cases} \quad (2.13)$$

where we have used as kernel of the transformation¹ $e^{i\omega t - i\mathbf{k} \cdot \mathbf{x}}$, with ω angular frequency, \mathbf{k} wave-number vector with modulus k and \mathbf{x} position vector. The hat-sign denotes the

¹ The particular kernel used is irrelevant to the final result.

Fourier transformation and $\hat{\delta} = \hat{\delta}\rho/\rho_b$. Expliciting the 5×5 matrix associated to this system we obtain

$$\begin{pmatrix} \omega & -\mathbf{k}^T & 0 \\ -\mathbf{k}c_s^2 & \omega\mathbf{I} & -\mathbf{k} \\ 4\pi G\rho_b & \mathbf{0}^T & k^2 \end{pmatrix} \begin{pmatrix} \hat{\delta} \\ \hat{\delta}\mathbf{u} \\ \hat{\delta}\phi \end{pmatrix} = \begin{pmatrix} 0 \\ \mathbf{0} \\ 0 \end{pmatrix}. \quad (2.14)$$

In the previous matrix (A.4), \mathbf{k}^T is the transposed of the vector \mathbf{k} , $\mathbf{0}^T$ the transposed of the null vector $\mathbf{0}$ and $\mathbf{I} = \mathbf{I}^T$ the 3×3 unity matrix. In 1D (spherical symmetry), the matrix becomes 3×3 and non trivial solutions exist for

$$\omega^2 k^2 - c_s^2 k^4 + 4\pi G\rho_b k^2 = 0. \quad (2.15)$$

This represents the dispersion relation between the Fourier variables ω and \mathbf{k} .

For $k \neq 0$, it reduces to

$$\omega^2 - c_s^2 k^2 + 4\pi G\rho_b = 0, \quad (2.16)$$

whereas, for $k = 0$ any ω satisfies the condition (2.15). Growing, exponentially unstable modes exist only for imaginary ω :

$$\omega^2 = c_s^2 k^2 - 4\pi G\rho_b < 0 \quad (2.17)$$

which means

$$k < 2 \frac{\sqrt{\pi G\rho_b}}{c_s} \equiv k_J. \quad (2.18)$$

The value k_J is the Jeans wave-number for the stability of spherical nebulae and it leads naturally to the Jeans length $\lambda_J \approx c_s/\sqrt{G\rho_b}$ and to the condition for gravitational instability, $\lambda > \lambda_J$, for nebulae with size λ .

The expected time-scale for collapse is called free-fall time and from a dimensional analysis, it is

$$t_{ff} \sim \frac{1}{\sqrt{G\rho_b}} \quad (2.19)$$

from which follows $\lambda_J \approx c_s t_{ff}$. The size of a collapsing object is given by the typical propagation velocity of a perturbation multiplied by the typical time during which it propagates and collapses. It is possible to define the corresponding Jeans mass as²

$$M_J \equiv \frac{4}{3}\pi\rho_b \left(\frac{\lambda_J}{2}\right)^3. \quad (2.20)$$

For an expanding universe, the previous equations must be slightly modified and the exponential behaviour of the growth corrected with a power-law behaviour. In particular,

²We point out that the definitions of Jeans mass and Jeans length are not unique and depend on the convention adopted.

the Fourier Transform for the density contrast in a matter dominated universe satisfies (in physical coordinates³)

$$\ddot{\delta} + 2\frac{\dot{a}}{a}\dot{\delta} + (c_s^2 k^2 - 4\pi G\rho_b)\hat{\delta} = 0 \quad (2.21)$$

where the “friction” term due to the change in time of the scale factor, a , is evident. In a universe dominated by radiation, the analogous of (2.21) is

$$\ddot{\delta} + 2\frac{\dot{a}}{a}\dot{\delta} + \left(c_s^2 k^2 - \frac{32}{3}\pi G\rho_b\right)\hat{\delta} = 0 \quad (2.22)$$

with

$$c_s = \frac{c}{\sqrt{3}}.$$

The differential equations (2.21) and (2.22) have solutions which are linear combinations of two power laws (or “modes”): one is growing, D_+ , and one is decaying, D_- , so $\delta \simeq D_+$. The behaviour depends both on the kind of fluid and on the cosmology, but, as the latter dependence is quite weak, we quote as a reference the growing mode or growth factor, $D_+(a)$, for the Einstein-de Sitter model:

- for $a < a_{eq}$, radiation dominates:

$$D_+(a) \sim a^2 \quad \text{and} \quad D_+(t) \sim t \quad (2.23)$$

- for $a > a_{eq}$, matter dominates:

$$D_+(a) \sim a \quad \text{and} \quad D_+(t) \sim t^{2/3}. \quad (2.24)$$

For an arbitrary cold dark matter scenario, with matter parameter Ω_m , the density contrast evolution is much less trivial to express analytically and it is given implicitly by (Heath, 1977; Carroll et al., 1992)

$$D_+(a) = \frac{5\Omega_m}{2a} \frac{da}{d\tau} \int_0^a \left(\frac{da'}{d\tau}\right)^{-3} da' = \frac{5}{2}\Omega_m H_0^3 E(a) \int_0^a \frac{da'}{[a'H(a')]^3} \quad (2.25)$$

where $\tau \equiv H_0 t$. This formula is normalized to the Einstein-de Sitter behaviour, so for $\Omega_m = 1$ and $\Omega_\Lambda = 0$, one gets $D(a) = a$.

A useful fit for plausible values of Ω_m and Ω_Λ is the following:

$$D_+(a) = a \frac{g(a)}{g(0)} \quad (2.26)$$

³Remind the substitution $k \rightarrow k/a$ to pass to comoving wave-numbers.

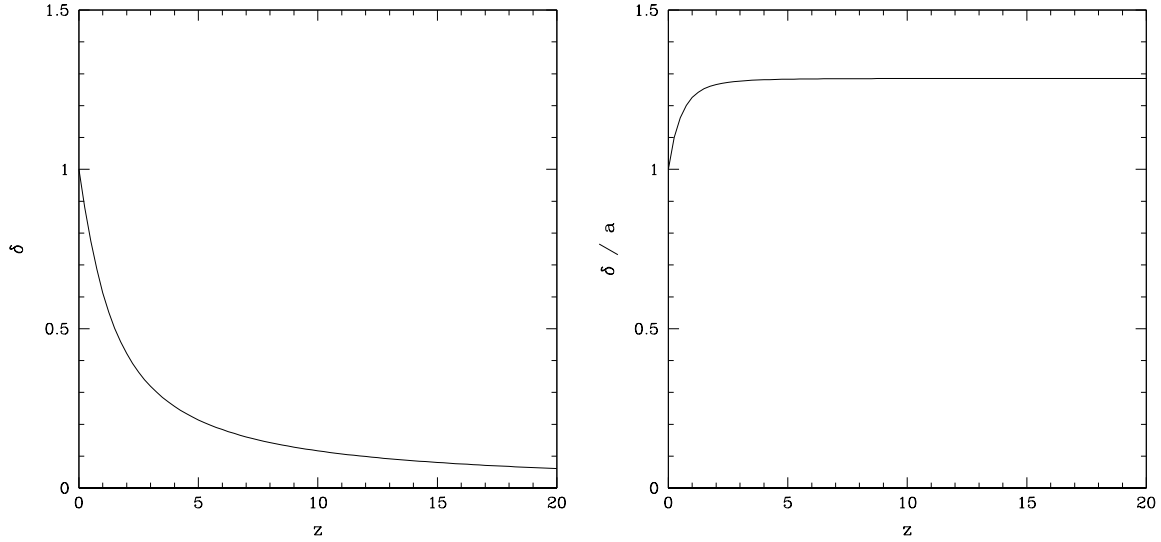


Figure 2.2: On the left, we show the density contrast δ normalized to the present-day value for a standard Λ CDM model with $\Omega_{0,m} = 0.3$, $\Omega_{0,\Lambda} = 0.7$, $\Omega_{0,tot} = 1$. At high redshift the Einstein-de Sitter behaviour is recovered, as emphasized by the plot of δ/a on the right side.

with

$$g(a) = \frac{5}{2} \Omega_m \left[\Omega_m^{4/7} - \Omega_\Lambda + (1 + \Omega_m/2)(1 + \Omega_\Lambda/70) \right]^{-1} \quad (2.27)$$

$\Omega_m = \Omega_m(a)$ and $\Omega_\Lambda = \Omega_\Lambda(a)$. We plot the growth factor of (2.25), normalized to the present-day, for the Λ CDM case in Figure 2.2.

From analyses of the CMB radiation, it is found that, at the “surface of last scattering” (decoupling time), when the scale factor is about 10^{-3} , the perturbations are of the order of 10^{-5} . Therefore a simple linear evolution would predict present-day structures with density contrast $\delta \sim 10^{-2}$, because of relation (2.24). Nevertheless, we observe over-densities with $\delta \gg 1$ which means that their evolution must have been strongly non-linear. In addition, a precise calculation of the Jeans mass relies on the particular cosmic fluid considered and also on the kind of matter considered: standard baryonic matter, dark matter acting only gravitationally, either hot (relativistic at the decoupling) and cold (non-relativistic at the decoupling), etc. Typically though it is found that the Jeans mass increases up to the equivalence and then decreases due to micro-physics dissipation effects. The values reached are:

- for baryonic matter, $M_{J,eq} \sim 10^{16} M_\odot$;
- for hot dark matter, $M_{J,eq} \gtrsim 10^{12} M_\odot$;

– for cold dark matter, $M_{J,eq} \sim 10^5 M_\odot$.

The most reliable model seems to be the cold dark matter one, in which dark matter dominates over the baryons and leads a kind of “bottom-up” scenario: small dark matter haloes are the first to collapse and then merge together to form more massive structures⁴. The main problem in models dominated by baryons or by hot dark matter is that they rely on fragmentation processes by which structures form. In these “top-down” scenarios, massive objects – like galaxy clusters – should always be older than smaller objects – like globular cluster – which is false, because Galactic globular clusters are among the oldest objects observed and galaxy clusters the youngest and biggest virialized ones.

2.2.2 Non-linear evolution

Once structure growth proceeds and enters an advanced stage, it becomes a highly non-linear problem ($\delta \geq 1$) and therefore the main viable mean to address it is via numerical approaches. The commonly adopted model is based on the “spherical top-hat” collapse (Coles and Lucchin, 1995, for example). It assumes that the overdensity is spherical and evolves according to the Friedmann equations on a flat background with density ρ_b . This shows a first phase during which the perturbation expands with the Universe and then a contraction and subsequent virialization of the system (a simple scheme is in Figure 2.3). The maximum radius, r_{max} , is reached at the instant t_{max} and the corresponding density of the perturbation is

$$\rho_p(t_{max}) = \left(\frac{3\pi}{4}\right)^2 \rho_b(t_{max}). \quad (2.28)$$

The collapse and the virialization process stop respectively at $t_c = 2t_{max}$ and $t_{vir} = 3t_{max}$. From the virial theorem it follows that the virialization radius is

$$r_{vir} = \frac{r_{max}}{2} \quad (2.29)$$

and the corresponding over-densities, for and Einstein-de Sitter cosmology, are

$$\Delta_{max} \equiv \frac{\rho_p(t_{max})}{\rho_{cr}(t_{max})} = \left(\frac{3\pi}{4}\right)^2 \simeq 5.6: \delta_{max} \simeq 4.6 \quad (2.30)$$

$$\Delta_c \equiv \frac{\rho_p(t_c)}{\rho_{cr}(t_c)} = \left(\frac{3\pi}{4}\right)^2 2^2 \cdot 8 = 18\pi^2 \simeq 178: \delta_c \simeq 177 \quad (2.31)$$

$$\Delta_{vir} \equiv \frac{\rho_p(t_{vir})}{\rho_{cr}(t_{vir})} = \left(\frac{3\pi}{4}\right)^2 3^2 \cdot 8 = \frac{81\pi^2}{2} \simeq 400: \delta_{vir} \simeq 399. \quad (2.32)$$

⁴This consideration is strictly valid only for dark matter, not for the baryons which feel the gravitational force of dark matter but also additional hydro-dynamical effects.

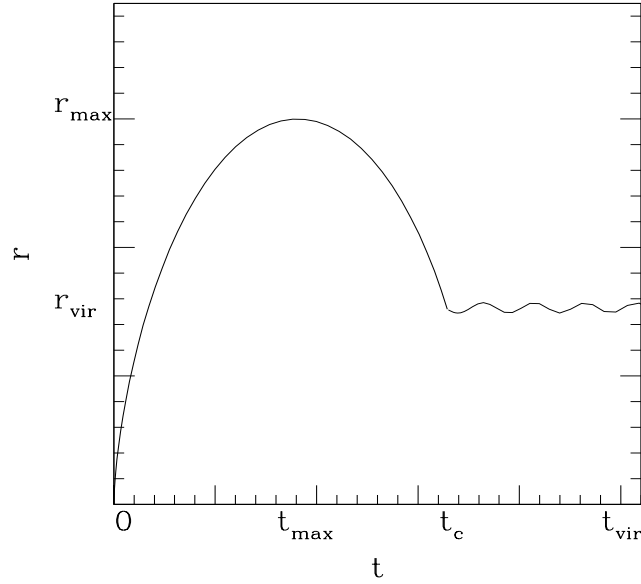


Figure 2.3: Scheme of the spherical “top-hat” model. The radius of the spherical perturbation, r , as a function of time, t , is plotted (in arbitrary units). The labels refer to the maximum radius, r_{max} , the virialization radius, r_{vir} , the time at which the maximum radius is reached, t_{max} , the collapse time, t_c , and the virialization time, t_{vir} .

This means that the total mass density of a virializing object is $\Delta_c \rho_{cr} = 18\pi^2 \rho_{0cr} E^2(z)$ and the corresponding number density is $18\pi^2 \rho_{0cr} E^2(z) / (\mu m_H) \sim 0.002(1+z)^3 \mu^{-1} h^2 \text{ cm}^{-3}$.

In a flat Λ CDM cosmology, there is a weak dependence on z and the over-density at the end of the collapse is $\Delta_c(z) = 18\pi^2 + 82[\Omega_m(z) - 1] - 39[\Omega_m(z) - 1]^2$ (Bryan and Norman, 1998). For non-linear growth in cosmologies with early dark energy see Bartelmann et al. (2006).

From linear theory (2.24) one would expect:

$$\delta_{max} \simeq \frac{3}{5} \left(\frac{3\pi}{4} \right)^{2/3} \simeq 1.07 \quad (2.33)$$

$$\delta_c \simeq \frac{3}{5} \left(\frac{3\pi}{4} \right)^{2/3} 2^{2/3} \simeq 1.68 \quad (2.34)$$

$$\delta_{vir} \simeq \frac{3}{5} \left(\frac{3\pi}{4} \right)^{2/3} 3^{2/3} \simeq 2.20. \quad (2.35)$$

These quantities are much smaller than the values estimated from non-linear theory.

The spherical top-hat is only a simple approach which can help our understanding of the general phenomenology, but, nonetheless, more detailed studies must rely on numerical simulations.

2.3 Statistics of structure formation

When information must be extracted from many processes or data it is useful to perform a statistical analysis of the sample. Similarly, it makes sense to describe structure formation in terms of statistical quantities which can tell us something about the global behaviour of the whole sample: e.g., which structures are the most typical ones, how rare or frequent are objects of a given mass, if small objects are more numerous than big objects, etc.

The statistical analysis of perturbations relies on two hypotheses: the usual *cosmological principle* and the *ergodic hypothesis*⁵. For Gaussian probability distribution functions the ergodic hypothesis is proven to be always true (therefore it is not an additional hypothesis but a consequence).

When such assumptions are met, a sample is considered to be a *fair sample* and in cosmology we will talk about *fair samples of the Universe*.

In the Fourier space we have defined the density contrast $\hat{\delta}$; let's define now the power spectrum $P(k)$:

$$(2\pi)^3 P(k) \delta^{(3)}(\mathbf{k} - \mathbf{k}') \equiv \langle \hat{\delta}(\mathbf{k}) \hat{\delta}^*(\mathbf{k}') \rangle \quad (2.36)$$

where $\delta^{(3)}$ is the three-dimensional Dirac delta. For a primordial power spectrum, in virtue of homogeneity and isotropy, we can write

$$P(k) = Ak^n \quad (2.37)$$

with A empirical normalization constant and n spectral index. A spectrum with $n = 1$ is said Harrison-Zeldovic power spectrum; recent observational data suggest $n = 0.96$ (Hinshaw et al., 2008).

We can also define the variance

$$\sigma^2 \equiv \langle \delta^2(\mathbf{r}) \rangle \quad (2.38)$$

to get

$$\sigma^2 = \frac{1}{2\pi^2} \int dk k^2 P(k). \quad (2.39)$$

The mass variance is defined as

$$\sigma_M^2 \equiv \frac{\langle (M - \langle M \rangle)^2 \rangle}{\langle M \rangle^2} = \frac{1}{2\pi^2} \int P(k) \hat{W}^2(kR) k^2 dk, \quad (2.40)$$

⁵ This states that the averages taken over all the possible realizations of an ensemble (population) are equal to the averages done over a sample of that population.

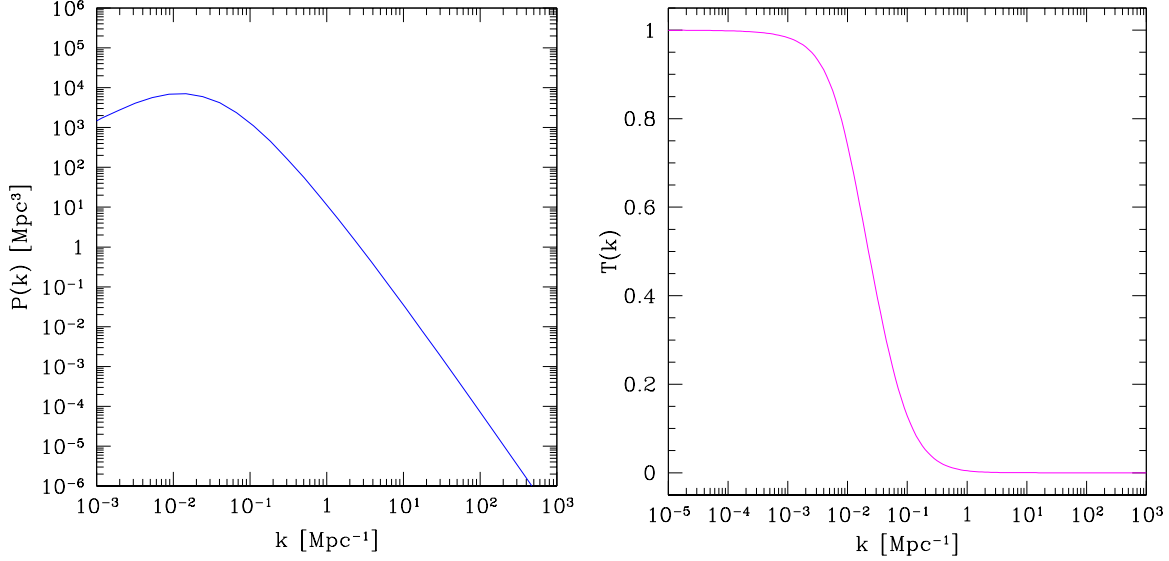


Figure 2.4: Power spectrum (left panel) computed using the Bardeen transfer function (right panel), for $h = 0.7$, $\Omega_{0,m} = 0.3$ and $\sigma_8 = 0.9$.

where the last passage holds for homogeneity and isotropy and \hat{W} is the so-called window function in the Fourier space

$$\hat{W}(kR) \equiv 3 \frac{\sin(kR) - (kR) \cos(kR)}{(kR)^3} \quad (2.41)$$

whose behaviour is

$$\hat{W}(x) \sim \begin{cases} 1 & \text{for } x \ll 1 \\ x^{-2} & \text{for } x \gg 1 \end{cases} . \quad (2.42)$$

Because of relations (2.39) and (2.40), $\sigma_M < \sigma$.

The suppression of growth before equivalence is parametrized by a transfer function, T , obtained via numerical simulations, so the primordial power spectrum results modified according to

$$P(k) = Ak^n T^2(k, a_{eq}) \quad (2.43)$$

where, e.g., for cold dark matter fluctuations, the following fit is often used (Bardeen et al., 1986):

$$T(k, a_{eq}) = \frac{\ln(1 + 2.34q)}{2.34q} [1 + 3.89q + (16.1q)^2 + (5.46q)^3 + (6.71q)^4]^{-1/4} \quad (2.44)$$

with

$$q = \frac{k\theta^{1/2}}{\Omega_{CDM} h^2 \text{Mpc}^{-1}} \quad \text{and} \quad \theta = 1.$$

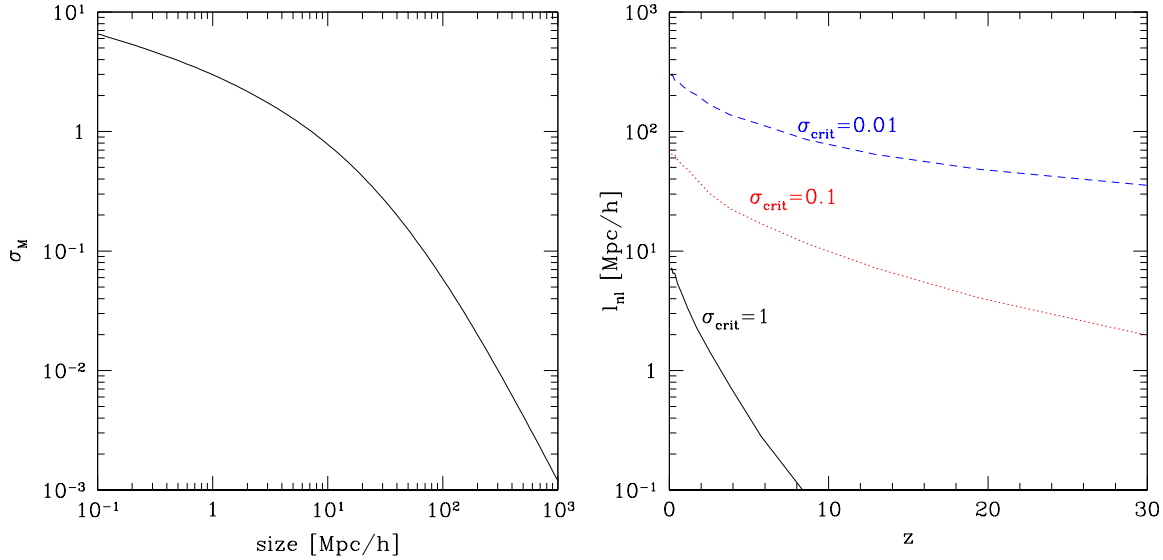


Figure 2.5: Left panel: mass variance as a function of the size. The cosmology adopted has $h = 0.7$, $\Omega_{0,m} = 0.3$, $\Omega_{0,\Lambda} = 0.7$ and $\sigma_8 = 0.9$. The value of σ_M is 0.9, for objects with size $8 \text{ Mpc}/h$. Right panel: the scale l_{nl} at which $\sigma_M D_+(z)$ reaches a minimum critical value of 1 (solid line), 0.1 (dotted line) and 0.01 (dashed line), as indicated by the labels, is plotted as a function of redshift, z .

Plots of the power spectrum and the transfer functions are presented in Figure 2.4. The qualitative behaviour of $P(k)$, for $n = 1$, is

$$P(k) \sim \begin{cases} k^n & \sim k & \text{for } k \ll k_{eq} \\ k^{n-4} & \sim k^{-3} & \text{for } k \gg k_{eq} \end{cases} . \quad (2.45)$$

Its peak is determined by the Γ shape-parameter

$$\Gamma = \Omega_{0,m} h \quad (2.46)$$

which holds for CDM only, but, if we consider also baryons, a better formula is (Sugiyama, 1995):

$$\Gamma = \Omega_{0,m} h \exp \left[-\Omega_{0,b} \left(1 + \frac{\sqrt{2h}}{\Omega_{0,m}} \right) \right] . \quad (2.47)$$

We stress the importance of the mass variance, as, being directly related to the power spectrum via (2.40), it is used as normalization: normally, the mass variance in a $8 \text{ Mpc } h^{-1}$ sphere, σ_8 , is given instead of A . In Figure 2.5, we show the mass variance for objects with different sizes at the mean density of the Universe and the scale at which it reaches a minimum critical value of 1 as a function of the redshift. This is interesting, because the scale at which $\sigma_M \sim 1$ is basically the scale below which non-linearities are important and the linear regime breaks down. For comparison, we also plot the same quantity for

minimum critical values of 0.1 and 0.01.

One last statistically interesting quantity is the mass function: it predicts the number of collapsed object per unit mass and per unit volume. Imposing that structures form statistically when the overdensity is above the minimum threshold δ_c and integrating the probability distribution function under such hypothesis, for spherical collapse it is (Press and Schechter, 1974; Bond et al., 1991)

$$\frac{dN}{dM dV} \equiv \frac{dn(M, z)}{dM} = \frac{\rho_b}{M} \frac{df}{dM} = \sqrt{\frac{2}{\pi}} \frac{\rho_b}{M^2} \frac{\delta_c(z)}{\sigma} \left| \frac{d \ln \sigma}{d \ln M} \right| \exp \left\{ -\frac{\delta_c^2(z)}{2\sigma^2} \right\}. \quad (2.48)$$

Calling df/dM the fraction of collapsed mass and defining $\nu \equiv \delta_c(z)/\sigma_M$, expression (2.48) becomes

$$\frac{df}{d\nu} = \sqrt{\frac{2}{\pi}} \exp \left(-\frac{\nu^2}{2} \right), \quad (2.49)$$

being

$$\frac{dn}{dM} = \frac{\rho_b}{M} \left| \frac{d\nu}{dM} \right| \frac{df}{d\nu}. \quad (2.50)$$

A different description, suggested by ellipsoidal collapse models, predicts for the mass function Sheth and Tormen (1999), Sheth et al. (2001):

$$\frac{df}{d\nu} = C \sqrt{\frac{2A}{\pi}} \left\{ 1 + \frac{1}{(A\nu^2)^q} \right\} \exp \left(-\frac{A\nu^2}{2} \right), \quad (2.51)$$

where $C = 0.3222$, $A = 0.707$ and $q = 0.3$. The Press & Schechter mass function is reproduced for $C = 1/2$, $A = 1$ and $q = 0$.

From direct comparisons with numerical simulations it was possible to give better fits, in particular at the high mass-end (Jenkins et al., 2001): the Jenkins mass function has the same shape as the Sheth & Tormen, but the parameter A is 0.75 causing a steeper exponential decay.

Examples and comparisons of mass functions are given in Figure 2.6 for a standard Λ CDM cosmology ($\Omega_{0,m} = 0.3$, $\Omega_{0,\Lambda} = 0.7$, $h = 0.7$), an open cosmology ($\Omega_{0,m} = 0.3$, $\Omega_{0,\Lambda} = 0.0$, $h = 0.7$) and an Einstein-de Sitter cosmology ($\Omega_{0,m} = 1.0$, $\Omega_{0,\Lambda} = 0.0$, $h = 0.7$), at redshifts $z = 10$ and $z = 0$. The shift of the Einstein-de Sitter mass function in the power-law regime, both at $z = 10$ and more evidently at $z = 0$, is due to the higher $\Omega_{0,m}$.

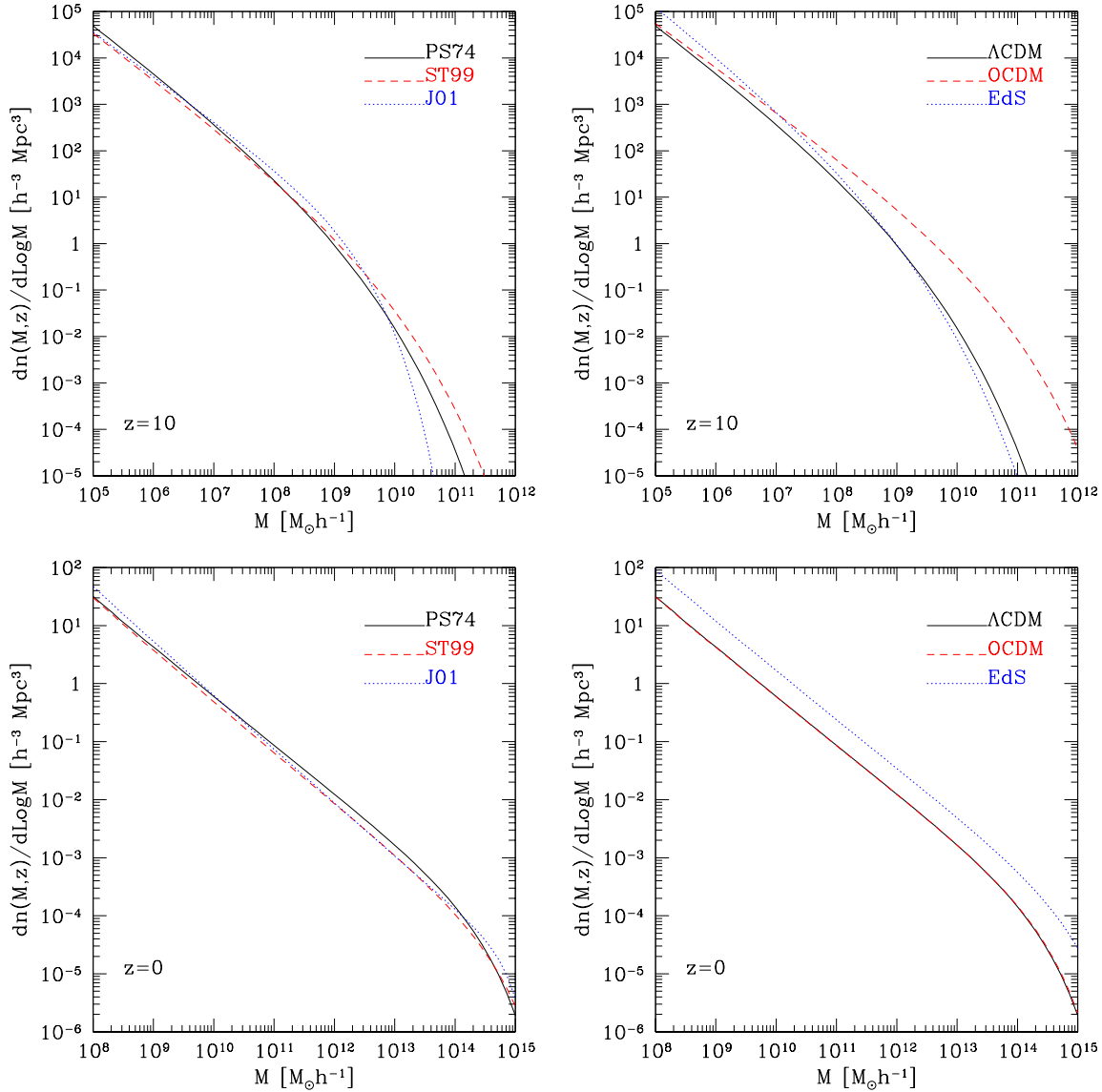


Figure 2.6: Left panels: Press & Schechter (solid line), Sheth & Tormen (dashed line), Jenkins et al. (dotted line) mass functions for the standard Λ CDM model. Right panels: Press & Schechter mass functions for the following models: standard Λ CDM cosmology (solid line), Einstein-de Sitter model (dotted line), open cosmology (dashed line). The upper row refers to redshift $z = 10$, the lower row to $z = 0$.

2.4 Dark matter haloes and baryonic structure formation

As dark matter is the dominant matter component, it is commonly believed that luminous objects should be formed by in-fall of gas into dark matter potential wells. During the in-fall, the gas is shock heated at the virial temperature of the halo, atoms and molecules get excited and, when they get de-excited, emit radiation. This process allows for cooling, condensation and fragmentation of gaseous systems and leads baryonic structure

formation details and references can be found e.g. in (details and references can be found e.g. in Barkana and Loeb, 2001; Ciardi and Ferrara, 2005).

2.4.1 Gas and halo properties

The basic properties a halo with mass M , at redshift z , are its virial radius, r_{vir} , its circular velocity, $v_{circ} = \sqrt{GM/r_{vir}}$, its virial temperature, $T_{vir} = \mu m_H v_{circ}^2 / 2k_B$, being μ the mean molecular weight and m_H the hydrogen mass, and its binding energy, $E_b = GM^2 / 2r_{vir}$.

The expected virial radius is computed from the definition of mass enclosed in a spherical collapsed perturbation with density $\rho_p(z) = \Delta_c \rho_{cr}(z)$, where $\rho_{cr}(z) = \rho_{0,cr} E^2(z)$ is the cosmological critical density – evolving according to (1.65), – $\rho_{0,cr}$ is the critical density of the Universe at the present time, $\rho_{0,cr} \simeq 1.9 \cdot 10^{-29} h^2 \text{ g cm}^{-3} \simeq 277.5 h^2 M_\odot \text{ kpc}^{-3}$ and Δ_c is the collapsing over-density defined in equation (2.31):

$$r_{vir} \equiv \left(\frac{3M}{4\pi\rho_p} \right)^{1/3} = \left[\frac{3M}{4\pi\Delta_c\rho_{0,cr}} \right]^{1/3} E^{-2/3}(z). \quad (2.52)$$

Expliciting the cosmological dependencies in r_{vir} and using (1.66) for $E^2(z)$

$$r_{vir}(M, z) = \left[\frac{3M\Omega_m(z)}{4\pi\Delta_c\rho_{0,cr}\Omega_{0,m}} \right]^{1/3} (1+z)^{-1} \quad (2.53)$$

$$v_{circ}(M, z) = \sqrt{\frac{GM}{r_{vir}(M, z)}} = G^{1/2} M^{1/3} \left[\frac{4\pi\Delta_c\rho_{0,cr}\Omega_{0,m}}{3\Omega_m(z)} \right]^{1/6} (1+z)^{1/2} \quad (2.54)$$

$$T_{vir}(M, z) = \frac{\mu m_H v_{circ}^2(M, z)}{2k_B} = \frac{\mu m_H}{k_B} G M^{2/3} \left[\frac{\pi\Delta_c\rho_{0,cr}\Omega_{0,m}}{6\Omega_m(z)} \right]^{1/3} (1+z) \quad (2.55)$$

$$E_b(M, z) = \frac{GM^2}{2r_{vir}(M, z)} = GM^{5/3} \left[\frac{\pi\Delta_c\rho_{0,cr}\Omega_{0,m}}{6\Omega_m(z)} \right]^{1/3} (1+z). \quad (2.56)$$

For $M = 10^8 h^{-1} M_\odot$, $\Delta_c = 178$, $\Omega_{0,m} = 0.25$, $\Omega_{0,\Lambda} = 0.75$, $z = 0$ and assuming $\mu = 1$, it is found $r_{vir} \simeq 7.848 \text{ kpc}/h$, $v_{circ} \simeq 7.4 \text{ km/s}$, $T_{vir} \simeq 3.3 \cdot 10^3 \text{ K}$ and $E_b \simeq 5.4 \cdot 10^{52} \text{ erg}/h$. The typical time-scales involved in the structure formation process are the free-fall time, t_{ff} , and the cooling time, t_{cool} . The free-fall time is defined as

$$t_{ff} = \sqrt{\frac{3\pi}{32G\rho}} \quad (2.57)$$

where G is the universal gravitational constant and ρ the density of the medium; the numeric factor $(3\pi/32)^{1/2}$ holds rigorously for spherical symmetry only. The cooling time is defined as

$$t_{cool} = \frac{3}{2} \frac{nk_B T}{\Lambda(T, n_i)} \quad (2.58)$$

where n is the number density of the gas, k_B the Boltzmann constant, T the temperature and $\Lambda(T, n_i)$ the cooling function (energy emitted per unit time and volume) dependent both on temperature and number densities, n_i , of the constituting species. This quantum-

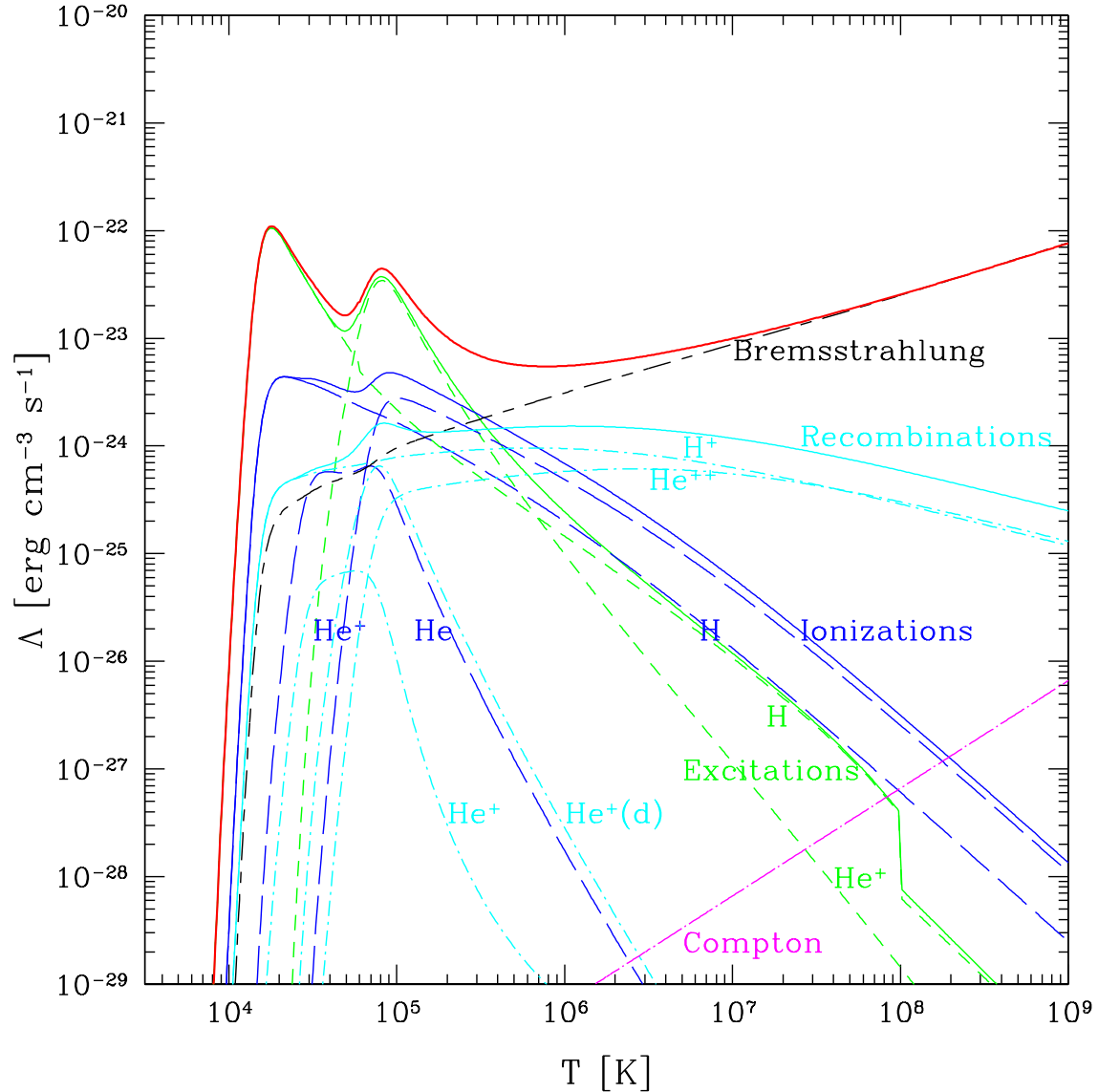


Figure 2.7: Cooling function (red solid line) for gas made of hydrogen and helium in primordial ratio. The different contributions from several processes are shown: excitations (green short-dashed lines), ionizations (blue long-dashed lines), recombinations (cyan dotted short-dashed lines), Compton scattering (magenta dotted long-dashed lines) and Bremsstrahlung (black long-dashed short-dashed lines). A gas number density of 1 cm^{-3} was assumed.

mechanical quantity (see Figure 2.7) takes into account all the possible atomic and/or molecular transitions of any given species and quantifies the associated radiative losses

(further details on the determination of the cooling function are found in appendix A).

The process of gas condensation happens if $t_{cool} \ll t_{ff}$, so only bound objects with a certain minimum mass can collapse and form structures (e.g. Tegmark et al., 1997, and discussion in the next section).

In the cooling function of Figure 2.7, we plot all the contributions coming from different processes for primordial gas, consisting of hydrogen and helium only.

As in the Universe hydrogen has the largest chemical abundance (about 76% in mass fraction or 93% in number fraction), it is the most relevant coolant for many astrophysical purposes (more exactly, for all the systems whose metallicity is $Z \lesssim 10^{-2} Z_{\odot}$ ⁶, at temperatures $T \gtrsim 10^4$ K) and the cooling function is dominated by H-H collisions.

2.4.2 Protogalaxies

In the commonly adopted scenario of structure formation the first haloes to collapse have low masses and virial temperatures below $\sim 2 \cdot 10^4$ K ($\mu = 0.59$), according to equation (2.55). In fact, at redshift $z \gtrsim 10$ or so, the most numerous structures are smaller than $\sim 10^8 h^{-1} M_{\odot}$, as expected by (2.48), (2.51) and as shown in Figure 2.6. From Figure 2.7, it is clear that, in the absence of additional coolants, it is not possible to reach temperatures below $\sim 10^4$ K. During cosmic evolution, though, molecules derived by hydrogen, e.g. H₂, HD, are formed. With their ro-vibrational transitions, they can emit energy and cool the plasma even at $T < 10^4$ K. This means that the very first objects require the presence of molecules as leading cooling agent in order to form.

As hydrogen is largely the dominant element in the Universe, we expect that the derived molecules will play a fundamental role in the cosmological gas chemistry. The first studies in this direction were made by Saslaw and Zipoy (1967) followed by Peebles and Dicke (1968); Hollenbach and McKee (1979); Lepp and Shull (1984); Shapiro and Kang (1987); Puy et al. (1993); Abel et al. (1997); Galli and Palla (1998); Stancil et al. (1998); Yoshida et al. (2003a) and many others, who highlighted the importance of H₂ in cooling gas down to temperatures of about 10^3 K.

In addition, one should also consider that, besides hydrogen, nucleosynthesis calculations predict the existence of primordial deuterium and lithium. Measurements and

⁶ We remind the value of the solar metallicity: $Z_{\odot} \simeq 0.02$.

observations give $\text{Log}[D/H] = -4.5$ (Burles and Tytler, 1998; Pettini and Bowen, 2001; O’Meara et al., 2006), while the abundance of Li (around 10^{-10}) is not very well determined and can vary by a factor of two or three when compared to the measurements in the atmospheres of old stars (Korn et al., 2006; Yong et al., 2006). Other Li-derived molecules (e.g. LiH and LiH^+) have much lower abundances (Lepp and Shull, 1984; Puy et al., 1993; Galli and Palla, 1998).

Another potentially interesting molecule is HD. Due to its permanent electric dipole moment⁷, HD has higher rotational transition probabilities and smaller rotational energy separations compared to H_2 and thus, despite its lower abundance (Lepp and Shull, 1984; Puy et al., 1993; Galli and Palla, 1998), HD can be an efficient coolant (Flower, 2000; Galli and Palla, 2002; Lipovka et al., 2005; Abgrall and Roueff, 2006) and bring the gas in primordial haloes to temperatures of the order of 10^2 K. This results into a smaller Jeans mass and a more efficient fragmentation process. For haloes with virial temperatures in the range 10^3 K – 10^4 K, HD cooling can be as relevant as H_2 .

The basic reactions ruling H_2 production are (Saslaw and Zipoy, 1967; Tegmark et al., 1997, for example):

- the H^- channel (effective at $z \lesssim 200$)



- the H_2^+ channel (effective at $z \gg 200$)



- three-body interactions (effective at densities higher than $\sim 10^8 \text{ cm}^{-3}$)



In the previous reactions, h is the Planck constant and ν the frequency of the radiation emitted. The maximum efficiency is reached at about $T \sim 2000 \div 3000$ K. The path (2.60) is limited by the necessity of free protons, which are rarer and rarer at low T , as they

⁷ Values of the permanent HD electric dipole moment range between $D = 8.3 \cdot 10^{-4}$ debye (Abgrall et al., 1982) and $D = 8.51 \cdot 10^{-4}$ debye (Thorson et al., 1985). The first data date back to McKellar et al. (1976); for a theoretical, *ab initio*, non relativistic, perturbative treatment, via radial Schroedinger equation, see also Ford and Browne (1977) and references therein.

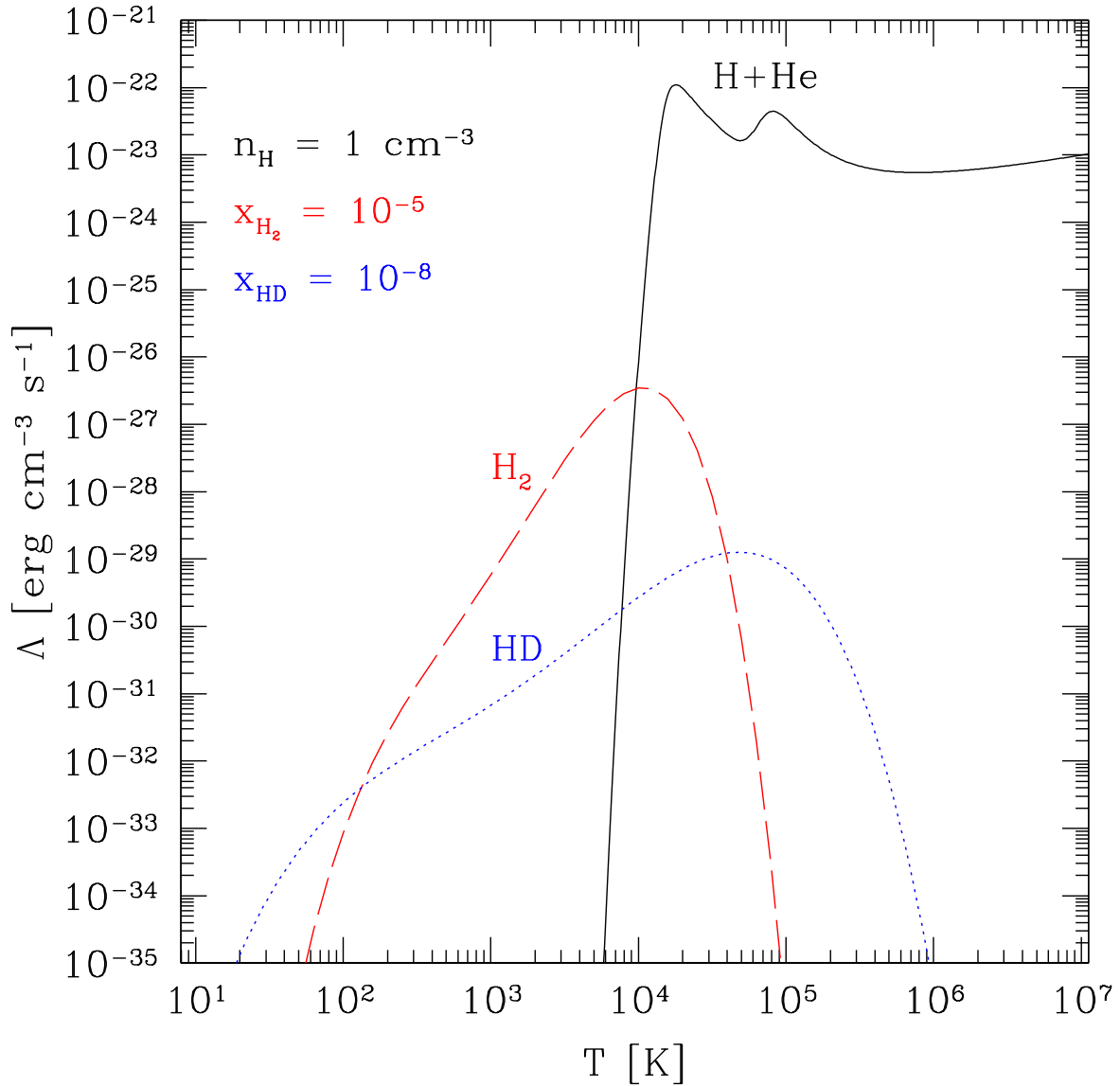


Figure 2.8: Contributions to the cooling function from hydrogen and helium (solid line) in primordial ratio, with a fraction of H_2 (long-dashed line) $x_{\text{H}_2} = 10^{-5}$ and of HD (dotted line) $x_{\text{HD}} = 10^{-8}$. A hydrogen number density of 1 cm^{-3} was assumed.

easily recombine with free electrons, and (2.61) is important only at very high densities (at least $\sim 10^8 \text{ cm}^{-3}$).

The production of HD molecules from primordial deuterium D and H_2 mainly follows from



Also these reactions are significant for $T < 10^4$ K and are strongly dependent on H_2 formation. A comparison between the primordial cooling function of Figure 2.7 and the molecular cooling functions is shown in Figure 2.8 for typical values of H_2 and HD fractions.

When the cooling time due to H_2 and/or HD in such pristine environments is shorter than the free-fall time, a protogalaxy is formed and we call it *population III* object.

Chapter 3

Star formation, initial mass function and feedback

*The heavens themselves, the planets, and this centre
Observe degree, priority, and place,
Insisture, course, proportion, season, form,
Office, and custom, in all line of order.*

SHAKESPEARE, TROILUS AND CRESSIDA

According to the general picture of structure formation, galaxies and stars form from in-fall of gas into dark matter haloes and subsequent fragmentation. In the following, we will deal with the main properties of stellar populations and in particular of first stars, paying our attention to their mass, statistical distribution, time evolution and physical features.

3.1 First stars and subsequent generations

In primordial conditions, no metals are present and the only viable coolants are hydrogen and helium, effective in rare, massive haloes, and some derived molecules (H_2 , HD), effective in more common, small haloes. As firstly suggested by Saslaw and Zipoy (1967), it is believed that the very first structures should be originated in the small primordial haloes, through molecular cooling (protogalaxies), where metal-free star formation is hosted and *population III* stars will be born. Considering only H_2 cooling, the Jeans mass for such stars is expected to be between $10^2 M_\odot$ and $10^3 M_\odot$ (Abel et al., 2002; Omukai and Palla, 2003; Yoshida et al., 2003a, 2006b; Gao et al., 2007, etc.). The first stars affect unavoidably the neighboring environment and the subsequent star formation. For example, they can re-ionise the nearby regions and, in presence of HD cooling, induce

star formation down to scales of $\sim 40 M_{\odot}$ (Yoshida et al., 2007). In addition, their natural evolution brings to the production of new elements in their inner core. These are eventually expelled, by SNe and stellar winds, into the surrounding medium and are able to enhance cooling at low temperatures (Bromm and Loeb, 2003; Santoro and Shull, 2006). With their hundred Kelvin fine-structure transitions they represent a much more efficient coolant with respect to molecules and have significant impact on structure formation. In fact, the higher the cooling, the lower the gas temperature and the Jeans mass: therefore, objects formed in polluted media are expected to have smaller typical masses. This class of structures is generally classified as *population II* (or even *population I* in metal-rich regimes) stars.

The reasons why one invokes the formation of population III stars is related to observational issues which cannot be explained with the known stellar population. Some of the most striking are (Ciardi and Ferrara, 2005, and references therein):

- The enhancement of α -elements¹ in galactic metal-poor stars and the existence of extremely metal-poor stars containing s-process elements² in their envelopes.
- The reionisation of the Universe due to first structure formation.
- The metal pollution of intergalactic medium, inferred from Lyman- α absorption lines.
- The formation of massive stellar black holes.

Population III stars could easily explain such problems, as they would be massive, as mentioned before, rapidly evolving towards their final state of explosive supernova (accompanied by spreading of material, like α -elements and/or s-process elements) or massive black hole. Their strong radiation could also re-ionise the early Universe, when its age is only some tenths of Gyr.

The existence of population III stars is merely speculative and not yet proven. The observability is highly improbable, considering their short typical life-times (less than 10^7 yr). So one must rely on indirect probes of their existence: for example, presence of enhanced heavy elements like Mg, C, N on stellar surface could imply metal enrichment from hypothetical previous population III stars (Christlieb et al., 2004; Bessell et al., 2004).

¹Elements formed via α -particle-capture-processes in the late evolutionary stages of massive stars.

²Heavy elements formed in slow-neutron-capture-processes, via β^- decay, in the interior of evolved stars (rapid-neutron-capture-processes allow the formation of different isotopes of the same element, but not the formation of new elements, as these processes dominate over the β^- decay).

According to galactic evolution models, it is not possible to prove or to disprove the past existence of such stars, as the galactic abundances would not be affected significantly by population III star formation (Ballero et al., 2006). As an alternative, one can look for very massive stars ($\sim 10^2 M_\odot$) born in pristine medium and still alive today (Figer et al., 1998) or check for the galaxy emission lines, like $Ly\alpha$ luminosity, which could have been boosted by population III stellar clusters (Tumlinson et al., 2001; Scannapieco et al., 2003; Nagao et al., 2008). More effects due to population III stars could derive from their emission in the near infra-red (Matsumoto et al., 2005; Salvaterra and Ferrara, 2006; Aharonian et al., 2006), their final evolution into gamma-ray bursts (Bromm and Loeb, 2006), or from the presence of black hole remnants and gravitational waves at frequencies $\sim 10^{-3}$ Hz (Schneider et al., 2000).

3.2 Stellar system properties

The most used parameterization of the star formation history of a stellar system is the stellar birthrate function: the number density of stars formed per unit time and mass,

$$B(M_\star, t) \equiv \frac{d^2n}{dM_\star dt}. \quad (3.1)$$

Usually, $B(M_\star, t)$ is factorized according to the *Ansatz*

$$B(M_\star, t)dM_\star dt \equiv \xi(M_\star)dM_\star \psi(t)dt \quad (3.2)$$

where ξ is the initial mass function (IMF) of the stellar population,

$$\xi(M_\star) \equiv \frac{dn}{dM_\star} \quad (3.3)$$

while ψ is the star formation rate (SFR) at a given time t

$$\psi(t) \equiv \frac{dn}{dt}. \quad (3.4)$$

The IMF is the number fraction of stars formed, df , per mass interval $[M, M + dM]$; it is normally denoted by $\phi(M)$. Salpeter (1955) performed its first empirical determination in the mass range $[0.5 M_\odot, 10 M_\odot]$ and he suggested the following power law fit:

$$\phi(M) \equiv \frac{df}{dM} \sim M^{-2.35}. \quad (3.5)$$

Over the years, many other different fitting formulæ have been proposed by, for example, Miller and Scalo (1979), Kennicutt (1983), Scalo (1986), Rana (1991), Kroupa et al.

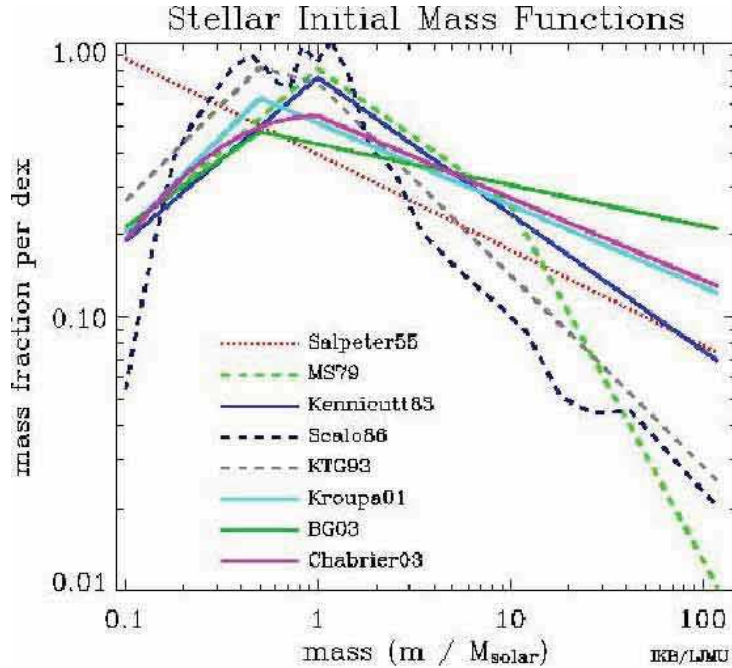


Figure 3.1: A comparison of popular stellar initial mass functions (Courtesy of Ivan Baldry in Ellis, 2008). The functional forms plotted (see labels in order from top to bottom) are the one suggested over several years by: Salpeter (1955), Miller and Scalo (1979), Kennicutt (1983), Scalo (1986), Kroupa et al. (1993), Kroupa (2001), Baldry and Glazebrook (2003), Chabrier (2003).

(1993), Kroupa (2001), Baldry and Glazebrook (2003), Chabrier (2003). The mass range has been extended down to about $0.01 M_{\odot}$ and up to more than $100 M_{\odot}$, but the Salpeter power law trend is in general preserved, although the IMF seems to flatten at the low-mass end ($M < 0.5 M_{\odot}$) and there is a significant fall-off and paucity of brown dwarves at masses lower than $0.1 M_{\odot}$ (Basri and Marcy, 1997). The behaviour in this mass regime is quite uncertain because the mass-luminosity relation for faint stars is not very well known and the mass distribution is dominated by binary systems.

A comparison between some of the most popular IMF fits is found in Figure 3.1.

The behaviour at high redshift is not known³, but presumably the first stars should have an IMF shifted toward high masses, as their Jeans mass is higher. A suggested trend is (Larson, 1998):

$$M_{\star}\xi(M_{\star}) \sim \left(1 + \frac{M_{\star}}{M_c}\right)^{-1.35} \quad (3.6)$$

where M_c is a critical mass related to the Jeans mass $M_c \sim M_J \sim T^{3/2}\rho^{-1/2}$, for (2.18) and (2.20). Relation (3.6) reproduces the Salpeter's shape for $M_{\star}/M_c \gg 1$.

³Some recent studies (van Dokkum, 2007) try to constraint the IMF as a function of the redshift, but the results are still unclear and contradictory.

As M_c increases with redshift, $\xi(M)$ has a power slope decrement around $M \sim 10^2 M_\odot$, while, for $z \rightarrow 0$, the local Salpeter IMF is recovered, with a critical mass of the order of $\sim M_\odot$.

The main, elementary, physical reason for the transition from a high-redshift Larson IMF to a low-redshift Salpeter IMF is the presence of different cooling agents, which determine different values for the Jeans mass. When, like in the primordial case, the cooling is led by molecules only (H_2 and/or HD, as said before), $M_J \sim 10 M_\odot - 10^2 M_\odot$; when also metals are present cooling is much stronger and more efficient, so one can reach $M_J \sim M_\odot$.

Regarding the SFR, we have indirect informations from related physical indicators, like luminosities in different bands – basically far-infrared and ultraviolet – and recombination or forbidden line – mainly H_α , $[\text{OII}]\lambda 3727$ (see Appendix B for further details on SFR indicators). In this way, one can get easy empirical relations to obtain estimates of ψ from L_{FIR} , L_{UV} , L_{H_α} , L_{OII} (Kennicutt, 1998, and references therein). Nowadays, it seems that the cosmological SFR peaks at redshift $z \sim 2 - 3$ (when the Universe was few Gyr old) and then decreases at lower and higher z . There are no observational constraints at high redshift ($z \gtrsim 6$) even if it is supposed to decrease, as, at those early times, there were fewer and fewer structures (see observed data points in Figure 3.2).

3.3 Features of primordial stars

Population III stars are quite different from standard population II or I star. Their mass is much higher (some tens or hundreds M_\odot) and the surface temperature can reach some 10^5 K, emitting at the Eddington limit. The spectrum is shifted to higher frequencies and peaks in the UV, with typical helium – HeI and HeII – absorption lines (helium lines do not show up in usual population II or I stars). Nonetheless, the fast evolution towards late stages does not allow these features to last long, as they are supposed to vanish in a life-time of some 10^7 yr, or less.

As they are made only of hydrogen and helium, their core is basically formed by a plasma of electrons, protons and α particles with a temperature of about 10^7 K. The only nuclear reactions which can be ignited and can sustain the whole star are proton-proton chains; 3α -processes ($3\text{}^4_2\text{He} \rightarrow \text{}^{12}_6\text{C} + \gamma$) can contribute only once the contraction of the core

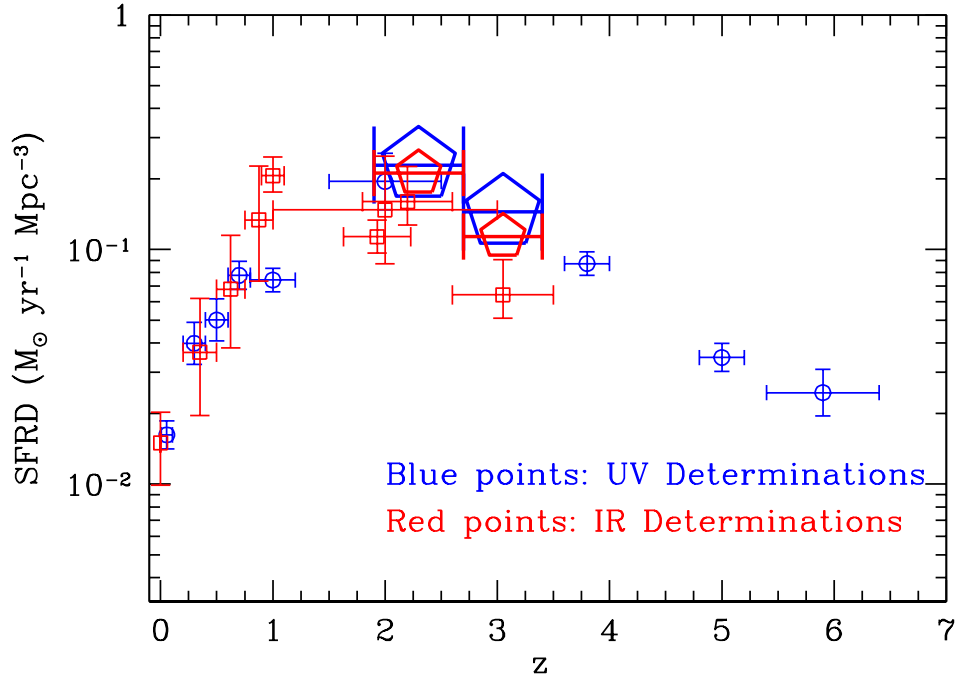


Figure 3.2: Observational determinations of the cosmological star formation rate as a function of redshift in the ultraviolet (UV) band (blue circles and pentagons) and infra-red (IR) band (red squares). See Reddy et al. (2008) and appendix B for further details.

due to the rapid exhaustion of proton nuclear burning raises temperatures to some 10^8 K. Afterwards, more heavy elements are produced in the interiors of the star and eventually ejected into the surrounding medium. Stellar evolution numerical models show several possible final fates, from the helium-burning-phase on, depending on the mass of the star, M_{\star} :

- $10 M_{\odot} \lesssim M_{\star} \lesssim 40 M_{\odot}$: all the elements up to iron are synthesized. When the nucleus exceeds the Chandrasekhar mass, $1.4 M_{\odot}$, it collapses and causes a supernova explosion (SNII) which pollutes the surrounding ambient. If the mass is $30 M_{\odot} \lesssim M_{\star} \lesssim 40 M_{\odot}$, the star explodes and eventually degenerates into a black hole (Woosley and Weaver, 1995);
- $40 M_{\odot} \lesssim M_{\star} \lesssim 100 M_{\odot}$: there is a formation of a black hole, accompanied either by complete collapse or by jets/ γ -ray bursts (Fryer, 1999).
- $100 M_{\odot} \lesssim M_{\star} \lesssim 260 M_{\odot}$: the helium burning core reaches $T \simeq 5 \cdot 10^8$ K, when electron-pair-creation-processes become possible ($\gamma \rightarrow e^+e^-$). The pairs increase the gravitational potential and make the nucleus collapse. Oxygen and Silicon

burning is ignited explosively and a *pair instability* supernova (PISN) is generated (Zeldovich and Novikov, 1971), by which the star would be partially or completely disrupted (Portinari et al., 1998; Fryer et al., 2001; Meynet et al., 2006a). The amount of kinetic energy released is of the order of $\sim 10^{51}$ erg- 10^{53} erg per explosion (standard supernova explosions produce energies of $\sim 10^{51}$ erg).

- $M_{\star} \gtrsim 260 M_{\odot}$: there is photo-disintegration of the core and formation of a massive black hole, accompanied either by complete collapse or by jets (Fuller et al., 1986).

A schematic summary of the possible fates of primordial stars with different initial masses is sketched in Figure 3.3 together with the mechanisms leading to the final stages.

3.4 Feedback processes

Once the first stars have formed and evolved, they can affect the subsequent structure and star formation process by a number of “feedback” effects.

Feedback effects are all those mechanisms whose effects act upon the starting causes, enhancing or inhibiting them. Taking into account their presence is fundamental, because they can seriously affect the properties and evolution of cosmic structures (star clusters, galaxies, galaxy clusters) and their environment (interstellar medium, intergalactic medium).

According to the particular phenomena involved, one distinguishes *mechanical feedback*, *radiative feedback* and *chemical feedback*. In the following we give a brief description of the main feedback processes; for a complete review see Ciardi and Ferrara (2005).

3.4.1 Mechanical feedback

They are purely mechanical effects, involving forces and displacements acting on a given body.

In astrophysics, a typical example is the ejection of mass or energy from evolved objects, like stars, during SN or PISN explosions. Such events can partially (blowout) or completely (blowaway) remove the ambient gas (Mac Low and Ferrara, 1999; Bromm et al., 2003; Whalen et al., 2008), decrease its density and halt the possible cooling mechanisms which were going on (negative feedback).

Also galactic structures are often characterized by winds and outflows (Sigward et al.,

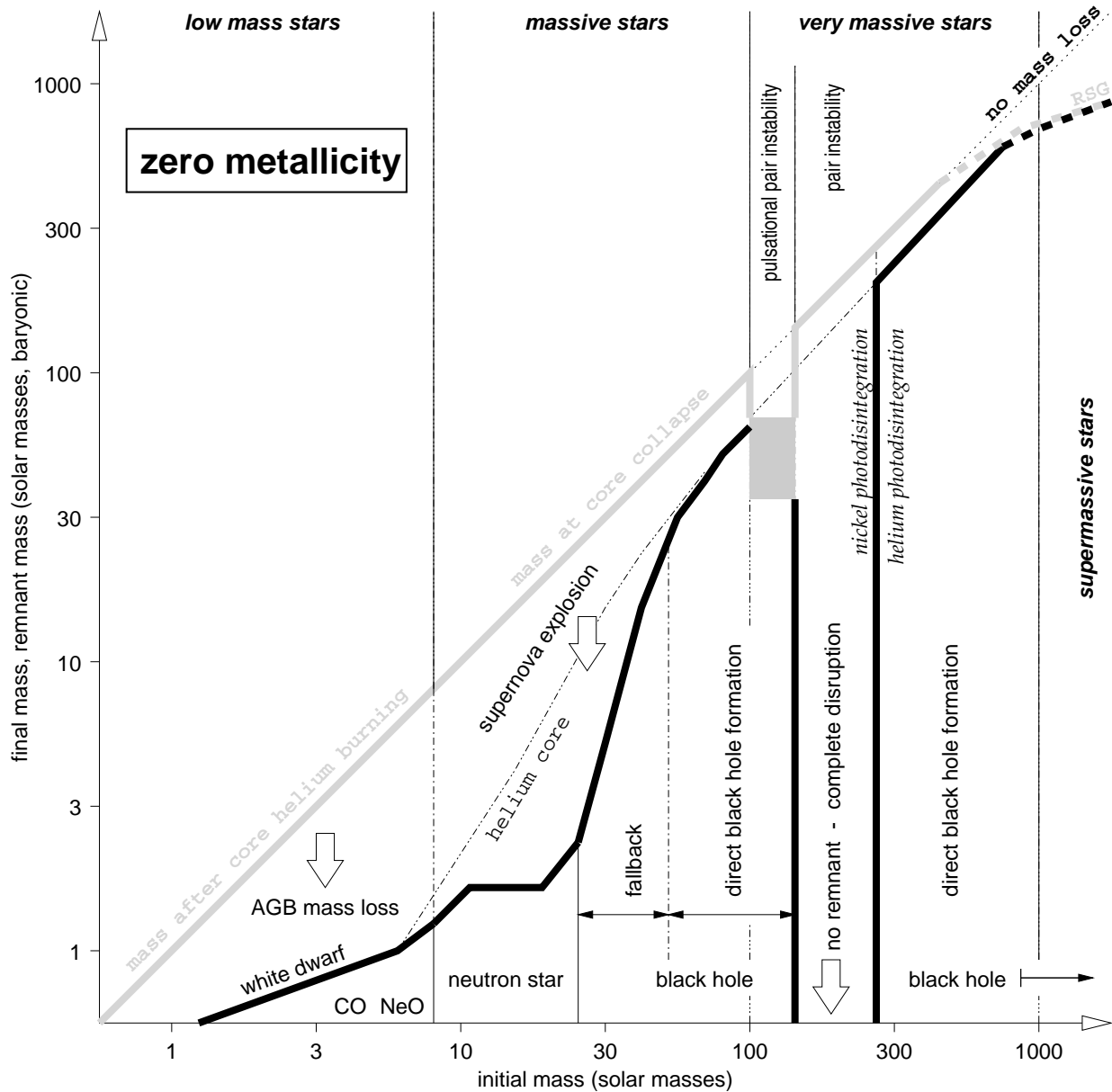


Figure 3.3: Scheme of the possible final fates of primordial population III stars (Heger and Woosley, 2002): the final/remnant mass (thick blue line) is plotted versus the initial stellar mass. In addition, the mass of the star at the beginning of the final stages is shown (thick grey line), with the helium core mass (dashed-double-dotted thin line) and the details relative to the physical process involved at each mass-scale (see labels).

2005) of gas not retained by the gravitational potential and generated during stellar evolution (e.g. still SN and/or PISN).

At the same time shocks can be originated (Vishniac, 1983) and boost molecule formation in the cold shells behind them (positive feedback). The rise of shocks or blast-waves during gas in-fall, instead, stops (temporarily) star formation (negative feedback).

A last process which might happen is the interaction between galaxies with the possible

stripping of gas due to tidal effects (negative feedback).

3.4.2 Radiative feedback

They are related to ionization or dissociation of atoms and molecules.

Radiation produced by stars or quasars – mostly the one in UV – can determine (Thoul and Weinberg, 1996; Haiman et al., 1997) photo-ionization of hydrogen and photo-dissociation of molecules limiting the cooling capabilities of the gas (negative feedback).

On the other hand, molecule formation is enhanced in presence of X-rays, which accelerate free electrons, or in HII regions, where there is plenty of free electrons (Ricotti et al., 2001) – see reactions (2.59), (2.60) and (2.62) – (positive feedback).

Photons from evolved structures can make the temperature of the IGM increase (preheating) and the Jeans mass, as well, so small structure formation can be inhibited or postponed (negative feedback).

A side effect is the particle evaporation caused by heating of radiation (negative feedback) (Haiman et al., 2001).

3.4.3 Chemical feedback

Chemical feedback effects involve the influence of the chemical composition of the medium on structure formation. The main astrophysical problem related to this issue is the pollution of the intergalactic medium. This is basically due to the spreading of metals by stars in their late evolutionary stages. In fact, the first stars form from pristine gas but, when they explode as SN or PISN, contaminate the surrounding regions altering the global chemical composition. In particular, they cause an increase in the amount of metals enhancing the cooling capabilities of the medium (positive feedback).

The next generations of stars will be born in a medium with different properties and larger varieties of coolants, even though it is believed that the behaviour of gas collapse and fragmentation does not change much until metallicities of $\sim 10^{-4}Z_{\odot}$ are reached (Yoshii and Sabano, 1980). This is the reason for the remarkable speculations on the dependence of the IMF on the metallicity of the ambient medium.

The topic is very controversial, but one believes that at a critical metallicity Z_{crit} the IMF should switch from a top-heavy to a Salpeter-like (see section 3.2), as metal and dust cooling becomes efficient in fragmenting gas clouds down to sub-solar masses. The

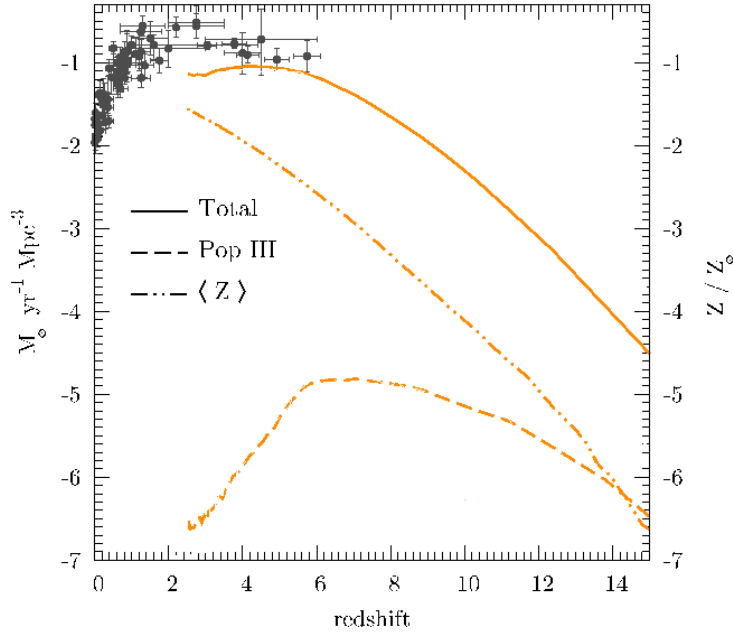


Figure 3.4: Total star formation rate (solid line), average metallicity (dotted-dashed line) and population III star formation rate (dashed line) plotted as a function of the redshift for a 10 Mpc box side simulation (Tornatore et al., 2007b). The left vertical axis refers to the decimal logarithm of the star formation rate in $M_{\odot} \text{ yr}^{-1} \text{ Mpc}^{-3}$, the right one to the decimal logarithm of the average metallicity in solar units; the circular points are measured values of the star formation rate.

exact value of Z_{crit} is quite uncertain and many debates have been done about it.

Definitely, the role of dust seems to be extremely important, as according to some recent estimates (Schneider et al., 2003) metals depleted onto dust grains allow to reach sub-solar scales already at $Z \sim 10^{-6} Z_{\odot}$, while in absence of dust formation the same scales are not even reached for $Z \sim 10^{-2} Z_{\odot}$.

Considering metal fine-structure transition cooling, one expect a critical metallicity of the order $Z_{crit} \sim 10^{-4} Z_{\odot} - 10^{-3} Z_{\odot}$ (Bromm and Loeb, 2003; Santoro and Shull, 2006).

From this discussions, it is evident that the metal enrichment of the first stars is very important to determine the features of the following structures and the duration of a population III star formation regime.

We point out that the chemical feedback process is not strictly cosmological, because metal pollution is prominent around star formation sites. It is rather a local, patchy and inhomogeneous effect, therefore, mostly at high z , regions already enriched will necessarily co-exist with regions preserving still a primordial chemical composition. This also means that the presence of population III or population II/I stars can easily be simultaneous and both of them can contribute to the global star formation rate. Recent

works (Tornatore et al., 2007b; Wyithe and Cen, 2007) suggest, anyway, that population III SFR should be negligible, at least at low redshift ($z \lesssim 10 - 15$) - see Figure 3.4.

Moreover, metal yields from primordial metal free stars can locally bring the metallicity up to $Z \sim 10^{-5} - 10^{-4}$ (equal to $Z \sim 10^{-3}Z_{\odot} - 10^{-2}Z_{\odot}$) already in the very first bursts. In a standard Λ CDM model ($\Omega_{0m} = 0.3$, $\Omega_{0\Lambda} = 0.7$, $h = 0.7$, $\sigma_8 = 0.9$, $n = 1$), the Universe could have been endowed with a metallicity floor, $Z_{min} > 10^{-4}Z_{\odot}$, since $z \sim 15$ (Bromm et al., 2003) and the transition to population II/I objects should have been very rapid.

3.5 Final remark

In this work, we will be focused mainly on the chemical feedback issues in numerical simulations of structure formation, studying how the scenario changes adopting different numerical approaches and different critical metallicity.

Part II

Cosmological simulations

Chapter 4

Numerical simulations of early structure formation

*Omnium rerum simulatio vitiosa est –
tollit enim iudicium veri idque adulterat –
delet enim veritatem.*

CICERO, DE AMICITIA

Numerical simulation codes have been, since long time, a powerful mean of studying the N-body problem in astrophysics (van Albada, 1968; Hénon, 1971; Ahmad and Cohen, 1973; White, 1976; Lucy, 1977; Gingold and Monaghan, 1977; Fall, 1978; Larson, 1978; White, 1978; Aarseth et al., 1979; Giuricin et al., 1984; Efstathiou et al., 1985; Barnes and Hut, 1986) and, joined with Hydrodynamics, in cosmology (Evrard, 1988; Hernquist and Katz, 1989; Cen and Ostriker, 1992; Katz et al., 1996; Bryan and Norman, 1997; Springel et al., 2001). Computational limitations, though, have always requested plausible sub-grid models to take into account star formation events (Cen and Ostriker, 1992; Katz et al., 1996; Springel and Hernquist, 2003). To this goal, typically semi-empirical relations are adopted even though their intrinsic physical meaning is actually lacking.

On one side this is not satisfying, as one would like to really model the underlying physics, on the other hand, this approach can be very helpful to investigate other different physical properties of cosmic structures.

In the next sections, we will give a brief overview of the techniques used to perform numerical simulations and we will describe the implementation we have done to predict the high-redshift physical state of the Universe.

4.1 Numerical techniques

The basic numerical techniques to follow structure formation also in non-linear regimes consist in finding an approximate, but accurate, solution for the potential of N particles under the reciprocal gravitational attraction (N-body problem). For baryonic matter one has to solve also the fluid-dynamic equations.

Briefly speaking, one calls collisionless those systems (like galaxies) ruled by gravity only and for which other interactions among particles are negligible; collisional those systems (like gases) for which the collisions among particles are relevant and determine their overall behaviour.

4.1.1 Treatment of gravitation

The gravitational (collisionless) interactions are described basically by the following dynamic system:

$$\begin{cases} \dot{\mathbf{x}} &= \mathbf{v} \\ m\dot{\mathbf{v}} &= -\nabla\phi \end{cases} \quad (4.1)$$

where \mathbf{v} is the particle velocity, \mathbf{x} the position, ϕ the gravitational potential, m the point mass and the dot denotes the time-derivative. The gradient of the gravitational potential gives by definition the force acting upon any point, $\mathbf{F} = -\nabla\phi$, and ϕ must satisfy the Poisson equation:

$$\Delta\phi = 4\pi G\rho \quad (4.2)$$

with ρ density of the mass distribution. Once the initial conditions and the time-step Δt are fixed, it is easy to get iteratively the new position and velocity, of each particle.

There are several methods to integrate the system (4.1). We summarize them below.

- The simple particle-particle (PP) approach consists in the direct summation of the gravitational forces acting on each particle. The total force acting on any particle i , with mass m_i , is then given by

$$\mathbf{F}_i = - \sum_{i \neq j} \frac{Gm_i m_j (\mathbf{r}_i - \mathbf{r}_j)}{(\|\mathbf{r}_i - \mathbf{r}_j\|^2 + \varepsilon_s^2)^{3/2}} \quad (4.3)$$

where the sum is done over all the other particles with mass m_j and position \mathbf{x}_j ; ε_s^2 is a positive, numerical parameter called softening length and needed to avoid possible

force divergences¹. This method is precise and accurate, but extremely slow, as the number of numerical iterations scales as $\frac{1}{2}N(N-1) \sim \mathcal{O}(N^2)$, being N the number of particles.

- In order to increase the performance it is possible to use a particle-mesh (PM) method. This consists in smoothing the mass distribution over a grid, where the gravitational potential and the resulting force can be easily and fastly computed from the Poisson equation (4.2) in the Fourier space,

$$\hat{\phi}(\mathbf{k}) = -\frac{4\pi G \hat{\rho}(\mathbf{k})}{k^2} \quad (4.5)$$

$$\hat{\mathbf{F}}(\mathbf{k}) = -i\mathbf{k}\hat{\phi}(\mathbf{k}). \quad (4.6)$$

This method is faster than the PP one, as it scales like $\mathcal{O}(N \log N)$, but is resolution limited by the presence of the grid.

- The problem can be avoided with the particle-particle-particle-mesh (P³M) method. In this approach, the particles close to or under the grid resolution limit are treated with the PP method, while the PM method is applied to resolved particles.
- Tree codes are probably the fastest and most efficient way to solve gravity problems (Barnes and Hut, 1986). They are based on a tree-structured, hierarchical, decomposition of space. At each time-step, the region considered is divided into eight cubic cells, each of which is recursively subdivided into eight sub-cells whenever more than one particle is found to occupy the same cell. At the end, one gets a tree of cells from the root, containing the whole particle sample, down to the daughter cells, containing either one particle or none. The force on any particle x is approximated by a recursive calculation starting from the root cell and considering the subsequent sub-cells. In this way, particles very “close” to x are actually treated according to the PP method, “distant” particles according to the first order gravitational multipole expansion² (see Figure 4.1). The time scaling to build the tree is $\mathcal{O}(N \log N)$.

¹ For “close” pairs (i.e. $r \equiv \|\mathbf{r}_i - \mathbf{r}_j\| < \varepsilon_s$), the force is computed assuming a particular density profile (Plummer) for the particle mass m_j :

$$\rho_{Plummer}(r) = \frac{3m_j}{4\varepsilon_s^2 \left(1 + \frac{r^2}{\varepsilon_s^2}\right)^{5/2}}. \quad (4.4)$$

² Let’s call

– l the dimension of the current cell;

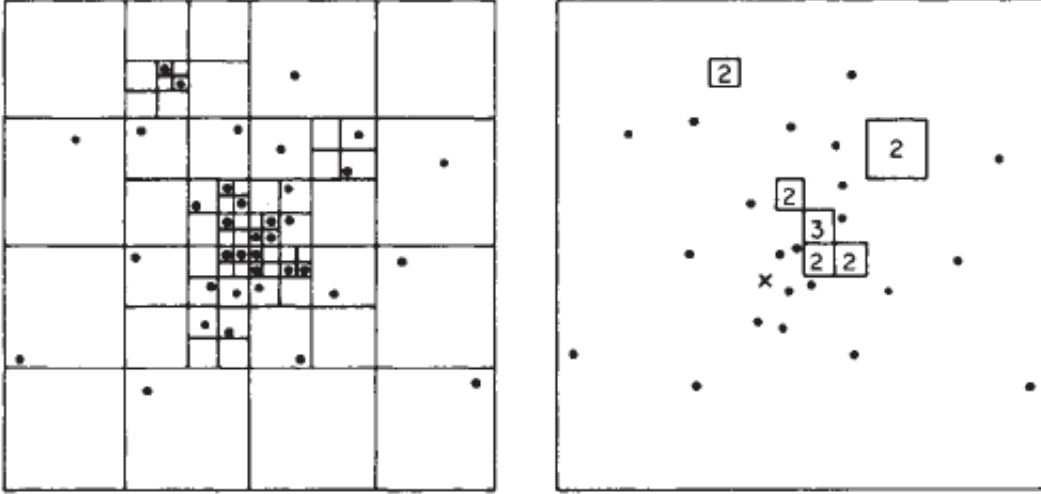


Figure 4.1: Examples of domain decomposition in 2 dimensions. In the left panel, a system of particles is shown and the recursive subdivision of the space induced by these particles, until each of them gets isolated. In the right panel, it is shown how force on particle x is calculated: fitted cells contain particles (whose number is indicated) that are lumped together by the “opening angle” criterion $\theta = 1$ (i.e. cell size over cell distance $l/D < \theta = 1$). Each such cell represents a single term in the force summation. Taken from Barnes and Hut (1986).

4.1.2 Treatment of fluid-dynamics

For a collisional fluid, in order to know the variables parameterizing the hydrodynamical interactions, one must solve numerically the

- continuity equation

$$\frac{d\rho}{dt} + \rho \nabla \cdot \mathbf{v} = 0 \quad (4.8)$$

- Euler equations

$$\frac{d\mathbf{v}}{dt} = -\frac{\nabla P}{\rho} - \nabla\phi \quad (4.9)$$

- energy equation

$$\frac{du}{dt} = -\frac{P}{\rho} \nabla \cdot \mathbf{v} - \frac{\Lambda}{\rho} \quad (4.10)$$

- equation of state

$$P = (\gamma - 1)\rho u \quad (4.11)$$

-
- D the distance of the center of mass of the current cell from x ;
 - θ the accuracy parameter or “opening angle”.

If the condition

$$\frac{l}{D} < \theta \quad (4.7)$$

is satisfied (i.e for “far” particles within “small” size cells and at “large” distance D), then the interaction between the particle x and the whole cell is included, otherwise the current cell is resolved into its sub-cells. Usually, values of $\theta \sim 1$ gives accuracies on the force computation of $\sim 1\%$. Smaller θ 's give even better results.

with Lagrangian derivative

$$\frac{d}{dt} = \frac{\partial}{\partial t} + \mathbf{v} \cdot \nabla, \quad (4.12)$$

ρ , P , \mathbf{v} and u mass density, pressure, velocity field and internal energy per unit mass of the fluid, γ adiabatic index, $\Lambda \equiv \Lambda(u, \rho)$ cooling function.

In computational fluidodynamics such equations are solved with two main techniques: Eulerian and Lagrangian methods.

- Eulerian (grid) methods: the fluid is smoothed on a grid, with spatial resolution Δx , and its temporal evolution is computed for successive time-steps, Δt , discretizing equations (4.8 – 4.10). All of them can be put in the form

$$\frac{\partial g(x, t)}{\partial t} = \frac{\partial f(x, t)}{\partial x} \quad (4.13)$$

with f and g suitable scalar functions. The recursive solution for the i -th grid point at the $(n + 1)$ -th time-step is (Lax scheme)

$$g_i^{n+1} = \frac{g_{i+1}^n + g_{i-1}^n}{2} + \frac{f_{i+1}^n - f_{i-1}^n}{2\Delta x} \Delta t \quad (4.14)$$

where n denotes the former time-step and $i + 1$ and $i - 1$ are the indices for the adjacent grid points. In equation (4.14), we have substituted g_i^n with the spatial average on the two nearest points $(g_{i+1}^n + g_{i-1}^n) / 2$, for stability reasons.

- Lagrangian (SPH) methods: the fluid is represented by particles and there is no use of grids. The relevant hydrodynamic quantities are computed from the surrounding particles, within a typical smoothing length h , weighted with a suitable smoothing kernel³, W (see Figure 4.2). The average value of a variable, f , for a given particle of interest, at position \mathbf{x} , is obtained via convolution with W :

$$\langle f(\mathbf{x}) \rangle = (f \star W)(\mathbf{x}) = \int f(\mathbf{x}') W(\mathbf{x} - \mathbf{x}'; h) d^3 x'. \quad (4.15)$$

If we call $\mathbf{r} \equiv \mathbf{x}' - \mathbf{x}$, with \mathbf{x}' any arbitrary position in space, the kernel is normalized by

$$\int W(\mathbf{r}; h) d^3 r = 1 \quad (4.16)$$

³ Often Gaussian or polynomial functions defined over a compact support.

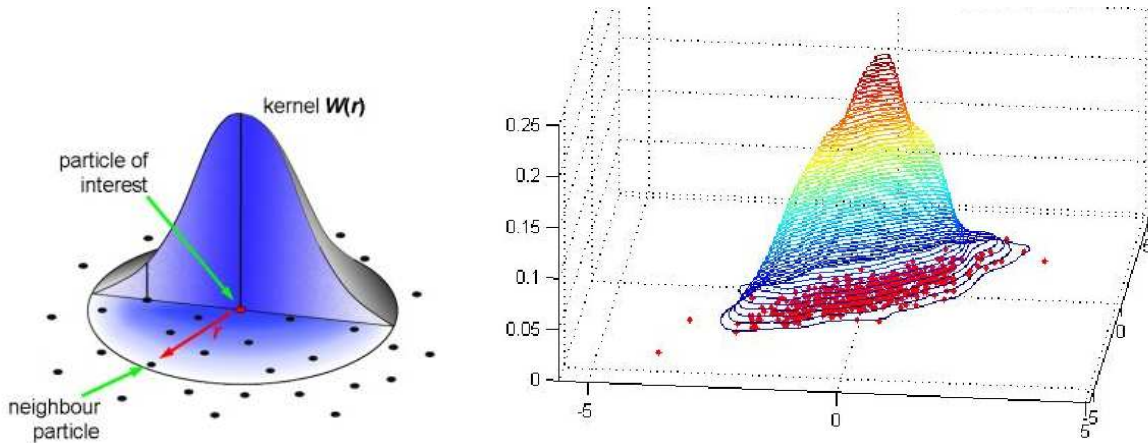


Figure 4.2: The left plot is a simplified pattern of SPH kernel for a bi-dimensional point distribution. The particle of interest, one neighbour particle and their distance, \mathbf{r} , are indicated. The shaded area covers all the particles in the kernel with darker nuance at the center, where the region contributing most is located, and lighter one toward the borders where the contribution is minor. The right panel shows, as an example, contour levels for the density calculation of a bi-dimensional point distribution (xy plane) using the SPH method (arbitrary units).

and must reduce to a three-dimensional Dirac delta distribution, δ_D^3 , in the limit $h \rightarrow 0^+$. Numerically, one just sums up over the closest particles weighted according to the kernel and writes the above integral (4.15) as

$$\langle f(\mathbf{x}) \rangle = \sum_j f_j W(\mathbf{x} - \mathbf{x}_j; h) \frac{m_j}{\rho_j} \quad (4.17)$$

where f_j , m_j and ρ_j indicate, respectively, the quantity of interest, mass and density of the particle at the position \mathbf{x}_j ; the ratio m_j/ρ_j is used as volume element.

Analogous relations can be written for any hydrodynamic quantity (see also Figure 4.2).

4.2 The code Gadget

The simulations we have done were performed using the basic tree-construction (as explained in section 4.1.1) and hydrodynamic SPH solver (as described in section 4.1.2) present in the publicly available, parallel code Gadget2 (Springel, 2005).

In the following we will give its main features and describe the changes implemented to study early structure formation and metal pollution.

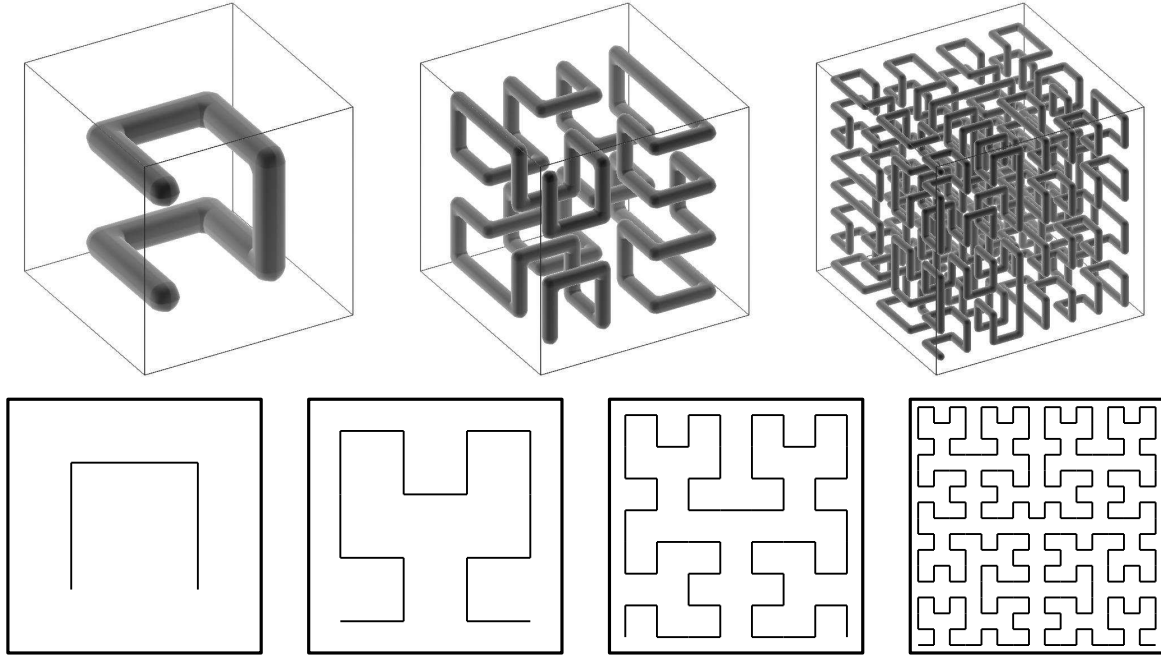


Figure 4.3: Top row: example of space-filling Peano-Hilbert curve. The basic structure in the left panel is replicated arbitrarily. The central panel and the right panel show the first and second replication level, respectively. Bottom row: a simplified 2D representation of the “U” shaped Peano-Hilbert curve is shown (Springel, 2005).

4.2.1 Overview

Gadget is a tree/SPH code which conserves energy and entropy. It computes all the different quantities using the closest neighbour particles located within the smoothing length h and the spherically symmetric, spline smoothing kernel (Monaghan and Lattanzio, 1985, equations (19) and (21) with the v variable replaced by $2r/h$)

$$W(r/h) = \frac{8}{\pi h^3} \begin{cases} 1 - 6(r/h)^2 + 6(r/h)^3 & 0 \leq r/h < 1/2 \\ 2(1 - r/h)^3 & 1/2 \leq r/h < 1 \\ 0 & r/h \geq 1 \end{cases} \quad (4.18)$$

where r is the inter-particle distance ($r \leq h$). We notice that such kernel is correctly normalized over the volume element $4\pi r^2 dr$ (according to 4.16), is continuous and differentiable, has a maximum in $W(0) = 8/\pi h^3$, decreases down to $W(1/2) = 2/\pi h^3$, where it becomes convex, and reaches its minimum at $W(1) = 0$.

The peculiarity of the “entropy” formulation of the code is that the smoothing length for each particle, h_i , is not fixed, but is computed assuming a constant mass content inside a

sphere with radius h_i . So h_i is defined as:

$$\frac{4}{3}\pi\rho_i h_i^3 \equiv \bar{m}N_{\text{SPH}} \quad (4.19)$$

where ρ_i is the estimated density, \bar{m} the average particle mass, N_{SPH} the number of neighbors used and $\bar{m}N_{\text{SPH}}$ the total mass inside the kernel. Such treatment, including the ∇h_i term in the fluid equations, conserves by construction energy and entropy⁴ (Lucy, 1977; Benz and Hills, 1987).

The implementation of dynamics and hydrodynamics follows the discretization of Newton’s law and fluid laws, respectively.

Time integration is performed by a symplectic leapfrog scheme, via drift and kick operators (Quinn et al., 1997), which advances alternatively space coordinates and velocity coordinates at each half time-step.

The parallelization strategy uses a space-filling, fractal curve, the Peano-Hilbert curve (Mandelbrot, 1982, and references therein), to map 3D space into a 1D space (Warren and Salmon, 1995) – see Figure 4.3 – and to reduce the communication costs. The curve is then chopped off into segments defining the individual domains (see Figure 4.4), particles are allocated on their target processor and density estimation, tree construction and force computation are executed.

Once the initial conditions are fixed, the code follows the gravitational evolution of dark and baryonic matter and the fluid evolution of gas particles only. This is done using a heating recipe for UV background (Haardt and Madau, 1996), H and He radiative cooling, multi-phase “sub-grid” model for star formation based on thermal instability criterion (Field, 1965), and a phenomenological approach for feedback from winds (with typical velocities ~ 500 km/s) powered by supernova explosions (Katz et al., 1996).

4.2.2 Star formation

The general structure of the effective “sub-grid” star formation model (Katz et al., 1996; Springel and Hernquist, 2003) is briefly described here. Each particle is assumed to be formed by an ambient hot gas, which might contain a cold phase and stars, when the density is high enough (the hydrogen number density for the onset of star formation is

⁴ SPH implementations neglecting the ∇h_i term can conserve energy fairly well, but do not conserve entropy.

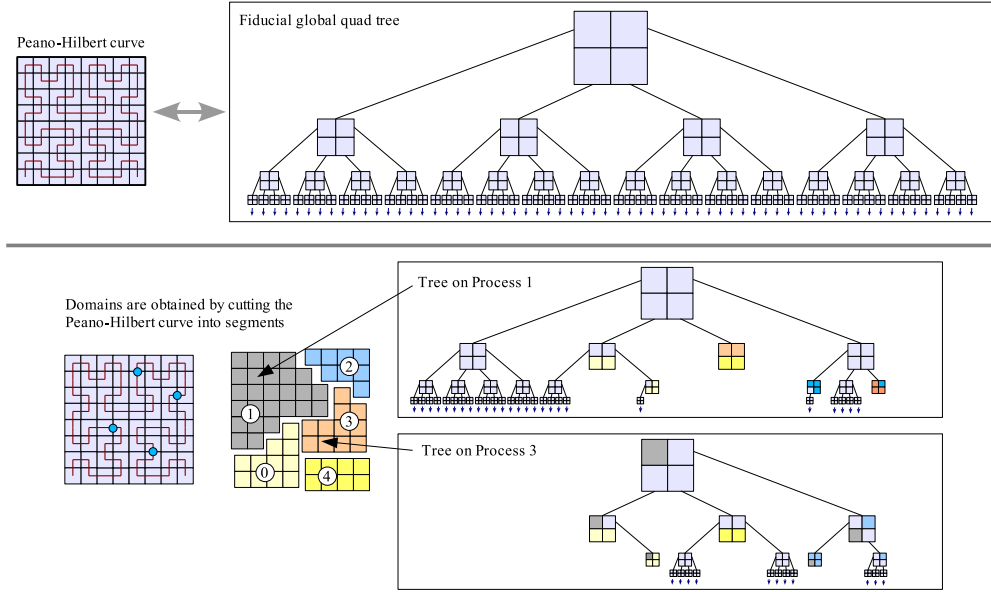


Figure 4.4: The top row relates the space-filling Peano-Hilbert curve (left side) with the simulation tree (right side). The simulation volume is cut into domains by segmenting the curve, so its branches reside entirely on single processors, as shown in the last row (Springel, 2005).

$n_{H,th} \simeq 0.1 \text{ cm}^{-3}$).

Basically, at any given time, the rate of star forming mass, \dot{m}_* , of a multi-phase gas particle with mass m is computed using

$$\dot{m}_* = \frac{xm}{t_*} \quad (4.20)$$

where x is the fraction of gas in cold clouds providing the reservoir for star formation and t_* is the star formation time-scale given by

$$t_*(\rho) = t_*^0 \left(\frac{\rho_{th}}{\rho} \right)^{1/2} \quad (4.21)$$

being ρ the mass density of the particle, ρ_{th} the star formation mass density threshold and t_*^0 a free parameter calibrated on the observed data in order to reproduce the known behaviour of the disc-averaged star formation rate as a function of the surface gas density (see Schmidt law in Appendix B).

The star formation rate of the *unstable, converging* flux, $\dot{\rho}$, is easily computed from

equation (4.20) and (4.21)

$$\dot{\rho} = \frac{\rho}{t_{\star}^0 (\rho_{th}/\rho)^{1/2}}. \quad (4.22)$$

Star particles are spawned, within a time-step Δt and for gas densities $\rho > \rho_{th}$ only, according to a stochastic approximation with exponential probability (Katz et al., 1996, section 4.2):

$$p = 1 - e^{-x\Delta t/t_{\star}}. \quad (4.23)$$

The number of stars produced per each gas particle is fixed by another free parameter, N_{\star} (generations), so that at each time-step the global amount of stars is pN_{\star} . Their mass distribution is known from the assumed IMF, which determines the fraction of stars per mass interval.

4.2.3 Metal enrichment

The primitive underlying star formation sub-grid model is extended including metal enrichment at each time-step (Tornatore et al., 2007a). This process is followed tracing ejecta and yields from SNIa (Thielemann et al., 2003), SNII (Woosley and Weaver, 1995), AGB (van den Hoek and Groenewegen, 1997), according to stellar masses and lifetimes (Padovani and Matteucci, 1993); metallicities are spread on the neighbour particles and weighted by the SPH kernel to derive the corresponding tabulated (Sutherland and Dopita, 1993) cooling term; stellar mass distribution is ruled by the possibility of choosing different initial mass functions, depending or not on the particle metallicity.

Similar works are also discussed, for example, by Raiteri et al. (1996); Gnedin (1998); Mosconi et al. (2001); Lia et al. (2002a,b); Kawata and Gibson (2003); Ricotti and Ostriker (2004); Kobayashi (2004); Scannapieco et al. (2005).

4.3 Implementation of molecule and metal chemistry

We have conveniently changed the code in order to follow also chemical (molecule and metal) evolution (Maio et al., 2007; Tornatore et al., 2007a) of forming structures and/or of the intergalactic medium.

Table 4.1: Set of reactions

Reactions	References for the rate coefficients
$\text{H} + \text{e}^- \longrightarrow \text{H}^+ + 2\text{e}^-$	A97 / Y06
$\text{H}^+ + \text{e}^- \longrightarrow \text{H} + \gamma$	A97 / Y06
$\text{He} + \text{e}^- \longrightarrow \text{He}^+ + 2\text{e}^-$	A97 / Y06
$\text{He}^+ + \text{e}^- \longrightarrow \text{He} + \gamma$	A97 / Y06
$\text{He}^+ + \text{e}^- \longrightarrow \text{He}^{++} + 2\text{e}^-$	A97 / Y06
$\text{He}^{++} + \text{e}^- \longrightarrow \text{He}^+ + \gamma$	A97 / Y06
$\text{H} + \text{e}^- \longrightarrow \text{H}^- + \gamma$	A97 / Y06
$\text{H}^- + \text{H} \longrightarrow \text{H}_2 + \text{e}^-$	A97 / Y06
$\text{H} + \text{H}^+ \longrightarrow \text{H}_2^+ + \gamma$	A97 / Y06
$\text{H}_2^+ + \text{H} \longrightarrow \text{H}_2 + \text{H}^+$	A97 / Y06
$\text{H}_2 + \text{H} \longrightarrow 3\text{H}$	A97
$\text{H}_2 + \text{H}^+ \longrightarrow \text{H}_2^+ + \text{H}$	S04 / Y06
$\text{H}_2 + \text{e}^- \longrightarrow 2\text{H} + \text{e}^-$	ST99 / GB03 / Y06
$\text{H}^- + \text{e}^- \longrightarrow \text{H} + 2\text{e}^-$	A97 / Y06
$\text{H}^- + \text{H} \longrightarrow 2\text{H} + \text{e}^-$	A97 / Y06
$\text{H}^- + \text{H}^+ \longrightarrow 2\text{H}$	P71 / GP98 / Y06
$\text{H}^- + \text{H}^+ \longrightarrow \text{H}_2^+ + \text{e}^-$	SK87 / Y06
$\text{H}_2^+ + \text{e}^- \longrightarrow 2\text{H}$	GP98 / Y06
$\text{H}_2^+ + \text{H}^- \longrightarrow \text{H} + \text{H}_2$	A97 / Y06
$\text{D} + \text{H}_2 \longrightarrow \text{HD} + \text{H}$	WS02
$\text{D}^+ + \text{H}_2 \longrightarrow \text{HD} + \text{H}^+$	WS02
$\text{HD} + \text{H} \longrightarrow \text{D} + \text{H}_2$	SLP98
$\text{HD} + \text{H}^+ \longrightarrow \text{D}^+ + \text{H}_2$	SLP98
$\text{H}^+ + \text{D} \longrightarrow \text{H} + \text{D}^+$	S02
$\text{H} + \text{D}^+ \longrightarrow \text{H}^+ + \text{D}$	S02
$\text{He} + \text{H}^+ \longrightarrow \text{HeH}^+ + \gamma$	RD82, GP98
$\text{HeH}^+ + \text{H} \longrightarrow \text{He} + \text{H}_2^+$	KAH79, GP98
$\text{HeH}^+ + \gamma \longrightarrow \text{He} + \text{H}^+$	RD82, GP98

Notes:

P71=Peterson et al. (1971); KAH79=Karpas et al. (1979); RD82=Roberge and Dalgarno (1982); SK87=Shapiro and Kang (1987); A97=Abel et al. (1997); GP98=Galli and Palla (1998); SLP98=Stancil et al. (1998); ST99=Stibbe and Tennyson (1999); WS02=Wang and Stancil (2002); S02=Savin (2002); GB03=Glover and Brand (2003); S04=Savin et al. (2004); Y06=Yoshida et al. (2006a).

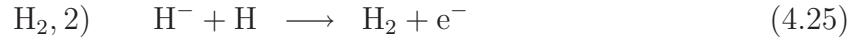
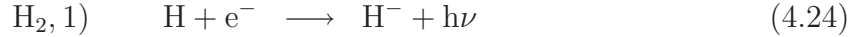
4.3.1 Molecules

In order to follow early structure formation in a detailed way, we implement molecular chemistry and cooling (Maio et al., 2007) in non-equilibrium regime.

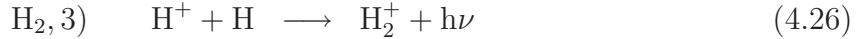
For molecule evolution, we base our implementation on the work by Yoshida et al. (2003b), which adopts the chemical rates from Abel et al. (1997). The network of reactions we implement allows us to follow the following species: e^- , H, H^+ , He, He^+ , He^{++} , H_2 , H_2^+ , H^- , D, D^+ , HD, HeH^+ (a complete list of the collisional and radiative reactions included is given in Table 4.1).

Standard atomic processes (ionization, recombination, Bremsstrahlung, Compton scattering) are implemented together with H_2 , HD and HeH^+ molecule evolution.

The reactions for molecular hydrogen, H_2 , considered are the H^- channel



and the H_2^+ channel



We neglect three-body processes, as the densities required to make them effective are extremely high with respect to the typical densities resolved in cosmological simulations.

The HD molecule primarily forms through reactions between primordial deuterium and hydrogen atoms or molecules: a complete model for its evolution involves at least 18 reactions (Nakamura and Umemura, 2002), but, as their solution becomes quite computationally expensive when implemented in cosmological simulations, we use only the set of most relevant reactions (Galli and Palla, 2002):



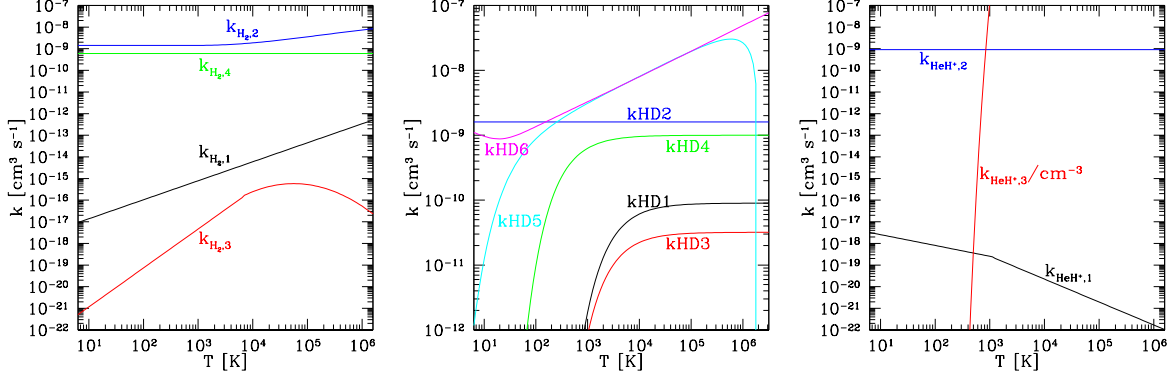
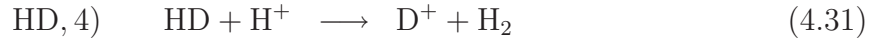
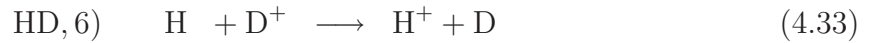


Figure 4.5: Temperature evolution of the reaction rates for molecular chemistry: left panel, H₂, central panel, HD, right panel HeH⁺. The subscripts refer to the labels of the corresponding reactions in the text.

which lead to HD formation;



for HD dissociation and H₂ formation; and



for charge exchange reactions.

From reactions (4.28 - 4.33), we see that HD abundance primarily depends on the amount of deuterium and on the H₂ fraction.

The molecule HeH⁺ is created by



and destroyed by



where γ indicates the photons.

For each species i , the variation in time of its number density n_i is

$$\frac{dn_i}{dt} = \sum_p \sum_q k_{pq,i} n_p n_q - n_i \sum_l k_{il} n_l, \quad (4.37)$$

where $k_{pq,i}$ in the first term on the right-hand side is the creation rate from species p and q , and k_{il} is the destruction rate from interactions of the species i with the species l . The rates are temperature dependent and are expressed in [$\text{cm}^3 \text{s}^{-1}$] for collisional events and [s^{-1}] for radiative interactions (see Appendix A.2.1, A.2.2 and A.2.3).

Plots are given in Figure 4.5, and the exact expressions and references in Appendix C.1.

From the figures, it is clear that H_2 formation is highly favored from reactions (4.25) and (4.27).

For deuterium chemistry, the most important reactions in the relevant range of temperatures are (4.32) and (4.33), and the HD creation rates of reactions (4.28) and (4.29) are always higher than the corresponding destruction rates of reactions (4.30) and (4.31), respectively.

The creation of HeH^+ molecule (4.34) instead is always disfavored with respect to its destruction in He and H_2^+ and in He and H^+ at $T \gtrsim 500 \text{ K}$. We expect therefore, that the interactions (4.35) and (4.36) will slightly enhance H_2 , because of (4.26) and (4.27).

Numerically, the set of differential equations (4.37) is evaluated via simple linearization, according to a backward difference formula: given the time step Δt , at each time t and for each species i , equation (4.37) can be re-written as

$$\frac{n_i^{t+\Delta t} - n_i^t}{\Delta t} = C_i^{t+\Delta t} - D_i^{t+\Delta t} n_i^{t+\Delta t} \quad (4.38)$$

where we have introduced the creation coefficient for the species i , in [$\text{cm}^{-3} \text{s}^{-1}$], as

$$C_i = \sum_p \sum_q k_{pq,i} n_p n_q \quad (4.39)$$

and the destruction coefficient, in [s^{-1}], as

$$D_i = \sum_l k_{il} n_l. \quad (4.40)$$

The number density, n_i^t , is then updated from equation (4.38):

$$n_i^{t+\Delta t} = \frac{C_i^{t+\Delta t} \Delta t + n_i^t}{1 + D_i^{t+\Delta t} \Delta t}. \quad (4.41)$$

We apply this treatment to all chemical species.

4.3.2 Metals

When the first objects have led star formation, metals are produced and ejected into the surrounding medium. Their presence is extremely important, as they dominate the radiative losses. Thence, we consider their cooling contribution for $T \leq 10^4$ K. At higher temperatures they are already tracked, via existing tables (Sutherland and Dopita, 1993). We explicitly follow oxygen, carbon, silicon and iron, because they are the most abundant heavy atoms released during stellar evolution and, therefore, they play the most important role in chemical enrichment and cooling. Indeed, supernovae type II (SNII) expel mostly oxygen and carbon, while supernovae type Ia (SNIa) silicon and iron (Thielemann et al., 2001; Park et al., 2003; Borkowski et al., 2004; Meynet et al., 2006b). We make the common assumption that carbon, silicon and iron are completely ionised, while oxygen is neutral. This is justified because, in a cosmological context, UV radiation below 13.6 eV (from various astrophysical sources, like quasars, stars, etc.) can escape absorption by neutral hydrogen and generate a UV background that can ionise atoms with first ionization potential lower than 13.6 eV (like carbon, silicon and iron), while oxygen remains predominantly neutral since its first ionization potential is 13.62 eV (Bromm and Loeb, 2003; Santoro and Shull, 2006).

As in the low-density regime of interest here thermodynamic equilibrium is never reached (see discussion of eq. 4.46), the Boltzmann distribution for the population of atomic levels can not be used. Thus, we will use the detailed balancing principle instead. For each level i of a given species, we impose that the number of transitions to that level (which *populate* it), per unit time and volume equals the number of transitions from the same level i to other levels (which *de-populate* it), per unit time and volume:

$$n_i \sum_j P_{ij} = \sum_j n_j P_{ji} \quad (i \neq j). \quad (4.42)$$

In formula (4.42), P_{ij} is the probability per unit time of the transition $i \rightarrow j$ and n_i and n_j are the number densities of atoms in the i -th and j -th (with $i \neq j$) level. The

left-hand side of the previous equation refers to de-populations of the i -th level, while the right-hand side refers to the transitions which can populate it.

The probability of a given transition can be easily computed once the Einstein coefficients and the collisional rates are known.

The further constraint which must be satisfied is the number particle conservation:

$$\sum_j n_j = n_{tot} \quad (4.43)$$

where n_{tot} is the total number density of the species considered and n_j the population of the generic level j .

In case of collisional events, the rate at which the transition $i \rightarrow j$ occurs is by definition (see also Appendix A):

$$n_i n_x \gamma_{ij} \equiv n_i n_x \langle u \sigma_{ij} \rangle = n_i n_x \int u \sigma_{ij} f(u) d^3u \quad (4.44)$$

where σ_{ij} is the cross section of the process, $f(u) d^3u$ is the velocity distribution function of the particles (typically a Maxwellian), γ_{ij} is the collisional rate, n_i the number density of the particles in the i -th level and n_x is the colliding particle number density. The integral is done over the whole velocity space.

The relation between γ_{ij} and γ_{ji} is:

$$g_i \gamma_{ij} = g_j \gamma_{ji} e^{-\beta \Delta E_{ji}}, \quad (4.45)$$

where g_i and g_j are the level multiplicities, $\beta = (k_B T)^{-1}$, ΔE_{ji} is the energy level separation and $i < j$.

In addition to collisionally induced transitions, spontaneous transitions can take place with an emission rate given by the Einstein A coefficient.

It is convenient to define the critical number density for the transition $i \rightarrow j$ as

$$n_{cr,ij} = \frac{A_{ij}}{\gamma_{ij}}. \quad (4.46)$$

This determines the minimum density above which thermal equilibrium can be assumed and low-density deviations from the Boltzmann distribution become irrelevant. At densities below $n_{cr,ij}$, we expect values of the excited level populations lower than in the thermodynamic limit, because of the reduced number of interactions⁵.

⁵The critical number density depends on the particular line transition considered; typical values for the fine structure transitions we are mostly interested in are of the order $\sim 10^5 \text{cm}^{-3}$.

For a two-level system, the low-density level populations arising from electron and hydrogen impact excitations can be found by solving the system of equations resulting from conditions (4.43) and (4.42):

$$\begin{cases} n_1 + n_2 = n_{tot} \\ n_1 n_H \gamma_{12}^H + n_1 n_e \gamma_{12}^e - n_2 n_H \gamma_{21}^H - n_2 n_e \gamma_{21}^e - n_2 A_{21} = 0 \end{cases} \quad (4.47)$$

where n_H and n_e are the hydrogen and electron number density, while γ_{12}^H and γ_{12}^e are the H-impact and e-impact excitation rate.

The solution of (4.47) is:

$$\frac{n_1}{n_{tot}} = \frac{\gamma_{21}^H + \gamma_{21}^e n_e/n_H + A_{21}/n_H}{\gamma_{12}^H + \gamma_{21}^H + (\gamma_{12}^e + \gamma_{21}^e) n_e/n_H + A_{21}/n_H} \quad (4.48)$$

$$\frac{n_2}{n_{tot}} = \frac{\gamma_{12}^H + \gamma_{12}^e n_e/n_H}{\gamma_{12}^H + \gamma_{21}^H + (\gamma_{12}^e + \gamma_{21}^e) n_e/n_H + A_{21}/n_H}. \quad (4.49)$$

The ratio between the two level populations

$$\frac{n_2}{n_1} = \frac{\gamma_{12}^H + \gamma_{12}^e n_e/n_H}{\gamma_{21}^H + \gamma_{21}^e n_e/n_H + A_{21}/n_H} \quad (4.50)$$

$$\stackrel{n_e \ll n_H}{\sim} \frac{\gamma_{12}^H}{\gamma_{21}^H + A_{21}/n_H} \quad (4.51)$$

will in general deviate from the Boltzmann statistic, because the spontaneous emission term dominates over the collisional term at low densities. In a neutral dense gas, instead, the level population saturates and simply reduces to a Boltzmann distribution, independently from the colliding particle number density.

In case of n -level systems, one must solve the $n \times n$ population matrix consisting of $n - 1$ independent balancing equations (4.42) and the constraint of particle conservation (4.43).

In the modeling, we approximate CII and SiIII as a two-level system, and OI and FeII as a five-level system (Santoro and Shull, 2006).

Further details on the atomic data and structures are reported in Appendix C.2.

4.3.3 Cooling

In addition to calculating the chemical evolution of the gas, we need to evaluate the cooling induced by different species. Therefore, atomic hydrogen and helium cooling from

collisional ionization, excitation and recombination (Hui and Gnedin, 1997), Compton cooling/heating and Bremsstrahlung (Black, 1981) are evaluated.

For the H_2 and H_2^+ cooling, the rates quoted in Galli and Palla (1998) and Hollenbach and McKee (1979) are adopted (see Appendix C.1 for the exact expression). We take the HD cooling function from Lipovka et al. (2005), who consider the HD ro-vibrational structure and perform calculations for $J \leq 8$ rotational levels and $v = 0, 1, 2, 3$ vibrational levels (see Appendix C.1 for the exact expression). Their results are somehow more accurate than other approximations (Flower, 2000; Galli and Palla, 2002) and valid for a wide range of number densities (up to 10^4 cm^{-3}) and temperatures ($10^2 \text{ K} - 2 \cdot 10^4 \text{ K}$).

In Figure 4.6 (left panel), we show cooling functions for H_2 , HD, H_2^+ molecules; for the latter case we distinguish between neutral hydrogen impact and electron impact cooling; we have assumed fractions $x_{\text{HD}} = 10^{-8}$, $x_{\text{H}_2} = 10^{-5}$, $x_{\text{H}_2^+} = 10^{-13}$, $x_{e^-} = 10^{-4}$ and a total hydrogen number density $n_{\text{H}} = 1 \text{ cm}^{-3}$. Due to its very low abundance, H_2^+ is less effective than neutral H_2 and HD, which remain the only relevant coolants over the plotted range of temperature.

The cooling for metal line transitions is computed as follows.

In case of two-level systems, we define

$$\Lambda \equiv n_2 A_{21} \Delta E_{21} \quad (4.52)$$

where n_2 is the atomic excited state number density, A_{21} is the probability per unit time of the transition $2 \rightarrow 1$ and ΔE_{21} is the energy separation of the levels. Combining (4.52) and (4.49) one can write the previous equation as a function only of the total number density of the species

$$\Lambda = \frac{\gamma_{12}^H + \gamma_{12}^e n_e/n_H}{\gamma_{12}^H + \gamma_{21}^H + (\gamma_{12}^e + \gamma_{21}^e) n_e/n_H + A_{21}/n_H} n_{\text{tot}} A_{21} \Delta E_{21}. \quad (4.53)$$

For $n_e \ll n_H$, the previous formula is consistent with the one quoted in Santoro and Shull (2006), who do not consider electron impact excitation effects. Using equations (4.50) and (4.46), Λ can also be written as a function of the fundamental level population

$$\Lambda = \frac{n_1 n_H \gamma_{12}^H + n_1 n_e \gamma_{12}^e}{n_H/n_{\text{cr},21}^H + n_e/n_{\text{cr},21}^e + 1} \Delta E_{21} \stackrel{n_e \ll n_H}{\sim} \frac{n_1 n_H \gamma_{12}^H}{n_H/n_{\text{cr},21}^H + 1} \Delta E_{21} \quad (4.54)$$

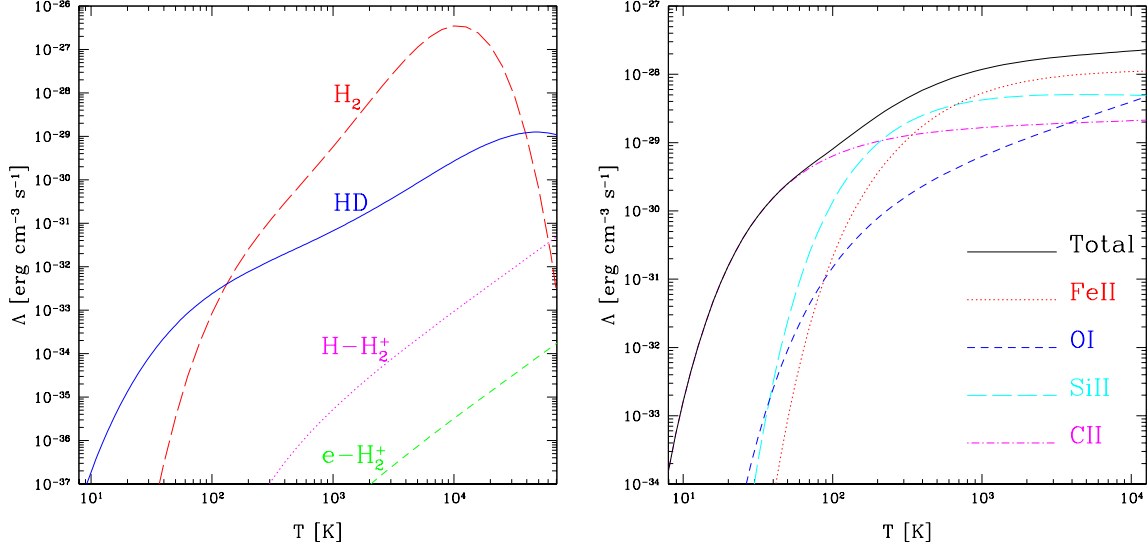


Figure 4.6: Left panel: cooling functions for a primordial gas with a hydrogen number density of 1 cm^{-3} and the following fractions for the different species: $x_{\text{HD}} = 10^{-8}$, $x_{\text{H}_2} = 10^{-5}$, $x_{\text{H}_2^+} = 10^{-13}$, $x_{e^-} = 10^{-4}$. The H_2 cooling function (long-dashed line) is plotted together with the HD (solid), H-impact H_2^+ (dotted line) and e-impact H_2^+ (short-dashed line) cooling functions. Right panel: cooling due to metals as a function of temperature. The computations are done for a gas with total number density of 1 cm^{-3} ; for each metal species we assume a number density of 10^{-6} cm^{-3} and we set the free electron over hydrogen fraction to a value of 10^{-4} .

where $n_{cr,21}^H$ and $n_{cr,21}^e$ are the critical densities for the transition $2 \rightarrow 1$ due to H- and e-impact excitations.

In particular, in the low-density limit ($n_{H,e} \ll n_{cr}$), the above equation becomes

$$\Lambda \simeq [n_1 n_H \gamma_{12}^H + n_1 n_e \gamma_{12}^e] \Delta E_{21} \quad (4.55)$$

$$\stackrel{n_e \ll n_H}{\simeq} n_1 n_H \gamma_{12}^H \Delta E_{21}. \quad (4.56)$$

In this regime, each excitation - see formulae (4.55) and (4.56) - is statistically followed by emission of radiation - see the general definition (4.52).

In the high-density limit, one finds the expected thermodynamic equilibrium cooling rate

$$\Lambda \simeq \frac{g_2}{g_1} e^{-\beta \Delta E_{21}} n_1 \frac{A_{21} \Delta E_{21}}{1 + n_e \gamma_{21}^e / n_H \gamma_{21}^H} + \frac{g_2}{g_1} e^{-\beta \Delta E_{21}} n_1 \frac{A_{21} \Delta E_{21}}{1 + n_H \gamma_{21}^H / n_e \gamma_{21}^e} \quad (4.57)$$

$$\stackrel{n_e \ll n_H}{\simeq} \frac{g_2}{g_1} e^{-\beta \Delta E_{21}} n_1 A_{21} \Delta E_{21}. \quad (4.58)$$

In the right-hand side, it is easy to recognize the Boltzmann distribution of populations for n_2 . It is interesting to note that the cooling function does not depend any more on the number density of the colliding particles, but only on the species abundance, in contrast with the low-density regime, where there is a linear dependence on both densities.

These arguments ensure that it is safe to use formula (4.53) to compute the gas cooling for two-level atoms.

For n -level systems, the cooling function is simply the sum of all the contributions from each transition

$$\Lambda \equiv \sum_{i \geq 1} \sum_{0 \leq j < i} n_i A_{ij} \Delta E_{ij}. \quad (4.59)$$

In general, once the number density of the cooling species is fixed, we expect the cooling function to grow linearly with the colliding particle number density and eventually to saturate, converging to the Boltzmann statistic, when the critical densities are reached. We notice (see the atomic data in Appendix C.2) that CII, SiII, FeII saturate when the colliding particle number density achieves values around $10^4 \text{ cm}^{-3} - 10^5 \text{ cm}^{-3}$, while for OI we will have a double phase of saturation: the first one at $\sim 10^5 \text{ cm}^{-3}$ involving the lower three states and the second one at $\sim 10^{11} \text{ cm}^{-3}$ involving the higher two states.

As an example, in Figure 4.6 (right panel), we show the cooling functions for a total number density 1 cm^{-3} and for each metal species 10^{-6} cm^{-3} ; the ratio between free electrons and hydrogen is chosen to be 10^{-4} . With these values, the presence of electrons can affect the results up to 10% with respect to the zero electron fraction case. We also notice that all the metals contribute with similar importance to the total cooling function and the main difference in the cooling properties of the gas will depend on their detailed chemical composition.

We also plot the cooling functions for all the temperature regime we are interested in: at temperatures higher than 10^4 K , we interpolate the Sutherland and Dopita tables (Sutherland and Dopita, 1993), at lower temperatures, we include metals and molecules as discussed previously. Figure 4.7 shows the cooling function for different individual metal number fractions with abundances in the range $10^{-6} - 10^{-3}$ and H_2 and HD fractions of 10^{-5} and 10^{-8} , respectively. These values for H_2 and HD are fairly typical for the IGM gas at the mean density (Galli and Palla, 1998). In the temperature range $10^4 \text{ K} - 10^5 \text{ K}$, the double peak due to hydrogen and helium collisional excitations is evident at low metallicity, while it is washed out by the contribution of different metal ionization processes as the metallicity increases. For example, complete collisional ionization of

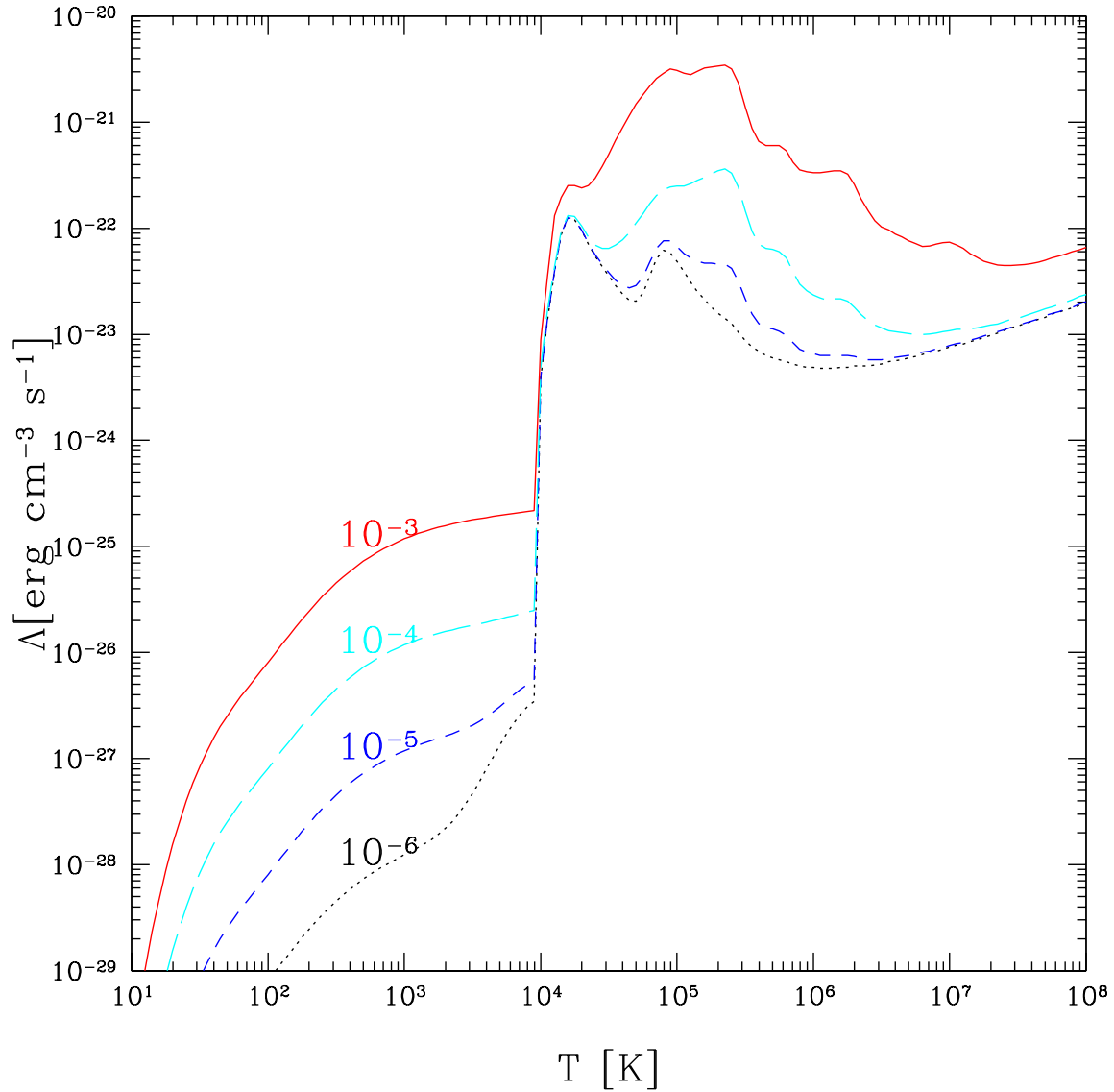


Figure 4.7: Total cooling due to hydrogen, helium, metals, H_2 and HD molecules as function of temperature, for gas having a hydrogen number density of 1 cm^{-3} . The fraction of H_2 and HD are fixed to 10^{-5} and 10^{-8} , respectively. The labels in the plot refer to different amount of metals, for individual metal number fractions of 10^{-3} (solid line), 10^{-4} (long-dashed line), 10^{-5} (short-dashed line) and 10^{-6} (dotted line).

carbon and oxygen produces the twin peak at 10^5 K, while complete ionization of iron is evident at about 10^7 K. At temperatures lower than 10^4 K and metal fractions lower than $\sim 10^{-6}$, the dominant cooling is given by molecules; instead, for larger metal fractions the effects of metals became dominant.

The general conclusion is that at very high redshift, when metals are not present, only H_2 and HD can be useful to cool the gas down to some 10^2 K, while after the first stars explode, ejecting heavy elements into the surrounding medium, metals quickly become the most efficient coolants.

4.4 Summary

In this chapter we have seen the main schemes of numerical codes in astrophysics and have shown our numerical implementation.

- Molecular chemistry is included according to an essential chemistry reaction network, in order to follow molecule formation and evolution (mainly H_2 , HD, HeH^+).
- We have performed computations of fine-structure transition metal cooling functions, which extend the standard cooling functions in the range $\sim 2.7 \text{ K} - 10^9 \text{ K}$.
- We have included such cooling in star formation recipes, in order to study the effects on structure formation.
- We have concluded that for very first objects, molecules are the leading cooling agents, while, as soon as the medium is polluted, metals give a more efficient contribution.

Chapter 5

Tests for star formation, molecule and metal chemistry

*Rex sedet in vertice - caveat ruinam!
nam sub axe legimus Hecubam reginam.*

CARMINA BURANA, FORTUNE PLANGO VULNERA

In the previous chapter, we have presented an implementation of time dependent calculations of the cooling properties of gas also in a “low-temperature” regime, using the contributions of several chemical species.

Hydrogen derived molecules are effective in cooling metal-free gas below a temperature of $\sim 10^4$ K, the typical temperature range of primordial objects. On the other hand, when the medium is polluted by material expelled from stars (via SN explosions, mass losses in AGB phase and winds), metals are expected to become the main coolants.

On the whole, we follow the evolution of e^- , H, H^+ , He, He^+ , He^{++} , H_2 , H_2^+ , H^- , D, D^+ , HD, HeH^+ , O, C^+ , Si^+ , Fe^+ ; so, the code is suitable to deal both with primordial and metal enriched gas.

In this chapter, we are going to test our implementation using different kind of simulations. In particular, we focus on the analysis of wind feedback (section 5.1), abundance redshift evolution (section 5.2), cosmic structure formation (section 5.3), and clusters (section 5.4).

5.1 Star formation and wind feedback

We check the effects of wind feedback running simulations of an isolated galaxy quiescently forming stars.

Therefore, we set-up a homogeneous gas distribution and put it in a dark matter potential halo. The dark matter distribution is set according to the density profile¹ (Navarro et al., 1997):

$$\frac{\rho(r)}{\rho_{crit}} = \frac{\delta_c}{(r/r_s)(1+r/r_s)^2} \quad (5.1)$$

where $\rho(r)$ is the density at radius r , ρ_{crit} is the critical density of the Universe, given by formula (1.60), r_s the scale radius of the particular system considered and δ_c is an adimensional parameter related to the abundance of matter in the halo.

A suitable way to fix the parameters is to define r_{200} . We will refer to this quantity as the distance from the center of the halo where the mass over-density is equal to 200 (see also chapter 2, in particular the non-linear evolution issue discussed in section 2.2.2): $\rho(r_{200}) \equiv 200 \rho_{crit}$. The halo mass included in $r \leq r_{200}$ is approximatively considered as the virialization mass, M_{vir} , because of (2.31).

In this way, from the definition of (spherical) virial mass, having the density profile (5.1),

$$M_{vir} \simeq M_{200} \equiv \frac{4\pi}{3}(200 \rho_{crit}) r_{200}^3 = 4\pi \int_0^{r_{200}} \rho(r) r^2 dr \quad (5.2)$$

$$= 4\pi \rho_{crit} \delta_c \int_0^{r_{200}} \frac{r^2 dr}{(r/r_s)(1+r/r_s)^2} \quad (5.3)$$

performing the integral calculation, one easily shows that

$$\delta_c = \frac{200}{3} \frac{c^3}{\ln(1+c) - c/(1+c)} \quad (5.4)$$

where we have defined the concentration parameter $c \equiv r_{200}/r_s$.

So, c (or equivalently δ_c) is the only free parameter, for any given mass distribution specified by M_{200} or r_{200} . Indeed, from c and M_{200} , one can compute r_{200} using definition (5.2), $r_s = r_{200}/c$ and fully determine $\rho(r)$ in relation (5.1).

In our tests, we use a concentration parameter $c = 20$ and we run simulations for $M_{vir} \simeq M_{200}$ equal to $(10^{12}, 10^{11.5}, 10^{11}, 10^{10}) h^{-1} M_\odot$, respectively. In each of them, the gas is sampled with 48461 SPH particles and the dark halo is set assuming a dark matter fraction of 0.9 (i.e. the baryon fraction is 0.1). The cooling included is the standard atomic cooling from hydrogen and helium (effective at $T \gtrsim 10^4$ K – see Figure 2.7), with no molecule contributions. We switch the wind feedback on and off (in total we perform

¹ Spatial or surface density of stellar populations can practically always be expressed by a generalized exponential law (Einasto, 1970, 1974).

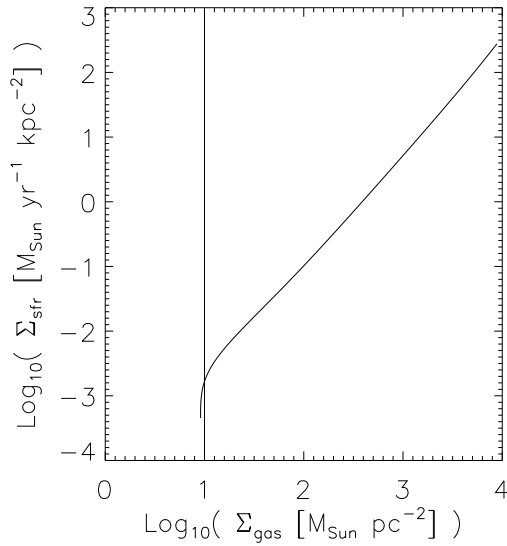


Figure 5.1: Star formation density as a function of the gas surface density (Schmidt law) for star forming quiescent galaxy, according to the multi-phase model. The vertical line refers approximately to the lower observational limit (see also Kennicutt, 1998, or Figure B.2, in appendix B).

8 simulations: 4 with wind feedback and 4 without) and compute the resulting star formation rate. The recipe adopted (see chapter 4) reproduces well the Schmidt law (see details in Appendix B). The star formation surface density obtained by the underlying multi-phase model is plotted in Figure 5.1 as a function of the gas surface density.

The calculations are stopped after 3 Gyr simulation time.

In Figure 5.2, we show a two-dimensional (left panel) and a three-dimensional (right panel) projection of the particle distribution for the $M_{vir} = 10^{12} h^{-1} M_{\odot}$ case. As expected, due to the power-law decrement of the density profile, the most of the particles clump in the center of the dark matter halo within some tens of parsecs.

This is very well seen in Figure 5.3, where we plot some number count statistics: in the left panel there is the number count as a function of the distance to the center, in the right panel, their cumulative distribution (normalized to 1). The sharp peak of the number counts covers a dimension of ~ 10 kpc, in which about one third of the particles is found. In correspondence, there is a steep increase of the cumulative distribution function, which passes from ~ 0 to ~ 1 in the close neighbourhood of the center, at distances $\lesssim 10^2$ kpc.

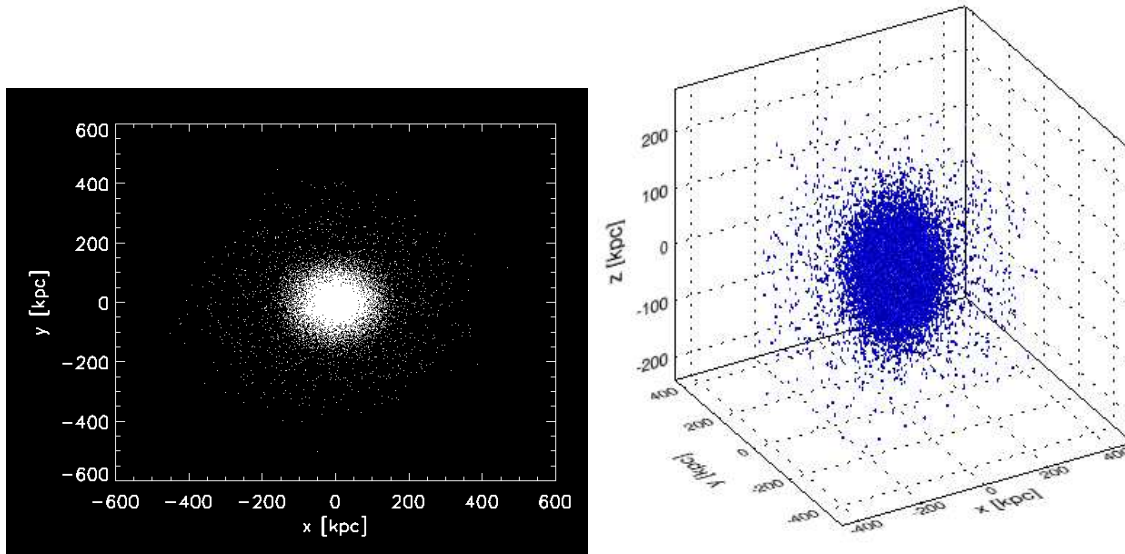


Figure 5.2: Two-dimensional (left panel) and a three-dimensional (right panel) projection of the particle distribution for the simulation discussed in section 5.1.

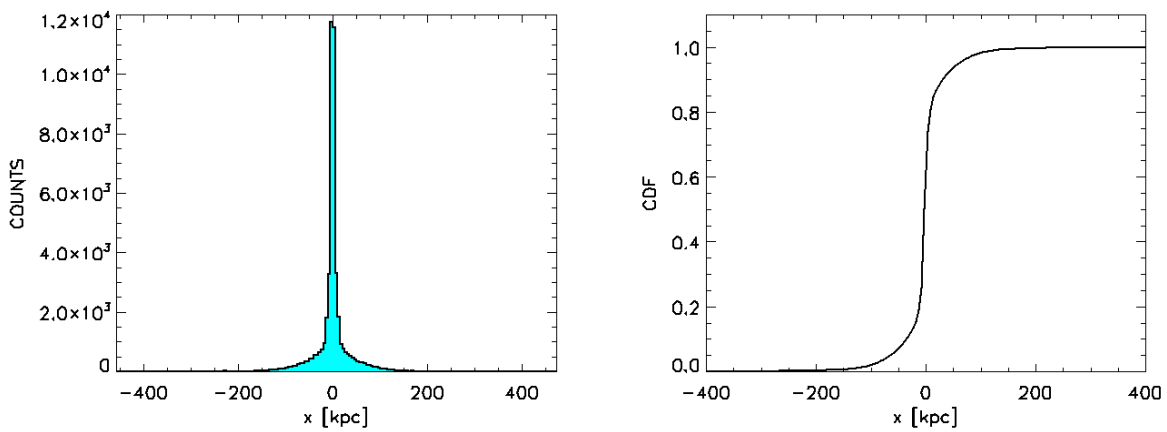


Figure 5.3: Left panel: number count as function from the distance to the center. Right panel: corresponding cumulative distribution function. The data correspond to the simulation discussed in section 5.1.

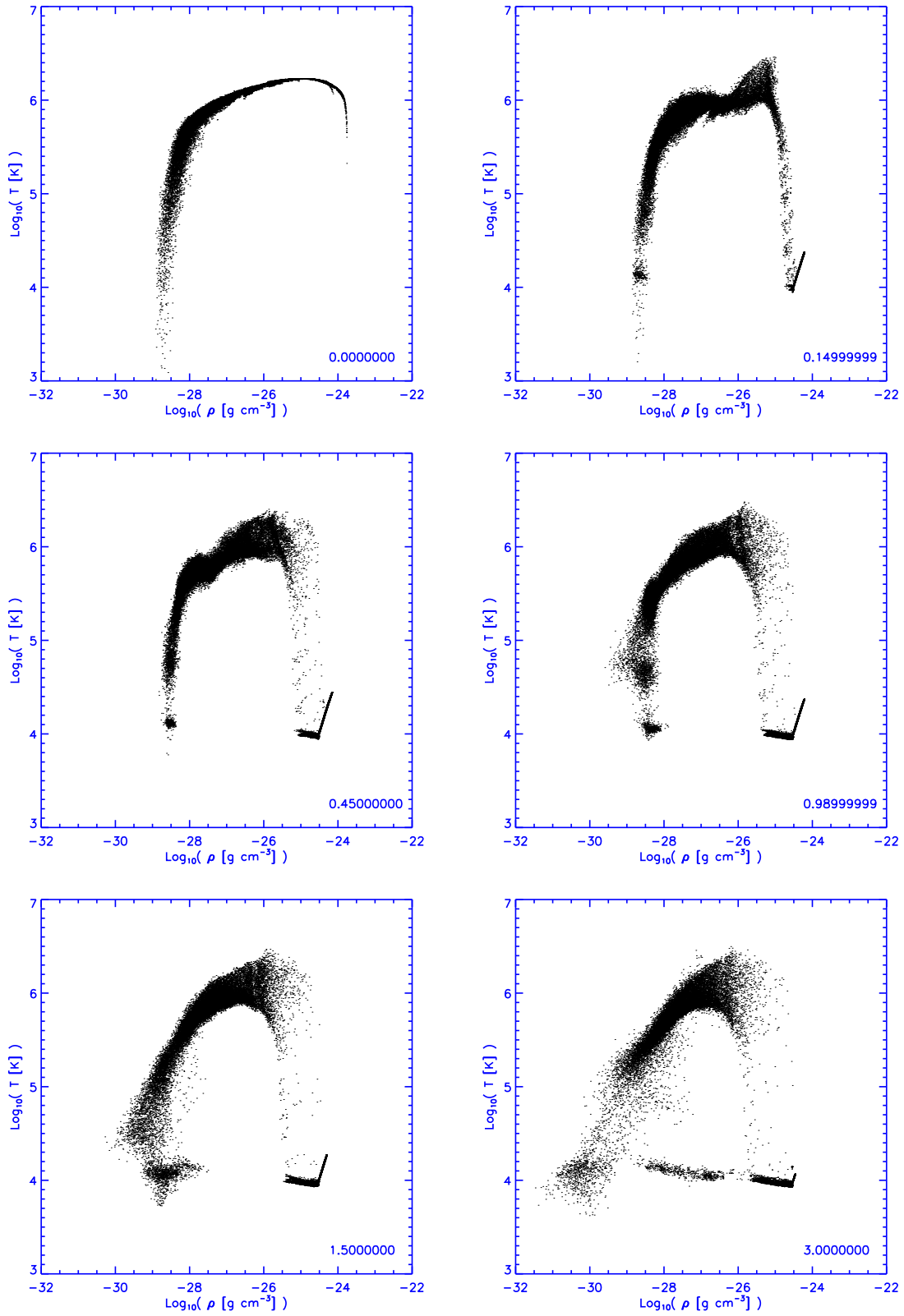


Figure 5.4: Phase diagrams at different times for the $M_{vir} = 10^{12} h^{-1} M_{\odot}$ case. The data correspond to density, ρ , and temperature, T , at the beginning of the run (top-left) and after about 0.15 Gyr (top-right), 0.45 Gyr (center-left), 1 Gyr (center-right), 1.5 Gyr (bottom-left), 3 Gyr (bottom-right).

In order to understand the dynamics of the system, we plot phase diagrams (density, ρ , versus temperature, T) at different times, in Figure 5.4.

We limit our discussion to the $M_{vir} = 10^{12} h^{-1} M_{\odot}$ case, as the global picture is similar also for the other cases.

We see that at the beginning, the gas distribution – led by the dark matter profile – is quite simple, with cold particles in the outer regions and hot, shock-heated particles in the central regions. Then, after $\sim 10^8$ yr, cooling is able to bring gas temperature down to $\sim 10^4$ K. The lack of any further coolant prevents to reach lower values. At the same time, the densest particles start undergoing star formation processes, as evident from the increasing straight edge located at $T \sim 10^4$ K and $\rho \sim (10^{-23} - 10^{-24}) \text{ g cm}^{-3}$. Star formation is the main event taking place for the first \sim Gyr of life in the inner part of the system. In the external regions the physical properties are left basically unaffected. At later times, when the gas reservoir diminishes, star formation is not effective any more, as seen from the lack of the edge in the last panel (bottom-left). Never the less, we notice that meanwhile also cold, low-density particles have had enough time to cool slowly and therefore a sort of minimal cooling branch is formed in the last ~ 1.5 Gyr at $T \sim 10^4$ K, over the whole range of densities.

To conclude and to stress the effect of wind feedback, we show the star formation rates obtained from the different simulations.

The obvious behaviour which one might immediately notice is the reduced star formation rate when winds are present. Indeed, the inclusion of winds determines a removal of particles from the star forming regions, because of which the amount of cooling gas which goes into star formation regime is reduced.

The peak of star formation rate is strongly dependent on the mass of the system, as smaller objects can gravitationally retain minor quantities of gas. However, in almost all the situations, the peak is attained within 1 Gyr. In the limiting case of $M_{vir} = 10^{10} h^{-1} M_{\odot}$, star formation is almost completely suppressed and only after ~ 2 Gyr the gas manages to cool and undergo little star formation. This happens because, given the characteristics of the system, gas does not condense rapidly and remains too rare to promptly cool down. In general, we notice a sort of self-regulated regime in which the fundamental processes are cooling and heating: dense gas cools down and forms stars, after typical stellar evolution

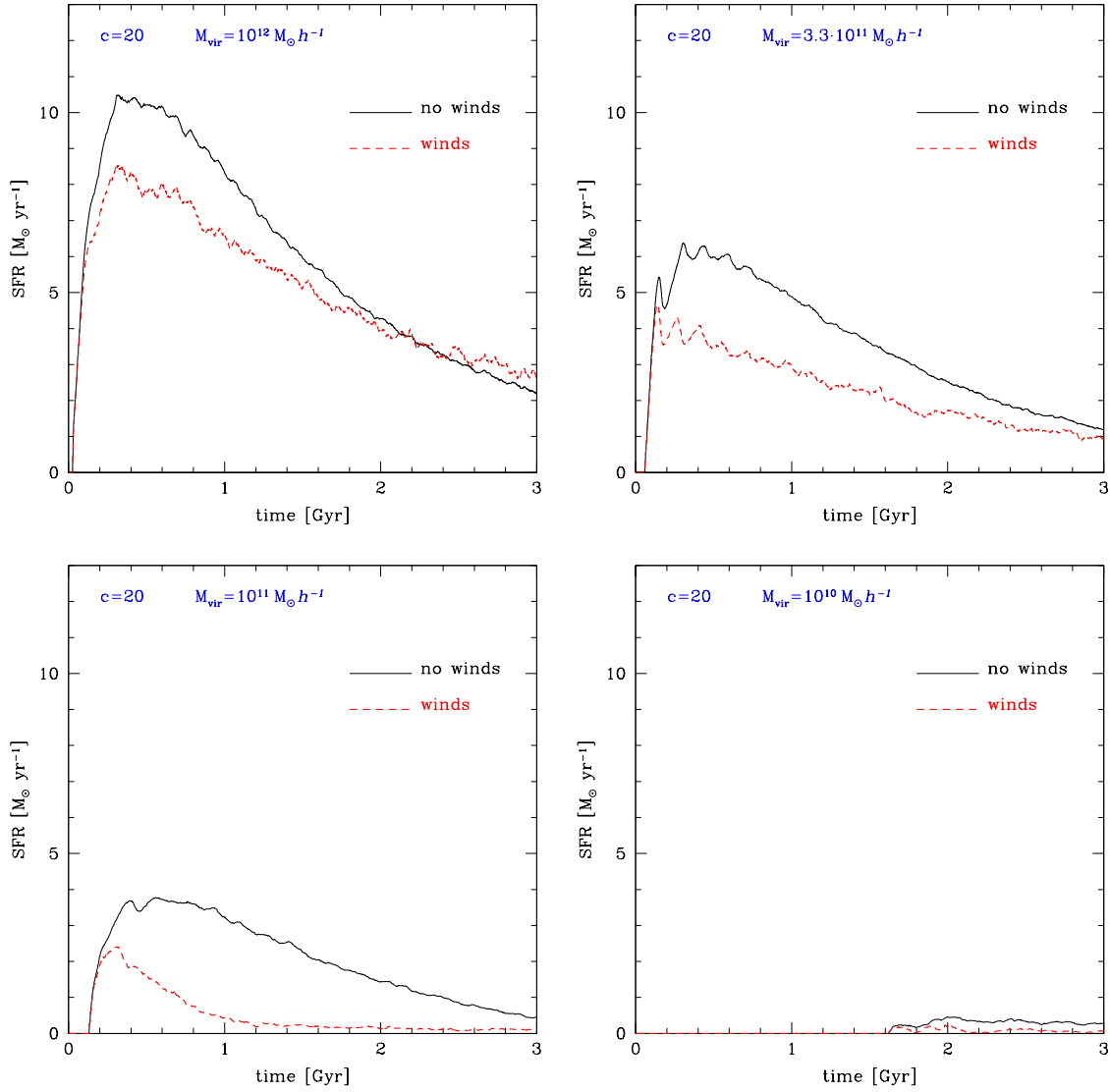


Figure 5.5: Star formation rate as a function of the time for different runs. The plots correspond the cases $M_{\text{vir}} = 10^{12}$ (top-left), $10^{11.5}$ (top-right), 10^{11} (bottom-left), $10^{10} h^{-1} M_{\odot}$ (bottom-right), respectively. Solid lines refer to star formation rates computed without wind prescriptions, dashed lines to the ones with stellar winds, as indicated by the legend.

time-scales the surrounding medium is heated by supernova explosions and cooling is inhibited.

The main role of winds is to bring hot gas particles away from the star formation sites towards the thin, colder neighbouring regions. In this way, one gets a mixture of hot and cold gas (“multi-phase” gas), in which the two components coexist together at the same times.

Moreover, the presence of winds will be highly relevant for metal pollution. Indeed, without particle spreading it would not be possible to locate metals outside the dense environments in which they are originated.

5.2 Redshift evolution of primordial chemical species

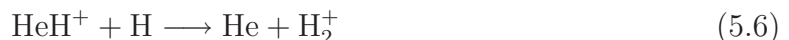
We investigate the behaviour of a plasma of primordial chemical composition (i.e. with no metals) looking at the redshift evolution of the single abundances. Our goal is to reproduce the results from Galli and Palla (1998), who calculate the redshift evolution of a metal-free gas at the mean density by following a detailed chemical network. For this reason, here, we perform our non-equilibrium computations on *isolated* particles, including the following chemical species: e^- , H, H^+ , He, He^+ , He^{++} , H_2 , H_2^+ , H^- , D, D^+ , HD, HeH^+ and assuming a flat cosmology with no dark energy content (matter density parameter $\Omega_{0m} = 1$), baryon density parameter $\Omega_{0b} = 0.037$, $h = 0.67$ and initial gas temperature of 1000 K.

Our evolution of the number fractions for the different species is plotted in the left panel of Figure 5.6; the electron abundance is given from charge conservation of neutral plasma and is normally very close to the H^+ value, this being the dominant ion. These results are in very good agreement with those of Galli and Palla (1998), plotted on the right panel, also considering the fact that we have used different rates.

In our set of reactions, due to the low initial gas temperature, the collisions are inefficient to ionise helium. The inclusion of HeH^+ creation



contributes to rise H_2^+ abundance mainly via reaction



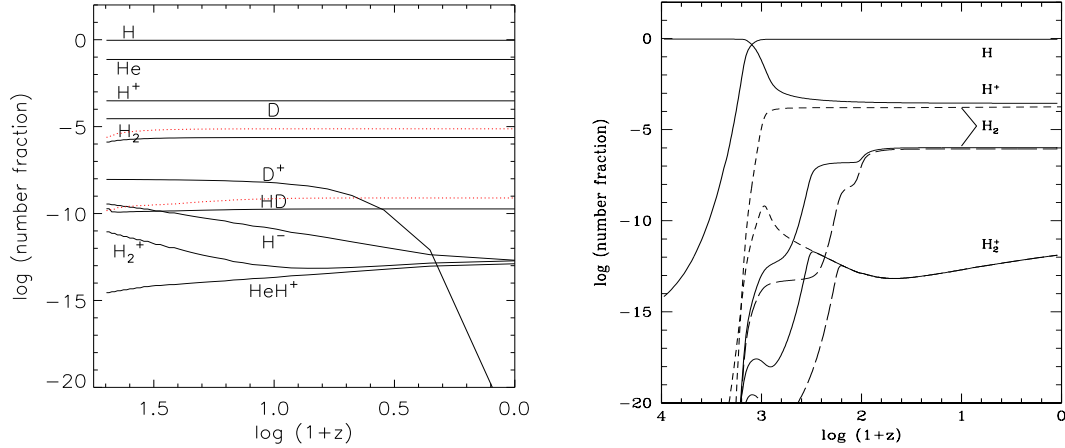


Figure 5.6: Abundances as a function of redshift for our implementation (left side) and Galli and Palla (1998)'s implementation. In both panels, the solid lines refer to the abundance evolution in a flat cold dark matter universe with $h = 0.67$, $\Omega_{0m} = 1$, $\Omega_{0b} = 0.037$. In the left panel, the dotted lines refers to H_2 and HD evolution in a Λ CDM model with $h = 0.73$, $\Omega_{0m} = 0.237$, $\Omega_{0\Lambda} = 0.763$, $\Omega_{0b} = 0.041$. In the right panel, the dashed lines correspond to a H_2^+ photodissociation rate from $v = 0$ (short-dashed line) and from $v = 9$ (long-dashed line) vibrational levels, respectively.

and weakly decrease the H^- number fraction via



where γ indicates the photons.

Because of the very low HeH^+ abundance reached, there is no substantial He atom abundance evolution. A *caveat* to take into account is the lack of reactions between D^+ and free electrons which would destroy the deuterium ions more efficiently, but without altering significantly the global amount of HD formed. We notice also the exponential decay of D^+ due to the rate coefficient of equation (4.32) and the freezing out of H^+ , H_2 , D and HD number fractions.

As a comparison, we also plot (dotted lines) the H_2 and HD abundance evolution in a flat Λ CDM model having $h = 0.73$, $\Omega_{0m} = 0.237$, $\Omega_{0\Lambda} = 0.763$, $\Omega_{0b} = 0.041$ (Spergel et al., 2007). The slight increase observed is due to the fact that in the cold dark matter cosmology the baryon fraction is about 4%, making the interactions among different species rarer than in the Λ CDM model, for which the baryon fraction is about 17%. In addition, the cosmological constant is dominant only at redshift below one. The evolution of the other species is similar in both cosmologies.

The evolution of H_2^+ and H_2 depends crucially on the adopted photodissociation rate, because this affects the H_2^+ channel via reaction (4.26) and its reverse process. This is clearly shown in the right panel, where the fractional abundances of H_2^+ and H_2 are showed with photodissociation of H_2^+ from $v = 0$ (short-dashed line) and from $v = 9$ (long-dashed line), vibrational levels. An enhancement of a factor ~ 200 of the final H_2 abundance in the former case is found. The asymptotic abundance of H_2^+ is instead left unchanged.

5.3 Cosmic structure formation from homogeneous initial conditions

To test the behaviour of the code in simulations of structure formation and evolution and the impact of HD, we run a cosmological simulation within the Λ CDM concordance model². We sample the cosmological field (in a periodic box of 1 Mpc comoving side length) with 324^3 dark matter particles and the same number of gas particles, having a mass of about $1040 M_\odot$ and $160 M_\odot$, respectively, at redshift $z = 100$. The comoving Plummer-equivalent gravitational softening length is fixed to 0.143 kpc. This allows us to resolve haloes with mass of about $10^5 M_\odot$.

The results are compared with those of Maio et al. (2006), whose Λ CDM simulation has the same features, but the chemical set does not follow the evolution of D, D^+ and HD and does not include H_2^+ cooling (see also Figure 4.6 and discussion).

A simple visualization of the simulations is given in the temperature maps of figure 5.7, from which one can easily infer the cosmic evolution of structure formation.

The change in chemical composition does not alter the underlying dark matter “web”, so the number densities (see Figure 5.8) are basically unaffected. From a theoretical point of view, different relations are available to predict their redshift evolution, once the cosmological model is fixed (see section 2.3). However, the theoretical mass functions have not yet been extensively tested in the regime of very low masses and very high redshifts which we are mainly interested in, where their predictions differ by orders of magnitude. This is due to the difficulty of combining sufficient resolution in space and mass with regions large enough to be considered a fair sample of our Universe. Moreover, the existing studies yield contradictory results.

² We remind that such cosmology is defined by the following set of parameters: $h = 0.7$, $\Omega_{\text{om}} = 0.3$, $\Omega_{\text{ob}} = 0.04$, $\Omega_{0\Lambda} = 0.7$; the power spectrum is normalized assuming a mass variance in a $8 \text{ Mpc}/h$ radius sphere $\sigma_8 = 0.9$ and the spectral index is equal to 1.

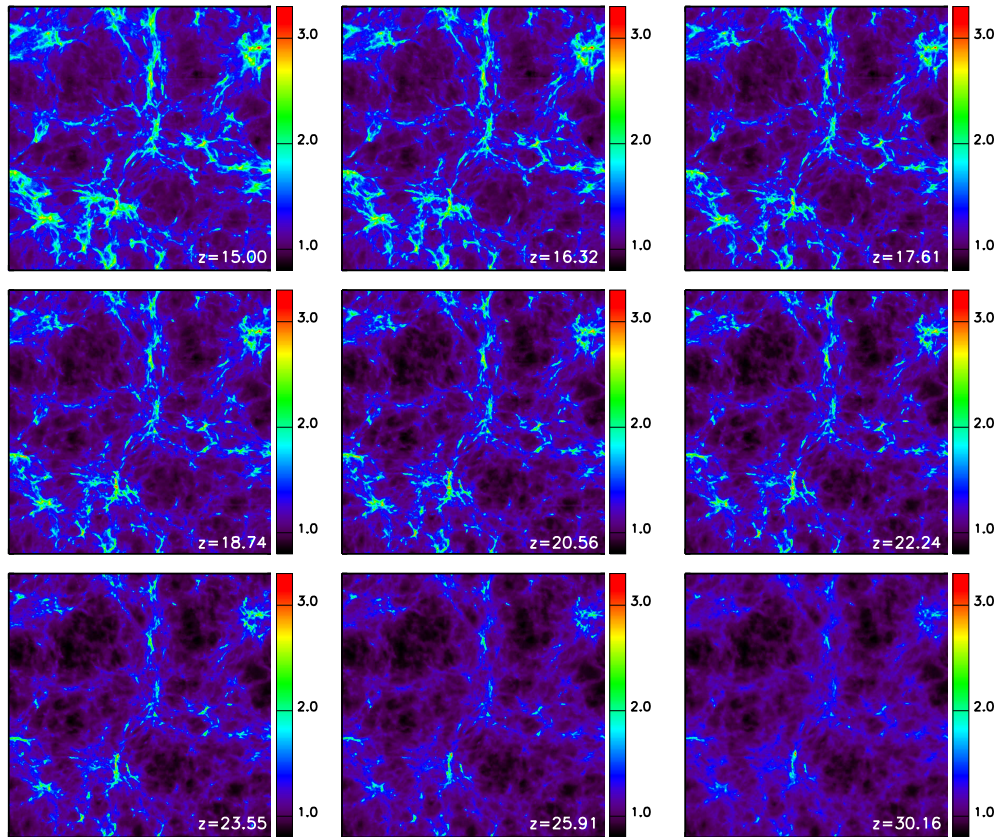


Figure 5.7: Temperature maps at different redshifts. The color scale refers to the decimal logarithm of the temperature in Kelvin.

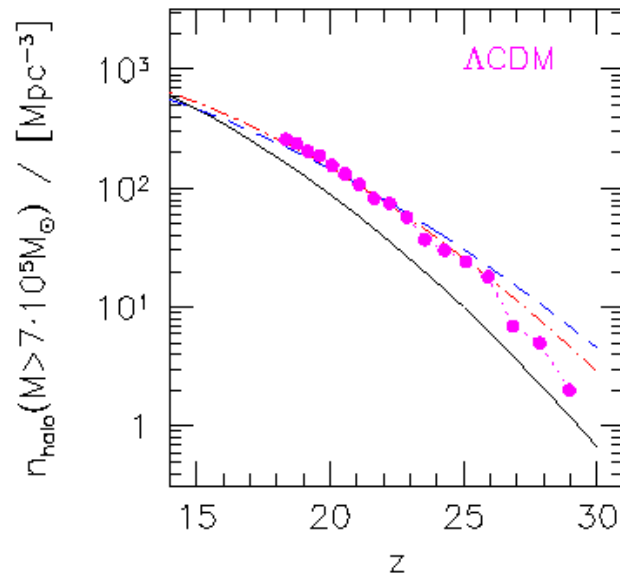


Figure 5.8: Number of haloes found in the simulation described in section 5.3 with mass exceeding $7 \cdot 10^5 M_{\odot}$ per unit comoving volume as function of redshift (filled circles and dotted lines), in the standard ΛCDM cosmology. Theoretical predictions based on the Press & Schechter (PS74, solid line), Sheth & Tormen (ST99, dashed line) and the Warren et al. (W06, dot-dashed line) relations are shown as well. See also (Maio et al., 2006).

We identify dark matter haloes in our simulations by running a friends-of-friends algorithm on the dark matter particles only and setting the linking length to 20% of the mean inter-particle separation. The resulting mass of each halo is then corrected by the factor $(1040 + 160)/1040 \approx 1.15$ to account for the (average) additional contribution by the gas particles. Figure 5.8 displays the redshift evolution of the number of haloes with masses exceeding $7 \times 10^5 M_\odot$ for our simulations (Maio et al., 2006, 2007). The figure compares the results with the predictions of the Press & Schechter (PS74, hereafter), the Sheth & Tormen (ST99, hereafter) and the Warren et al. (W06, hereafter) models, indicated by solid, dashed and dot-dashed lines, respectively. Note that we do not consider the relation found by Jenkins et al. (2001), because it cannot be extrapolated to the mass and redshift ranges considered here.

The results indicate that the W06 formula agrees better with the simulations than the ST99 and PS74 formulae. Some small deviations are seen at very high redshifts where, however, counts are low and the statistical uncertainty is high. The ST99 mass function tends to slightly overestimate the simulation results, again mainly at high redshift, where the discrepancies with W06 are more evident. On the contrary, the PS74 mass function always underestimates the halo abundances, with differences up to a factor ~ 3 . Thus, our results agree with the previous analyses by Reed et al. (2003), Springel et al. (2005) and Heitmann et al. (2006). However, this conclusion is in conflict with other former studies (Jang-Condell and Hernquist, 2001; Yoshida et al., 003b,c).

To quantify the differences between the two runs with different chemistry and the efficiency of the HD cooling we focus on the gas and calculate the clumping factor, C , in the simulation box, as follows

$$C = \frac{\sum_i m_i \rho_i \sum_j m_j \rho_j^{-1}}{(\sum_k m_k)^2} \quad (5.9)$$

where for each SPH particle, i , we indicate with m_i its mass and with ρ_i its mass density; the indices i , j and k run over all the gas particles. We calculate C using only particles with density below a given overdensity³, δ_M , and we make δ_M vary in the range [100, 500].

The results are plotted in Figure 5.9 for both simulations. We see that the inclusion of HD makes the clumping factor increase at all redshifts, quite independently from the

³ This because we want to compute C for the IGM densities only, excluding the collapsing objects.

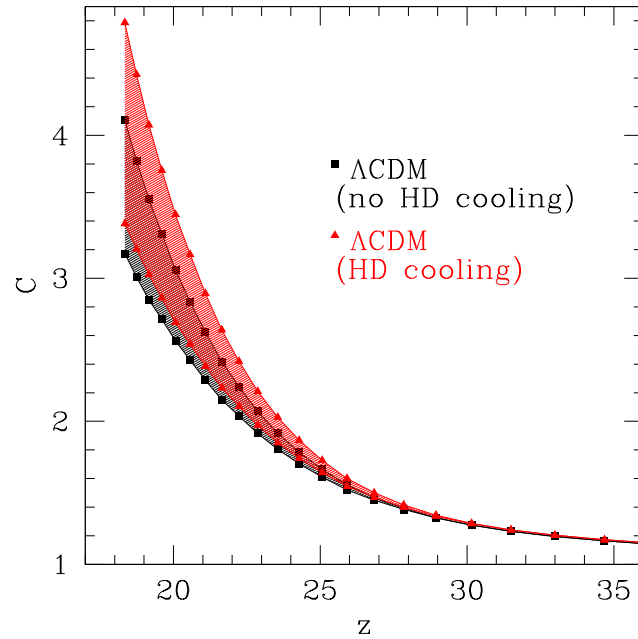


Figure 5.9: Gas clumping factor as a function of redshift for two Λ CDM models with different chemistry set. The squares refer to the clumping factor computed with standard atomic line cooling and H_2 cooling, while the triangles refer to a case which includes also HD cooling. The shaded regions correspond to the variation of the maximum overdensity between 100 (lower line in both cases) and 500 (upper line in both cases).

density threshold. This means that the gas is, on average, denser and more clumped, with an increment of about 10% at $z \sim 22$ and about 20% at $z \sim 17$.

5.4 Formation and evolution of a cluster

So far, we have considered primordial gas with no metal pollution. Now, we are going to couple our cooling function with a model for chemical enrichment and test this implementation within a simulation that follows the formation of a cluster. In addition to testing the validity of our implementation, it is of interest to check whether there are regions inside the simulations where the polluted medium is cooling below 10^4 K due to its metal content.

The “zoomed initial condition technique” (Tormen et al., 1997) is used to extract from a dark matter-only simulation with box size of 479 Mpc/h, within a standard Λ CDM cosmology, a smaller region and to re-simulate it at higher resolution introducing also gas particles. The cluster evolution is simulated with about $2 \cdot 10^5$ particles. The comoving Plummer-equivalent gravitational softening length is 5 kpc/h. At redshift zero,

the selected cluster has a virial mass of about $10^{14}M_{\odot}/h$, a virial radius of about $1\text{Mpc}/h$ and a virial temperature of $2 \cdot 10^7$ K (Dolag et al., 2004).

We start the simulation with no metallicity content. Then, the metal abundances are consistently derived following the star formation history of the system, according to a Salpeter IMF and adopting appropriate stellar yields (see details in section 4.2.3). Once the medium gets polluted with metals, their contribution is added (see Figure 4.7).

We will discuss the effect of metal fine-structure cooling (only) in the next section 5.4.1 and we will add also molecules in section 5.4.2. In section 5.4.3 we will focus on the cluster star formation and metal pollution history.

5.4.1 Metal fine-structure cooling

As first step, we include in our simulation metal fine-structure cooling only and do not follow molecule evolution. This means that the only coolant available are H, He and metals when produced from star formation episodes.

A projection of the particle distribution at $z = 0$ of the cluster is presented in Figure 5.10. Dark matter particles are black; hot ($T \geq 10^4$ K) gas particles are red; cold ($T < 10^4$ K) and diffuse gas particles are blue; hot ($T \geq 10^4$ K) star particles are yellow; cold ($T < 10^4$ K) star particles are cyan.

The different particles types arise simply from the star formation sub-grid model, according to which particles denser than $n_{\text{H}} = 0.1 \text{ cm}^{-3}$ produce stars (see section 4.2.1). From the plot one notices the overlap between gas and dark matter structures and finds the sites of star formation in the deep, dense potential wells where the gas can efficiently cool. Dark matter filaments are populated by hot gas which is shock-heated (with temperature reaching up to $\sim 10^7 \text{ K} - 10^8 \text{ K}$), but has not yet cooled down (at such temperatures the main cooling mechanism is the emission of Bremsstrahlung radiation). The diffuse gas instead remains cold.

The left panel of Figure 5.11 shows the cooling diagram of our simulation at redshift $z = 0$; each SPH particle is represented by a point. In the plot, different areas can be identified. The one at high temperatures (bottom right) represents the hot intra-cluster

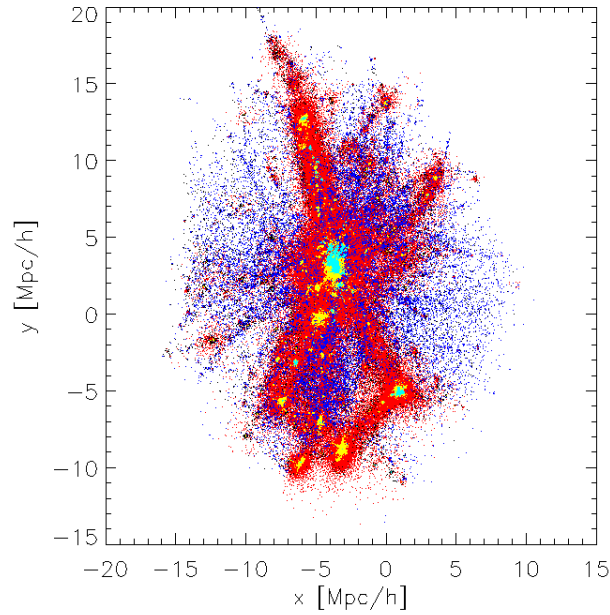


Figure 5.10: Projection of the particle distribution on the xy plane: dark matter particles are black; hot ($T \geq 10^4$ K) gas particles are red; cold ($T < 10^4$ K) and diffuse gas particles are blue; hot ($T \geq 10^4$ K) star particles are yellow; cold ($T < 10^4$ K) star particles are cyan.

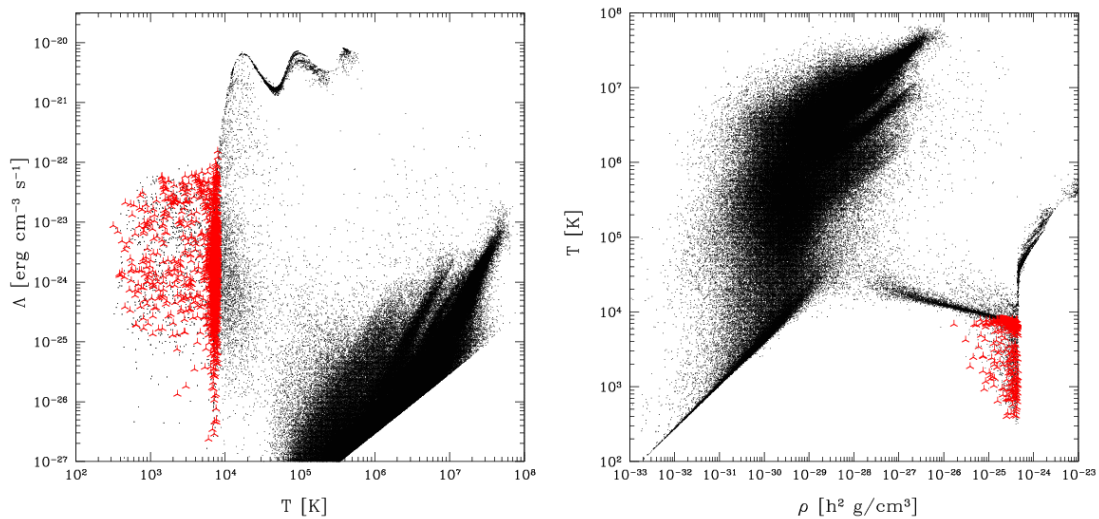


Figure 5.11: Left panel: distribution of particles of the cluster simulation described in section 5.4.1 in the $T - \Lambda$ space. Right panel: Distribution of particles in the phase diagram. The three-pointed star symbols correspond to particles which are located within twice the virial radius of the cluster and have a temperature lower than 8000 K. We remind that the critical density of the Universe at the present time is $\rho_{0,cr} \simeq 1.9 \cdot 10^{-29} h^2 \text{ g cm}^{-3}$.

medium (ICM). When the ICM starts to get denser, cooling gets more efficient: the corresponding gas particles are represented by the points belonging to the upper branch of the cooling function and they are brought to lower and lower temperatures. Feedback from star formation partially pushes some of them away from the cooling curve to slightly higher temperatures. Below 10^4 K, only particles which are metal enriched can further cool down to about 300 K, while gas particles with primordial composition are stacked at $\sim 10^4$ K. The three-pointed stars refer to particles within twice the virial radius and with a temperature below 8000 K, indicating that this region of the $T - \Lambda$ space is also populated by gas associated with the galaxy cluster.

The sharp cut-off in the bottom-right is relative to the hot and thin ICM whose cooling efficiency is limited by the CMB Compton heating (see Figure 2.7), proportional to $(T - T_{CMB})$. The spread is due to the different particle number densities.

The corresponding phase diagram is shown in the right panel of Figure 5.11. The hot and thin intra-cluster medium populates the central-left area of the plot, while the dense and cool regions occupy the lower-right part. Particles heated by feedback are represented by points in the central-right side ($\rho \gtrsim 10^{-24} h^2 \text{g cm}^{-3}$, $T \sim 10^5$ K). The main effect of our metal cooling implementation is to lower the temperature of the dense medium, generating the sharp triangular area visible in the ρ - T space, at $T < 10^4$ K and $\rho > 10^{-26} \text{g cm}^{-3}$. The points at very low densities are associated with diffuse metal free gas; this suggests that the spread in the cooling diagram of Figure 5.11 at temperature lower than 10^4 K is mainly due to different fractional metal enrichment of the particles, rather than to their different densities.

The standard case, without metal-fine structure transition contributions would lead to cooling and phase diagrams limited to $T \gtrsim 10^4$ K and lacking of the areas covered by three-pointed star symbols.

Global properties of the ICM and star formation are not significantly changed compared to the reference run without the metal line cooling from fine structure transitions. This happens because the simulation was merely meant to be a test case of the implementation of metal line cooling below 10^4 K under realistic conditions, but the haloes resolved are large enough to cool and form stars without the aid of such cooling. In order to investigate in more detail the effects of the additional cooling by molecules and metals at

low temperatures on the ICM and the star formation, higher resolution simulations are needed. However, this opens interesting grounds for further investigations on the interplay between formation of small objects, with virial temperatures in the range of interest for our extended cooling function, and metal pollution from first stars.

5.4.2 Adding molecules

The next step is to run the same cluster with the whole chemistry and metal pollution schemes, in order to take into account also primordial molecular cooling.

Derived maps of temperature, density, “entropy”⁴ $k_B T / \rho^{\gamma-1}$ ($\gamma \simeq 5/3$) – see also Appendix D – Jeans mass, molecular fraction and metallicity are shown in Figure 5.12 and a zoom of the central region in Figure 5.13.

The presence of a central, hot, star forming region with a high density, cool core (well visible in the “entropy” and Jeans mass maps) is evident. The presence of star formation events makes the temperature raise and dissociate molecules. Therefore, the molecular fraction steeply decreases in correspondence of the central hot region. Thanks to winds, metal pollution shows up, as we find enriched areas also in places remote from the cluster center.

The maximum average temperature (upper-left panel) is some tens of million Kelvin and is reached in correspondence of the highest densities in the simulations (the central spot and few neighbouring regions). The presence of the central core is not visible, as it is surrounded by very hot gas. On the density map (upper-right panel) instead, it is easier to recognize the substructures of the cluster.

The central row displays the two main physical quantities derived from temperature and density: “entropy” (central-left) and Jeans mass (central-right). The entropy is particularly useful to better define the thermodynamic structure of the system. Indeed, because of its definition, $\sim T / \rho^{\gamma-1}$ ($\gamma \simeq 5/3$), it allows us to highlight the presence of the cold regions surrounded by hot gas: that is clearly seen in the drop at the very center of the main hot spot, for example. The average Jeans mass, M_J , reveals some further details on the dynamical state: local hot gas makes M_J increase up to $\sim 10^{15} M_\odot - 10^{16} M_\odot$ and

⁴ The quantity which we call entropy, $k_B T / \rho^{\gamma-1}$, is not exactly the entropy S of a particle of perfect gas, according to the Sackur-Tetrode formula, but can be related to it, as $S \sim k_B \ln(C P / \rho^\gamma)$, with C constant, P pressure, ρ density, γ adiabatic index. See also Appendix D.

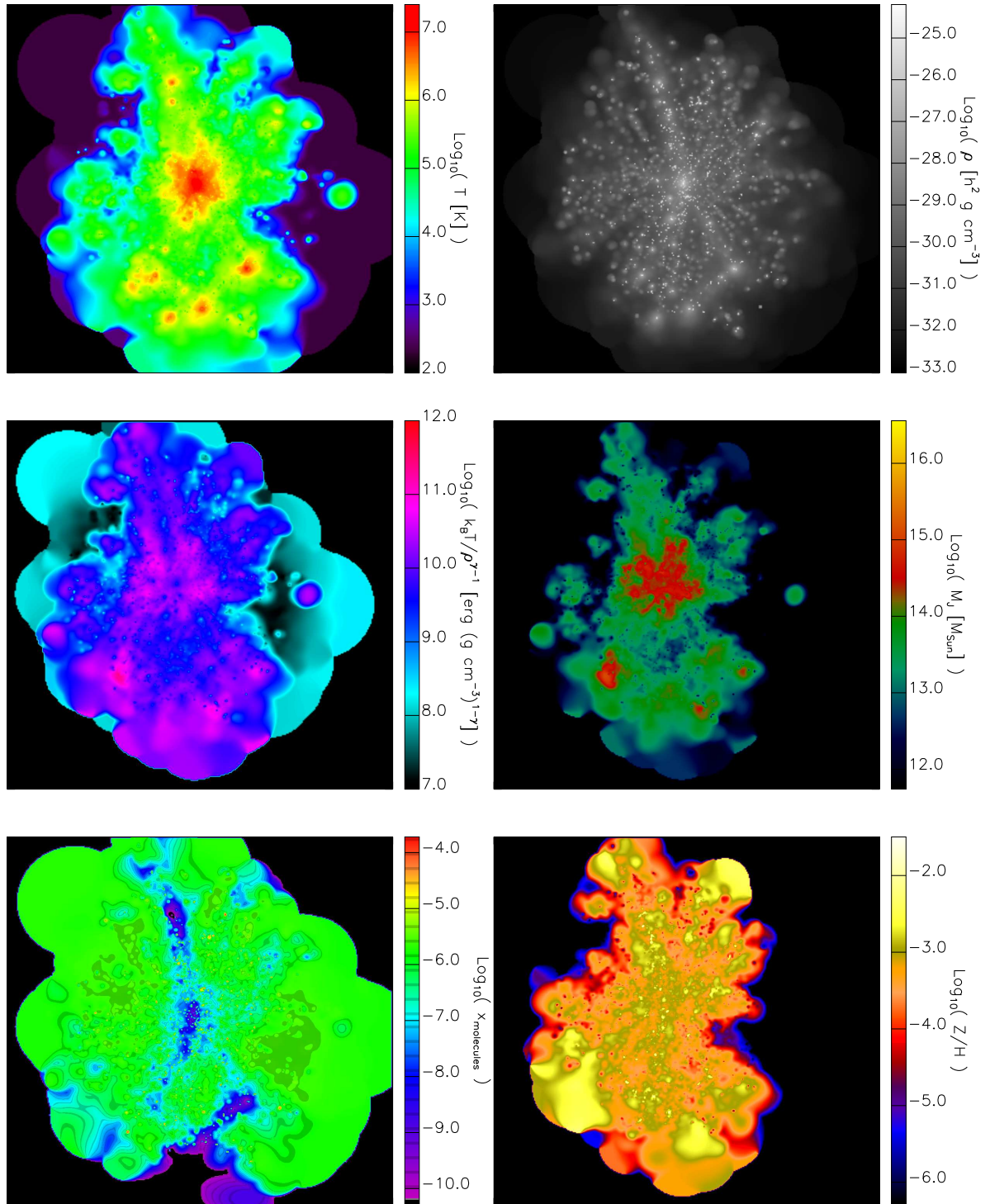


Figure 5.12: Upper-left panel: projected temperature distribution, T . Upper-right panel: average gas density distribution, ρ . Central-left panel: projected distribution of $k_B T / \rho^{\gamma-1}$, with $\gamma = 5/3$ ("entropy"). Central-right panel: Jeans mass. Bottom-left panel: projected total molecular fraction, $x_{\text{molecules}}$. Bottom-right panel: projected metallicity distribution over hydrogen mass, Z/H .

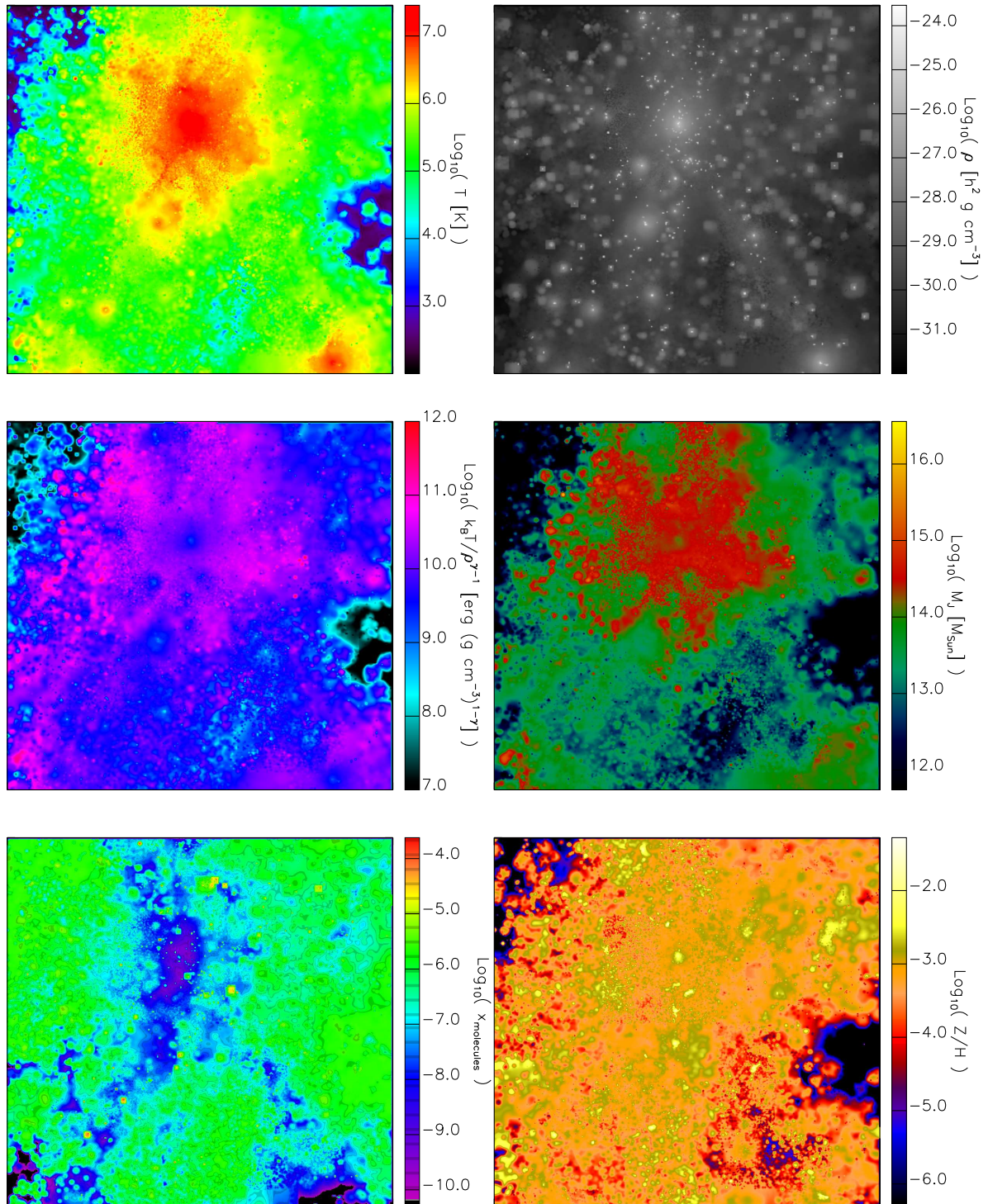


Figure 5.13: Central region of the cluster. The different quantities are as in the Figure 5.12.

allows the system to be partly gravitationally unbound. This means that such gas cannot be retained and could be lost by the system, generating outflows.

The last row gives the complete chemical information. The molecule distribution map is shown in the bottom-left panel and the metallicity in the bottom right one. We highlight that the molecule abundance is fully dominated by H_2 by some order of magnitudes. In fact, the thin regions not affected by star formation events still maintain abundances close to the initial ones (see section 5.2 and Figure 5.6), while the ones which experienced star formation are characterized by hot temperature and consequent molecule dissociation. Metallicity, on the other hand, is strongly ruled by star formation and winds. Therefore, even though metals are produced in high-density regions, we easily find polluted areas located far from those sites.

The phase diagram and the density distribution of molecules and metals are presented in Figure 5.14.

The phase diagram is color coded according to metallicity (upper-left panel) and molecular abundance (upper- right panel). The metal and molecular density distributions (bottom row, left and right panel respectively) are color coded by temperature. The metals are spread randomly, with no particular correlation. In the molecule distribution, instead, a double tail related to the hot (lower tail) and cold (higher tail) phases of the thin IGM is present.

With respect to the previous case (section 5.4.1), the phase diagram presents some differences. The addition of molecular cooling makes the gas colder since the beginning of the in-fall process. Also the subsequent condensation process is affected, as, in the former case, Hydrogen and Helium atoms are the only relevant primordial coolants, while, in the latter case, H_2 and HD enhance the cooling process at any evolutionary stage, together with metals. So, the fraction of gas with temperature below $\sim 10^4$ K is higher.

5.4.3 Star formation and metal pollution history

In Figure 5.15, redshift evolution of the star formation rate (left) and metallicity (right) are plotted.

Between the two different runs there is not much difference, as the underlying star

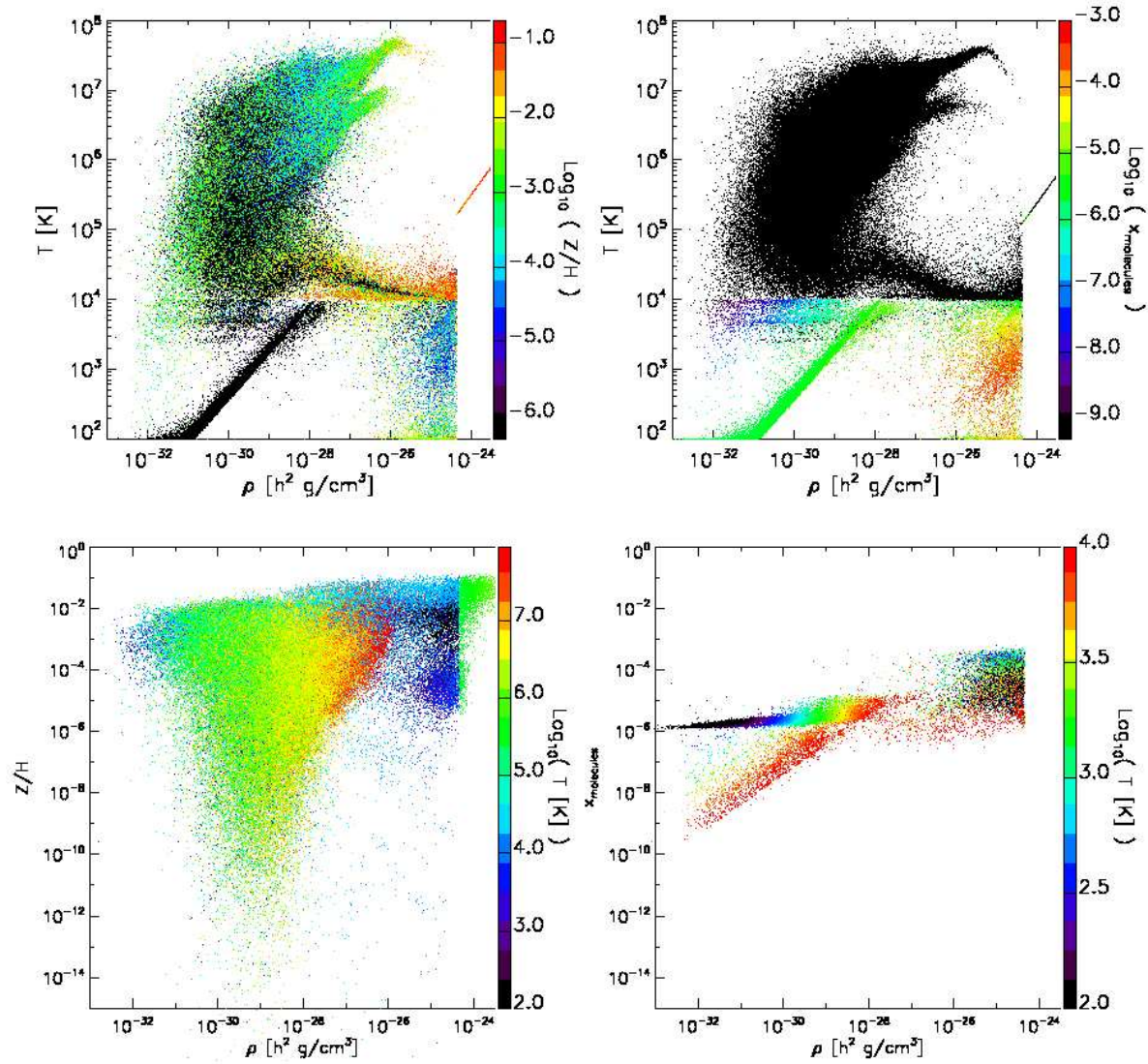


Figure 5.14: Upper row: phase diagram $\rho - T$ for the cluster at redshift $z = 0$, color coded according to metallicity (left panel) and molecular abundance (right panel). Bottom row: metallicity (left panel) and molecule (right panel) distribution as a function of the density and color coded according to temperature in Kelvin.

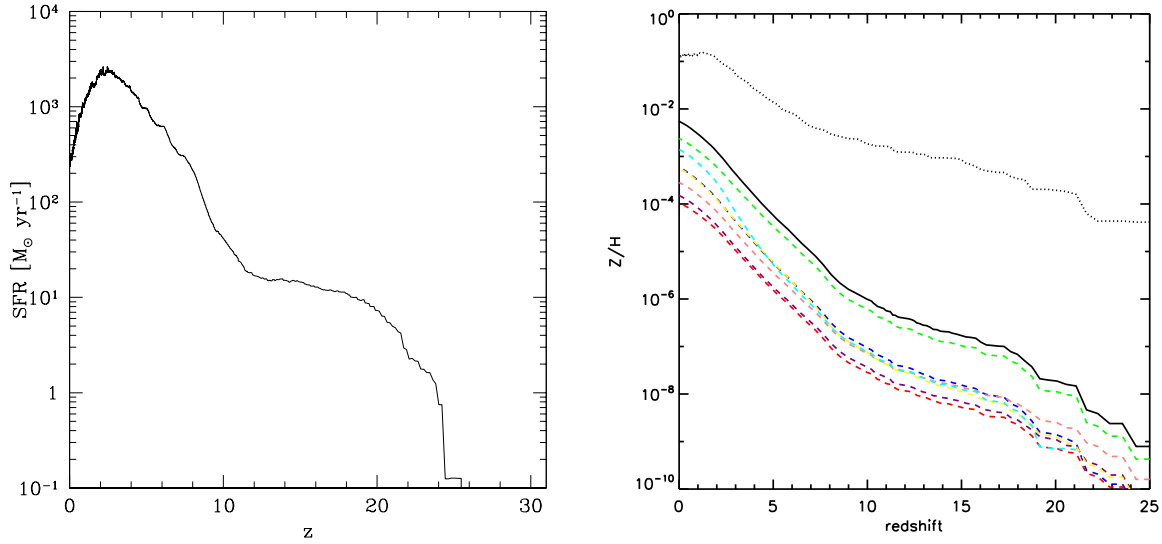


Figure 5.15: Left panel: total star formation rate. Right panel: redshift evolution for the total metallicity (solid line) and the different metals (dashed lines) averaged over the whole simulation box: carbon (blue), oxygen (green), magnesium (red), Sulphur (purple), silicon (pink), iron (yellow), other metals (cyan). The dotted line denotes the maximum of the metallicity reached (locally) in the cluster averaged over the whole simulation box.

formation sub-grid model is almost insensitive to the chemical composition of the medium and depends only on the gas total number density. This is a crucial lack in the commonly adopted standard recipes, which do not really follow and resolve the gas in-fall, but somehow “assume” it. For such motivations, the onset of star formation is basically unaltered, as well as the metal enrichment characteristics.

The star formation rate starts getting significant at $z \simeq 25$, when first objects are assembling and their density becomes higher than the threshold for star formation. Later the star formation rate increases until it reaches a peak at $z \simeq 2 - 4$ and eventually decreases. This behaviour is due to the transition to an accelerated Λ -dominated expansion.

Of course, simultaneously, metallicity increases as well. The right panel shows the evolution of the mean metallicities for the different metal components (dashed lines) and of the total metallicity (solid line). The dotted line refers to the maximum metallicity reached locally in the simulation. We highlight that, while at high redshift α elements expelled by short-lived stars via SNII explosions are predominant (e.g. oxygen - green dotted line), at lower redshift long-lived stars SNIa’s produce more and more iron and other heavy elements enhancing their abundances and filling the gap with oxygen.

5.5 Summary

In conclusion, we summarize the main outcomes of our implementation and tests.

- We have successfully tested the implementation of the most relevant features of gas cooling, in both pristine and polluted environments, for the temperature range $2.7 \text{ K} - 10^9 \text{ K}$ (see chapter 4).
- We have seen that HD cooling has some influence on the high-redshift gas clumping properties, while low-temperature metal cooling has a significant impact on the formation and evolution of cold objects.
- In addition to investigate the above topics, this implementation can now be used to study the detailed enrichment history of the IGM and its possible interplay with the transition between a primordial, massive star formation mode and a more standard one.

Chapter 6

On the onset of star formation

*Well do I know that I am mortal, a creature of one day.
But if my mind follows the winding paths of the stars
Then my feet no longer rest on earth, but standing by
Zeus himself I take my fill of ambrosia, the divine dish.*

PTOLEMY'S EPIGRAM, ALMAGEST

The next step to study early structure formation is to establish when the very first onset happens and to find star formation criteria to follow stellar evolution in cosmological, numerical simulations. These, indeed, usually lack of resolution to properly account for star formation, so a sub-grid or semi-analytic argumentation needs to be implemented in simulation codes.

Inspired by such concerns and supported by the discussions in the previous chapters, in the following we will give an overview of how it is possible to proceed and we will show our method to account for star formation events.

6.1 On the onset of star formation events

For sake of clarity, we remind that, in chapter 4, we have seen how hydrodynamical simulation codes have been a powerful tool in astrophysics (Evrard, 1988, for example), but we have also alluded to the fact that computational limitations have always required plausible sub-grid models to take into account star formation (Cen and Ostriker, 1992; Katz et al., 1996; Springel and Hernquist, 2003, e.g.).

Such simulations follow the converging gas in-fall into dark matter potential wells: during this process gas is shock heated and subsequently cools via energy level transitions. The typical time-scales involved in the process (see chapter 2) are the free-fall time, t_{ff} , and

the cooling time, t_{cool} . Gas condensation is expected to take place only if $t_{cool} < t_{ff}$.

We remind also that the free-fall time is defined as (2.57):

$$t_{ff} = \sqrt{\frac{3\pi}{32G\rho}} \quad (6.1)$$

where G is the universal gravitational constant and ρ the density of the medium; the numeric factor $(3\pi/32)^{1/2}$ is exact for spherical symmetry only. The cooling time is defined as (2.58)

$$t_{cool} = \frac{3}{2} \frac{nk_B T}{\Lambda(T, n_i)} \quad (6.2)$$

where n is the number density of the gas, k_B the Boltzmann constant, T the temperature and $\Lambda(T, n_i)$ the cooling function (energy emitted per unit time and volume) dependent both on temperature and number densities, n_i , of the species constituting the gas. In the low-density limit¹, for two-body interactions, between e.g. particle x and particle y , Λ can be written as (see also 4.3 and Appendix A)

$$\Lambda(T, n_x, n_y) = \mathcal{L}(T)n_x n_y \quad (6.3)$$

with \mathcal{L} quantum-mechanical function (accounting for energy level gaps, collisional and spontaneous decay coefficients, atomic level fractional population) depending on the temperature of the species considered, n_x and n_y . At $T \geq 10^4$ K, the cooling is dominated by collisions of hydrogen atoms, which is the most abundant species in nature – about 93% in number fraction – and Λ scales approximatively as n_H^2 (we indicate with n_H the hydrogen number density).

The physical conditions in which the first structures form are characterized by a primordial chemical composition: mostly hydrogen, deuterium, helium and some simple molecules, e.g. H₂ and HD.

In order to follow the whole process of structure and star formation in numerical simulations, one should implement the entire set of chemical reactions and hydrodynamical equations (see chapter 4) and from those calculate the abundance evolution and the corresponding cooling terms. In practice, to perform such computations is very expensive and time consuming and it becomes extremely challenging to follow the formation of structures from the initial gas in-fall into the dark matter potential wells to the final birth

¹ This widely-used approximation is appropriate as, according to the classical spherical “top-hat” model, a virialized object has a total mass density of $18\pi^2$ times the critical density, which corresponds, on average, to a total number density of $\sim 2h^2 \text{ cm}^{-3}$ at $z \sim 15$, for a WMAP5 cosmology and a mean molecular weight $\mu \simeq 1$. The transition to a high-density statistical equilibrium regime happens at critical number densities of $\sim 10^4 \text{ cm}^{-3}$.

of stars. Nevertheless, efforts are being made in this direction (Abel et al., 2000, 2002; Bromm and Larson, 2004; Yoshida et al., 2007; Whalen et al., 2008, for example).

For this reason, more practical, even if sometimes coarse, approximations are adopted. In brief, star formation relies on semi-empirical and numerical recipes based on chosen criteria to convert gas into stars and obtain the star formation rate, carefully normalized to fit observational data at the present day. The standard method used is to assume that once the gas has reached a given density threshold it automatically forms stars (e.g. Katz et al., 1996), regardless of the time between the moment when the threshold is reached and the effective run-away collapse which typically takes place at densities $\sim 10^2 \text{ cm}^{-3} - 10^4 \text{ cm}^{-3}$.

While this might be a reasonable approximation at low redshift, at high redshift this interval occupies a large fraction of the cosmological time and thus this assumption can induce large artificial off-sets on the onset of star formation and influence the evolution of the derived star formation rate. Thus, extrapolations to high redshifts of the low-density thresholds (few 0.1 cm^{-3}) used to model the star formation rate in the low-redshift Universe, may not always be justifiable. For this reason, high-redshift applications require larger resolutions and a higher density threshold.

In the following, we will discuss the importance of the choice of the density threshold in simulations of early structure formation and the first stars. We propose a criterion to choose such threshold (section 6.2) and present some interesting cases and results from high-resolution simulations (section 6.3 and 6.4). Then, we discuss our results (section 6.5).

6.2 Threshold for star formation

According to the usual scenario of structure formation, the Jeans mass (Jeans, 1902) is the fundamental quantity which allows one to distinguish collapsing from non-collapsing objects, under gravitational instability. For a perfect, isothermal gas it is given by: (2.20):

$$M_J = \frac{\pi}{6} \left(\frac{k_B T}{\mu m_H G} \right)^{3/2} \rho^{-1/2} \quad (6.4)$$

where m_H is the mass of the hydrogen atom and T and ρ the temperature and density of the gas, respectively. At very high redshift ($z \sim 30 - 20$), typical haloes have masses of

$\sim 10^5 M_\odot - 10^6 M_\odot$ which can grow up to $\sim 10^8 M_\odot - 10^9 M_\odot$ at $z \sim 10$.

As mentioned in section 6.1, in numerical simulations the density threshold for star formation is usually fixed to some constant value, irrespectively of the resolution of the simulation. It would be desirable instead to have a star formation criterion that allows one to reach scales that resolve the Jeans mass.

If M_{res} is the gas mass resolution of a given simulation, we can require that:

$$M_J = NM_{res} \quad (6.5)$$

with $N > 1$ and impose that the critical threshold is

$$\rho_{th} = \frac{\pi^2}{36N^2M_{res}^2} \left(\frac{k_B T}{\mu m_H G} \right)^3 \quad (6.6)$$

$$\simeq \frac{1.31 \cdot 10^{-13}}{N^2} \left(\frac{M_{res}}{M_\odot} \right)^{-2} \left(\frac{T}{10^3 \text{ K}} \right)^3 \left(\frac{1}{\mu} \right)^3 [\text{g cm}^{-3}]. \quad (6.7)$$

For $M_{res} = 10^2 M_\odot$, $T = 10^3 \text{ K}$, $\mu = 1$ and using $N = 10^2$ gas particles, one has $\rho_{th} \sim 10^{-21} \text{ g cm}^{-3}$, corresponding to a number density of $\sim 10^2 \text{ cm}^{-3}$. Commonly adopted density thresholds are of the order of $\sim 10^{-1} \text{ cm}^{-3}$.

To investigate the effects of different choices of star formation threshold on structure formation at high redshift, we implement the above model in numerical simulations. In the next, we describe the simulations performed and discuss the results obtained.

6.3 Simulation set-up

In order to study the effect of different threshold prescriptions on the onset of star formation we run high-resolution, three-dimensional, hydrodynamic simulations including non-equilibrium atomic and molecular chemistry, star formation and wind feedback.

We use the code Gadget-2 (Springel, 2005) in the modified version which includes (see details in chapter 4) stellar evolution and metal pollution (Tornatore et al., 2007a), primordial molecular chemistry (following the evolution of e^- , H, H^+ , He, He^+ , He^{++} , H_2 , H_2^+ , H^- , D, D^+ , HD, HeH^+) and fine structure metal transition cooling (O, C^+ , Si^+ , Fe^+) at temperatures lower than 10^4 K (Maio et al., 2007, 2008) (see also section 5.3).

The simulations have a comoving box size of $L = 1 \text{ Mpc}$ and sample the cosmological medium with a uniform realization of 320^3 particles for both gas and dark matter species

(for a total number of 2×320^3). The initial conditions (set at redshift $z = 100$) are generated² with a fast Fourier transform grid with $N_{mesh} = 320$ meshes and a maximum wave-number (Nyquist frequency)

$$k_{Nyquist} = \frac{2\pi N_{mesh}}{2L} \simeq 1 \text{ kpc}^{-1}$$

(i.e. a minimum wavelength of $2L/N_{mesh} \simeq 6.25 \text{ kpc}$) so that, for each wave-number, $\|\mathbf{k}\| < k_{Nyquist}$.

We will refer to such sampling with the term ‘‘mean region’’.

For our studies we consider two different sets of cosmological parameters:

- *standard model*: $\Omega_{0,m} = 0.3$, $\Omega_{0,\Lambda} = 0.7$, $\Omega_{0,b} = 0.04$, $h = 0.7$, $\sigma_8 = 0.9$ and $n = 1$, where the symbols have the usual meanings. The corresponding dark matter and gas particle masses are $\sim 755 M_\odot/h$ and $\sim 116 M_\odot/h$, respectively.
- *WMAP5 model*: recent data from 5-year WMAP (WMAP5) satellite (Hinshaw et al., 2008) suggest: $\Omega_{0,m} = 0.258$, $\Omega_{0,\Lambda} = 0.742$, $\Omega_{0,b} = 0.0441$, $h = 0.72$, $\sigma_8 = 0.796$ and $n = 0.96$. In this case, the corresponding dark matter and gas particle masses are $\sim 621 M_\odot/h$ and $\sim 128 M_\odot/h$, respectively.

Following the discussion in the previous sections, we also consider two different models for the star formation density threshold:

- a *low-density* threshold of $0.2 h^2 \text{cm}^{-3}$ (physical), compatible with the one adopted in Gadget code and the ones widely used in the literature (Katz et al., 1996; Springel and Hernquist, 2003; Tornatore et al., 2007b; Pawlik et al., 2008, for example);
- a *high-density* threshold of $135 h^2 \text{cm}^{-3}$ (physical), as computed from equations (6.6) and (6.7). This value is adequate to follow atomic processes even in small $\sim 10^5 M_\odot$ haloes at $z \sim 20$. Moreover, typically this threshold falls in density regimes where cooling dominates over heating and thus allows us to properly resolve gas condensation down to the bottom of the cooling branch.

A summary with all the features of the simulations is given in Table 6.1 and Table 6.2. We denote with the labels ‘‘std’’ and ‘‘wmap5’’ the runs with standard and WMAP5

² We use the code N-GenIC.

Table 6.1: Cosmological parameters adopted for the simulations. The columns (from left to right) specify: name of the run, Ω_{0M} , $\Omega_{0\Lambda}$, Ω_{0b} , h , σ_8 , spectral index.

Model	Ω_{0M}	$\Omega_{0\Lambda}$	Ω_{0b}	h	σ_8	n
wmap5-ht	0.258	0.742	0.0441	0.72	0.8	0.96
wmap5-lt	0.258	0.742	0.0441	0.72	0.8	0.96
std-ht	0.300	0.700	0.0400	0.70	0.9	1.00
std-lt	0.300	0.700	0.0400	0.70	0.9	1.00
zoom-std-ht	0.300	0.700	0.0400	0.70	0.9	1.00

Table 6.2: Parameters adopted for the simulations. The columns (from left to right) refer to: name of the run, number of particles used, gas particle mass, dark matter particle mass, star formation density threshold.

Model	number of gas+dm particles	M_{gas} [M_{\odot}/h]	M_{dm} [M_{\odot}/h]	SF density threshold [$h^2\text{cm}^{-3}$]
wmap5-ht	2×32768000	128	621	135
wmap5-lt	2×32768000	128	621	0.2
std-ht	2×32768000	116	755	135
std-lt	2×32768000	116	755	0.2
zoom-std-ht	2×41226712	3.9	25.6	135

cosmology, respectively; with “lt” and “ht” the runs with low- and high-density thresholds, respectively.

Finally, to investigate primordial star formation events in local high-density regions, we perform a very high-resolution numerical simulation of a rare high-sigma peak with comoving radius $\sim 140 \text{ kpc}/h$. Such a region is selected using the zoomed initial condition technique on a $\sim 10^9 M_\odot$ halo formed in a dark-matter-only simulation (Gao et al., 2007)³. We split each particle in gas and dark matter component, according to the standard model parameters. The resulting gas particle mass is $\sim 4 M_\odot/h$ while dark matter particles have a mass of $\sim 26 M_\odot/h$. In Table 6.1 and Table 6.2 this simulation is labelled by “zoom-std-ht”.

6.4 Results

In this section we present results from simulations with the sets of parameters described above. We discuss first the mean region of the Universe (section 6.4.1) and then the high-density region (section 6.4.2). Simple visualizations for the two cases are presented in Figure 6.1.

6.4.1 Mean-region simulation

Our reference run is the wmap5-ht model with initial composition given by the values quoted in Galli and Palla (1998) at $z = 100$. We assume a primordial neutral gas with residual electron and H^+ fractions $x_{e^-} \simeq x_{\text{H}^+} \simeq 4 \cdot 10^{-4}$, H_2 fraction $x_{\text{H}_2} = 10^{-6}$, H_2^+ fraction $x_{\text{H}_2^+} = 3 \cdot 10^{-21}$, D fraction $x_{\text{D}} = 3.5 \cdot 10^{-5}$, HD fraction $x_{\text{HD}} = 7 \cdot 10^{-10}$, D^+ fraction $x_{\text{D}^+} = 4 \cdot 10^{-9}$, HeH^+ fraction $x_{\text{HeH}^+} = 10^{-14}$.

We show some evolutionary stages in Figure 6.1 (upper set of panels). In the maps, the first column refers to temperature, the second to gas density and the third to molecular fraction at $z = 30.16$ and $z = 12.17$, respectively. The creation of new molecules is evident, together with the related growth of structure. More specifically, as time passes, one can see the heating undergone by the gas in dense regions, due to structure formation shocks. The temperature increases from a few hundreds Kelvin in the low-density regions, to $\sim 10^4 \text{ K}$ in the denser regions. In the meantime, also the molecular fraction increases

³ We use the “R4” initial conditions presented there.

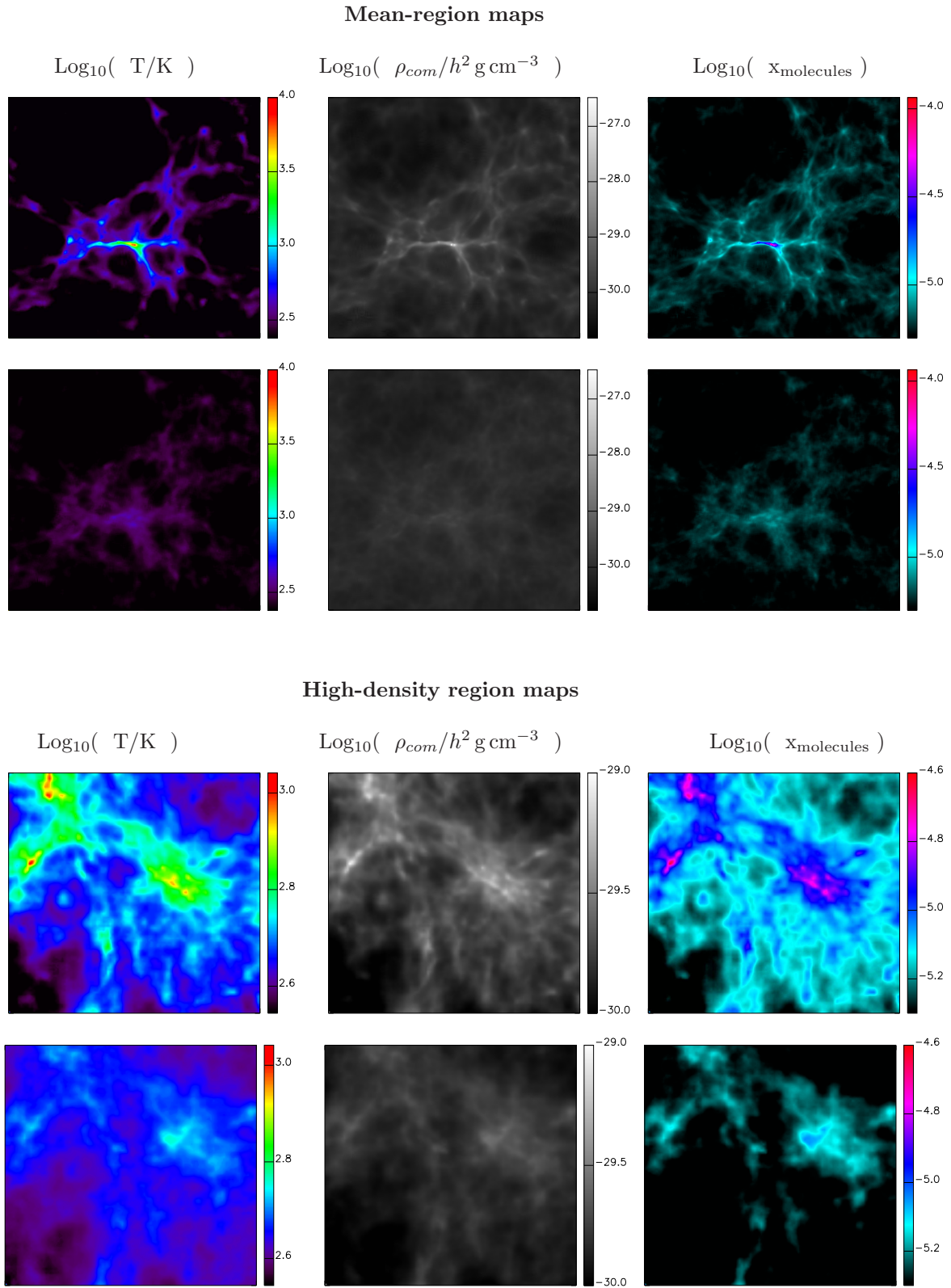


Figure 6.1: First, second and third column are respectively temperature, density and molecule maps. The first two rows refer to the mean-region simulation at redshift 12.17 (top) and 30.16 (bottom). The box size is 1 Mpc comoving. The last two rows refer to the high-density region at redshift 50 (top) and 70 (bottom). The region size is $\sim 140 \text{ kpc}/h$ comoving. All quantities are smoothed on a 276 pixel side grid.

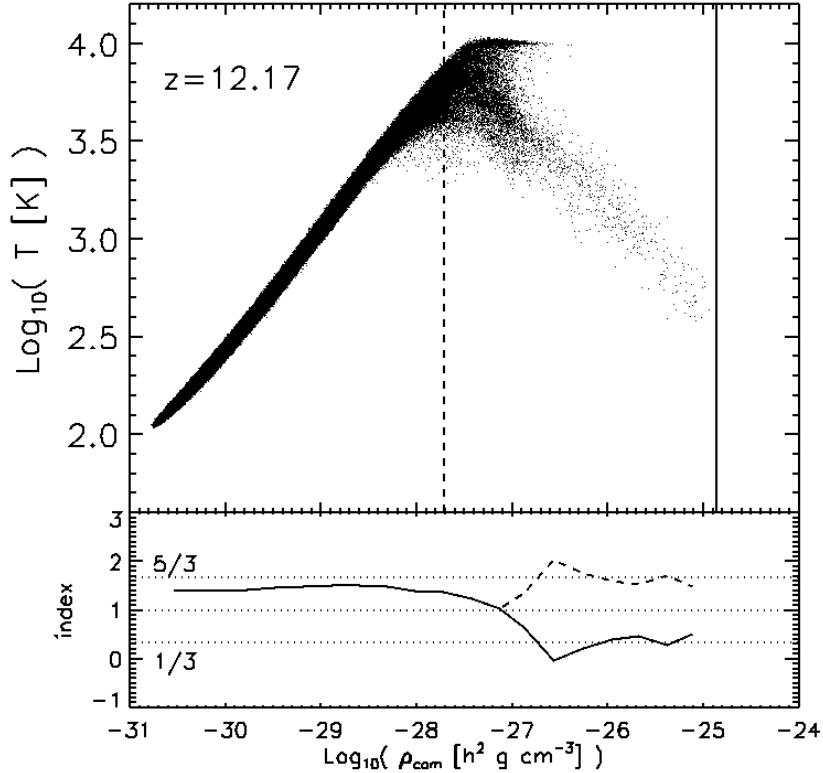


Figure 6.2: Upper panel: phase diagram at redshift $z = 12.17$ (just before the onset of star formation) for the wmap5-ht simulation. The vertical straight lines indicate a low physical critical-density threshold of $0.2 \text{ h}^2 \text{ cm}^{-3}$ (dashed line) and a higher physical critical-density threshold of $135 \text{ h}^2 \text{ cm}^{-3}$ (solid line). Lower panel: average effective index computed over the whole range of densities. The three horizontal dotted lines show values of $5/3$, 1 and $1/3$, respectively from top to bottom. The solid line shows α and the dashed line shows γ (see text for definitions).

to values larger than 10^{-4} . Soon after, the production of molecules increases rapidly (up to $\sim 10^{-2}$) aiding the star formation process which, for this simulation, starts at $z \sim 12$.

In Figure 6.2, we show the phase diagram (comoving density versus temperature) at redshift $z \sim 12$, i.e. just before the onset of star formation.

The low-density gas which is shock heated by the collapse of the first primordial haloes is seen on the left side of the panel. Starting from values for the temperature of $\sim 10^2 \text{ K}$, the gas is progressively heated to $\sim 10^4 \text{ K}$ and moves along the rising branch. At this stage, collisions become more frequent due to the higher temperature. The upper energy levels of particles get excited and the subsequent de-excitation is accompanied by emission of radiation. This effect is negligible at low densities, because collisions are rare and the fraction of energy converted into radiation is small. When the densities increase, the cooling becomes comparable to the heating and an isothermal regime with no significant

net change in the temperature is reached. This appears at the tip of the phase diagram (and in the behaviour of the effective index, as discussed below), at $T \sim 10^4$ K, where the cooling is dominated by atomic Ly α transitions and accompanied by fragmentation, as the Jeans mass becomes proportional to $\rho^{-1/2}$.

At higher densities, radiative losses overtake heating and induce a fast cooling phase (dominated by molecules, mostly H₂). This eventually halts the fragmentation process freezing the minimum mass of gas clouds and enhancing star formation.

The solid vertical line corresponds to the physical high-density star formation threshold ($135 h^2 \text{ cm}^{-3}$) and, for comparison, we plot also the dashed line for a physical number density of $0.2 h^2 \text{ cm}^{-3}$.

We stress that by adopting a low-density threshold for star formation one completely misses the isothermal and cooling part of the phase diagram, and thus a correct modeling of the cooling regions within the simulations. This can affect the onset of star formation, particularly at high redshift, when the time needed for the gas to evolve from the low-density threshold to the high-density threshold ($\sim 2 \cdot 10^8$ yr) can be a substantial fraction of the cosmological time ($\sim 4 \cdot 10^8$ yr at $z \sim 12$). Note that the time elapsed between the attainment of the isothermal peak in the phase diagram and the end of the cooling branch is $\sim 6 \cdot 10^7$ yr. This problem is less severe at lower redshift, when it becomes of the order of several Gyr.

As a consequence, the onset of star formation can happen much earlier in models adopting a low-density threshold (as we will show in the following).

The evolution that follows the end of the cooling branch is characterized by the formation of a dense core which accretes gas on the free-fall time-scales (Yoshida et al., 2006b). This phase is pretty fast ($\sim 10^6 - 10^7$ yr) and rapidly raises central densities to $\sim 10^{16} \text{ cm}^{-3}$.

In addition, density and temperature behaviour can also be described by an effective index⁴ which depends on the physical conditions of the gas regime considered. In the lower panel of Figure 6.2 we plot the effective index as a function of density. Its expression is easily derived from the perfect gas equation of state.

The solid line refers to the value $\alpha \equiv 1 + (dT/T)/(d\rho/\rho)$, which takes into account changes in the sign of the temperature derivative distinguishing the heating regime ($\alpha > 1$) from

⁴ By effective index of the gas, γ , we mean $P \propto \rho^\gamma$, with P pressure and ρ density. This is simply related to the polytropic index.

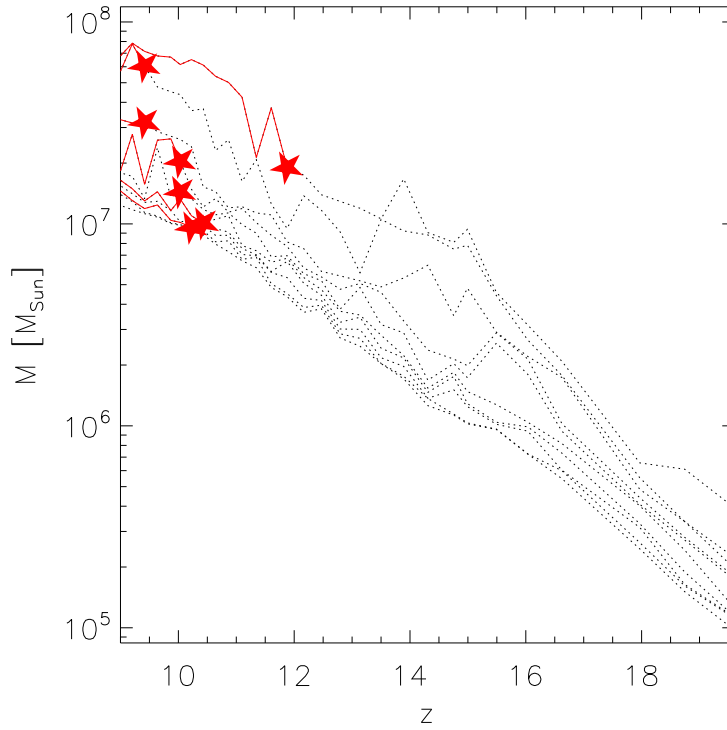


Figure 6.3: Evolution of the ten most massive haloes in the wmap5-ht cosmological simulation (dotted lines). The halo mass range where stars are formed is marked by solid red lines. The redshift at which the first star forms in each halo is indicated by the filled star symbols. After that, star formation continues along the solid lines.

the cooling regime ($\alpha < 1$). The dashed line refers to $\gamma \equiv 1 + |(dT/T)/(d\rho/\rho)|$, so that γ is always ≥ 1 . Dotted horizontal straight lines show values of $5/3$, 1 and $1/3$.

In correspondence of the isothermal peak in the $T - \rho$ plane, it is $\alpha = \gamma = 1$, which marks the transition from the heating to the cooling regime. At this stage we expect the gas run-away collapse to begin and last for the following cooling regime, at which point α oscillates around the value $1/3$ and the process is halted. Indeed, gas condensation and accretion act against further cooling, heating up the whole system. When central temperatures raise to $\sim 10^7$ K, the proton-proton chain becomes efficient and sustains a H nuclear burning stellar core (Yoshida et al., 2006b, 2007).

Figure 6.3 displays the evolution of the ten most massive haloes found in the simulation. We also show the redshift when stars are produced (filled star symbols) in each object. The haloes are found using a friend-of-friend algorithm with a linking length equal to 20% of the mean inter-particle separation. Typical halo masses at redshift $z \sim 12$, when star

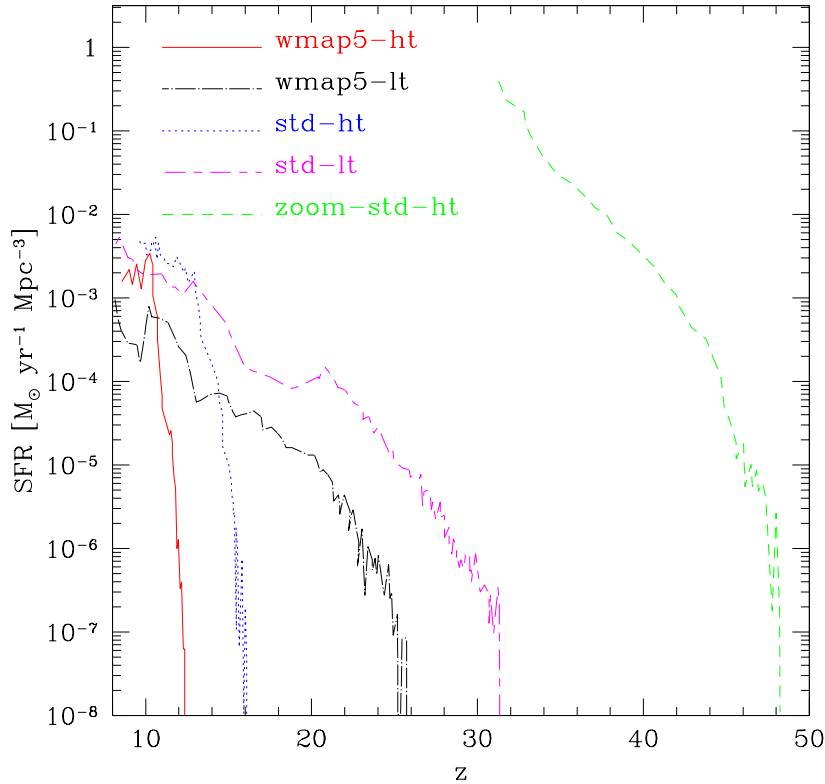


Figure 6.4: Star formation rate as a function of redshift for the different models, from left to right: WMAP5 cosmological parameters and high-density threshold (solid red line), standard cosmological parameters and high-density threshold (dotted blue line), WMAP5 cosmological parameters and low-density threshold (dot-dashed black line), standard cosmological and low-density threshold (long-dashed-short-dashed magenta line). The green short-dashed line refers to the simulation of the high-density region with standard parameters and high-density threshold.

formation starts, are of the order of $10^7 M_{\odot}$ and reach densities of $\sim 10^2 \text{ cm}^{-3}$.

For comparison, we have run the same simulation using standard cosmological parameters (std-ht run). In this case we expect a faster evolution, with earlier structure formation. The first star formation events are detected at redshift $z \sim 15 - 16$ in haloes with masses $\sim 10^7 M_{\odot}$.

This can be clearly seen in Figure 6.4, where we plot the star formation rate as a function of redshift for the different simulations. In order to compute the star formation rate, we adopt the implementation described by (Springel and Hernquist, 2003).

The onset of star formation in the wmap5-ht model (red solid line) is delayed compared to the std-ht model (blue dotted line). For the wmap5-lt (black dashed line) and std-lt (magenta short-long-dashed line) models, star formation starts at $z \sim 25$ and 31 , respectively. Thus, at such high redshifts, even small changes in the cosmology can be

significant for the onset of star formation. This is easily understood in terms of spectral parameters: the standard cosmology has higher spectral index and higher normalization, therefore, assigning more power on all scales with respect to WMAP5 values, leads to structure formation much earlier.

The choice of the density threshold makes an even larger difference in the onset of star formation. The star formation rates corresponding to the `wmap5-lt` (black dot-dashed line) and `wmap5-ht` (red solid line) show that star formation starts at $z \sim 25$ and 12, respectively. The major difference between low- and high-density threshold models is due to the fact that in the former, the gas reaches the critical density much earlier. So, the redshift difference in the onset corresponds to the time that the gas needs to move from the low- to the high-density threshold (see Figure 6.2).

In addition, as expected, the simulations adopting the high-density thresholds slightly overtake the respective low-threshold cases. This happens because the former did not remove the gas at higher redshifts, it accumulated and ended in delayed bursts of star formation. Later, the star formation rates are restored at the same level.

As already mentioned, the low-density threshold model is very widely used both in numerical and semi-analytical works, because it does not require the incorporation molecular chemistry (as the threshold is lower than the typical densities at which molecules become efficient coolants) and therefore it is easier to implement and allows for faster simulations. However, it can compromise the whole picture if the results are extrapolated to high redshift, when molecules are the main coolants and the time delay occupies a significant fraction of the age of the Universe.

6.4.2 High-density region simulation

In this section we show results for the high-density region described in section 6.3 and initialized at redshift $z = 399$.

In this case, the physical number densities at the beginning of the simulation ($z \sim 200$) are in the range $\sim [0.5 h^2 \text{ cm}^{-3}, 50 h^2 \text{ cm}^{-3}]$, with an average of $\sim 4 h^2 \text{ cm}^{-3}$, higher than the typical value adopted for the low-density threshold for star formation. Therefore, the conventional low-density model would result in unreasonable star formation at $z \sim 200$. In order to avoid this, it is common to add a further, additional, *ad hoc* constraint, which permits star formation only if the over-densities are higher than a given minimum value –

usually between ~ 50 and ~ 100 – (Katz et al., 1996, in section 4.2, suggest 55.7, for example), but, in this situation, it is the additional constraint which determines when the onset of star formation occurs, rather than the low-density threshold.

So, we run a simulation only with a high-density threshold. For the sake of comparison, we still use the value of $135 h^2 \text{cm}^{-3}$, although rigorously, following (6.6) and (6.7), one should adopt a value $\sim 9 \cdot 10^4 h^2 \text{cm}^{-3}$ for a $3.9 M_\odot/h$ gas particle mass. Nonetheless, we have checked that this choice does not affect our conclusions, as we are already beyond the isothermal peak, in the fast cooling regime, where the time-scales are extremely short ($\sim 10^6 \text{yr}$).

All the initial abundances are set according to the values suggested by Galli and Palla (1998), consistent with a primordial neutral gas having residual electron and H^+ fractions of $x_{e^-} \simeq x_{\text{H}^+} = 10^{-3}$, H_2 fraction $x_{\text{H}_2} = 10^{-10}$, H_2^+ fraction $x_{\text{H}_2^+} = 3 \cdot 10^{-15}$, D fraction $x_{\text{D}} = 3 \cdot 10^{-5}$, D^+ fraction $x_{\text{D}^+} = 3 \cdot 10^{-8}$, HD fraction $x_{\text{HD}} = 10^{-14}$, HeH^+ fraction $x_{\text{HeH}^+} = 5.6 \cdot 10^{-18}$. The simulation maps are shown in Figure 6.1 (lower panels).

In Figure 6.5, we show the phase diagram and the behaviour of the effective index as a function of the comoving gas density at redshift $z \simeq 45$. Physical critical-density thresholds of $0.2 h^2 \text{cm}^{-3}$ (dashed line), $135 h^2 \text{cm}^{-3}$ (solid line) and $\sim 9 \cdot 10^4 h^2 \text{cm}^{-3}$ (dot-dashed line) are marked in the figure. While the first two are the same as for the mean-density region simulation, the last one corresponds to the value obtained using equations (6.6) and (6.7). To emphasize the different characteristics of the phase diagram compared to the one obtained for the mean-density region, we plot in addition the particles that lay above the density threshold in a purely non-equilibrium chemistry run (i.e. without star formation).

The isothermal peak is reached at redshift $z \sim 50$. Unlike the mean-density simulation, the gas does not spend time on the isothermal plateau, but cools very rapidly (in less than $7 \cdot 10^6 \text{yr}$) from $\sim 10^{3.5} \text{K}$ to $\sim 10^2 \text{K}$ and condenses into comoving densities of $\rho_{\text{com}} \sim 10^{-21} h^2 \text{g}/\text{cm}^3$. The rapidity of these events is reflected in the lack of particles in the intermediate stages of the cooling branch.

As before, we also plot the effective gas index. The usual initial shock-heating behaviour and the following cooling is recovered up to much higher densities. At the bottom of the cooling branch we find values of γ oscillating around $5/3$ and 1 . As the last stages are quite fast, the low number of particles present introduces some statistical noise which is

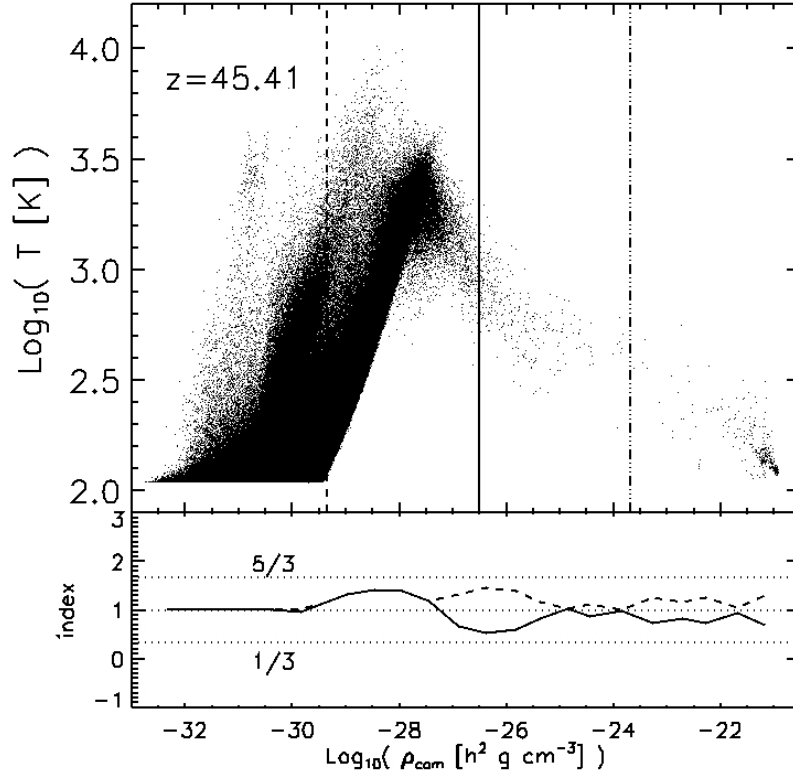


Figure 6.5: Upper panel: phase diagram at redshift $z \sim 45.41$ for the high-density region simulation. The vertical straight lines are drawn in correspondence of a physical critical-density threshold of $0.2 \text{ h}^2 \text{cm}^{-3}$ (dashed line), $135 \text{ h}^2 \text{cm}^{-3}$ (solid line) and $8.9 \cdot 10^4 \text{ h}^2 \text{cm}^{-3}$ (dot-dashed line). Lower panel: average effective index computed over the whole range of densities. The three horizontal dotted lines are drawn in correspondence of the values $5/3$, 1 and $1/3$, respectively, from top to bottom. The solid line refers to α and the dashed line to γ (see text for the definitions).

evident in the plot.

With our choice of the threshold, star formation sets in at $z \sim 48$ (see Figure 6.4). The additional time needed to reach the highest densities at the bottom of the cooling branch is extremely short ($\sim 10^6 \text{ yr}$), so our choice assures that the onset of star formation is correctly estimated. As there is no obvious, standard way of quantifying the star formation rate in these simulations, we do it dividing the stellar mass formed at each time-step by the volume of the gas contained in the high-density region (a sphere of about $140 \text{ kpc}/h$ radius).

6.5 Discussion

We have studied the effect of different choices of the density threshold for the creation of stellar particles on the onset of star formation in numerical SPH simulations (Maio et al., 2007; Tornatore et al., 2007a, for technical details). We have run simulations using initial conditions appropriate for both a region of the Universe with mean density and, using the zoom technique, a high-density peak.

The basic process which leads to star formation, i.e. gas shock heating up to $\sim 10^3 \text{ K} - 10^4 \text{ K}$ by in-fall to dark matter haloes followed by radiative losses due mainly to molecular collisional excitations, is common to both scenarios. The main difference is associated with the global dynamics and time-scales of the process. In fact, following the rare high-sigma peak we see that, because of the higher densities, chemical reactions are faster and much more efficient with respect to the simulations with mean-density initial conditions. Therefore, the molecular abundance increases more rapidly, reaching a number fraction of $\sim 10^{-4}$ by $z \sim 50 - 40$ (compared to $z \sim 20$, for the corresponding mean-density case). Such values are enough to make collisional cooling dominant over heating and to induce star formation episodes.

For all the simulations, we have checked the effect of altering the initial molecular fractions of some orders of magnitude and found no significant change in structure formation. Indeed, only the very thin, rare regions keep memory of the initial composition, as chemical reactions are not effective there. In denser environments, instead, the abundances are quite independent from the starting values. This is clearly seen, e.g., in Figure 6.6, where, for each SPH particle of the pure non-equilibrium chemistry run of the zoom simulation, we plot the H_2 number fractions as function of the comoving density, at different redshift. The presence of an asymptotic trend determined by the chemical-reaction network is well recognizable at higher densities and independent from the initial conditions.

Density and temperature behaviour can be described with an effective index which depends on the physical conditions of the gas considered. Roughly, it is isothermal during

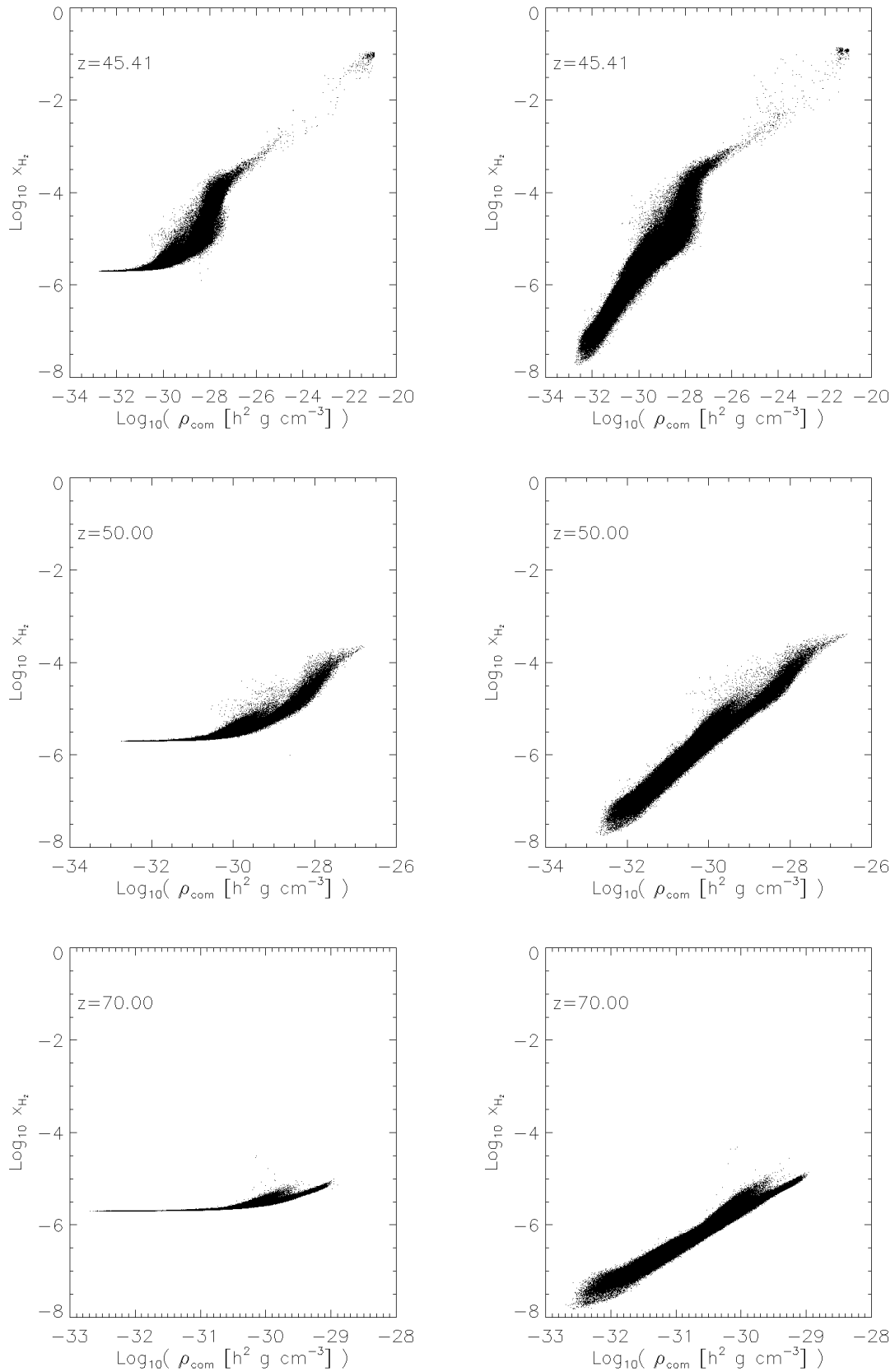


Figure 6.6: Molecular hydrogen fractions x_{H_2} as function of the comoving density ρ_{com} , for redshift $z = 45.41$ (top row), $z = 50.00$ (middle row), $z = 70.00$ (bottom row). The left column refers to the initial abundances inferred from RecFast code, the right column to the ones we have adopted.

the transition from the heating to the cooling regime, then $\alpha \simeq 1/3$ (see the effective index computed in the lower panel of Figure 6.2) until the bottom of the cooling branch is reached. At that point isothermality is recovered, as gas condensation and accretion act against further cooling, thereby heating the system. When central temperatures raise to $\sim 10^7$ K, the proton-proton chain becomes efficient and sustains a H nuclear burning stellar core.

More quantitatively, when cooling is dominated by H_2 , the cooling time (2.58, 6.2) can be approximated as

$$t_{cool} \simeq \frac{3}{2} \frac{k_B T}{\Lambda_{\text{H}_2}(T) x_{\text{H}_2} n_{\text{H}}} \quad (6.8)$$

where x_{H_2} is the H_2 number fraction, $\Lambda_{\text{H}_2}(T)$ is the H_2 cooling function at temperature T and the other symbols have their usual meanings.

For gas at the beginning of the cooling branch, $T \sim 10^{3.5}$ K and $x_{\text{H}_2} \sim 10^{-4}$, giving $t_{cool} \sim 7 \cdot 10^6 n_{\text{H}}^{-1}$ yr (n_{H} in cm^{-3}). In the mean-density case (see phase diagram in Fig. 6.2), $n_{\text{H}} \simeq 0.3 \text{ cm}^{-3}$, while in the high-density region (see phase diagram in Fig. 6.5), $n_{\text{H}} \simeq 6 \text{ cm}^{-3}$. This translates into a characteristic cooling time of $\sim 2 \cdot 10^7$ yr for the former case and $\sim 10^6$ yr for the latter.

Such rough estimates show the relevance of following the full cooling branch when simulating star formation at high redshift in regions of mean density, because the characteristic cooling time occupies a substantial fraction of the cosmological time. This problem is less severe for simulations of high-density peaks, in which the time-scales are much shorter.

For this reason it is important to use a high-density threshold for star formation, rather than imposing star formation even before the isothermal peak is reached. Otherwise an artificially high redshift for the onset of star formation could result.

For the test cases presented in this paper, the value adopted for the high-density threshold is $135 h^2 \text{ cm}^{-3}$, well beyond the isothermal peak of the gas. This allows for a correct estimate of the relevant time-scales, as the gas spends most of the time in the isothermal phase. In addition, following the evolution of the gas to higher densities allows for a better resolution of, e.g., the morphology and disk galaxy structure (Saitoh et al., 2008), the clumpiness of the gas (see also the next Figure 6.7) and the features of the interstellar or intergalactic medium. On the other hand, running high-density threshold

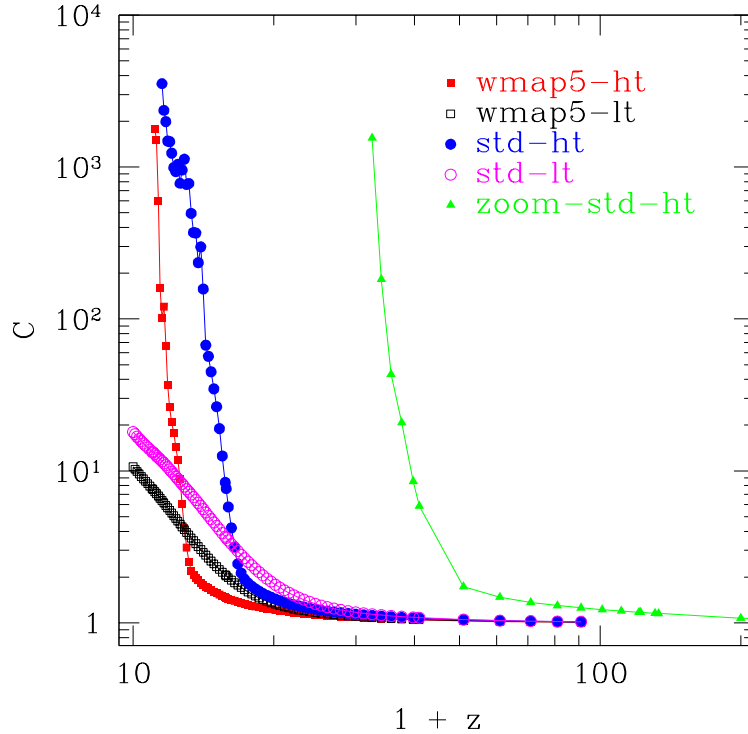


Figure 6.7: Global clumping factor for the different simulations as a function of redshift.

simulations down to the present age ($z = 0$) is computationally very challenging because of the extremely short time-scales involved in the calculations. Only simulations performed with a low-density threshold are currently run to $z = 0$ and fine-tuned to reproduce the observed low-redshift evolution of the star formation density.

A possible approach to correctly model the star formation process at all redshifts would be to smoothly scale the density threshold with z . This would allow one to properly follow the gas cooling in the early stages of structure formation (adopting a high-density threshold) and at the same time to recover the expected behaviour at low redshift (via a low-density threshold).

The density threshold used in simulations strongly affects the clumpiness of the gas, preventing reliable estimates of the recombination times. In Figure 6.7 we compare, for the different simulations, the global clumping factors, C , defined as

$$C \equiv \frac{\sum_i m_i \rho_i^{-1} \sum_j m_j \rho_j}{(\sum_k m_k)^2} \quad (6.9)$$

where the indices i , j and k run over the total number of gas particles. At high z , the

clumping factor remains quite flat with $C \sim 1$ until $z \sim 30 - 20$, for the mean-density simulations, and $z \sim 70 - 60$, for the high-density region. Afterward, there is a steep increase due to gas cooling and subsequent condensation.

As expected, the low-threshold models underestimate C . The difference can be up to several orders of magnitude: in the low-threshold simulations C is only $\sim 10 - 20$ at $z \simeq 10$, but in the high-threshold ones, we get $C \sim 10^3$ at the same redshift.

The clumpiness of the high-density region is $C(z \simeq 33) \sim 200$ and $C(z \simeq 31) \sim 10^3$.

The difference in clumping factors occurs since in the low-density threshold model high-density gas particles are turned into stars and then removed by winds relatively early, while in the high-density threshold case they are allowed to reach values which are about three orders of magnitude larger.

6.6 Summary

In summary, we have performed high-resolution, three-dimensional, N-body/SPH simulations including non-equilibrium atomic and molecular chemistry, star formation prescriptions and feedback effects to investigate the onset of primordial star formation. We have studied how the primordial star formation rate changes according to different gas-density threshold, different cosmological parameters and different simulation set-ups. Our main findings are summarized in the following.

- The typical low-density thresholds (below $\sim 1 \text{ cm}^{-3}$) are inadequate to describe star formation episodes in mean regions of the Universe at high redshift. To correctly estimate the onset of star formation high-density thresholds are necessary.
- In rare, high-density peaks, the density can already be higher than the usual low-density thresholds since very early times. Therefore, density thresholds lying beyond the isothermal peak (several particles per cm^3 , in our case) are still required, but given the faster evolution in the phase diagram of the cooling particles in dense environments, the exact value of the threshold is not crucial, as long as it is larger than $\sim 10^2 \text{ cm}^{-3}$ (physical).
- Different values of the threshold and the cosmological parameters can lead the onset of star formation at very different epochs: with a low-density threshold ($0.2 h^2 \text{ cm}^{-3}$)

star formation starts at $z \sim 25-31$ (depending on the cosmology), while high-density threshold models ($135 h^2 \text{ cm}^{-3}$) predict a much later onset, $z \sim 12-16$ (depending on the cosmology).

- Performing primordial, rare, high-density region simulations within the high-density threshold model, we find that the local star formation can set in as early as $z \sim 48$.

Chapter 7

Early structure formation and critical metallicity

Ita res accendent lumina rebus.

LUCRETIVS, DE RERUM NATURA

An interesting topic related to the possible existence of a critical metallicity at which the IMF changes from a top-heavy to a standard Salpeter one (see also sections 3.2 and 3.4.3) is how structure formation results are affected.

In fact, for different Z_{crit} we expect different epochs for the onset of the population II-I regime. Moreover, also the abundance of population III structures will be highly connected to the critical metallicity, as a lower value of Z_{crit} implies an earlier transition to population II-I and earlier decay of population III birth. This has an impact on their observability.

In order to address such issues, we perform several numerical simulations of early structure formation adopting different values for Z_{crit} .

The details on the simulation set-up are given in the next section 7.1 and the main results about the effects on star formation are presented in the following sections 7.2, 7.3.

7.1 Simulation set-up

The simulations were performed in the frame of the standard Λ CDM cosmological model (with geometrical parameters $\Omega_{0,m} = 0.3$, $\Omega_{0,\Lambda} = 0.7$, $\Omega_{0,b} = 0.04$, $h = 0.7$, and spectral parameters $n = 1$, $\sigma_8 = 0.9$). The initial conditions (see section 6.3) were generated sampling 1 Mpc^3 of the cosmic fluid at redshift $z = 100$, with 320^3 particles per gas and dark matter species, having masses of $116 M_\odot/h$ and $755 M_\odot/h$, respectively.

In order to properly constrain the onset of primordial structure formation, we include the whole set of chemistry equations leading molecule (H_2 , HD, HeH^+) creation and cooling (see section 4.3, Table 4.1, Figure 4.6 and Figure 4.7). As in section 6.4.1, we assume a primordial neutral plasma with residual electron and H^+ fractions $x_{e^-} \simeq x_{\text{H}^+} \simeq 4 \cdot 10^{-4}$, H_2 fraction $x_{\text{H}_2} = 10^{-6}$, H_2^+ fraction $x_{\text{H}_2^+} = 3 \cdot 10^{-21}$, D fraction $x_{\text{D}} = 3.5 \cdot 10^{-5}$, HD fraction $x_{\text{HD}} = 7 \cdot 10^{-10}$, D^+ fraction $x_{\text{D}^+} = 4 \cdot 10^{-9}$, HeH^+ fraction $x_{\text{HeH}^+} = 10^{-14}$.

We set the star formation threshold at the bottom of the cooling branch, as discussed in section 6.2.

For the very first bursts, we adopt a top-heavy IMF, according to which massive stars in the range $[100, 500] M_\odot$ are formed (population III stars). The stellar life-times lie between about $3 \cdot 10^6$ yr, for the $100 M_\odot$ stars, and ~ 0 yr (instantaneous death), for the $500 M_\odot$ stars. The relevant mass range for metal pollution is approximately $[140, 260] M_\odot$ (see section 3.3 and Figure 3.3, for details), because of the formation of pair-instability supernovæ. They spread around the first metals which will pollute the neighbouring areas and will also increase the cooling capabilities of the medium (see Figure 4.6 and Figure 4.7).

Once the particle metallicity reaches the critical value, Z_{crit} , population II-I star formation is assumed to set in, in place of population III, and subsequent stars will have masses in the range $[0.1, 100] M_\odot$, distributed accordingly to a Salpeter IMF. Population II-I stellar life-times are usually much larger than population III, ranging between about $2 \cdot 10^{10}$ yr, for the $0.1 M_\odot$ stars, and $3 \cdot 10^6$ yr, for the $100 M_\odot$.

We perform four numerical simulations considering critical metallicities of $Z_{crit}/Z_\odot = 10^{-3}, 10^{-4}, 10^{-5}, 10^{-6}$, respectively, in order to study how and if structure formation is influenced. In Figure 7.1 and in Figure 7.2, we present simulation maps at redshift $z = 11$ for temperature, gas density and molecular abundance (Figure 7.1) and metallicity distribution for all the cases considered (Figure 7.2). We note that the differences in the metallicities are only due to the value of Z_{crit} adopted. In particular, the metal enrichment is higher for the $Z_{crit} = 10^{-3} Z_\odot$ case than for the other cases. This is due to the longer time needed to reach the critical level, Z_{crit} . Once this happens, population II-I star formation sets in and delays further metal pollution.

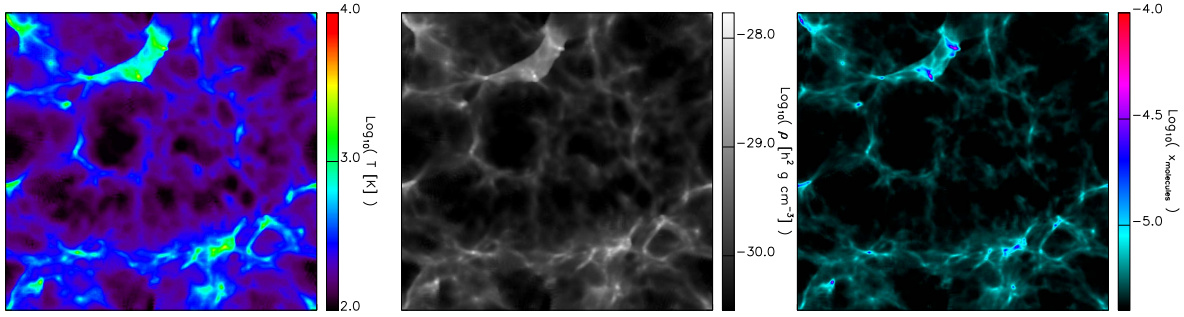


Figure 7.1: Temperature (left panel), density (central panel) and molecules (right panel) maps at redshift $z = 11$ (for the $Z_{crit} = 10^{-3} Z_{\odot}$ case: in the other cases the maps are very similar, with differences of only $\sim 1\%$, or less). The different quantities are smoothed over a 276 pixel grid. Each slice has a thickness of $1/14$ the boxsize.

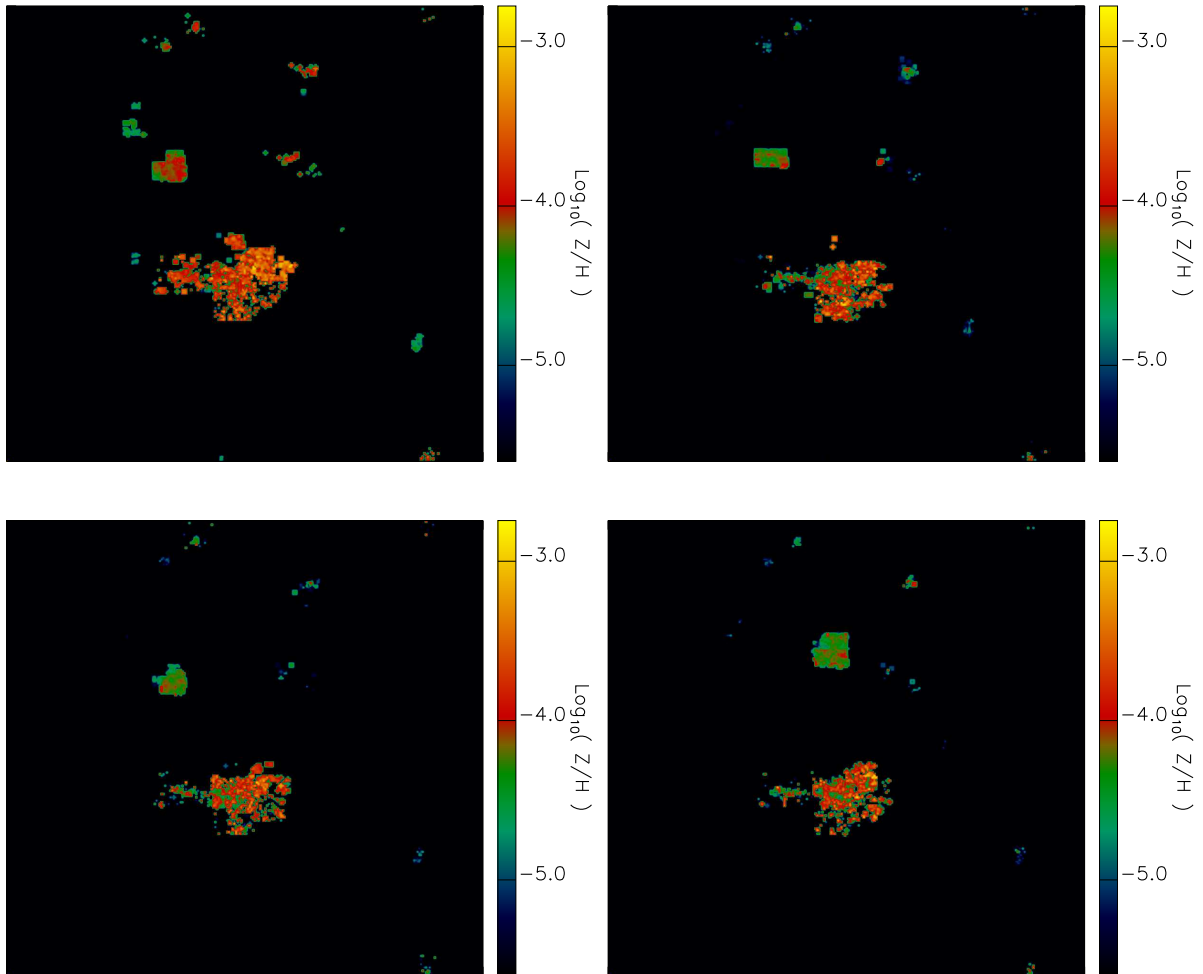


Figure 7.2: Line-of-sight average metallicity maps at redshift $z = 11$ for $Z_{crit} = 10^{-3} Z_{\odot}$ (top-left panel), $Z_{crit} = 10^{-4} Z_{\odot}$ (top-right panel), $Z_{crit} = 10^{-5} Z_{\odot}$ (bottom-left panel), $Z_{crit} = 10^{-6} Z_{\odot}$ (bottom-right panel). The different quantities are smoothed over a 276 pixel grid, projecting the whole simulation box.

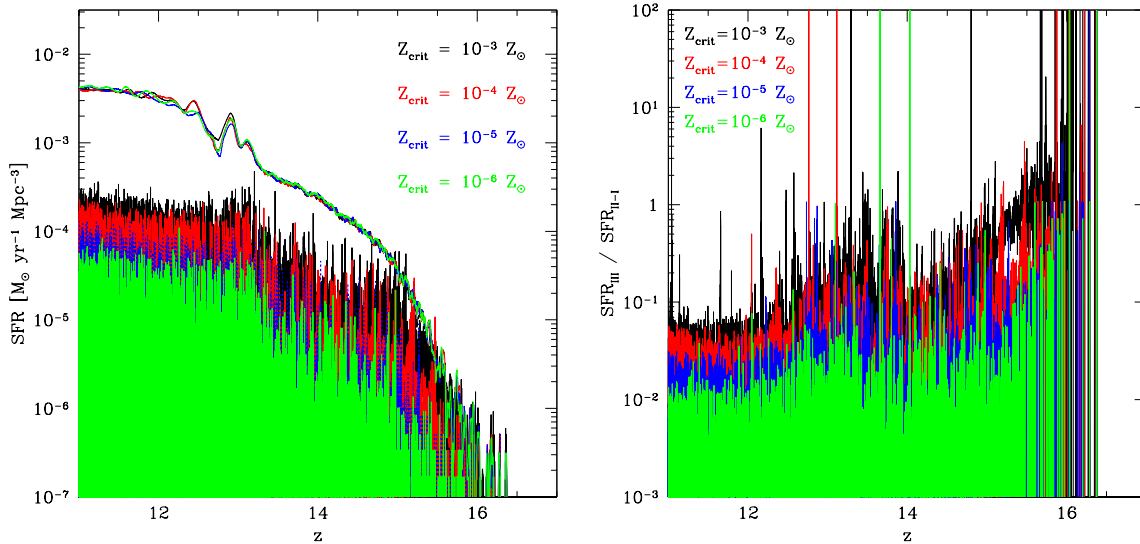


Figure 7.3: The plots refer to the star formation rates derived from the simulations described in the text for $Z_{crit} = 10^{-3} Z_{\odot}$ (black), $Z_{crit} = 10^{-4} Z_{\odot}$ (red), $Z_{crit} = 10^{-5} Z_{\odot}$ (blue), $Z_{crit} = 10^{-6} Z_{\odot}$ (green), respectively, as indicated by the legends. In the left panel, the solid lines refer to the total star formation rate, while the shaded areas to the population III regime. In the right panel, we plot the ratio between population III (SFR_{III}) and population II-I (SFR_{II-I}) star formation rate.

7.2 Effects of Z_{crit} on SFR

For all the simulations the onset of star formation is at $z \simeq 16.33$, when the Universe has about $2.3 \cdot 10^8$ yr, independently from Z_{crit} , which plays a role only in the following epochs (see Figure 7.3).

A metallicity of $10^{-6} Z_{\odot}$ is locally reached after only $\sim 10^5$ yr ($\Delta z \sim 5 \cdot 10^{-3}$) and metallicities of the order of $10^{-5} Z_{\odot}$ are reached after about $2 \cdot 10^5$ yr ($\Delta z \sim 10^{-2}$). In approximately $\sim 5 \cdot 10^6$ yr ($\Delta z \sim 10^{-1}$) it is possible to get $Z \simeq 10^{-4} Z_{\odot}$ or even $Z \simeq 10^{-3} Z_{\odot}$. An average enrichment of $Z \sim Z_{crit}$ is always reached in less than $\Delta z \sim 1$ after the onset of star formation (see also Figure 7.4). Once the critical metallicity is reached, population II-I star formation sets in and contributes as well to metal enrichment. We also notice that the enrichment process is very local and therefore also the transition to a different regime. So, we will find the coexistence of population III and population II-I structures. The global star formation rate and population III star formation rate derived from the different simulations are plotted in Figure 7.3 (left panel). At the very beginning population III contribution is dominant, but rapidly fades away and the population II-I regime is established. The noise in the plots is just due to the small time-steps induced

by the chemical and numerical network, when high densities are reached, and the net star formation can be null.

We see that the total star formation rate is only mildly influenced by the value adopted for Z_{crit} , meaning that population III star formation does not affect the global behaviour significantly and the bulk of star formation is mainly led by population II-I objects.

The reason for that is simply understood in terms of time-scales, as population III objects have a short lifetime (at most $\sim 10^6$ yr) and rapidly pollute the medium up to the critical Z . Therefore, after the very first bursts, it is much easier to match the condition for standard population II-I star formation, rather than for metal free, population III star formation (see also Figure 7.6).

This is very well seen in Figure 7.4, where we display the metal evolution in the simulations. First metals spread during the final stages of stellar evolution have typical $Z \sim (10^{-5} - 10^{-4}) Z_{\odot}$ and they immediately reach values of $Z \sim (10^{-4} - 10^{-3}) Z_{\odot}$ between redshift $z \sim 16$ and $z \sim 15$. Therefore, the critical metallicity Z_{crit} is easily reached, despite its precise, actual value. The leading element is always oxygen, as it is the most abundant one produced by supernova explosions.

We point out that for higher Z_{crit} the population III regime lasts longer, so one has more massive star explosions which can pollute the medium up to higher metallicities, before population II-I star formation regime sets in. This results in a quicker Z increase in the very early stages, but, on average, the differences between the two extremes are not exagerately big.

In addition, for what said in the beginning of this section, the simultaneous presence of different star formation regimes is naturally expected since soon after the onset. We check this, plotting the ratio between population III star formation rate, SFR_{III} , and population II-I star formation, SFR_{II-I} in the right panel of Figure 7.3. The presence of spikes is due to divergencies arising when there is no standard star formation (i.e. $SFR_{II-I} \sim 0 M_{\odot} \text{yr}^{-1} \text{Mpc}^{-3}$) and it is, obviously, particularly strong in the high- z tail. None the less, residual, isolated population III bursts are still ongoing at lower redshifts, where on average this regime becomes negligible.

In Figure 7.5, for sake of clarity, we consider only those redshifts at which population III and population II-I star formation are non-zero. In this way we just avoid the divergencies

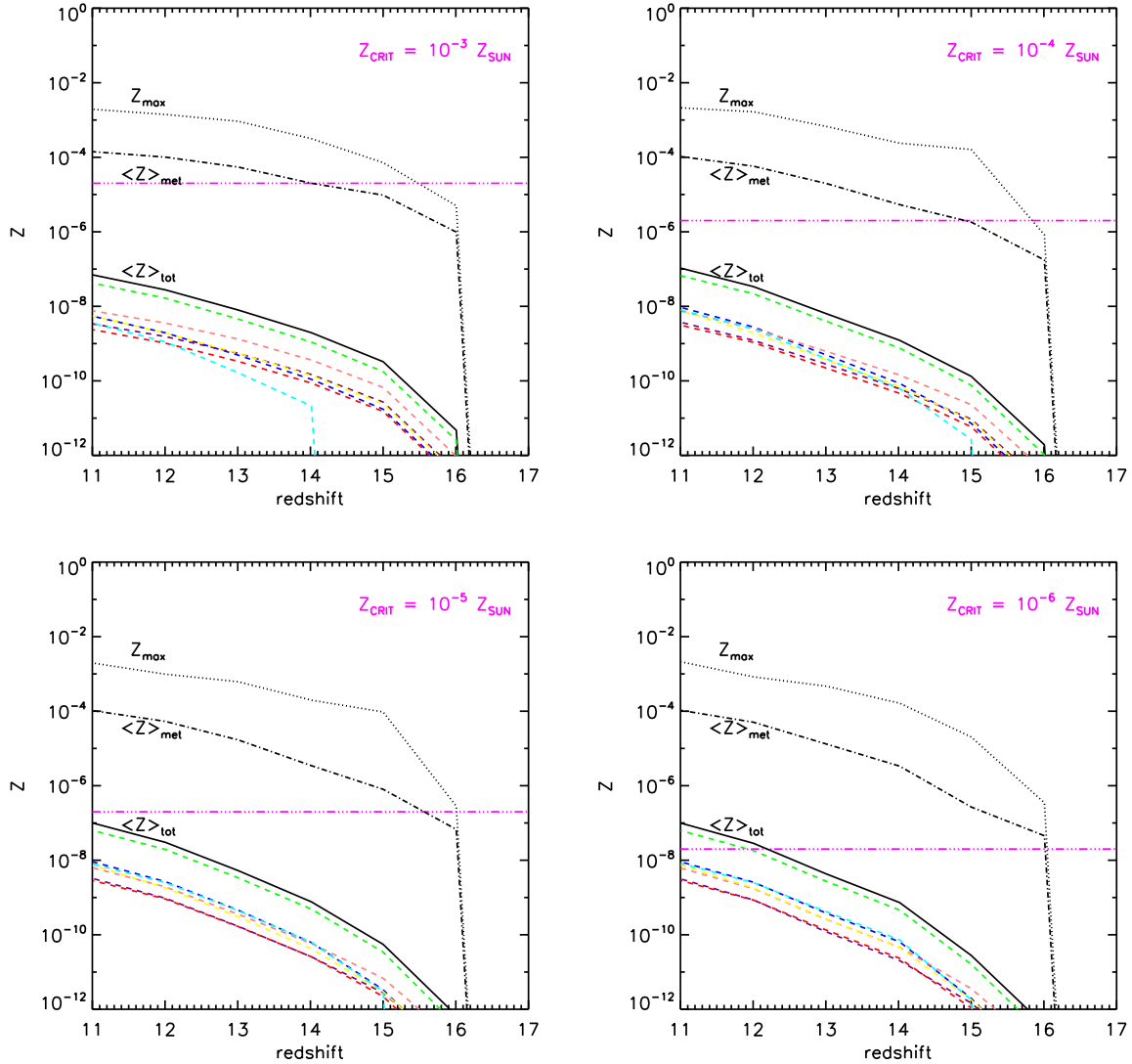


Figure 7.4: The plots show metal evolution as function of redshift for the $Z_{crit} = 10^{-3}$ (upper-left panel), 10^{-4} (upper-right panel), 10^{-5} (bottom-left panel), and $10^{-6} Z_{\odot}$ (bottom-right panel) case. The magenta horizontal dot-dot-dot-dashed line indicates, in each panel, the critical metallicity; the dotted line is the maximum metallicity; the dot-dashed line is the average metallicity of the spread metals; the solid line is the total metallicity averaged over the whole simulation box and the dashed lines the corresponding individual metallicities: carbon (blue), oxygen (green), magnesium (red), sulphur (purple), silicon (pink), iron (yellow), other metals (cyan).

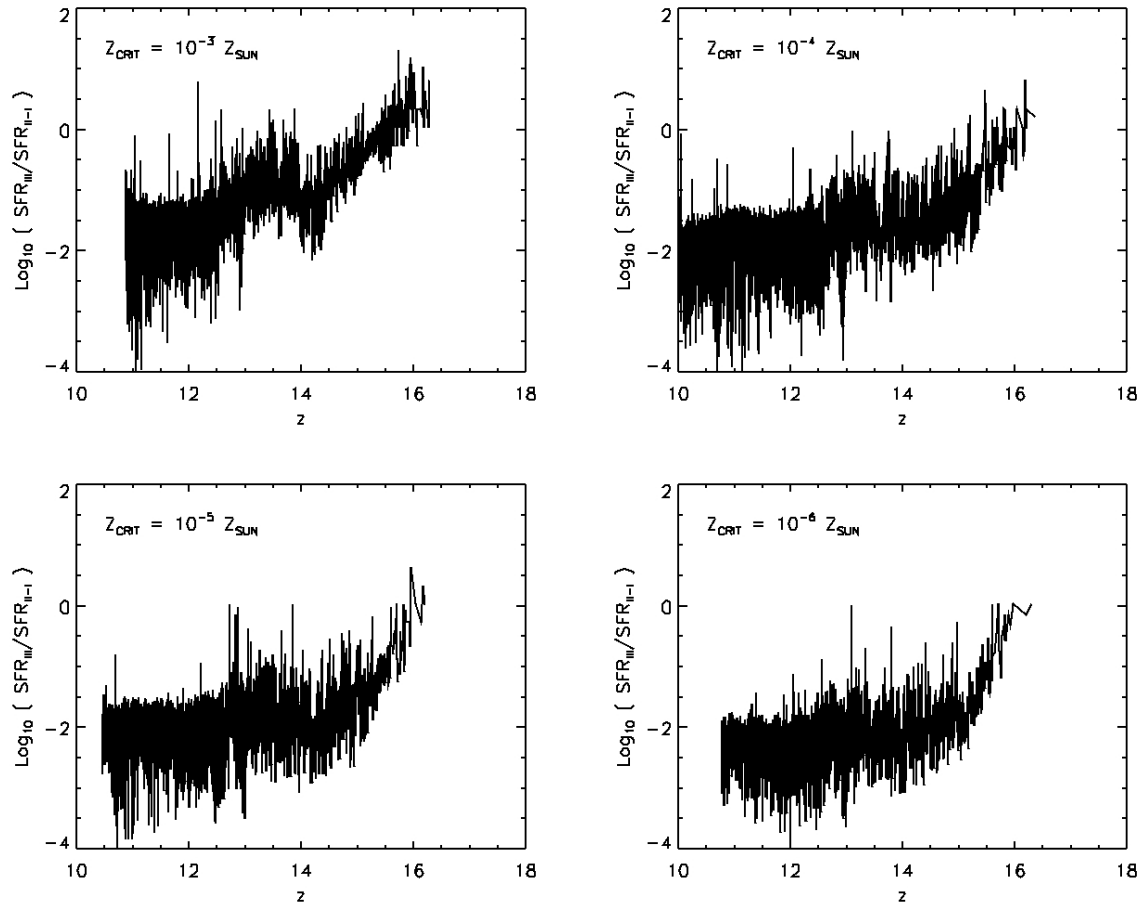


Figure 7.5: The plots are similar to Figure 7.3, but here the ratio between population III star formation rate (SFR_{III}) and population II-I star formation rate ($\text{SFR}_{\text{II-I}}$) is shown. The critical metallicity for the transition from population III regime to population II-I regime is assumed to be $Z_{crit} = 10^{-3} Z_{\odot}$ (top-left), $Z_{crit} = 10^{-4} Z_{\odot}$ (top-right), $Z_{crit} = 10^{-5} Z_{\odot}$ (bottom-left), $Z_{crit} = 10^{-6} Z_{\odot}$ (bottom-right).

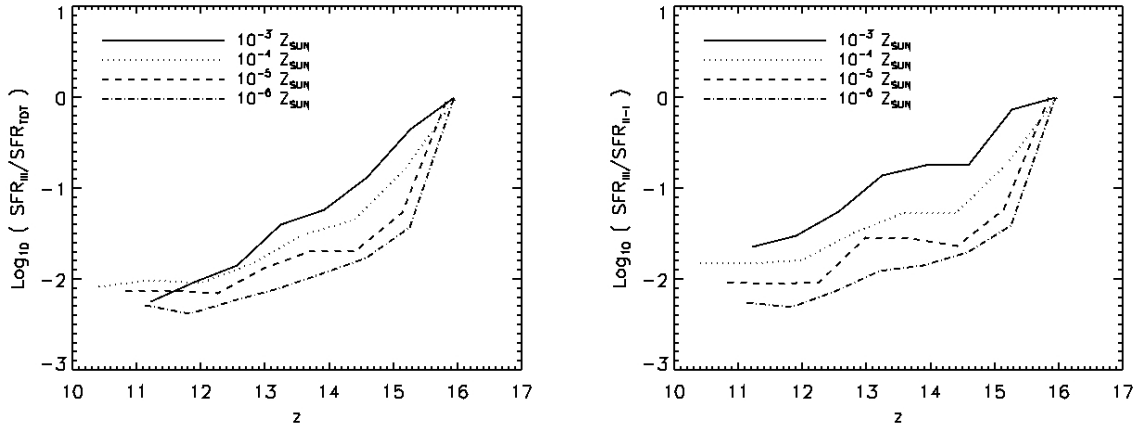


Figure 7.6: The plots show the quantity $\text{Log}_{10}(\text{SFR}_{\text{III}}/\text{SFR}_{\text{TOT}})$ (left panel) and $\text{Log}_{10}(\text{SFR}_{\text{III}}/\text{SFR}_{\text{II-I}})$ (right panel) as function of redshift for $Z_{\text{crit}} = 10^{-3} Z_{\odot}$ (solid line), $Z_{\text{crit}} = 10^{-4} Z_{\odot}$ (dotted line), $Z_{\text{crit}} = 10^{-5} Z_{\odot}$ (dashed line), $Z_{\text{crit}} = 10^{-6} Z_{\odot}$ (dot-dashed line), as indicated by the legend. The data are the same as in Figure 7.5, averaged and plotted in decimal logarithmic scale.

in the early epochs, where population III star formation is the only regime and $\text{SFR}_{\text{II-I}}$ is zero. We see that the contribution from population III star formation is relevant only in the very early phases, when star formation sets in. In this period (corresponding to a ratio greater or equal to unity) star formation is lead by metal-free star formation, according to a top-heavy IMF (see section 7.1). In the four different panels, we see that the main effect of changing Z_{crit} is altering the duration of population III regime. Indeed, this is slightly longer in the $Z_{\text{crit}} = 10^{-3} Z_{\odot}$ case and decreases gradually with Z_{crit} . For $Z_{\text{crit}} = 10^{-3} Z_{\odot}$ (top-left panel), population III is relevant for $\Delta z \simeq 1$ (a time interval of $\sim 2 \cdot 10^7$ yr at $z \simeq 16$), while for $Z_{\text{crit}} = 10^{-6} Z_{\odot}$ (bottom-right panel), there is a sudden drop at $z \simeq 16$, immediately after the onset of star formation. This behaviour, the smaller Z_{crit} , the earlier the transition from population III to population II-I dominated star formation, is expected, because the time needed to pollute the IGM is shorter.

We also highlight that population III contributions are about 2 or 3 orders of magnitude smaller than population II-I already at redshift $z \sim 12$, so the effect on large-scale structure formation can be neglected.

In Figure 7.6, we summarize the discussion showing, for the different critical metallicities adopted, a plot of the average ratio of simultaneous population III and population II-I star formation, $\text{SFR}_{\text{III}}/\text{SFR}_{\text{II-I}}$ (left panel), and a plot of the average ratio of population III and total star formation rate, $\text{SFR}_{\text{III}}/\text{SFR}_{\text{TOT}}$ (right panel).

In both cases, the trends for different critical metallicities are distinguishable and the differences span a range of roughly one order of magnitude.

7.3 Filling factor and Z_{crit}

Another interesting quantity is the filling factor of metals. We define it as

$$f \equiv \frac{N(0 < Z < Z_{crit})}{N(Z > 0)} \quad (7.1)$$

i.e., f is the ratio between the number of particles enriched up to the critical level, $N(0 < Z < Z_{crit})$, and the total number of polluted particles $N(Z > 0)$.

We stress that a global filling factor – defined as equation 7.1, but with $N(Z > 0)$ replaced by the total number of particles N – would be simply a rescaling of the number of enriched particles found in the simulations.

It is again evident the dominance of population III star formation in the very first bursts at $z \simeq 16$, for all Z_{crit} . Later, the filling factor decreases steeply, as $N(0 < Z < Z_{crit})$ becomes smaller and smaller than $N(Z > 0)$. In other words, the medium is rapidly enriched above the critical level, Z_{crit} , and the population III regime becomes negligible. Depending on Z_{crit} , the filling factor at $z \simeq 11$ ranges between 0.065, for $Z_{crit} = 10^{-6} Z_{\odot}$, 0.21, for $Z_{crit} = 10^{-5} Z_{\odot}$, 0.34, for $Z_{crit} = 10^{-4} Z_{\odot}$, 0.48, for $Z_{crit} = 10^{-3} Z_{\odot}$. These values span a factor of 7 or 8 among the four cases.

7.4 Remarks

Before concluding, it is worthwhile stressing that in order to better understand the topics we have discussed here, we plan to perform more simulations to study numerical effects of box dimension, resolution, IMF.

In addition, even if in our study it seems that population III star formation is not very relevant, we will check such issue analyzing what happens changing feedback prescriptions or adding more detailed treatments of back-reaction from star formation episodes.

In fact, in principle these could still change the overall picture.

Moreover, metal pollution is quite a patchy phenomenon, therefore, the fact that primordial population III star formation is negligible does not mean that in rare, isolated

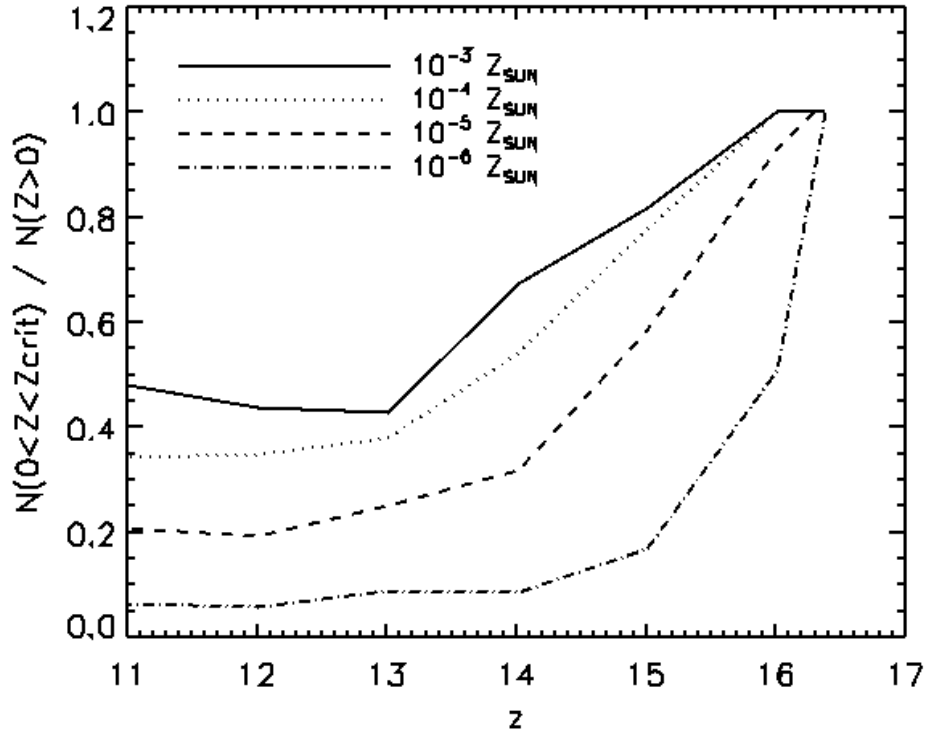


Figure 7.7: The plot shows the filling factor relative to population III star formation. The x-axis is redshift and the y-axis is the number fraction of enriched particles with metallicity $0 < Z < Z_{crit}$, undergoing star formation. The critical metallicities are $Z_{crit} = 10^{-3} Z_{\odot}$ (solid line), $Z_{crit} = 10^{-4} Z_{\odot}$ (dotted line), $Z_{crit} = 10^{-5} Z_{\odot}$ (dashed line), $Z_{crit} = 10^{-6} Z_{\odot}$ (dot-dashed line), as indicated by the legend.

regions pristine environments cannot exist at later times. In such regions, we expect to find population III objects also at lower redshift.

7.5 Summary

In the present chapter, we have seen the main results from numerical simulations of early structure formation, including primordial, molecular evolution, star formation treatment, metal enrichment and the switch for a double IMF regime, below and above a critical metallicity Z_{crit} .

We have performed four relevant simulations differing by Z_{crit} , only. We choose $Z_{crit}/Z_{\odot} = 10^{-3}, 10^{-4}, 10^{-5}, 10^{-6}$. This parameter rules the IMF used for each particle: in unpolluted environments, for $Z < Z_{crit}$ (population III regime), the IMF adopted is top-heavy in the range $[100, 500] M_{\odot}$; for $Z \geq Z_{crit}$ (population II-I regime) a standard Salpeter IMF is assumed.

We summarize here our findings.

- The effect of the population III regime on the global star formation rate is negligible.
- The critical metallicity in star forming particles is reached relatively soon, so the transition from population III to population II-I regime happens in a very short period, after the onset of star formation ($\sim 10^6$ yr), because of the population III stellar life-times.
- Population III regime is dominant only for a very short duration, immediately after the onset of star formation; later on, almost irrespectively from the threshold metallicity, population II-I sets in, giving contributions to the SFR of 2 or 3 orders of magnitude higher than the population III one.
- Given the very local character of metal pollution, it is highly probable that population III stars can be formed in isolated regions also at lower redshift.
- The average contribution to the SFR for different Z_{crit} is, anyway, distinguishable with differences reaching about one order of magnitude.
- The filling factors for different Z_{crit} are very different and span more than a factor 7, among the four cases.

Chapter 8

A model for the IMF

*“Da quel punto
depende il cielo e tutta la natura.
Mira quel cerchio che più li è congiunto,
e sappi che 'l suo muovere è sì tosto
per l'affocato amore ond'elli è punto.”*

DANTE, PARADISO

The IMF is a crucial quantity for any stellar system, as it describes the mass distribution of its components. It can be regarded as sort of “initial conditions” of a stellar system, determining its overall properties and time evolution (luminosity, colour, chemical enrichment, etc.).

As we already said (see section 3.2), we do not know its exact form at high redshift, but we have much clearer information at low redshift, in the local Universe, because of the many observational evidences (see Figure 3.1).

In this chapter, a model describing the determination of the observed initial mass function from turbulent cloud fragmentation will be presented. Our model relies on the assumption that star formation is triggered by turbulent dissipation which allows for fragmentation below the Jeans mass.

An analytic expression relating the energy spectrum of turbulence, $E(k) \propto k^{-\alpha}$, to the resulting shape of the IMF, $\phi(M)$, will be found: the high mass end has a predicted behaviour $\phi(M) \propto M^{-3+\alpha/3}$, while the peak position depends on dissipation decay at small masses.

Adopting a Kolmogorov spectrum corrected for intermittency effects, $E(k) \propto k^{-1.83}$, the tail of the IMF goes like $\phi(M) \propto M^{-2.39}$, with a peak arising at about $0.4 M_{\odot}$. A pure shock spectrum implies the scaling $\phi(M) \propto M^{-2.33}$, instead a magnetic field dominated spectrum gives the scaling $\phi(M) \propto M^{-2.5}$.

8.1 Properties of the star forming regions

Given its relevance for our aims, in this section we will deal more in detail with the role of the IMF, previously only mentioned (section 3.2).

Many different studies give nice overviews of the IMF and its connection with other physical processes, but a true understanding remains still elusive. Some directions of research have involved probabilistic or geometrical approaches (Auluck and Kothari, 1954; Larson, 1992; Elmegreen, 1997), fragmentation models based on temperature, density, opacity and molecular weight variations (Takebe et al., 1962; Yoshii and Saio, 1985; Kanjilal and Basu, 1992), cloud internal motions (Arny, 1971), with or without magnetic fields (Padoan, 1995), heat balance (Silk, 1977), Lagrangian formalism joined to space parameter explorations (Ferrini et al., 1983, 1990), semi-empirical calculations (Adams and Fatuzzo, 1996), random supersonic flows (Kolesnik and Ogul'Chanskii, 1990; Padoan and Nordlund, 2002), accretion (Bate and Bonnell, 2005).

Broadly speaking, the process of star formation is commonly supposed to happen in dense and cold regions of the interstellar medium, like molecular clouds. These sites are rich in molecules (e.g., H_2 , CO , H_2O , NH_3 , et cetera), have sizes between few parsecs and hundreds of parsecs (giant molecular clouds), typical number densities of $\sim 10^3 - 10^5 \text{ cm}^{-3}$ and temperatures $T \sim 10 \text{ K} - 50 \text{ K}$. Smaller fragments within molecular clouds are detected and their dimensions are inferred to be of the order of 10^{-2} pc , with masses of $\sim 0.1 M_\odot$. There are even smaller substructures reaching $\sim 0.01 M_\odot$, but they appear to be completely gravitationally unbound (Langer et al., 1995). Velocity gradients are observed (Pety and Falgarone, 2003) and they are interpreted as shear flows (as in the dissipative regions of subsonic turbulence) or as low Mach number supersonic shocks (Smith et al., 2000; Elmegreen and Scalo, 2004).

Analyses of spatial clustering properties of pre-main sequence stars exhibit self-similar or fractal clustering on the largest scales, but there is a clear break at a scale of $\sim 0.04 \text{ pc}$, corresponding to a mass-scale of $\sim 0.5 M_\odot$ (Gomez et al., 1993; Larson, 1995; Simon, 1997). This has been interpreted as a transition from a large-scale chaotic, turbulent regime to a more regular coherent regime.

Indeed, the ISM seems to be very turbulent, also in locations not associated with stellar activity.

The first empirical evidences of a turbulent ISM date back to Scheuer (1968), who realized how every small fluctuation of the ISM mean density can cause diffraction of radio waves at scales of 0.01 – 0.1 pc and frequencies of 100 MHz. In this way he justified the scintillation features observed in pulsar signals. For a statistical description of the ISM, Lee and Jokipii (1976) proposed to adopt a turbulent Kolmogorov spectrum. Later, more indirect probes of turbulence were found.

Studies of cosmic ray transport established the existence of ISM irregularities on scales much smaller than 1 pc (up to some AU). However, it is not clear yet whether the turbulence that scatters cosmic rays is part of an energy cascade from larger scales or is only local (Scalo and Elmegreen, 2004, and references therein).

Different analyses are based on studies of abundance variations of field stars, cluster stars and diffuse interstellar medium. These usually suggest very small metallicity fluctuations, as the metallicity gradients are washed out by efficient turbulent mixing, at scales ranging between 1 pc and 100 pc (Edmunds, 1975; Friel and Boesgaard, 1992, for example), or by intermittency effects (Elmegreen and Scalo, 2004).

The last indirect way to probe interstellar turbulence is through its effects on chemistry, like molecule formation and destruction. From such investigations, it seems that turbulent diffusion can heavily affect many chemical species produced in molecular clouds, mainly carbon-bearing species and H₂-based intermediaries (Xie et al., 1995). With the help of hydrodynamical turbulence simulations, including the relevant chemical network (Pavlovski et al., 2002), it has been possible to recover the pattern of shells, filaments, clumps and diffuse gas typical of the ISM and at the same time to give estimates for the mixing time of abundances: they turned out to be fairly uniform after only 100 years.

An example of observed turbulence in the interstellar medium is given in Figure 8.1, where a map of the Large Magellanic Cloud (LMC) with its evident turbulent patterns is showed.

The global picture emerging from these numerous studies is that of an interstellar medium (including molecular clouds and their substructures) whose behaviour is strongly dominated by dynamical turbulent motions. Thus, star formation seems to happen in clumpy, turbulent regions which are just transient objects forming, stretching, distorting and dissolving in the large turbulent flow. Quasi-hydrostatic configurations cannot be

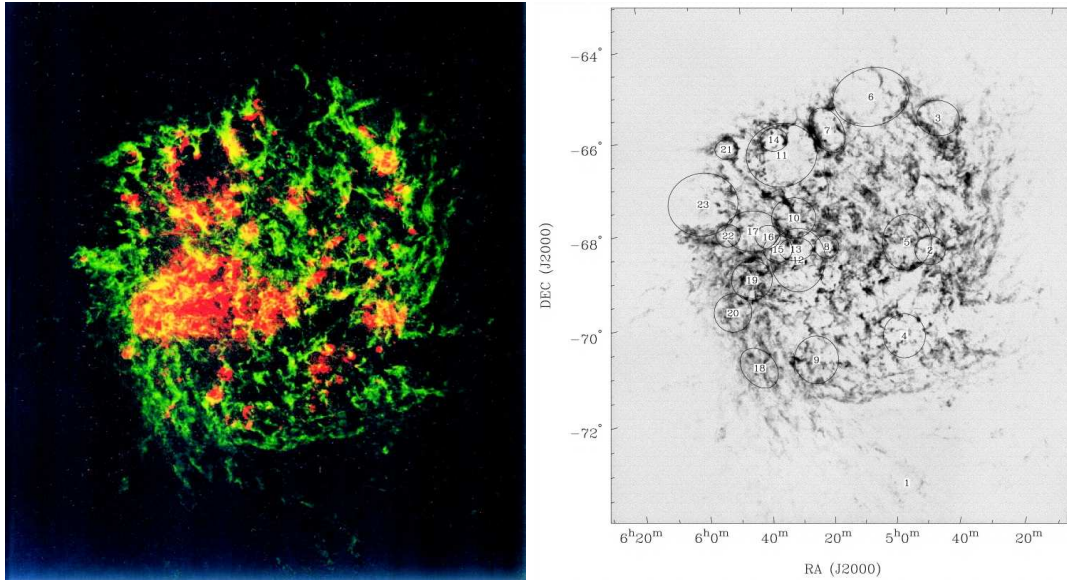


Figure 8.1: Left panel: peak 21 cm neutral H surface brightness map (green) with overlaid H α image (the continuum subtracted) of the Large Magellanic Cloud (red). Right panel: position of supergiant shells (diameter larger than 360 pc) overlaid as ellipses on peak 21 cm neutral H surface brightness map. Many smaller arcs, bubbles and shells are evident. Pictures taken from Kim et al. (1999).

produced from turbulent fluctuations and pressure equilibrium is irrelevant for cloud confinement or for their substructures, up to scale $\sim 10^{-2}$ pc (Ballesteros-Paredes et al., 1999). The loss of turbulent energy and density substructure may trigger star formation (Elmegreen, 1999) and may lead to the idea that the stellar initial mass function reflects the state of the turbulent medium from which it originates.

In the next, we will show how it is possible to link the observed IMF with the features of the ambient medium and how the turbulent initial state leaves its imprint on the final outcome. In fact, we will present a statistical prediction whose main characteristic is the dependence on the energy spectral distribution of turbulent motions in star forming regions and we will write an easy analytical formula which is in very good agreement with the current observational data.

In particular, in section 8.2, we discuss the interplay between turbulence and gravitational instability; in section 8.3, we overview the statistical properties of turbulence (section 8.3.1) and show its connections with the IMF (section 8.3.2). We conclude discussing our findings in section 8.4.

In appendix E, we revisit Jeans's theory considering viscosity effects and their impact on

the fragmentation of gas clouds.

8.2 Turbulence and fragmentation processes

The presence of turbulence as the probably dominant process in the ISM (Elmegreen and Scalo, 2004; Scalo and Elmegreen, 2004; Mac Low and Klessen, 2004; Burkert, 2006) introduces hard complications in the study of structure formation, because of the lack of a satisfying basic understanding of this phenomenon in connection to gravitational instability. This topic and its impact on structure formation and cloud fragmentation has been commonly discussed since the 1940s (see the early works by Weizsäcker, 1943; Chandrasekhar, 1949; Weizsäcker, 1951; Chandrasekhar, 1951a,b; Sasao, 1973), but the very first study on the gravitational instability of gas nebulae was made by Jeans (1902). According to his arguments (see also section 2.2.1), a spherical nebula can be gravitationally stable only if its dimensions do not exceed a critical value, denoted as Jeans length $\lambda_J \approx c_s/\sqrt{G\rho}$, with c_s sound speed, G gravitational constant and ρ average density of the medium. The collapsing wave-numbers \mathbf{k} are only those whose modulus k is below (2.18)

$$k_J \equiv 2 \frac{\sqrt{\pi G \rho}}{c_s}. \quad (8.1)$$

In correspondence of the Jeans length, it is possible to define the Jeans mass as (2.20)

$$M_J = \frac{4}{3}\pi\rho \left(\frac{\lambda_J}{2}\right)^3 \approx \frac{\pi}{6} \frac{c_s^3}{G^{3/2}\rho^{1/2}}. \quad (8.2)$$

When the mass is larger than the above critical value the gravitational force is stronger than the gas pressure force and the nebula collapses. Jeans's treatment considers only gravity and gas pressure, but also other physical phenomena can be involved in the process. Mestel (1965), Mouschovias (1976a,b), and Mouschovias and Spitzer (1976) calculated the equivalent of M_J in the presence of a magnetic field

$$M_{crit,B} = \frac{c_1^3 5^{3/2}}{48\pi^2} \frac{B^3}{G^{3/2}\rho^2} \quad (8.3)$$

where $c_1 \simeq 0.53$, and B is the strength of the magnetic field.

Nowadays it seems that star forming regions in the local Universe are dominated by turbulence, while at high redshift its role, as well as the one of magnetic fields, is still unclear. So, it is worth exploring what the critical wave-number in the presence

of viscosity, ν , is. Also in this case it is possible, via the Navier-Stokes equations (see appendix E), to find a critical dissipation wave-number (and an equivalent length with the same meaning as the Jeans length) given by

$$k_d \equiv 2 \left(\frac{\pi G \rho}{\nu^2} \right)^{1/4} \quad (8.4)$$

and to define the corresponding “collapsing dissipation mass”, M_d , as the minimum mass needed for the gas to collapse, in the presence of viscosity. This means that turbulent gas fragments with masses smaller than M_d are expected to be gravitationally unbound.

For number densities of $\sim 10^3 - 10^4 \text{ cm}^{-3}$ and an average, global viscosity of the cloud $\nu \sim 10^{16} \text{ cm}^2 \text{ s}^{-1}$ (Elmegreen and Scalo, 2004), it is found $k_d \sim (2 - 4) \cdot 10^{-15} \text{ cm}^{-1}$.

The scales associated with k_d (of the order of $\sim 10^{15} \text{ cm}$, the size of accretion disks around protostars) are much smaller than the Jeans length (for the same densities and temperatures, one gets $c_s \sim 10^5 \text{ cm/s}$ and $\lambda_J \sim 10^{18} - 10^{19} \text{ cm}$, typical sizes of molecular clouds), but the dissipation time is comparable to the free-fall time (see appendix E).

This means that, if turbulence is the leading process of the ISM dynamics, we expect to find – and they are found – gas clouds hosting much smaller fragments, because the limiting scale due to viscous dissipation is well below the usual Jeans length (by three to four orders of magnitude).

Such considerations are extremely helpful for our general understanding of the fragmentation process and will lead our investigations in the next sections.

8.3 Turbulence and IMF

Strictly speaking, turbulence arises from the non-linear, advection term, $(\mathbf{u} \cdot \nabla)\mathbf{u}$, and the dissipative term, $\nu \nabla^2 \mathbf{u}$, in the equations of motion (Navier-Stokes equations) for a fluid medium whose velocity field is \mathbf{u} and viscosity is ν .

The (adimensional) Reynolds number quantifies the effects of viscosity with respect to the “inertia forces” and can be estimated as:

$$R \equiv \frac{\| (\mathbf{u} \cdot \nabla)\mathbf{u} \|}{\| \nu \nabla^2 \mathbf{u} \|} \sim \frac{ul}{\nu}, \quad (8.5)$$

where l is the scale and u the modulus of turbulent velocity at that scale. The characteristic dimension of the system will be denoted by l_0 and the initial (large-scale) Reynolds number will be $R_0 = u_0 l_0 / \nu$. When R tends to zero the system is viscosity

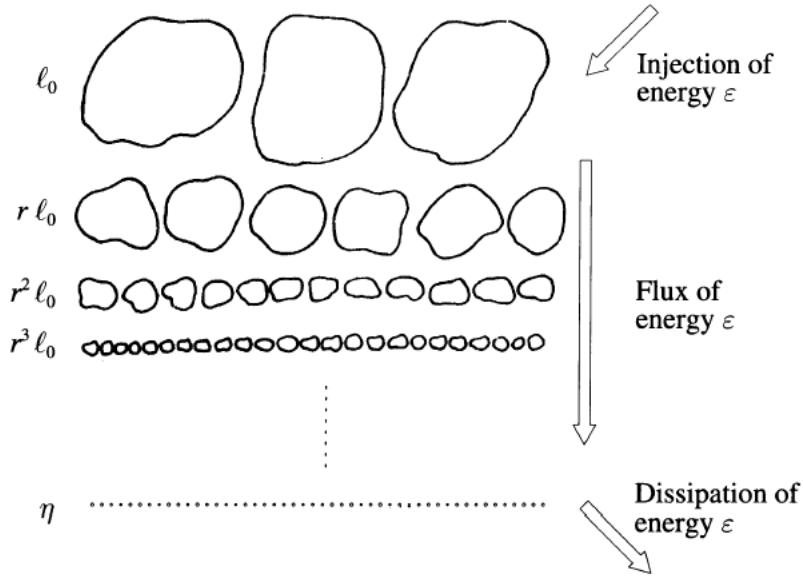


Figure 8.2: Schematic representation of the energy cascade process: energy is transferred from the largest (l_0) to the smallest (η , in the scheme correspond to l_d in the text) scales cascading through the intermediate scales. At each step, n , the typical scale $r^n l_0$ is smaller than the previous one by a fraction r . After Frisch (1996).

dominated, while when $R \gg 1$ the advection term dominates and the influence of viscous forces is negligible. The scale for which $R = 1$ is called dissipation scale, l_d , and $k_d \equiv 1/l_d$ is the dissipation wave-number in the Fourier space.

In the cool ISM, it is now well established that the Reynolds number assumes values between 10^5 and 10^7 and that the injection scale l_0 is $\sim 10^2$ pc, ranging from several tens of parsecs (Armstrong et al., 1995) up to 500 pc (Cordes et al., 1985).

We expect that, if a statistical equilibrium among the different turbulent modes exists, it will be at scales $l_d \ll l \ll l_0$, or $k_0 \ll k \ll k_d$ (inertial range) and the transport of energy will become independent of the exact details of viscosity forces. According to Kolmogorov’s hypotheses of similarity (Kolmogorov, 1941a,b), the viscous dissipation at small scales is fed by inertial transfer of energy at larger scales. This is often referred to as “disorder hypothesis” (Weizsäcker, 1948). The whole process is called “cascade process” (Onsager, 1945) and a schematic view is presented in Figure 8.2.

In the Fourier space, this means requiring that different Fourier modes are independent. From the above hypothesis it follows that du^2/dt is constant and $l \propto u^3$. Thus equation

(8.5) gives

$$R = \left(\frac{l}{l_d}\right)^{4/3} = \left(\frac{k}{k_d}\right)^{-4/3}. \quad (8.6)$$

From dimensional analyses, it follows that $l_d \approx (\nu^3/\bar{\epsilon})^{1/4}$, where ν is viscosity and $\bar{\epsilon}$ is the energy transfer rate, i.e. the energy transferred from large scales to smaller scales per unit time and divided by the total mass of the system; its dimensions are $[L^2T^{-3}]$. A quantitative analysis for a typical cloud having $R \sim 10^7$ and $l_0 \sim 10^2$ pc leads to $l_d \sim 10^{15}$ cm, similar to what we expect from equation (8.4). Such apparent “coincidence” suggests that the interplay between gravity and viscosity is very tight, as the structures collapsing because of gravitational instability in viscous media (see again appendix E) turn out to be also the most dissipative structures.

Despite these idealizations, in reality turbulence is not uniformly distributed, but shows clear spatial and temporal intermittency effects: regions particularly active coexist with regions completely inactive. In the following, we will consider also this problem and show how to deal with it, statistically.

We will clarify the basics of the statistical treatment of turbulence in section 8.3.1 and we will show the connections with the IMF in section 8.3.2.

8.3.1 Treatment of turbulence

Studies of turbulence based on a statistical approach started with Taylor (1921) Taylor (1935), von Kármán (1937), von Kármán and T. Howarth (1938), Millionshtchikov (1939), Obukhov (1941), Kolmogorov (1941a,b). These authors put the bases for the standard mathematical formalism which is commonly adopted.

Let us define the velocity correlation tensor and the energy tensor.

The velocity correlation tensor correlates different turbulent velocity components – say the i -th and the j -th – at two different points \mathbf{x} and $\mathbf{x} + \mathbf{r}$ according to

$$R_{ij}(\mathbf{r}) \equiv \overline{u_i(\mathbf{x})u_j(\mathbf{x} + \mathbf{r})}, \quad (8.7)$$

where i and j assume values from 1 to 3 and the over-line indicates the time¹ average.

The energy tensor is the tensor whose components are the Fourier transforms of $R_{ij}(\mathbf{r})$:

$$\Phi_{ij}(\mathbf{k}) \equiv \frac{1}{(2\pi)^3} \int R_{ij}(\mathbf{r}) e^{-i\mathbf{k}\cdot\mathbf{r}} d^3r, \quad (8.8)$$

¹ In virtue of the ergodic hypothesis, time averages are equivalent to space averages.

the integral being extended over the whole space.

To specify the two tensors, further assumptions are required: we will assume *homogeneity and isotropy* of turbulence.

Mathematically, homogeneity and isotropy of the tensorial components $R_{ij}(\mathbf{r})$ and $\Phi_{ij}(\mathbf{k})$ means that, at *each point* of the turbulent field, they must not depend on any direction, or, in other words, they can take, as *only argument*, $r = \|\mathbf{r}\|$ and $k = \|\mathbf{k}\|$, respectively. Under this assumption, they can be written in the following way (von Kármán and T. Howarth, 1938):

$$R_{ij}(r) = u^2 \left[\frac{f(r) - g(r)}{r^2} r_i r_j + g(r) \delta_{ij} \right] \quad (8.9)$$

$$\Phi_{ij}(k) = \frac{E(k)}{4\pi k^4} (k^2 \delta_{ij} - k_i k_j) \quad (8.10)$$

with δ_{ij} Kronecker's delta, u^2 mean square velocity, $g(r) = f(r) + \frac{1}{2} r f'(r)$ because of the continuity equation, $f(r)$ and $E(k)$ scalar functions. The former function is related to the correlation component parallel to the motion of the fluid and must be determined from experiments; the latter is related to the turbulent kinetic energy at any given point \mathbf{x} . Taking the trace of $R_{ij}(r)$ and $\Phi_{ij}(k)$,

$$\frac{3}{2} u^2 = \frac{1}{2} \overline{u_i(\mathbf{x}) u_i(\mathbf{x})} = \frac{1}{2} R_{ii}(0) = \frac{1}{2} \int \Phi_{ii}(k) d^3 k = \int E(k) dk. \quad (8.11)$$

Because of this relation, $E(k)$ is called energy spectrum. We stress that homogeneity allows us to specify the two tensors with only one scalar function in real space and Fourier space, respectively. In addition, for the evolution of statistical properties of turbulence, the general dynamics of decay predicts a change of total energy described by (Batchelor, 1953):

$$\frac{d}{dt} \frac{3}{2} u^2 = \frac{d}{dt} \frac{1}{2} \overline{u_i(\mathbf{x}) u_i(\mathbf{x})} = -2\nu \int E(k) k^2 dk \quad (8.12)$$

and implies an energy loss proportional to the viscosity and dependent on the energy spectrum. Relation (8.12) does not rely upon any particular assumption, it just follows from homogeneity and the Navier-Stokes equations. It tells us that viscosity is the main source of dissipation, while pressure and inertia forces redistribute energy, but conserve it. We also notice that $E(k)$ is defined in the unidimensional wave-space – see equation (8.11) – so, *a fortiori*, in relation (8.12), the k^2 has a physically very relevant meaning, since it reflects the Laplacian of the viscosity term in the Navier-Stokes equations. The

energy dissipated per unit time and per wave-number interval is

$$\varepsilon(k) \equiv -\frac{d^2}{dt dk} \frac{3}{2} u^2 = 2\nu E(k) k^2. \quad (8.13)$$

This means that the dissipation is overall determined by the energy dispersion (flux) around the origin of wave-numbers and this process is faster and more efficient for small scales than for large scales, when the energy spectrum $E(k)$ has a slope greater than -2 . Other useful quantities are the structure functions defined as

$$S_p(\mathbf{r}) \equiv \overline{\|\mathbf{u}(\mathbf{x}) - \mathbf{u}(\mathbf{x} + \mathbf{r})\|^p}. \quad (8.14)$$

For homogeneous turbulence, it is typically assumed

$$S_p(r) \sim r^{\zeta_p} \quad (8.15)$$

where the scaling ζ_p depends on the order p of the structure function considered. In particular, S_2 has an important physical meaning, as it is directly connected to the energy spectrum by

$$S_2(r) = 4 \int E(k) \left(1 - \frac{\sin kr}{kr}\right) dk \sim r^{\zeta_2}. \quad (8.16)$$

If the spectrum can be written as $E(k) \propto k^{-\alpha}$,

$$\alpha = 1 + \zeta_2. \quad (8.17)$$

Kolmogorov's model (Kolmogorov, 1941a,b) predicts the energy spectrum to be $E(k) = C(\bar{\varepsilon})^{2/3} k^{-5/3}$, where C is a constant of the order of unity² and $\bar{\varepsilon}$ the energy transfer rate; the corresponding energy dissipation per unit time and wave-number interval, $\varepsilon(k)$, is proportional to $k^{1/3}$. The scaling for the structure functions is $\zeta_p = p/3$. The measured values are consistent with the expectations for low p and with the exact result $\zeta_3 = 1$ (von Kármán and T. Howarth, 1938; Frisch, 1996), but exhibit non simple scaling at $p > 3$. That is due to intermittency effects, which determine departures from homogeneity and isotropy (Falgarone and Phillips, 1990; Rickett and Coles, 2004; Falgarone et al., 2005), so appropriate corrections must be taken into account. In case of shocks (which can easily arise in a supersonic medium), $E(k) \propto k^{-2}$ and $\varepsilon(k)$ is constant, independently of the wave-number.

In the ISM and in molecular clouds, supersonic events are detected, but, globally, the

² Normalization: $C = 3/2$ (Kolmogorov, 1941b) (nowadays estimated $C \simeq 1.4$).

Table 8.1: Power spectrum slope, β , and derived energy spectrum slope, $\alpha = \beta/2$, according to measurements by different authors. In the header, $P(k)$ is the power spectrum and $E(k)$ is the energy spectrum. A Kolmogorov energy spectrum predicts $\alpha = 5/3 \simeq 1.67$.

References	$P(k) \propto k^{-\beta}$	$E(k) \propto k^{-\alpha}$
Lovelace et al. (1970)	$\beta \simeq 4$	$\alpha \simeq 2$
Pynzar et al. (1975)	$3.4 \leq \beta \leq 4.0$	$1.7 \leq \alpha \leq 2$
Rickett (1977)	$\beta > 3.5$	$\alpha > 1.75$
Armstrong and Rickett (1981)	$3.6 \leq \beta \leq 3.9$	$1.8 \leq \alpha \leq 1.95$
Armstrong et al. (1981)	$\beta = 3.7 \pm 0.6$	$\alpha = 1.9 \pm 0.3$
Cordes et al. (1985)	$\beta = 3.63 \pm 0.20$	$\alpha = 1.82 \pm 0.10$
Wilkinson et al. (1988)	$\beta = 3.88 \pm 0.05$	$\alpha = 1.94 \pm 0.03$
Spangler and Gwinn (1990)	$11/3 \leq \beta \leq 4$	$5/3 \leq \alpha \leq 2$
Bhat et al. (1999)	$11/3 \leq \beta \leq 3.8$	$5/3 \leq \alpha \leq 1.9$
Stinebring et al. (2000)	$3.5 < \beta < 3.7$	$1.75 < \alpha < 1.85$
Shishov et al. (2003)	$\beta = 3.5 \pm 0.05$	$\alpha = 1.75 \pm 0.03$

observed power spectrum (squared modulus of the energy spectrum) seems to be much more compatible with a Kolmogorov one: some observational values for the slope of the power and energy spectra are summarized in Table 8.1. The values commonly obtained are in agreement with a cascade slope accounting for intermittency effects.

Indeed, fractal energy cascade models in fully developed homogeneous turbulence (She and Lévéque, 1994; She and Waymire, 1995) correct the Kolmogorov spectrum by some percents, according to a formula which, maintaining the same formalism as She and Lévéque (1994)'s, we re-write as

$$\zeta_p = \frac{p}{9} + C_0 \left[1 - \left(1 - \frac{2}{3C_0} \right)^{p/3} \right] \quad (8.18)$$

being $C_0 = 3 - D$ the co-dimension, and D the fractal dimension³ of the most dissipative structures. It refers to a cascade model based on a 2-possibility Poisson distribution for the intermittent transfer of turbulent energy as a function of the scale. In our scenario, star formation events in clouds are rare, random phenomena triggered by turbulence. Therefore the Poisson statistics seems particularly well suited to describe them.

For singular, point-like dissipation, $D = 0$, $C_0 = 3$, and, using equation (8.17), $\alpha \simeq 1.685$,

³ The fractal dimension, D , of a set of replicable, self-similar structures (also called similarity dimension) is defined via the limiting process

$$D \equiv \frac{\ln N}{\ln(1/r)} = \lim_{k \rightarrow \infty} \frac{\ln N^k}{\ln(1/r)^k} \quad (8.19)$$

where N is the number of substructures at each replication level, $1/r$ is the similarity ratio and k is the number of replications. The fractal dimension is always larger or equal to the usual topological dimension (Mandelbrot, 1982, chapter 6).

very close to Komogorov's $5/3$. Dissipation happening in filamentary vortices, $D = 1$, would lead to $C_0 = 2$, and $\alpha \simeq 1.696$, less than 2% larger than Kolmogorov's expectations. For ribbon or sheet-like dissipative structures, $D = 2$, $C_0 = 1$, and $\alpha \simeq 1.741$, i.e. 4% larger than in the Kolmogorov case.

For the diffuse ISM, $D \simeq 1.4$ and $\alpha \simeq 1.705$. Conversely, detailed measurements in the most dissipative regions suggest $D \simeq 2.3$ (Elmegreen and Elmegreen, 2001; Chappell and Scalo, 2001) and $\alpha \simeq 1.830$. This fractal dimension implies a slope almost 10% bigger than $5/3$ and corresponds to roughly disordered, sheet-like ("flake") processes (Mandelbrot, 1982, chapters 2, 28, 32, for example).

Such formalism allows for a description of statistical properties of turbulence and a link to observable quantities, namely the energy spectrum, its slope and the fractal dimension of the turbulent system considered.

8.3.2 Connection to the IMF

What we want to do, now, is to consider the effects of turbulence on the scenario of structure formation and check their impact on the shaping of the initial mass function. According to equation (8.13), viscosity is the main source of energy dissipation in a turbulent environment. In order to form any object, it is fundamental that the gas condenses and this happens only if its kinetic energy is lost. In fact, star formation is supposed to take place through collapse of overdense gas and accretion disks, where the energy is dissipated by friction and viscosity. This partially heats up the surrounding regions, partially allows for condensation towards the central part of the disk. So, the more energy gets dissipated the higher the probability to form stars. Therefore, it is possible to assume that structure formation is regulated by the energy dissipation in the turbulent flow. In a mathematical form this translates into the assumption that the total mass of forming stars, m_* , follows

$$dm_* \propto \varepsilon(k)dk. \quad (8.20)$$

This is consistent with observational and numerical studies of the ISM which point out the importance of the loss of turbulent energy and its probable connection with the IMF (Ballesteros-Paredes et al., 1999; Elmegreen, 1999) .

In this picture, turbulence rules the collapse produced in the dense and dissipative regions,

which are supposed to be transient entities, neither confined by thermal or inter-cloud pressure, nor resulting from gravitational instabilities. The ability of non-gravitating turbulence to fragment the ISM and the giant molecular clouds down to stellar masses (or below) introduces the concept of “turbulent fragmentation” (Kolesnik and Ogul’Chanskii, 1990). Then, lumps and clouds are supposed to be formed, distorted, dissolved or disrupted by turbulent activities and the hierarchy of structures.

Hereafter, we derive an expression for the initial mass distribution assuming the validity of equation (8.20).

The number fraction of objects formed at a given mass scale ($\sim k^{-3}$) can be written as

$$df \propto \frac{\varepsilon(k)}{k^{-3}} dk \quad (8.21)$$

and normalized via

$$\frac{df}{dk} = \frac{\varepsilon(k)k^3}{\int \varepsilon(k)k^3 dk} = \frac{E(k)k^5}{\int E(k)k^5 dk}. \quad (8.22)$$

The calculation of this quantity requires a specification of an energy power spectrum $E(k)$. To generalize, we will write $E(k) \propto k^{-\alpha}$, defined in the range between $k_0 = 1/l_0$ and $k_d = 1/l_d$, usually with $k_d \gg k_0$. Integrating the denominator in equation (8.22), one gets

$$\frac{df}{dk} = \frac{-\alpha + 6}{k_d} \left(\frac{k}{k_d} \right)^{-\alpha+5} \frac{1}{1 - (k_0/k_d)^{-\alpha+6}} \quad (8.23)$$

with the asymptotic relation

$$\frac{df}{dk} \underset{k_d \gg k_0}{\approx} \frac{-\alpha + 6}{k_d} \left(\frac{k}{k_d} \right)^{-\alpha+5} \quad (8.24)$$

valid for $(-\alpha + 6) > 0$. The ratio k_0/k_d is related to the Reynolds number through (8.6). To derive $\phi(M)$, equations (8.23) and (8.24) need to be written as a function of the mass. This can be done by differentiating the usual relation

$$M = s\rho k^{-3}, \quad (8.25)$$

with s a numeric factor depending on the shape of the fragments and the exact definition for the length-scale, l (e.g., for $l \equiv 1/k$ and spherical symmetry, it holds $s = 4\pi/3$) and ρ the mean mass density of the medium. We get

$$\frac{df}{dM} = \frac{1}{|-3s\rho k^{-4}|} \frac{df}{dk} \quad (8.26)$$

and

$$\phi(M) = \frac{-\alpha + 6}{3M_d} \left(\frac{M}{M_d} \right)^{-3+\alpha/3} \frac{1}{1 - (M_0/M_d)^{-2+\alpha/3}} \quad (8.27)$$

with M_0 and M_d the masses at the scales l_0 and l_d , respectively. Exploiting relations (8.5) and (8.6), we obtain

$$\phi(M) = \frac{-\alpha + 6}{3M_d} \left(\frac{M}{M_d} \right)^{-3+\alpha/3} \frac{1}{1 - R_0^{-3(6-\alpha)/4}}. \quad (8.28)$$

and, asymptotically,

$$\phi(M) \stackrel{R_0 \gg 1}{\sim} \frac{-\alpha + 6}{3M_d} \left(\frac{M}{M_d} \right)^{-3+\alpha/3}. \quad (8.29)$$

In these formulæ, the factors 3 at the denominator and $1/3$ in the exponent come from the scaling of M as the cube of length, while M_d is the reference mass. In the ISM there is evidence for small clumps down to scales of $(2 - 3) \cdot 10^{-2}$ pc, containing typical masses between about $0.1 M_\odot$ and $0.3 M_\odot$ (Gomez et al., 1993; Langer et al., 1995; Elmegreen and Scalo, 2004). As already mentioned, much smaller fragments exist, but they are gravitationally unbound by a large factor (Langer et al., 1995). In light of our considerations on formula (8.4), the minimum mass for collapse, in the presence of viscosity (the collapsing dissipation mass), must be of the same order of the smallest bound clumps, therefore, we guess $M_d \sim 0.2 M_\odot$.

So far, we have not considered the decay of the energy spectrum while the star formation process takes place, but this can affect the resulting IMF. In the following, we will discuss this issue. For large wave-numbers ($k \approx k_d$) leading the global decay, the equations of motion are determined by viscous dissipation:

$$\frac{\partial \mathbf{u}}{\partial t} \simeq \nu \nabla^2 \mathbf{u}. \quad (8.30)$$

Solving in the Fourier space, equation (8.30) implies an exponential time decay of the velocity field $\sim e^{-\nu k^2 t}$ and of the power spectrum

$$E(k, t) = E(k, 0) e^{-2\nu k^2 t} \quad (8.31)$$

because of the relations (8.8 - 8.11). The time t is the life-time of the turbulent system and $E(k, 0)$ is the initial energy spectrum (Kolmogorov spectrum, shock spectrum, intermittent spectrum etc., depending on the particular situation).

Equation (8.22) assumes the form

$$\frac{df}{dk} = \frac{E(k, 0) k^5 e^{-2\nu k^2 t}}{\int E(k, 0) k^5 e^{-2\nu k^2 t} dk} \quad (8.32)$$

and, as a consequence,

$$\phi(M) = \frac{(M/M_d)^{-3+\alpha/3} e^{-2\nu k_d^2 t (M/M_d)^{-2/3}}}{M_d \int x^{-3+\alpha/3} e^{-2\nu k_d^2 t x^{-2/3}} dx} \quad (8.33)$$

with $x = M/M_d$ integration variable. The exponential cut-off influences small mass-scales and generates a peak proportional to M_d ,

$$M_{peak} = \left(\frac{4\nu k_d^2 t}{9 - \alpha} \right)^{3/2} M_d. \quad (8.34)$$

In the limit of large mass-scales ($M \gg M_{peak}$), the exponential factor approaches unity asymptotically and the foreseen power law tail $-3 + \alpha/3$ of equations (8.27) and (8.28) is recovered.

In our calculations we use $\alpha = 1.83$, because this is the value obtained including intermittency corrections to the Kolmogorov energy spectrum, for the typical fractal dimension observed in dissipative regions of molecular clouds ($D = 2.3$). The value adopted for viscosity is $\nu = 10^{16} \text{ cm}^2 \text{ s}^{-1}$ (Elmegreen and Scalo, 2004), compatible with a cloud of temperature $\sim 50 \text{ K}$ and average number density $\sim 10^4 \text{ cm}^{-3}$. The most clumpy and dissipating regions are suggested to be at scales of order of several tens of AU (Armstrong et al., 1995). Moreover, it seems that formation of protostars happens on very viscous accretion disks, whose size is comparable with the one of our Solar System. This is consistent with the outcome of gravitational instability in dissipative media – see equation (8.4) and appendix E – as well, so $k_d = 3 \cdot 10^{-15} \text{ cm}^{-1}$ and $M_d = 0.2 M_\odot$. The turbulence life-time is assumed to be $t = 10^6 \text{ yr}$, as in the solar neighborhood almost all the molecular clouds appear to host star formation activity and to have an age smaller than few Myrs (Burkert, 2006).

A plot showing the behaviour of $\phi(M)$ is presented in Figure 8.3. The peak is located at $M_{peak} \simeq 1.989 M_d \simeq 0.398 M_\odot$. The power-law trend of the tail is $\phi(M) \sim M^{-2.39}$ and it is followed down to about $1 M_\odot$, where the curve starts deviating towards the peak. The overall behaviour is $\phi(M) \propto M^{-2.39} e^{-5.67(M/M_d)^{-2/3}}$. In the smaller inset, we also plot the predictions for an IMF computed with a shock index, $\alpha = 2$, and a pure Kolmogorov index, $\alpha = 5/3$, which are very similar.

The results are fully consistent with the observed flattening at the low mass end and the observed fall-off below $0.1 M_\odot$ (Basri and Marcy, 1997).

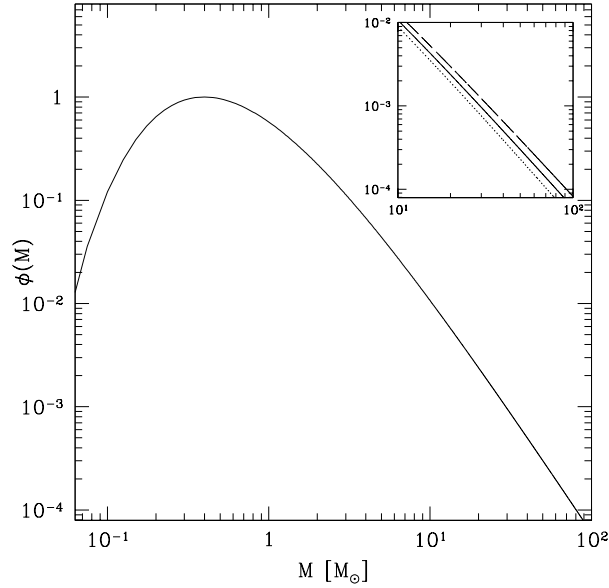


Figure 8.3: Predicted initial mass function, normalized to its peak value, for a turbulent cloud having $\alpha = 1.83$, $\nu = 10^{16} \text{ cm}^2\text{s}^{-1}$, $k_d = 3 \cdot 10^{-15} \text{ cm}^{-1}$, $M_d = 0.2 M_\odot$ and $t = 10^6 \text{ yr}$. The peak is located at $M_{peak} \simeq 1.989 M_d \simeq 0.398 M_\odot$ and the overall behaviour of the curve is $\phi(M) \propto M^{-2.39} e^{-5.67(M/M_d)^{-2/3}}$. In the inset, a zoom of the high mass end is plotted for the three cases: $\alpha = 1.83$ and $\phi(M) \sim M^{-2.39}$ (solid line); $\alpha = 2$ and $\phi(M) \sim M^{-2.33}$ (dashed line); $\alpha = 5/3$ and $\phi(M) \sim M^{-2.44}$ (dotted line).

8.4 Discussion

The derivation of (8.27), (8.28) and (8.29) holds for $(-\alpha + 6) > 0$ and relies on equations (8.12) and (8.13), representing the amount of energy dissipated by viscosity under quite general conditions (the only hypothesis is homogeneity). The derivation of (8.33) extends the same treatment in order to consider also the time decay of small scales during the turbulent process.

There is no dependence of $\phi(M)$ on the exact shape of the fragments and weak dependence on the global dimension of the turbulent system, as l_0 appears only via M_0 or R_0 in equations (8.27) and (8.28). Nonetheless, the IMF keeps memory of the triggering turbulent medium from which it is originated through α , the turbulence energy spectral index, which regulates the power law behaviour of the mass distribution. On the low mass end, the relevant physical quantity is the dissipation scale: lengths comparable to l_d get dissipated and decay, so do not have time to host star formation and at the same time the energy spectrum is suppressed (see appendix E). This produces a cut in the mass distribution due to the fact that after some million years (observed typical time-scales of

star forming regions) “small” scales are rarer and rarer.

We notice the peak scale, given by M_d , is a function of the environment, so, for star formation happening in molecular clouds with similar physical conditions, we expect to find the same IMF (and indeed it is what observations find locally). However, star formation episodes in extremely different situations will be described by a different IMF. For instance, in much denser regions (like in the high redshift Universe), where M_d is probably larger (assuming that l_d is roughly the same), we will expect to find an IMF shifted to higher masses: that would hidden a possible change of $\phi(M)$ with redshift.

As α is a sensitive quantity in our modeling, it is worth commenting on its determination. Kolmogorov’s classical value of $5/3$ provides a good description of turbulence in the inertial regime, under the hypothesis of incompressibility, so it has some problems in describing its intermittent character or the presence of shocks. In order to account for them, several models have been developed proposing corrections (like β -models, fractal models, random cascade models) and the value $5/3$ is substituted with slightly higher values between roughly ~ 1.7 and 2 . The pure Kolmogorov spectrum leads to $\phi(M) \sim M^{-2.44}$, at $M > M_{peak}$, but different possible values for α suggest:

- $\alpha = 5/3$: $\phi(M) \sim M^{-2.44}$
- $\alpha \simeq 1.7$: $\phi(M) \sim M^{-2.43}$
- $\alpha \simeq 1.8$: $\phi(M) \sim M^{-2.40}$
- $\alpha \simeq 1.9$: $\phi(M) \sim M^{-2.36}$
- $\alpha \simeq 2.0$: $\phi(M) \sim M^{-2.33}$.

Among the many sophisticated intermittency models, we have considered the one by She and L ev eque (1994): it is a cascade model based on a 2-possibility Poisson distribution for the intermittent transfer of turbulent energy as a function of the scale. In our scenario, star formation events in clouds are rare, random phenomena triggered by turbulence. Therefore the Poisson statistics is particularly well suited to describe them. The expected energy spectral index is $\alpha = 1.83$, which implies $\phi(M) \sim M^{-2.39}$, for the power law tail. A pure shock spectrum, $\alpha = 2$, would instead imply $\phi(M) \sim M^{-2.33}$.

Finally, we notice that often magnetic fields are observed: if they dominate the energetics, the power slope would be $\alpha = 3/2$ (Iroshnikov, 1963; Kraichnan, 1965) and the predicted

IMF would scale as $M^{-5/2}$.

The peak of the distribution is very weakly dependent on α , but depends linearly on M_d . We have estimated this value from the mass of the smallest observed gravitationally bound structures which are supposed to undergo star formation through an accretion disk. It has values of order of fractions of M_\odot .

8.5 Summary

To summarize, we have shown how it is possible to bind baryonic structure formation with the turbulent environment from which it is originated.

- Inclusion of viscosity – the source of turbulence – in the analysis of gravitational instability (detailed calculations are in appendix E) clarifies why fragmentation of gas clouds happens down to scales smaller than the usual Jeans length (which consider only gravity and gas pressure).
- Relying on that, we have derived analytical predictions for the shape of the IMF which are well in agreement with the observational data. Our modeling is based on the assumption that star formation is triggered by viscous dissipation and it links the turbulent energy spectrum of the medium with the slope of the IMF.
- In particular, we find that the spectral slope leads the behaviour of the mass function at the high mass end, while at the low mass end there is a cut-off due to the decay of small scales which have not got enough time to trigger star formation. The transition between the two regimes is marked by the “collapsing dissipation mass”, M_d : the minimum mass able to collapse in viscous environments.
- The final formula we get is

$$\phi(M) \sim (M/M_d)^{-3+\alpha/3} e^{-2\nu k_d^2 t (M/M_d)^{-2/3}} \quad (8.35)$$

where α , ν , k_d and t are respectively the energy spectral slope, the viscosity, the dissipation wave-number and the life-time of the turbulent cloud.

- Using reasonable numbers and intermittency corrections for the most dissipative regions, the energy spectrum scales like $E(k) \propto k^{-1.83}$ and the resulting IMF reads $\phi(M) \propto (M/M_d)^{-2.39} e^{-5.67(M/M_d)^{-2/3}}$, whose peak is at about twice the value of M_d .

Chapter 9

Conclusions

E quinci uscimmo a riveder le stelle

DANTE, INFERNO

In the present work a study of cosmological evolution of the Universe at very early times has been presented. We have investigated the main features of high-redshift structure formation and the transition from a primordial metal-free star formation regime to a more standard, metal-enriched one.

In order to do that, we have implemented non-equilibrium molecule formation, which is the only viable cooling mechanism in the early phases of the Universe, and metal fine-structure transition effects, as, once the medium is polluted, metals are a more efficient coolant (chapter 4).

The main results of our implementation are that H_2 molecule is the most relevant one in primordial environment. Other species, like HD, can influence high-redshift cosmic-gas clumping properties at level of 10% – 20%, while low-temperature metal cooling has a significant impact on the formation and evolution of cold objects (chapter 5).

We have applied our treatment to investigate the onset epoch of the cosmological star formation, the enrichment history of the intergalactic medium and its possible interplay with the transition from a primordial, massive star formation mode to a more standard one, performing high-resolution, three-dimensional, N-body/SPH simulations. Star formation prescriptions and feedback effects are considered – as “sub-grid” modeling – above a given gas density threshold.

For a correct estimate of the onset of star formation, high-density thresholds are necessary to follow the whole molecular cooling process, consisting of initial shock-heating,

subsequent isothermal phase and final cooling branch (chapter 6). Different values of the threshold and of the cosmological parameters can produce very different epochs of the onset of star formation: with a low-density threshold ($0.2 h^2 \text{ cm}^{-3}$) star formation starts at $z \sim 25 - 31$ (depending on the cosmology), while high-density threshold models ($135 h^2 \text{ cm}^{-3}$) predict a much later onset, $z \sim 12 - 16$ (depending on the cosmology). Performing primordial, rare, high-density region simulations within the high-density threshold model, we find that the local star formation can set in as early as $z \sim 48$.

In addition, we have performed numerical simulations with the switch for a double initial mass function, below and above a fixed critical metallicity Z_{crit} (chapter 7). We have chosen $Z_{crit}/Z_{\odot} = 10^{-3}, 10^{-4}, 10^{-5}, 10^{-6}$. In unpolluted environments, for $Z < Z_{crit}$ (population III regime), the stellar mass function adopted is top-heavy, in the range $[100, 500] M_{\odot}$; for $Z \geq Z_{crit}$ (population II-I regime) a standard Salpeter one is assumed. We have found that the effect of population III regime on the global star formation rate is negligible. The critical metallicity in star forming particles is reached relatively soon, so the transition from population III to population II-I regime happens in a very short period, after the onset of star formation ($\sim 10^6$ yr), because of the fast population III stellar lifetimes. Population III regime is dominant only for such short period, immediately after the onset of star formation; later on, almost irrespectively from the threshold metallicity, population II-I sets in, giving contributions of 2 or 3 orders of magnitude higher than the population III one. However, for the very local character of metal pollution, it is probable that population III stars can be formed in isolated regions also at lower redshift. The average contribution to the star formation rate for different Z_{crit} is, anyway, distinguishable with differences reaching about one order of magnitude. The filling factors for different Z_{crit} span a factor of about 7 or 8, among the different cases.

We have shown how it is possible to bind baryonic structure formation with the turbulent environment from which it is originated developing an analytical model for the initial mass function (chapter 8). We have derived analytical predictions which are well in agreement with the observational data. In particular, our modeling is based on the assumption that star formation is triggered by viscous dissipation and it links the turbulent energy spectrum of the medium with the slope of the mass distribution. We find that the spectral slope leads the behaviour of the mass function at the high-mass end, while at the low-mass end there is a cut-off due to the decay of small scales which have not got enough time to

trigger star formation. The final result is a Salpeter shape.

Part III

Appendices

Appendix A

Cooling function

A.1 Definition of cooling function

Given a plasma made of different species, the cooling function of each species is defined as

$$\Lambda = \sum_{i \geq 1} \sum_{0 \leq j < i} n_i A_{ij} \Delta E_{ij} \quad (\text{A.1})$$

where n_i is the energy level population (number density), the indices i and j run over all the energy levels, A_{ij} is the Einstein coefficient for the transition $i \rightarrow j$ and ΔE_{ij} its line emission. The cooling function of the plasma is just the sum of the cooling functions relative to each species.

The hardest part in the calculations is the determination of the level populations, as often the atomic or molecular data are not available (because unknown or badly determined) and this can affect strongly the results, mostly at low densities.

In the following we will show how to properly compute Λ .

A.2 Statistical equilibrium of atoms and molecules

The first task here is the calculation of the level populations of particles, given the temperature and the density. As in cosmic environments media are usually very rarefied and the number of particles is extremely “low”, we cannot safely rely on the Boltzmann distribution, but we must follow the detailed balancing principle. For each level i -th of a given species, we impose that the probability per unit time per unit volume of the transitions to that level (which *populate* it) equals the probability per unit time per unit

volume of transitions from the same i -th level to other levels (which *de-populate* it):

$$\sum_j n_j P_{ji} = n_i \sum_j P_{ij} \quad (i \neq j) \quad (\text{A.2})$$

respectively. In formula (A.2), P_{ij} is the probability of the transition $i \rightarrow j$ and n_i and n_j are the number densities of atoms in the i -th and j -th (with $i \neq j$) level. A further constraint which has to be satisfied is the number particle conservation:

$$\sum_j n_j = n_{tot} \quad (\text{A.3})$$

where n_{tot} is the total number density of the species considered. In the general case of N -level particles, one must solve the $N \times N$ system consisting of $N - 1$ independent balancing equations (A.2) and the constraint of particle conservation (A.3):

$$\begin{pmatrix} 1 & 1 & \dots & 1 \\ p_{21} & p_{22} & \dots & p_{2N} \\ \vdots & \vdots & \ddots & \vdots \\ p_{N1} & p_{N2} & \dots & p_{NN} \end{pmatrix} \begin{pmatrix} n_1 \\ n_2 \\ \vdots \\ n_N \end{pmatrix} = \begin{pmatrix} n_{tot} \\ 0 \\ \vdots \\ 0 \end{pmatrix} \quad (\text{A.4})$$

with $i, j = 1, 2, 3, \dots, N$ and the matrix elements p_{ij} related the probability per unit time of the transition $i - j$. In (A.4), the first line is the constraint of particle conservation and the rest the balancing equations. The elements with $i < j$ describe the de-excitations, the diagonal elements ($i = j$) all the possible transitions from the level i to the other levels and the elements with $i > j$ describe the excitations of the levels.

The next step is to calculate the transition probabilities to substitute in (A.2) and (A.4).

A.2.1 Collisional rates

Let us consider two-body interactions: $\sigma_{ij} u dt$ is the probability over volume V to have collisional events leading to the level transition $i \rightarrow j$, experienced in a time interval dt by one particle, a , moving with a relative velocity u against a colliding particle, x . Here σ_{ij} is the cross section for the process.

If N_x is the number of colliding particles in V , then the total number of events experienced by one particle a in the interval dt is $N_x dP_{ij}$, with

$$dP_{ij} = \frac{\langle \sigma_{ij} u \rangle dt}{V}, \quad (\text{A.5})$$

where the collision probability has been averaged over the particle velocity distribution¹.

When we consider N_i particles of type a in the atomic state i interacting with N_x particles,

¹ We remind that the cross section is typically energy (velocity) dependent.

the total number of events per unit time and volume is simply

$$\frac{N_i N_x}{V} \frac{dP_{ij}}{dt} = n_i n_x V \frac{dP_{ij}}{dt} = n_i n_x \langle \sigma_{ij} v \rangle, \quad (\text{A.6})$$

being n_i and n_x the particle number densities of species a in the level i and of species x , respectively.

At any temperature T , the collisional rate for the atomic transition $i \rightarrow j$, with $i < j$ (excitation), caused by two-body scattering is defined as

$$\gamma_{ij} \equiv \langle u \sigma_{ij} \rangle = \int u \sigma_{ij} f(u) d^3 u, \quad (\text{A.7})$$

where the integral is done over all the velocity space and $f(u) d^3 u$ is the velocity distribution function of the particles. The quantity γ_{ij} is the probability per unit time of *one* given process multiplied by the volume. It is independent from the number density of the particles considered, but depends on the temperature of the medium (via the velocity distribution). If we assume a Maxwellian velocity distribution,

$$f(u) d^3 u = \left(\frac{m}{2\pi k_B T} \right)^{3/2} e^{-\frac{mu^2}{2k_B T}} 4\pi u^2 du, \quad (\text{A.8})$$

and define

$$\sigma_{ij} \equiv \frac{\pi}{g_i} \left(\frac{h}{2\pi m u} \right)^2 \Omega_{ij} = \frac{\pi}{g_i} \left(\frac{\hbar}{m u} \right)^2 \Omega_{ij}, \quad (\text{A.9})$$

where m is the mass of the colliding particles and g_i the multiplicity of the i -th level, substituting the previous two relations in (A.7) and integrating, it is obtained

$$\gamma_{ij} = \frac{h^2}{g_i (2\pi m)^{3/2} \sqrt{k_B T}} \Omega_{ij} = \frac{\hbar^2}{g_i m^{3/2}} \sqrt{\frac{2\pi}{k_B T}} \Omega_{ij}. \quad (\text{A.10})$$

Via definition (A.9), the rate coefficients are related to a dimensionless parameter (the collision strength Ω_{ij}) accounting for the deviations of the cross section from a section having a radius approximatively equal to the De Broglie wavelength. For many common transitions, it is of the order of unity. In case of electron impacts, a typical number for the rate is

$$\gamma_{ij} \simeq 8.629 \cdot 10^{-6} \frac{\Omega_{ij}}{g_i \sqrt{T}} \text{ cm}^3 \text{ s}^{-1} \quad (\text{A.11})$$

with some temperature dependence for Ω_{ij} .

Once γ_{ij} is known, it is also possible to compute the reverse process rates γ_{ji} using the thermodynamic limit: this means that if we write the steady state collisional equilibrium

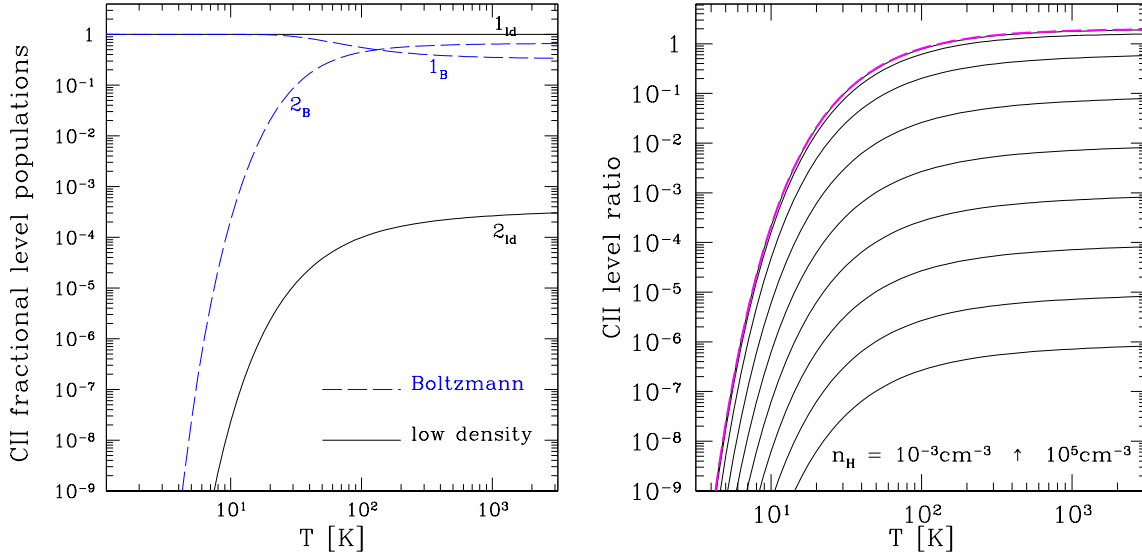


Figure A.1: Fractional level populations as a function of temperature T resulting from collisions between CII atoms (2 level system) and hydrogen atoms. Left panel: the two fractional level populations are plotted assuming a Boltzmann distribution (dashed line) and the low-density limit (solid line). The first and second level populations expected by the Boltzmann predictions are denoted by 1_B and 2_B , respectively, while the ones expected in the low-density regime are denoted by 1_{ld} and 2_{ld} , respectively. The colliding hydrogen number density is 0.6 cm^{-3} . Right panel: fractional level population ratio, n_2/n_1 , as a function of temperature T . The CII number density is kept constant at 1 cm^{-3} and colliding particle number densities ranging from 10^{-3} cm^{-3} up to 10^5 cm^{-3} , with a one order of magnitude step, are assumed. The dashed line is the Boltzmann prediction.

including excitations and spontaneous decay between levels i and j , with $i < j$ and A_{ji} probability per unit time of the decay (Einstein A coefficient), it is found

$$n_i n_x \gamma_{ij} = n_j n_x \gamma_{ji} + n_j A_{ji}. \quad (\text{A.12})$$

In the high-density limit, $n_j n_x \gamma_{ji} \gg n_j A_{ji}$, or, equivalently, $n_x \gg A_{ji}/\gamma_{ji} \equiv n_{cr,ji}$, equation (A.12) becomes

$$\frac{\gamma_{ij}}{\gamma_{ji}} = \frac{n_j}{n_i}. \quad (\text{A.13})$$

As, in the high-density limit, the level population follows a Boltzmann distribution:

$$\gamma_{ij} g_i = \gamma_{ji} g_j e^{-\beta \Delta E_{ji}} \quad (\text{A.14})$$

where $\beta = (k_B T)^{-1}$ and ΔE_{ji} is the energy level separation. The previous relation is supposed to be valid in any density regime (transition probabilities do not depend on the densities - see definition) and is only temperature dependent. Therefore, we can use the relation (A.14) in (A.12) and get

$$\frac{n_j}{n_i} = \frac{g_j}{g_i} e^{-\beta \Delta E_{ji}} \frac{1}{1 + n_{cr,ji}/n_x}. \quad (\text{A.15})$$

This shows that in low-density environments ($n_x \leq n_{cr,ji}$ or in general $n_x \sim n_{cr,ji}$) the levels are less populated than in the Boltzmann case of a factor depending on the critical density (i.e. the particular atomic properties) of the individual atoms.

Figure A.1 shows, as an example, the deviations from the Boltzmann distribution (dashed line in the plot) of the level populations of CII interacting with H-atoms and the transition from a low-density regime to a collisional regime when the level populations become independent from the colliding particle number density and are simply ruled by the Boltzmann distribution. In this case, the transition occurs at densities of about $10^4 - 10^5 \text{ cm}^{-3}$, as the critical density is $n_{cr} = 3 \cdot 10^4 (\text{T}/100\text{K})^{-0.07} \text{ cm}^{-3}$.

A.2.2 Radiative rates

A very similar problem is the rate calculations when we consider ionization and recombination of atoms or, in general, photon interactions, like $\text{H}_2 + \gamma \rightarrow 2\text{H}$, where γ denotes the photon and H and H_2 the hydrogen atom and molecule, respectively. Similar processes are ionizations and recombinations of atoms or molecules and effects of radiation in the presence of radiative fields. The simplest and most general case is of type



We want to write an equation equivalent to (A.6) and to compute the corresponding rate, as in (A.7), considering that the photon number density and the cross section are frequency dependent. So, we consider the number of events for each photon frequency and eventually integrate over the whole spectrum.

Let us indicate with $J(\nu)$ the spectral distribution of the photons – in $[\text{erg cm}^{-2} \text{ s}^{-1} \text{ Hz}^{-1} \text{ sr}^{-1}]$; the energy density is given by the integral over the solid angle according to

$$u(\nu) = \int \frac{d\Omega}{c} J(\nu, \Omega) \quad [\text{erg cm}^{-3} \text{ Hz}^{-1}] \quad (\text{A.17})$$

with $d\Omega$ differential of the solid angle. The number of photons of a given frequency ν per second, per unit frequency, per solid angle, passing through a surface orthogonal to the beam, Σ , is then

$$n_{\Sigma}(\nu, \Omega) = \frac{J(\nu, \Omega)}{h\nu} \Sigma \quad [\text{s}^{-1} \text{ Hz}^{-1} \text{ sr}^{-1}]. \quad (\text{A.18})$$

The probability of each photon having frequency ν to interact with the species a is $\sigma_{a\gamma}(\nu)/\Sigma$, being $\sigma_{a\gamma}(\nu)$ the cross section for the process as a function of ν . This means

that at that frequency the number of photons interacting with one particle a per unit time, per unit frequency, per solid angle is

$$n_{int}(\nu, \Omega) = n_{\Sigma}(\nu, \Omega) \frac{\sigma_{a\gamma}(\nu)}{\Sigma} \quad [\text{s}^{-1} \text{ Hz}^{-1} \text{ sr}^{-1}]. \quad (\text{A.19})$$

The radiative rate $k_{a\gamma}$ is obtained integrating $n_{int}(\nu, \Omega)$ over all frequencies and directions. From (A.19), it results

$$k_{a\gamma} = \int \int n_{\Sigma}(\nu, \Omega) \frac{\sigma_{a\gamma}(\nu)}{\Sigma} d\nu d\Omega \quad [\text{s}^{-1}]. \quad (\text{A.20})$$

Assuming that $\sigma_{a\gamma}$ does not depend on Ω and using (A.18) and (A.17), the above equation becomes

$$k_{a\gamma} = \int \int \frac{J(\nu, \Omega)}{h\nu} \sigma_{a\gamma}(\nu) d\nu d\Omega = c \int \frac{u(\nu)}{h\nu} \sigma_{a\gamma}(\nu) d\nu. \quad (\text{A.21})$$

If all the quantities in the integral are orientation independent

$$k_{a\gamma} = 4\pi \int \frac{J(\nu)}{h\nu} \sigma_{a\gamma}(\nu) d\nu \quad [\text{s}^{-1}]. \quad (\text{A.22})$$

The number of interactions per unit time per unit volume with n_a atoms is

$$n_a k_{a\gamma} \quad [\text{cm}^{-3} \text{ s}^{-1}] \quad (\text{A.23})$$

being n_a the number density of the species a . This last expression (A.23) is equivalent to the expression (A.6), valid for collisional events.

A.2.3 General expressions

We define the average value of a generical physical quantity $f(\nu)$ over the photon spectral distribution as follows:

$$\langle f \rangle \equiv \int \int \frac{d\Omega}{c} \frac{J(\nu, \Omega)}{h\nu} f(\nu) d\nu = \int \frac{u(\nu)}{h\nu} f(\nu) d\nu. \quad (\text{A.24})$$

We notice that the ratio between the energy density $u(\nu)$ and the energetic quantum $h\nu$

$$n_{\gamma}(\nu) = \frac{u(\nu)}{h\nu} \quad (\text{A.25})$$

simply gives the photon number density. Averaging the quantity $\sigma_{a\gamma}c$, the radiative rate $k_{a\gamma}$ of (A.21) becomes

$$k_{a\gamma} = \langle cn_{\gamma} \sigma_{a\gamma} \rangle. \quad (\text{A.26})$$

Formally, there is a similarity for the number of *collisional interactions* per unit time and unit volume (A.6)

$$n_i \langle n_x \sigma_{ij} v \rangle = n_i n_x \langle \sigma_{ij} v \rangle \quad (\text{A.27})$$

and the number of *radiative absorptions* per unit time and unit volume

$$n_a \langle n_\gamma \sigma_{a\gamma} c \rangle = n_a \langle n_\gamma \sigma_{a\gamma} \rangle c \quad (\text{A.28})$$

obtained from equations (A.21), (A.23) and (A.26), being the weight functions the velocity distribution of the colliding particles, in the former case, and the spectral number density distribution of the photons, in the latter case.

Appendix B

Star formation rate indicators

B.1 Stellar luminosities and star formation

The main indicators for galactic star formation rate are the UV continuum, far-infrared continuum, H_α Balmer 3 – 2 recombination line and $[\text{OII}]\lambda 3727$ forbidden line. We indicate the respective luminosities with L_{UV} , L_{FIR} , L_{H_α} , L_{OII} . Their connection to the star formation rate (SFR) is summarized by the following classical relations (Kennicutt, 1998):

- $\text{SFR} [\text{M}_\odot \text{yr}^{-1}] = 1.4 \cdot 10^{-28} L_{\text{UV}} [\text{erg s}^{-1} \text{Hz}^{-1}]$
- $\text{SFR} [\text{M}_\odot \text{yr}^{-1}] = 4.5 \cdot 10^{-44} L_{\text{FIR}} [\text{erg s}^{-1}]$ (starbusts)
- $\text{SFR} [\text{M}_\odot \text{yr}^{-1}] = 7.9 \cdot 10^{-42} L_{H_\alpha} [\text{erg s}^{-1}]$
- $\text{SFR} [\text{M}_\odot \text{yr}^{-1}] = (1.4 \pm 0.4) \cdot 10^{-41} L_{\text{OII}} [\text{erg s}^{-1}]$

They are qualitatively understood in terms of the impact of star formation on the surroundings and calibrated using stellar population synthesis models with a Salpeter IMF.

The $\text{SFR} - L_{\text{UV}}$ relation is justified by the fact that usually massive stars evolve very rapidly and emit in the UV. Therefore L_{UV} is a measure of the number of massive, young stars formed and is related, via the assumed IMF, to the total amount of stars formed. The UV emission from other low-mass stars is negligible, as their contribution peaks in the visible. Uncertainties derive from dust extinction which causes underestimations of L_{UV} .

The $\text{SFR} - L_{\text{FIR}}$ relation is still related to massive, young stars, whose UV-visible

luminosity is easily absorbed from dust and re-emitted, via photoelectric effect, in the far-infrared ($8 - 1000\mu m$, though for starburst most of the emission falls in the range $10 - 120\mu m$). The scatter of this relation is essentially due to the contamination from low-mass stars, as they can emit in the same wavelength. Non the less, this is probably the best relation to quantify the SFR.

The SFR – $L_{H\alpha}$ relation is another way to probe young, massive stellar populations. In fact, the integrated stellar luminosity is re-emitted by many nebular lines (not only Balmer $H\alpha$, but also $H\beta$, P_α , P_β , Br_α , Br_β). The contribution to the ionizing flux arising during star formation is strongly dominated by massive ($M > 10 M_\odot$), young stars, so recombination lines provide a nearly instantaneous measure of the SFR.

The SFR – L_{OII} relation is important to estimate SFR of distant (redshift $z \geq 0.5$) galaxies, as the OII forbidden-line doublet gives the strongest emission in the blue and can be observed in the visible out to $z \sim 1.6$ (where the wavelength is redshifted to about 9690\AA). The calibration of the SFR from L_{OII} is done using $H\alpha$ emission, therefore, the SFR – L_{OII} relation inherits the same IMF dependence as SFR – $L_{H\alpha}$ relation.

Additional indicators can be molecules, like CO, which are easily created in cool, star forming regions: in these cases the situation is much more complicated, as the ratio \mathcal{R} between luminosity and star formation depends on the molecular rotational level considered. An example is shown in Figure B.1, where the distribution of \mathcal{R} ratios is plotted against the upper rotational quantum number, as inferred for many astrophysical sources (Righi et al., 2008).

B.2 Schmidt law

In disk galaxies, the surface star formation rate is best-fitted by a power law of the surface gas density (Schmidt law):

$$\Sigma_{\text{SFR}} = (2.5 \pm 0.7) \cdot 10^{-4} \left(\frac{\Sigma_{\text{gas}}}{M_\odot \text{ pc}^{-2}} \right)^{1.4 \pm 0.15} [\text{M}_\odot \text{ yr}^{-1} \text{ kpc}^{-2}].$$

Detailed theoretical explanations of this relation are still missing. Some observational data are showed in Figure B.2. The straight line on the left panel is the best-fit to the data, the one on the right panel shows the correlation between SFR and $\Sigma_{\text{gas}}/\tau_{\text{dyn}}$, where τ_{dyn} is the average orbital time in the disk. The fact that these quantities correlate relatively

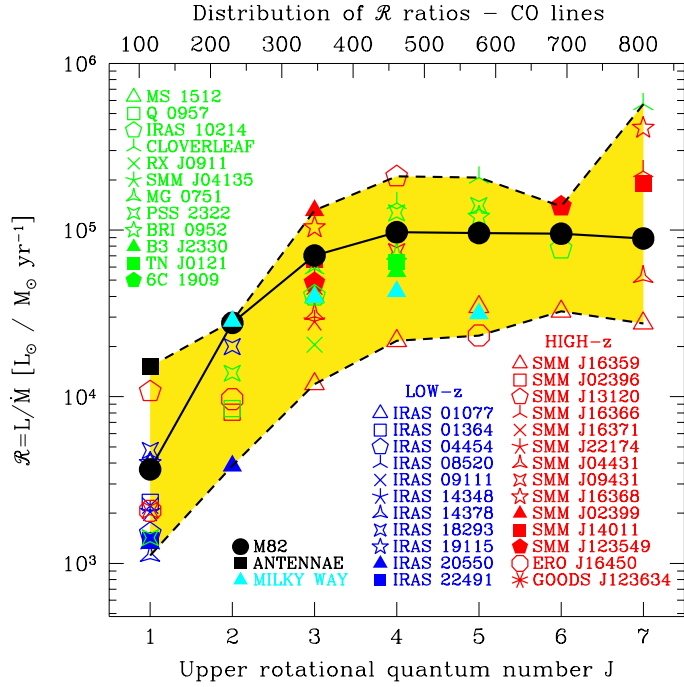


Figure B.1: Distribution of \mathcal{R} ratios (ordinate) plotted against the upper rotational quantum number of the CO transitions $J \rightarrow J - 1$ (abscis), as inferred for the astrophysical objects listed in the labels. The scale on the top refers to the corresponding frequency in GHz. Dashed lines around the shaded area represent the lower and upper limits for \mathcal{R} in the sample (Righi et al., 2008, and references therein).

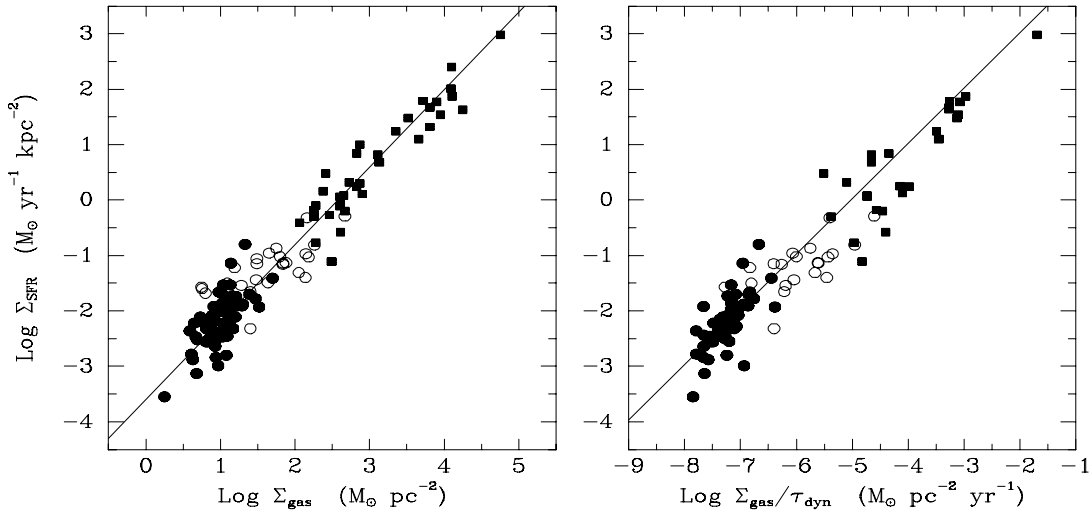


Figure B.2: Left panel: the global Schmidt law in galaxies. The samples consider normal spirals (solid points) and circumnuclear starbusts (squared). The open circles refer to central regions of normal disks. Right panel: correlation of SFR and the ratio between the surface gas density and average orbital time in the disk for the same data as left panel. Plots from Kennicutt (1998).

well must hidden some link between star formation and gas activity in the disk.

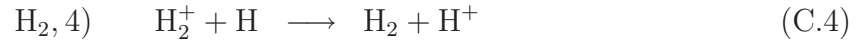
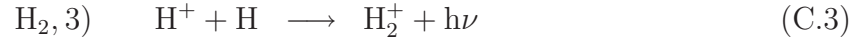
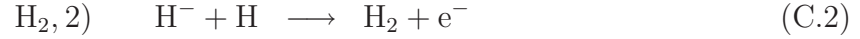
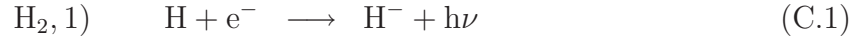
Appendix C

Molecular and atomic data

In the following sections we quote molecular rates (C.1) and atomic data (C.2) used in our calculations.

C.1 Molecular rates

The reactions involving molecular hydrogen are:



The respective rates are (Abel et al., 1997; Galli and Palla, 1998):

$$k_{\text{H}_2,1} = 6.77 \cdot 10^{-15} T_{eV}^{0.8779} \text{ cm}^3 \text{ s}^{-1} \quad (\text{C.5})$$

$$k_{\text{H}_2,2} = \begin{cases} 1.43 \cdot 10^{-9} \text{ cm}^3 \text{ s}^{-1}, & T_{eV} \leq 0.1 \\ e^{-20.069138 + 0.22898006 \ln T_{eV} + 0.035998377 \ln^2 T_{eV}} \times \\ e^{-0.004555120 \ln^3 T_{eV} - 0.00031051154 \ln^4 T_{eV} + 0.00010732940 \ln^5 T_{eV}} \times \\ e^{-8.366719 \cdot 10^{-6} \ln^6 T_{eV} - 2.2383062 \cdot 10^{-7} \ln^7 T_{eV}} \text{ cm}^3 \text{ s}^{-1}, & T_{eV} > 0.1 \end{cases} \quad (\text{C.6})$$

$$k_{\text{H}_2,3} = \begin{cases} 1.85 \cdot 10^{-23} T^{1.8} \text{ cm}^3 \text{ s}^{-1}, & T \leq 6.7 \cdot 10^3 \text{ K} \\ 5.81 \cdot 10^{-16} \left(\frac{T}{56200} \right)^{-0.6657 \text{Log}_{10}(T/56200)} \text{ cm}^3 \text{ s}^{-1}, & T > 6.7 \cdot 10^3 \text{ K} \end{cases} \quad (\text{C.7})$$

$$k_{\text{H}_2,4} = 6.0 \cdot 10^{-10} \text{ cm}^3 \text{ s}^{-1} \quad (\text{C.8})$$

where $T_{eV} = T/11605$ K is the temperature expressed in eV¹.

The fit for the cooling rate arising from H₂ and neutral H atom interactions is:

$$\Lambda_{\text{H}_2, \text{H}}(T) = \frac{\Lambda_{\text{HDL}}(T)}{1 + [\Lambda_{\text{HDL}}(T)/\Lambda_{\text{LDL}}(T)]}. \quad (\text{C.9})$$

The (local thermodynamic equilibrium) high-density limit is (Hollenbach and McKee, 1979):

$$\Lambda_{\text{HDL}} = (\Lambda_{\text{HDLR}} + \Lambda_{\text{HDLV}})/n_{\text{H}} \quad \text{erg cm}^3 \text{ s}^{-1} \quad (\text{C.10})$$

where the rotational and vibrational contributions are, respectively,

$$\Lambda_{\text{HDLR}} = \frac{9.5 \cdot 10^{-22} T_3^{3.76}}{(1 + 0.12 T_3^{2.1}) e^{-(0.13/T_3)^3}} + 3 \cdot 10^{-24} e^{-0.51/T_3} \quad \text{erg s}^{-1} \quad (\text{C.11})$$

$$\Lambda_{\text{HDLV}} = 6.7 \cdot 10^{-19} e^{-5.86/T_3} + 1.6 \cdot 10^{-18} e^{-11.7/T_3} \quad \text{erg s}^{-1} \quad (\text{C.12})$$

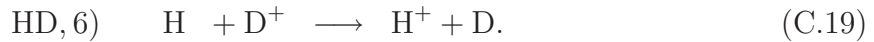
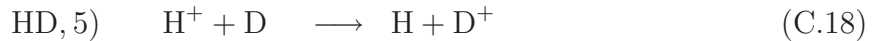
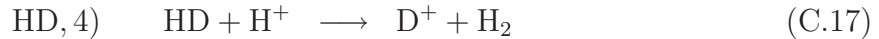
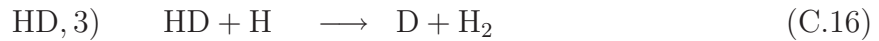
$T_3 \equiv T$ [K] / 1000 K and n_{H} is the neutral hydrogen number density².

The low-density limit contribution is (Galli and Palla, 1998):

$$\Lambda_{\text{LDL}} = 10^{-103.0+97.59t-48.05t^2+10.80t^3-0.9032t^4} \quad \text{erg cm}^3 \text{ s}^{-1} \quad (\text{C.13})$$

where $t \equiv \text{Log}_{10}(T / [\text{K}])$, for the relevant temperature range $10 \text{ K} \lesssim T \lesssim 10^5 \text{ K}$.

We consider the following set of equations involving HD creation and destruction:



We use the temperature dependent rate coefficients from Wang and Stancil (2002):

$$k_{\text{HD},1} = 9.0 \cdot 10^{-11} e^{-3876/T} \text{ cm}^3 \text{ s}^{-1} \quad (\text{C.20})$$

$$k_{\text{HD},2} = 1.6 \cdot 10^{-9} \text{ cm}^3 \text{ s}^{-1} \quad (\text{C.21})$$

¹ 1 eV corresponds to ~ 11605 K, as $1 \text{ eV} = 1.60217646 \cdot 10^{-19} \text{ C} \cdot 1 \text{ V} = 1.60217646 \cdot 10^{-19} \text{ J} = 1.60217646 \cdot 10^{-12} \text{ erg}$, therefore $T(1 \text{ eV}) \equiv 1 \text{ eV}/k_B \simeq 11605 \text{ K}$.

² We point out that the numerical values in the exponentials correspond to the dominant energy level transitions.

from Stancil et al. (1998):

$$k_{\text{HD},3} = 3.2 \cdot 10^{-11} e^{-3624/T} \text{ cm}^3 \text{ s}^{-1} \quad (\text{C.22})$$

$$k_{\text{HD},4} = 10^{-9} e^{-464/T} \text{ cm}^3 \text{ s}^{-1} \quad (\text{C.23})$$

and from Savin (2002):

$$k_{\text{HD},5} = 2 \cdot 10^{-10} T^{0.402} e^{-37.1/T} - 3.31 \cdot 10^{-17} T^{1.48} \text{ cm}^3 \text{ s}^{-1} \quad (\text{C.24})$$

$$k_{\text{HD},6} = 2.06 \cdot 10^{-10} T^{0.396} e^{-33.0/T} + 2.03 \cdot 10^{-9} T^{-0.332} \text{ cm}^3 \text{ s}^{-1}. \quad (\text{C.25})$$

The fit for the cooling rate due to H atom impacts is (Lipovka et al., 2005):

$$\Lambda_{\text{HD,H}}(T) = 10^{-42.45906+21.90083t-10.1954t^2+2.19788t^3-0.17286t^4} \text{ erg cm}^3 \text{ s}^{-1} \quad (\text{C.26})$$

with $t \equiv \text{Log}_{10}(T / [\text{K}])$.

We consider the main equations for HeH^+ formation and evolution (Galli and Palla, 1998), namely:



and the rates from Roberge and Dalgarno (1982):

$$k_{\text{HeH}^+,1} = \begin{cases} 7.6 \cdot 10^{-18} T^{-0.5} \text{ cm}^3 \text{ s}^{-1}, & T \leq 10^3 \text{ K} \\ 3.45 \cdot 10^{-16} T^{-1.06} \text{ cm}^3 \text{ s}^{-1}, & T > 10^3 \text{ K} \end{cases} \quad (\text{C.30})$$

from Karpas et al. (1979):

$$k_{\text{HeH}^+,2} = 9.1 \cdot 10^{-10} \text{ cm}^3 \text{ s}^{-1} \quad (\text{C.31})$$

and from Roberge and Dalgarno (1982):

$$k_{\text{HeH}^+,3} = 6.8 \cdot 10^{-1} T_r^{1.5} e^{-22750/T_r} \text{ s}^{-1}. \quad (\text{C.32})$$

In the previous expressions, T stands for the gas temperature and T_r for the radiation temperature.

C.2 Metal atomic data

In the following, the atomic data adopted are provided (Osterbrock, 1989; Hollenbach and McKee, 1989; Santoro and Shull, 2006). We will use the usual spectroscopic notation for many electron atoms: \mathbf{S} is the total electronic spin quantum operator, \mathbf{L} the total electronic orbital angular momentum operator and $\mathbf{J} = \mathbf{L} + \mathbf{S}$ the sum operator; S, L, J are the respective quantum numbers. With X we indicate the orbitals S, P, D, F, ..., according to L=0, 1, 2, 3, ..., respectively; then $^{2S+1}X_J$ will indicate the atomic orbital X, with spin quantum number S and total angular momentum quantum number J; its multiplicity is equal to $2J + 1$.

In the following, we are going to discuss the models adopted for each species and the lines considered in a more detailed way.

We will often use the notation $T_{100} = T/100$ K and T_{exc} for the excitation temperature.

- * **CII**: we model CII as a two-level system considering the fine structure transition $(2p)[^2P_{3/2} - ^2P_{1/2}]$ between the quantum number $J = 3/2$ and $J = 1/2$ states. The data are (Hollenbach and McKee, 1989):

$$\gamma_{21}^H = 8 \cdot 10^{-10} T_{100}^{0.07} \text{ cm}^3 \text{ s}^{-1};$$

$$\gamma_{21}^e = 2.8 \cdot 10^{-7} T_{100}^{-0.5} \text{ cm}^3 \text{ s}^{-1};$$

$$A_{21} = 2.4 \cdot 10^{-6} \text{ s}^{-1};$$

$$\Delta E_{21} = 1.259 \cdot 10^{-14} \text{ erg} \quad (T_{exc} = 91.2 \text{ K}, \lambda = 157.74 \mu\text{m}).$$

- * **SiIII**: we model SiIII as a two-level system with the fine structure transition $(3p)[^2P_{3/2} - ^2P_{1/2}]$. Data were taken from Hollenbach and McKee (1989):

$$\gamma_{21}^H = 8 \cdot 10^{-10} T_{100}^{-0.07} \text{ cm}^3 \text{ s}^{-1};$$

$$\gamma_{21}^e = 1.7 \cdot 10^{-6} T_{100}^{-0.5} \text{ cm}^3 \text{ s}^{-1};$$

$$A_{21} = 2.1 \cdot 10^{-4} \text{ s}^{-1};$$

$$\Delta E_{21} = 5.71 \cdot 10^{-14} \text{ erg} \quad (T_{exc} = 413.6 \text{ K}, \lambda = 34.8 \mu\text{m}).$$

- * **OI**: neutral oxygen is a metastable system formed by the (S=1, L=1) triplet and (S=0, L=0,2) doublet, $(2p)[^3P_2 - ^3P_1 - ^3P_0 - ^1D_2 - ^1S_0]$, in order of increasing level,

with the following excitations rates (Hollenbach and McKee, 1989):

$$\gamma_{21}^H = 9.2 \cdot 10^{-11} T_{100}^{0.67} \text{ cm}^3 \text{ s}^{-1};$$

$$\gamma_{31}^H = 4.3 \cdot 10^{-11} T_{100}^{0.80} \text{ cm}^3 \text{ s}^{-1};$$

$$\gamma_{32}^H = 1.1 \cdot 10^{-10} T_{100}^{0.44} \text{ cm}^3 \text{ s}^{-1};$$

$$\gamma_{41}^H = \gamma_{42}^H = \gamma_{43}^H = 10^{-12} \text{ cm}^3 \text{ s}^{-1};$$

$$\gamma_{51}^H = \gamma_{52}^H = \gamma_{53}^H = 10^{-12} \text{ cm}^3 \text{ s}^{-1};$$

$$\gamma_{21}^e = 1.4 \cdot 10^{-8} \text{ cm}^3 \text{ s}^{-1};$$

$$\gamma_{31}^e = 1.4 \cdot 10^{-8} \text{ cm}^3 \text{ s}^{-1};$$

$$\gamma_{32}^e = 5.0 \cdot 10^{-9} \text{ cm}^3 \text{ s}^{-1};$$

$$\gamma_{41}^e = \gamma_{42}^e = \gamma_{43}^e = 10^{-10} \text{ cm}^3 \text{ s}^{-1};$$

$$\gamma_{51}^e = \gamma_{52}^e = \gamma_{53}^e = 10^{-10} \text{ cm}^3 \text{ s}^{-1}.$$

Radiative A coefficients (Osterbrock, 1989; Hollenbach and McKee, 1989):

$$A_{21} = 8.9 \cdot 10^{-5} \text{ s}^{-1};$$

$$A_{31} = 1.0 \cdot 10^{-10} \text{ s}^{-1};$$

$$A_{32} = 1.7 \cdot 10^{-5} \text{ s}^{-1};$$

$$A_{41} = 6.3 \cdot 10^{-3} \text{ s}^{-1};$$

$$A_{42} = 2.1 \cdot 10^{-3} \text{ s}^{-1};$$

$$A_{43} = 7.3 \cdot 10^{-7} \text{ s}^{-1};$$

$$A_{51} = 2.9 \cdot 10^{-4} \text{ s}^{-1};$$

$$A_{52} = 7.3 \cdot 10^{-2} \text{ s}^{-1};$$

$$A_{54} = 1.2 \text{ s}^{-1};$$

energy separations are derived from Hollenbach and McKee (1989):

$$\Delta E_{21} = 3.144 \cdot 10^{-14} \text{ erg} \quad (T_{exc} = 227.7 \text{ K}, \lambda = 63.18 \mu\text{m});$$

$$\Delta E_{32} = 1.365 \cdot 10^{-14} \text{ erg} \quad (T_{exc} = 98.8 \text{ K}, \lambda = 145.5 \mu\text{m});$$

$$\Delta E_{43} = 3.14 \cdot 10^{-12} \text{ erg} \quad (T_{exc} = 2.283 \cdot 10^4 \text{ K}, \lambda = 6300 \text{ \AA});$$

$$\Delta E_{53} = 3.56 \cdot 10^{-12} \text{ erg} \quad (T_{exc} = 2.578 \cdot 10^4 \text{ K}, \lambda = 5577 \text{ \AA}).$$

* **FeII**: we adopt a model for a five-level system including the transitions $(3d)[^6D_{9/2} - ^6D_{7/2} - ^6D_{5/2} - ^6D_{3/2} - ^6D_{1/2}]$ in order of increasing level. For the data see also Santoro and Shull (2006) and references therein:

$$\gamma_{21}^H = 9.5 \cdot 10^{-10} \text{ cm}^3 \text{ s}^{-1};$$

$$\begin{aligned}
\gamma_{32}^H &= 4.7 \cdot 10^{-10} \text{ cm}^3 \text{ s}^{-1}; \\
\gamma_{43}^H &= 5. \cdot 10^{-10} \text{ cm}^3 \text{ s}^{-1}; \\
\gamma_{54}^H &= 5 \cdot 10^{-10} \text{ cm}^3 \text{ s}^{-1}; \\
\gamma_{31}^H &= 5.7 \cdot 10^{-10} \text{ cm}^3 \text{ s}^{-1}; \\
\gamma_{41}^H &= 5 \cdot 10^{-10} \text{ cm}^3 \text{ s}^{-1}; \\
\gamma_{51}^H &= 5 \cdot 10^{-10} \text{ cm}^3 \text{ s}^{-1}; \\
\gamma_{42}^H &= 5 \cdot 10^{-10} \text{ cm}^3 \text{ s}^{-1}; \\
\gamma_{52}^H &= 5 \cdot 10^{-10} \text{ cm}^3 \text{ s}^{-1}; \\
\gamma_{53}^H &= 5 \cdot 10^{-10} \text{ cm}^3 \text{ s}^{-1}; \\
\gamma_{21}^e &= 1.8 \cdot 10^{-6} T_{100}^{-0.5} \text{ cm}^3 \text{ s}^{-1}; \\
\gamma_{32}^e &= 8.7 \cdot 10^{-7} T_{100}^{-0.5} \text{ cm}^3 \text{ s}^{-1}; \\
\gamma_{43}^e &= 10^{-5} T^{-0.5} \text{ cm}^3 \text{ s}^{-1}; \\
\gamma_{54}^e &= 10^{-5} T^{-0.5} \text{ cm}^3 \text{ s}^{-1}; \\
\gamma_{31}^e &= 1.8 \cdot 10^{-6} T_{100}^{-0.5} \text{ cm}^3 \text{ s}^{-1}; \\
\gamma_{41}^e &= 10^{-5} T^{-0.5} \text{ cm}^3 \text{ s}^{-1}; \\
\gamma_{51}^e &= 10^{-5} T^{-0.5} \text{ cm}^3 \text{ s}^{-1}; \\
\gamma_{42}^e &= 10^{-5} T^{-0.5} \text{ cm}^3 \text{ s}^{-1}; \\
\gamma_{52}^e &= 10^{-5} T^{-0.5} \text{ cm}^3 \text{ s}^{-1}; \\
\gamma_{53}^e &= 10^{-5} T^{-0.5} \text{ cm}^3 \text{ s}^{-1};
\end{aligned}$$

we assume a fiducial normalization of 10^{-5} for missing data on e -impact rates. We have checked that the level populations are almost insensitive to the adopted values.

Radiative transition probabilities:

$$\begin{aligned}
A_{21} &= 2.13 \cdot 10^{-3} \text{ s}^{-1}; \\
A_{32} &= 1.57 \cdot 10^{-3} \text{ s}^{-1}; \\
A_{31} &= 1.50 \cdot 10^{-9} \text{ s}^{-1}; \\
A_{43} &= 7.18 \cdot 10^{-4} \text{ s}^{-1}; \\
A_{54} &= 1.88 \cdot 10^{-4} \text{ s}^{-1};
\end{aligned}$$

Energy separations:

$$\begin{aligned}
\Delta E_{21} &= 7.64 \cdot 10^{-14} \text{ erg} \quad (T_{exc} = 553.58 \text{ K}, \lambda = 25.99 \mu\text{m}); \\
\Delta E_{32} &= 5.62 \cdot 10^{-14} \text{ erg} \quad (T_{exc} = 407.01 \text{ K}, \lambda = 35.35 \mu\text{m}); \\
\Delta E_{43} &= 3.87 \cdot 10^{-14} \text{ erg} \quad (T_{exc} = 280.57 \text{ K}, \lambda = 51.28 \mu\text{m}); \\
\Delta E_{54} &= 2.27 \cdot 10^{-14} \text{ erg} \quad (T_{exc} = 164.60 \text{ K}, \lambda = 87.41 \mu\text{m}).
\end{aligned}$$

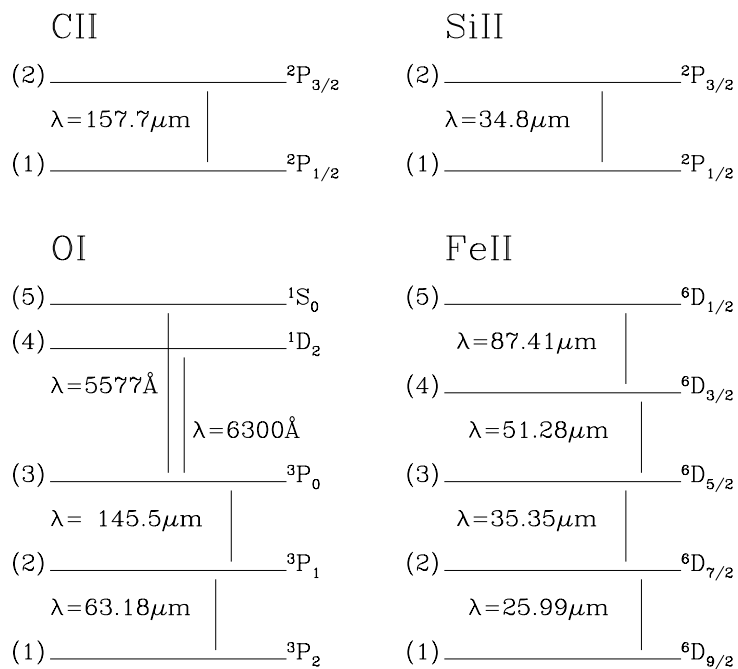


Figure C.1: Scheme of the level models adopted for the different atoms with respective line transition data.

A scheme of the atomic states, with wavelengths of the transitions between different levels, is given in Figure C.1.

Appendix D

Entropy

The well known Sackur-Tetrode formula for mono-atomic, non-degenerate, perfect, free gas is:

$$S = Nk_B \ln \left[\frac{\Sigma V}{h^3 N} (2\pi m k_B T)^{3/2} e^{5/2} \right] \quad (\text{D.1})$$

where S is the entropy, k_B is the Boltzmann constant, h is the Planck constant, N the number of particles, Σ the particle state degeneracy, V the volume, T the temperature, m the mass of the particles. If m_H is the hydrogen mass and μ the mean molecular weight of the gas, the total mass of the system is $M = mN = (\mu m_H)N$.

As $N/V \equiv n = \rho/\mu m_H$,

$$S = Nk_B \ln \left[\frac{\Sigma (\mu m_H)^{5/2}}{h^3 \rho} (2\pi k_B T)^{3/2} e^{5/2} \right] = \frac{3}{2} Nk_B \ln \left(C_1 \frac{k_B T}{\rho^{2/3}} \right), \quad (\text{D.2})$$

where C_1 is the constant factor in the logarithm.

More generally, calling γ the adiabatic index, one gets

$$S = Nk_B \ln \left[\frac{\Sigma (\mu m_H)^{\gamma/(\gamma-1)}}{h^3 \rho} (2\pi k_B T)^{1/(\gamma-1)} e^{\gamma/(\gamma-1)} \right] = \frac{1}{\gamma-1} Nk_B \ln \left(C \frac{k_B T}{\rho^{\gamma-1}} \right) \quad (\text{D.3})$$

with C constant determined by the kind of gas considered.

Because of formulæ (D.1), (D.2), and (D.3), the entropy is related to the logarithm of the ratio between the pressure of the gas, $P = nk_B T$, and the adiabatic scaling ρ^γ by

$$S = \frac{1}{\gamma-1} Nk_B \ln \left(C \mu m_H \frac{P}{\rho^\gamma} \right), \quad (\text{D.4})$$

that is why the quantities P/ρ^γ or $k_B T/\rho^{\gamma-1}$ are often called (maybe improperly) “entropy” or “entropic function”.

Appendix E

Gravitational instability and viscous dissipation

The classical approach to gravitational instability is to write the equations governing the evolution of a fluid in a gravitational field ϕ , and to expand them in perturbative series assuming that the perturbations are “small” and the change of entropy is negligible.

E.1 Perturbative treatment

A fluid is described by its density ρ , pressure P and velocity field \mathbf{u} . The equations ruling its behaviour are

- the continuity equation

$$\frac{\partial \rho}{\partial t} + \nabla \cdot (\rho \mathbf{u}) = 0 \quad (\text{E.1})$$

- the Navier-Stokes equations including viscosity ν

$$\frac{\partial \mathbf{u}}{\partial t} + (\mathbf{u} \cdot \nabla) \mathbf{u} = -\frac{\nabla P}{\rho} - \nabla \phi + \nu \nabla^2 \mathbf{u} \quad (\text{E.2})$$

- the Poisson equation

$$\nabla^2 \phi = 4\pi G \rho. \quad (\text{E.3})$$

The different quantities can be decomposed in a background average value and a perturbation as follows

$$\left\{ \begin{array}{l} \rho = \rho_b + \delta\rho \equiv \rho_b(1 + \delta) \\ P = P_b + \delta P \\ \mathbf{u} = \delta \mathbf{u} \\ \phi = \phi_b + \delta\phi \end{array} \right. \quad (\text{E.4})$$

with $|\delta| = |\delta\rho/\rho_b| \ll 1$, $|\delta P/P_b| \ll 1$, $|\delta\phi/\phi_b| \ll 1$ and the velocity identified with the perturbation because we assume the reference frame of the fluid. The sound speed at constant entropy S is

$$c_s^2 = \left(\frac{\partial P}{\partial \rho} \right)_S = \frac{\delta P}{\delta \rho}. \quad (\text{E.5})$$

The linearization of the system leads to the linearized

- continuity equation

$$\frac{\partial \delta \rho}{\partial t} + \rho_b \nabla \cdot (\delta \mathbf{u}) = 0 \quad (\text{E.6})$$

- Navier-Stokes equations

$$\frac{\partial \delta \mathbf{u}}{\partial t} = -\frac{c_s^2}{\rho_b} \nabla \delta \rho - \nabla \delta \phi + \nu \nabla^2 \delta \mathbf{u} \quad (\text{E.7})$$

- Poisson equation

$$\nabla^2 \delta \phi = 4\pi G \delta \rho. \quad (\text{E.8})$$

In Fourier space, the system reads

$$\begin{cases} \omega \hat{\delta} - \mathbf{k} \cdot (\hat{\delta} \mathbf{u}) = 0 \\ \omega (\hat{\delta} \mathbf{u}) = \mathbf{k} \left[c_s^2 \hat{\delta} + (\hat{\delta} \phi) \right] - \nu k^2 (\hat{\delta} \mathbf{u}) \\ -k^2 (\hat{\delta} \phi) = 4\pi G \rho_b \hat{\delta} \end{cases} \quad (\text{E.9})$$

where we have used as kernel of the transformation¹ $e^{i\omega t - i\mathbf{k} \cdot \mathbf{x}}$, with ω angular frequency, \mathbf{k} wave-number vector with modulus k and \mathbf{x} position vector. The hat-sign denotes the Fourier transformation and $\hat{\delta} = \hat{\delta}\rho/\rho_b$. Expliciting the 5×5 matrix associated to this system leads to

$$\begin{pmatrix} \omega & -\mathbf{k}^T & 0 \\ -\mathbf{k} c_s^2 & (\omega + \nu k^2) \mathbf{I} & -\mathbf{k} \\ 4\pi G \rho_b & \mathbf{0}^T & k^2 \end{pmatrix} \begin{pmatrix} \hat{\delta} \\ \hat{\delta} \mathbf{u} \\ \hat{\delta} \phi \end{pmatrix} = \begin{pmatrix} 0 \\ \mathbf{0} \\ 0 \end{pmatrix}. \quad (\text{E.10})$$

In the previous matrix (E.10), \mathbf{k}^T is the transposed of the vector \mathbf{k} , $\mathbf{0}^T$ the transposed of the null vector $\mathbf{0}$ and $\mathbf{I} = \mathbf{I}^T$ the 3×3 unity matrix. In 1D, the matrix becomes 3×3 and non trivial solutions exist for

$$\omega^2 k^2 + \omega \nu k^4 - c_s^2 k^4 + 4\pi G \rho_b k^2 = 0. \quad (\text{E.11})$$

This represents the dispersion relation between the Fourier variables ω and \mathbf{k} .

For $k \neq 0$, it reduces to

$$\omega^2 + \omega \nu k^2 - c_s^2 k^2 + 4\pi G \rho_b = 0, \quad (\text{E.12})$$

¹ The particular kernel used is irrelevant to the final result.

whereas, for $k = 0$ any ω satisfies the condition (E.11).

In the simple case of no-viscosity dissipation,

$$\omega^2 - c_s^2 k^2 + 4\pi G \rho_b = 0 \quad (\text{E.13})$$

which admits growing, unstable modes for imaginary ω :

$$\omega^2 = c_s^2 k^2 - 4\pi G \rho_b < 0. \quad (\text{E.14})$$

Being k a positive quantity and $k = 0$ the condition for which the original dispersion relation (E.11) is identically always satisfied by any value of ω and the relation (E.14) has always imaginary solutions, one obtains

$$0 \leq k < 2 \frac{\sqrt{\pi G \rho_b}}{c_s} \equiv k_J. \quad (\text{E.15})$$

The value k_J is the usual Jeans wave-number for the stability of spherical nebulae and it leads naturally to the Jeans length $\lambda_J \approx c_s / \sqrt{G \rho_b}$ and to the condition for gravitational instability, $\lambda > \lambda_J$, for nebulae with size λ .

In the more interesting case of gravitational instability in the presence of viscosity dissipation, we must look for the complex solutions of ω , i.e., a negative discriminant of (E.12)

$$\nu^2 k^4 + 4c_s^2 k^2 - 16\pi G \rho_b < 0. \quad (\text{E.16})$$

This bi-quadratic disequation has as solutions

$$0 \leq k < \sqrt{-\frac{2c_s^2}{\nu^2} + \sqrt{\frac{4c_s^4}{\nu^4} + \frac{16\pi G \rho_b}{\nu^2}}} \quad (\text{E.17})$$

or also

$$0 \leq k < \frac{\sqrt{2}c_s}{\nu} \sqrt{-1 + \sqrt{1 + \frac{k_J^2 \nu^2}{c_s^2}}}. \quad (\text{E.18})$$

When the viscosity term dominates (for examples at small scales we expect $\nu^2 k^2 \gg 4c_s^2$), we have

$$0 \leq k < 2 \left(\frac{\pi G \rho_b}{\nu^2} \right)^{1/4} \equiv k_d. \quad (\text{E.19})$$

For the definitions in (E.15) and (E.19), k_d and k_J satisfy the relation

$$k_d = \sqrt{\frac{2c_s k_J}{\nu}}. \quad (\text{E.20})$$

For $\nu \sim 10^{16} \text{ cm}^2 \text{ s}^{-1}$ and a number density of $\sim 10^3 - 10^4 \text{ cm}^{-3}$, at low temperatures, it is found $k_d \sim (2 - 4) \cdot 10^{-15} \text{ cm}^{-1}$ and $k_J \sim 10^{-19} - 10^{-18} \text{ cm}^{-1}$. The fragmenting scales associated to k_d ($\sim 10^{15} \text{ cm}$) are much smaller than the corresponding scales associated to k_J ($\sim 10^{18} - 10^{19} \text{ cm}$).

This is easily understood from the Navier-Stokes equations (E.2), where the viscous term has a sign opposite to the pressure term. So, viscosity acts against gas pressure and causes losses of the kinetic support of the cloud against gravitational collapse. Objects of Jeans size (which would be otherwise stable), can therefore collapse down to smaller scales.

E.2 Time-scales

One last comment on the typical time-scales. From (E.15) and (E.19) we can re-write:

$$k_d = 2 \left(\frac{\pi G \rho}{\nu^2} \right)^{1/4} \quad \text{and} \quad k_J = 2 \left(\frac{\pi G \rho}{c_s^2} \right)^{1/2} \quad (\text{E.21})$$

and the corresponding length-scales are

$$l_d \approx \left(\frac{\nu^2}{G \rho} \right)^{1/4} \quad \text{and} \quad \lambda_J \approx \left(\frac{c_s^2}{G \rho} \right)^{1/2} \quad (\text{E.22})$$

From a dimensional analysis, $\bar{\epsilon} \sim G \rho \nu$ is the average energy transfer rate, with dimensions $[L^2 T^{-3}]$. This allows us to write $l_d \approx (\nu^3 / \bar{\epsilon})^{1/4}$, as stated in section 8.3, and to estimate the time during which the energy, ϵ , will be dissipated: $t_d = \epsilon / \bar{\epsilon}$.

The naturally arising time-scales are then the dissipation time and the free-fall time, respectively:

$$t_d \sim \frac{l_d^2}{\nu} \sim \frac{1}{k_d^2 \nu} \quad \text{and} \quad t_{ff} \sim \frac{\lambda_J}{c_s} \sim \frac{1}{k_J c_s}. \quad (\text{E.23})$$

A comparison between (E.23) and (E.22) immediately shows that, independently from ν and c_s ,

$$t_d \sim t_{ff} \sim \frac{1}{\sqrt{G \rho}}. \quad (\text{E.24})$$

We notice that, for cascade turbulence, t_d rules the whole dissipation process at scales larger than $\sim l_d$ (see section 8.3). Therefore, these scales have a typical dissipation time comparable with the free-fall time. This means that while a cloud collapses, it dissipates energy because of viscosity and gets fragmented.

Scales l below l_d ($l \ll l_d$) get dissipated much faster (in a typical time $\sim l^2 / \nu$) and have not got time to collapse.

Part IV

Bibliography

Bibliography

- Aarseth, S. J., Turner, E. L., and Gott, III, J. R. (1979). N-body simulations of galaxy clustering. I - Initial conditions and galaxy collapse times. *ApJ*, 228:664–683.
- Abel, T., Anninos, P., Zhang, Y., and Norman, M. L. (1997). Modeling primordial gas in numerical cosmology. *New Astronomy*, 2:181–207.
- Abel, T., Bryan, G. L., and Norman, M. L. (2000). The Formation and Fragmentation of Primordial Molecular Clouds. *ApJ*, 540:39–44.
- Abel, T., Bryan, G. L., and Norman, M. L. (2002). The Formation of the First Star in the Universe. *Science*, 295:93–98.
- Abgrall, H. and Roueff, E. (2006). Theoretical calculations of excited rovibrational levels of HD. Term values and transition probabilities of VUV electronic bands. *A&A*, 445:361–372.
- Abgrall, H., Roueff, E., and Viala, Y. (1982). Vibration-rotation transition probabilities for the ground electronic $\chi^1/\text{-sigma}/+$ state of HD. *A&A Supp.*, 50:505–522.
- Adams, F. C. and Fatuzzo, M. (1996). A Theory of the Initial Mass Function for Star Formation in Molecular Clouds. *ApJ*, 464:256–+.
- Aharonian, F., Akhperjanian, A. G., Bazer-Bachi, A. R., Beilicke, M., Benbow, W., Berge, D., Bernlöhr, K., Boisson, C., Bolz, O., Borrel, V., Braun, I., Breitling, F., Brown, A. M., Chadwick, P. M., Chounet, L.-M., Cornils, R., Costamante, L., Degrangé, B., Dickinson, H. J., Djannati-Ataï, A., Drury, L. O., Dubus, G., Emmanoulopoulos, D., Espigat, P., Feinstein, F., Fontaine, G., Fuchs, Y., Funk, S., Gallant, Y. A., Giebels, B., Gillessen, S., Glicenstein, J. F., Goret, P., Hadjichristidis, C., Hauser, D., Hauser, M., Heinzlmann, G., Henri, G., Hermann, G., Hinton, J. A., Hofmann, W., Holleran, M., Horns, D., Jacholkowska, A., de Jager, O. C., Khélifi, B., Klages, S., Komin, N., Konopelko, A., Latham, I. J., Le Gallou, R., Lemièrre, A., Lemoine-Goumard, M., Leroy, N., Lohse, T., Martin, J. M., Martineau-Huynh, O., Marcowith, A., Masterson, C., McComb, T. J. L., de Naurois, M., Nolan, S. J., Noutsos, A., Orford, K. J., Osborne, J. L., Ouchrif, M., Panter, M., Pelletier, G., Pita, S., Pühlhofer, G., Punch, M., Raubenheimer, B. C., Raue, M., Raux, J., Rayner, S. M., Reimer, A., Reimer, O., Ripken, J., Rob, L., Rolland, L., Rowell, G., Sahakian, V., Saugé, L., Schlenker, S., Schlickeiser, R., Schuster, C., Schwanke, U., Siewert, M., Sol, H., Spangler, D., Steenkamp, R., Stegmann, C., Tavernet, J.-P., Terrier, R., Théoret, C. G., Thuczykont, M., van Eldik, C., Vasileiadis, G., Venter, C., Vincent, P., Völk, H. J., and Wagner, S. J. (2006). A low level of extragalactic background light as revealed by γ -rays from blazars. *Nature*, 440:1018–1021.
- Ahmad, A. and Cohen, L. (1973). A numerical integration scheme for the N-body gravitational problem. *Journal of Computational Physics*, 12:389–402.
- Aristoteles (IVbC). *Physica*. (unknown), IV cen. b.C.
- Armstrong, J. W., Cordes, J. M., and Rickett, B. J. (1981). Density power spectrum in the local interstellar medium. *Nature*, 291:561–564.
- Armstrong, J. W. and Rickett, B. J. (1981). Power spectrum of small-scale density irregularities in the interstellar medium. *MNRAS*, 194:623–638.
- Armstrong, J. W., Rickett, B. J., and Spangler, S. R. (1995). Electron density power spectrum in the local interstellar medium. *ApJ*, 443:209–221.

- Army, T. (1971). Importance of the Internal Velocity Field in Star Formation. *ApJ*, 169:289–+.
- Auluck, F. C. and Kothari, D. S. (1954). Random fragmentation. *Nature*, 174:565–+.
- Baldry, I. K. and Glazebrook, K. (2003). Constraints on a Universal Stellar Initial Mass Function from Ultraviolet to Near-Infrared Galaxy Luminosity Densities. *ApJ*, 593:258–271.
- Ballerio, S. K., Matteucci, F., and Chiappini, C. (2006). The effects of Population III stars and variable IMF on the chemical evolution of the Galaxy. *New Astronomy*, 11:306–324.
- Ballesteros-Paredes, J., Vázquez-Semadeni, E., and Scalo, J. (1999). Clouds as Turbulent Density Fluctuations: Implications for Pressure Confinement and Spectral Line Data Interpretation. *ApJ*, 515:286–303.
- Bardeen, J. M., Bond, J. R., Kaiser, N., and Szalay, A. S. (1986). The statistics of peaks of Gaussian random fields. *ApJ*, 304:15–61.
- Barkana, R. and Loeb, A. (2001). In the beginning: the first sources of light and the reionization of the universe. *Phys. Rep.*, 349:125–238.
- Barnes, J. and Hut, P. (1986). A Hierarchical O(NlogN) Force-Calculation Algorithm. *Nature*, 324:446–449.
- Bartelmann, M., Doran, M., and Wetterich, C. (2006). Non-linear structure formation in cosmologies with early dark energy. *A&A*, 454:27–36.
- Basri, G. and Marcy, G. W. (1997). Early Hints on the Substellar Mass Function. In Holt, S. S. and Mundy, L. G., editors, *American Institute of Physics Conference Series*, volume 393 of *American Institute of Physics Conference Series*, pages 228–+.
- Batchelor, G. K. (1953). *The Theory of Homogeneous Turbulence*. Cambridge University Press, 1953. 197 p.
- Bate, M. R. and Bonnell, I. A. (2005). The origin of the initial mass function and its dependence on the mean Jeans mass in molecular clouds. *MNRAS*, 356:1201–1221.
- Benz, W. and Hills, J. G. (1987). Three-dimensional hydrodynamical simulations of stellar collisions. I - Equal-mass main-sequence stars. *ApJ*, 323:614–628.
- Bernoulli, D. (1738). *Hydrodynamica*. Strasbourg, Johann Reinhold Dulsseker, 1738.
- Bessell, M. S., Christlieb, N., and Gustafsson, B. (2004). On the Oxygen Abundance of HE 0107-5240. *ApJL*, 612:L61–L63.
- Bhat, N. D. R., Gupta, Y., and Rao, A. P. (1999). Long-Term Scintillation Studies of Pulsars. II. Refractive Effects and the Spectrum of Plasma Density Fluctuations. *ApJ*, 514:249–271.
- Black, J. H. (1981). The physical state of primordial intergalactic clouds. *MNRAS*, 197:553–563.
- Bond, J. R., Cole, S., Efstathiou, G., and Kaiser, N. (1991). Excursion set mass functions for hierarchical Gaussian fluctuations. *ApJ*, 379:440–460.
- Borkowski, K. J., Hendrick, S. P., and Reynolds, S. P. (2004). Supernova ejecta in Magellanic Clouds remnants. In *35th COSPAR Scientific Assembly*, volume 35 of *COSPAR, Plenary Meeting*, pages 3560–+.
- Brax, P. H. and Martin, J. (1999). Quintessence and supergravity. *Physics Letters B*, 468:40–45.
- Bromm, V. and Larson, R. B. (2004). The First Stars. *ARA&A*, 42:79–118.
- Bromm, V. and Loeb, A. (2003). The formation of the first low-mass stars from gas with low carbon and oxygen abundances. *Nature*, 425:812–814.
- Bromm, V. and Loeb, A. (2006). High-Redshift Gamma-Ray Bursts from Population III Progenitors. *ApJ*, 642:382–388.
- Bromm, V., Yoshida, N., and Hernquist, L. (2003). The First Supernova Explosions in the Universe. *ApJL*, 596:L135–L138.
- Bruno, G. (1584). *De l'infinito universo et Mondi*. London: John Charlewood.

- Bryan, G. L. and Norman, M. L. (1997). A Hybrid AMR Application for Cosmology and Astrophysics. *ArXiv Astrophysics e-prints*.
- Bryan, G. L. and Norman, M. L. (1998). Statistical Properties of X-Ray Clusters: Analytic and Numerical Comparisons. *ApJ*, 495:80–+.
- Burkert, A. (2006). The Turbulent Interstellar Medium. *ArXiv Astrophysics e-prints*.
- Burles, S. and Tytler, D. (1998). The Deuterium Abundance toward QSO 1009+2956. *ApJ*, 507:732–744.
- Carroll, S. M., Press, W. H., and Turner, E. L. (1992). The cosmological constant. *ARA&A*, 30:499–542.
- Cen, R. and Ostriker, J. P. (1992). Galaxy formation and physical bias. *ApJL*, 399:L113–L116.
- Chabrier, G. (2003). Galactic Stellar and Substellar Initial Mass Function. *Publ. Astr. Soc. Pac.*, 115:763–795.
- Chandrasekhar, S. (1949). Turbulence - a Physical Theory of Astrophysical Interest. *ApJ*, 110:329–+.
- Chandrasekhar, S. (1951a). . *Proc. R. Soc. London A*, 210:18.
- Chandrasekhar, S. (1951b). . *Proc. R. Soc. London A*, 210:26.
- Chappell, D. and Scalo, J. (2001). Multifractal Scaling, Geometrical Diversity, and Hierarchical Structure in the Cool Interstellar Medium. *ApJ*, 551:712–729.
- Christlieb, N., Beers, T. C., Barklem, P. S., Bessell, M., Hill, V., Holmberg, J., Korn, A. J., Marsteller, B., Mashonkina, L., Qian, Y.-Z., Rossi, S., Wasserburg, G. J., Zickgraf, F.-J., Kratz, K.-L., Nordström, B., Pfeiffer, B., Rhee, J., and Ryan, S. G. (2004). The Hamburg/ESO R-process Enhanced Star survey (HERES). I. Project description, and discovery of two stars with strong enhancements of neutron-capture elements. *A&A*, 428:1027–1037.
- Ciardi, B. and Ferrara, A. (2005). The First Cosmic Structures and Their Effects. *Space Science Reviews*, 116:625–705.
- Coles, P. and Lucchin, F. (1995). *Cosmology. The origin and evolution of cosmic structure*. Chichester: Wiley.
- Copernicus, N. (1543). *De revolutionibus orbium coelestium, Libri VI*. Norimbergæ, apud Ioh. Petreium, Anno M. D. XLIII.
- Cordes, J. M., Weisberg, J. M., and Boriakoff, V. (1985). Small-scale electron density turbulence in the interstellar medium. *ApJ*, 288:221–247.
- Crociani, D., Viel, M., Moscardini, L., Bartelmann, M., and Meneghetti, M. (2008). Cosmic reionization in dynamic quintessence cosmology. *MNRAS*, 385:728–736.
- Dabrowski, M. P. and Stelmach, J. (1987). Astrophysical formulas for Friedman models with cosmological constant and radiation. *AJ*, 94:1373–1379.
- D’Alembert, J. B. (1743). *Traité de Dynamique*. Paris: David; XVIII, 186 p. : tavn. ; in 8.; DCC.4.115.
- Dolag, K., Jubelgas, M., Springel, V., Borgani, S., and Rasia, E. (2004). Thermal Conduction in Simulated Galaxy Clusters. *ApJL*, 606:L97–L100.
- Edmunds, M. G. (1975). Is the galactic disk well mixed. *Ap&SS*, 32:483–491.
- Efstathiou, G., Davis, M., White, S. D. M., and Frenk, C. S. (1985). Numerical techniques for large cosmological N-body simulations. *ApJS*, 57:241–260.
- Einasto, J. (1970). On the structure and evolution of the Galaxy. *Tartu Astrofüüsika Observatoorium Teated*, 26:1–22.
- Einasto, J. (1974). Galactic Models and Stellar Orbits (Invited Lecture). In Mavridis, L. N., editor, *Stars and the Milky Way System*, pages 291–+.
- Einstein, A. (1916). Die Grundlage der allgemeinen Relativitätstheorie. *Annalen der Physik*, 354:769–822.

- Einstein, A. (1917). Kosmologische betrachtungen zur allgemeinen relativitätstheorie. *Sitzungsberichte der Königlich Preußischen Akademie der Wissenschaften (Berlin)*, pages 142–152.
- Ellis, R. S. (2008). Observations of the High Redshift Universe. *First Light in the Universe. Saas-Fee Advanced Courses*, pages 259–364.
- Elmegreen, B. G. (1997). The Initial Stellar Mass Function from Random Sampling in a Turbulent Fractal Cloud. *ApJ*, 486:944–+.
- Elmegreen, B. G. (1999). Formation and Loss of Hierarchical Structure in Two-dimensional Magnetohydrodynamic Simulations of Wave-driven Turbulence in Interstellar Clouds. *ApJ*, 527:266–284.
- Elmegreen, B. G. and Elmegreen, D. M. (2001). Fractal Structure in Galactic Star Fields. *AJ*, 121:1507–1511.
- Elmegreen, B. G. and Scalo, J. (2004). Interstellar Turbulence I: Observations and Processes. *ARA&A*, 42:211–273.
- Evrard, A. E. (1988). Beyond N-body - 3D cosmological gas dynamics. *MNRAS*, 235:911–934.
- Falgarone, E., Hily-Blant, P., Pety, J., and Pineau Des Forêts, G. (2005). Intermittency of interstellar turbulence: observational signatures in diffuse molecular gas. In de Gouveia dal Pino, E. M., Lugones, G., and Lazarian, A., editors, *Magnetic Fields in the Universe: From Laboratory and Stars to Primordial Structures.*, volume 784 of *American Institute of Physics Conference Series*, pages 299–307.
- Falgarone, E. and Phillips, T. G. (1990). A signature of the intermittency of interstellar turbulence - The wings of molecular line profiles. *ApJ*, 359:344–354.
- Fall, S. M. (1978). On the evolution of galaxy clustering and cosmological N-body simulations. *MNRAS*, 185:165–178.
- Fermi, E. (1956). *Thermodynamics*. New York: Dover, 1956.
- Ferrini, F., Marchesoni, F., and Vulpiani, A. (1983). On the initial mass function and the fragmentation of molecular clouds. *MNRAS*, 202:1071–1086.
- Ferrini, F., Penco, U., and Palla, F. (1990). Bimodality versus multimodality - Do fragmentation theories support a bimodal IMF? *A&A*, 231:391–403.
- Field, G. B. (1965). Thermal Instability. *ApJ*, 142:531–+.
- Figer, D. F., Najarro, F., Morris, M., McLean, I. S., Geballe, T. R., Ghez, A. M., and Langer, N. (1998). The Pistol Star. *ApJ*, 506:384–404.
- Flower, D. R. (2000). HD in the primordial gas. *MNRAS*, 318:875–878.
- Ford, A. L. and Browne, J. C. (1977). Ab initio calculation of the line strengths in the electric dipole vibration-rotation spectrum of the HD molecule. *Phys. Rev. A*, 16:1992–2001.
- Freedman, W. L., Madore, B. F., Gibson, B. K., Ferrarese, L., Kelson, D. D., Sakai, S., Mould, J. R., Kennicutt, Jr., R. C., Ford, H. C., Graham, J. A., Huchra, J. P., Hughes, S. M. G., Illingworth, G. D., Macri, L. M., and Stetson, P. B. (2001). Final Results from the Hubble Space Telescope Key Project to Measure the Hubble Constant. *ApJ*, 553:47–72.
- Friedmann, A. (1922). Über die Krümmung des Raumes. *Z. Phys.*, pages 142–152.
- Friel, E. D. and Boesgaard, A. M. (1992). Chemical composition of open clusters. III - Iron and carbon in F dwarfs in Coma, Praesepe, and M67. *ApJ*, 387:170–180.
- Frisch, U. (1996). *Turbulence*. Turbulence, by Uriel Frisch, pp. 310. ISBN 0521457130. Cambridge, UK: Cambridge University Press, January 1996.
- Fryer, C. L. (1999). Mass Limits For Black Hole Formation. *ApJ*, 522:413–418.
- Fryer, C. L., Woosley, S. E., and Heger, A. (2001). Pair-Instability Supernovae, Gravity Waves, and Gamma-Ray Transients. *ApJ*, 550:372–382.

- Fuller, G. M., Woosley, S. E., and Weaver, T. A. (1986). The evolution of radiation-dominated stars. I - Nonrotating supermassive stars. *ApJ*, 307:675–686.
- Galilei, G. (1610). *Sidereus Nuncius*. Venetiis, Apud Thomam Baglionum. MDCX.
- Galilei, G. (1623). *Il saggiatore nel quale con bilancia esquisita e giusta si ponderano le cose contenute nella libra astronomica e filosofica di Lotario Sarsi Sigensano scritto in forma di lettera all'Ill.mo et reuer.mo d. Virginio Cesarini*. In Roma, appresso Giacomo Mascardi, MDCXXIII.
- Galilei, G. (1632). *Dialogo sopra i due massimi sistemi del mondo tolemaico e copernicano*. In Florenza, Per Gio:Batista Landini MDCXXXII.
- Galli, D. and Palla, F. (1998). The chemistry of the early Universe. *A&A*, 335:403–420.
- Galli, D. and Palla, F. (2002). Deuterium chemistry in the primordial gas. *P&SS*, 50:1197–1204.
- Gao, L., Yoshida, N., Abel, T., Frenk, C. S., Jenkins, A., and Springel, V. (2007). The first generation of stars in the Λ cold dark matter cosmology. *MNRAS*, 378:449–468.
- Gingold, R. A. and Monaghan, J. J. (1977). Smoothed particle hydrodynamics - Theory and application to non-spherical stars. *MNRAS*, 181:375–389.
- Giuricin, G., Mardirossian, F., Mezzetti, M., and Santangelo, P. (1984). N-body simulations of small groups of galaxies. *ApJ*, 277:38–42.
- Glover, S. C. O. and Brand, P. W. J. L. (2003). Radiative feedback from an early X-ray background. *MNRAS*, 340:210–226.
- Gnedin, N. Y. (1998). Metal enrichment of the intergalactic medium. *MNRAS*, 294:407–+.
- Gomez, M., Hartmann, L., Kenyon, S. J., and Hewett, R. (1993). On the spatial distribution of pre-main-sequence stars in Taurus. *AJ*, 105:1927–1937.
- Gunn, J. E. and Gott, J. R. I. (1972). On the Infall of Matter Into Clusters of Galaxies and Some Effects on Their Evolution. *ApJ*, 176:1–+.
- Haardt, F. and Madau, P. (1996). Radiative Transfer in a Clumpy Universe. II. The Ultraviolet Extragalactic Background. *ApJ*, 461:20–+.
- Haiman, Z., Abel, T., and Madau, P. (2001). Photon Consumption in Minihalos during Cosmological Reionization. *ApJ*, 551:599–607.
- Haiman, Z., Rees, M. J., and Loeb, A. (1997). Destruction of Molecular Hydrogen during Cosmological Reionization. *ApJ*, 476:458–+.
- Heath, D. J. (1977). The growth of density perturbations in zero pressure Friedmann-Lemaitre universes. *MNRAS*, 179:351–358.
- Heger, A. and Woosley, S. E. (2002). The Nucleosynthetic Signature of Population III. *ApJ*, 567:532–543.
- Heitmann, K., Lukić, Z., Habib, S., and Ricker, P. M. (2006). Capturing Halos at High Redshifts. *ApJL*, 642:L85–L88.
- Hénon, M. H. (1971). The Monte Carlo Method (Papers appear in the Proceedings of IAU Colloquium No. 10 Gravitational N-Body Problem (ed. by Myron Lecar), R. Reidel Publ. Co. , Dordrecht-Holland.). *Ap&SS*, 14:151–167.
- Hernquist, L. and Katz, N. (1989). TREESPH - A unification of SPH with the hierarchical tree method. *ApJS*, 70:419–446.
- Hinshaw, G., Weiland, J. L., Hill, R. S., Odegard, N., Larson, D., Bennett, C. L., Dunkley, J., Gold, B., Greason, M. R., Jarosik, N., Komatsu, E., Nolte, M. R., Page, L., Spergel, D. N., Wollack, E., Halpern, M., Kogut, A., Limon, M., Meyer, S. S., Tucker, G. S., and Wright, E. L. (2008). Five-Year Wilkinson Microwave Anisotropy Probe (WMAP) Observations: Data Processing, Sky Maps, and Basic Results. *ArXiv e-prints*, 803.

- Hollenbach, D. and McKee, C. F. (1979). Molecule formation and infrared emission in fast interstellar shocks. I Physical processes. *ApJS*, 41:555–592.
- Hollenbach, D. and McKee, C. F. (1989). Molecule formation and infrared emission in fast interstellar shocks. III - Results for J shocks in molecular clouds. *ApJ*, 342:306–336.
- Hubble, E. (1929). A Relation between Distance and Radial Velocity among Extra-Galactic Nebulae. *Proceedings of the National Academy of Science*, 15:168–173.
- Hubble, E. and Humason, M. L. (1931). The Velocity-Distance Relation among Extra-Galactic Nebulae. *ApJ*, 74:43–+.
- Hui, L. and Gnedin, N. Y. (1997). Equation of state of the photoionized intergalactic medium. *MNRAS*, 292:27–+.
- Iroshnikov, P. S. (1963). Turbulence of a Conducting Fluid in a Strong Magnetic Field. *Astronomicheskii Zhurnal*, 40:742–+.
- Jang-Condell, H. and Hernquist, L. (2001). First Structure Formation: A Simulation of Small-Scale Structure at High Redshift. *ApJ*, 548:68–78.
- Jeans, J. H. (1902). The Stability of a Spherical Nebula. *Phil. Trans.*, 199:A p.1+.
- Jenkins, A., Frenk, C. S., White, S. D. M., Colberg, J. M., Cole, S., Evrard, A. E., Couchman, H. M. P., and Yoshida, N. (2001). The mass function of dark matter haloes. *MNRAS*, 321:372–384.
- Kanjilal, T. and Basu, B. (1992). A study of the fragmentation of molecular clouds and the form of initial mass-function for low-mass protostellar fragments. *Ap&SS*, 193:17–28.
- Kant, I. (1755). *Allgemeine Naturgeschichte und Theorie des Himmels. Versuch von der Verfassung und dem mechanischen Ursprunge des ganzen Weltgebäudes, nach Newtonischen Grundsätzen abgehandelt.* Johannes Rahts, MDCCLV.
- Karpas, Z., Anicich, V., and Huntress, Jr., W. T. (1979). An ion cyclotron resonance study of reactions of ions with hydrogen atoms. *J. Chem. Phys.*, 70:2877–2881.
- Katz, N., Weinberg, D. H., and Hernquist, L. (1996). Cosmological Simulations with TreeSPH. *ApJS*, 105:19–+.
- Kawata, D. and Gibson, B. K. (2003). GCD+: a new chemodynamical approach to modelling supernovae and chemical enrichment in elliptical galaxies. *MNRAS*, 340:908–922.
- Kennicutt, Jr., R. C. (1983). The rate of star formation in normal disk galaxies. *ApJ*, 272:54–67.
- Kennicutt, Jr., R. C. (1998). Star Formation in Galaxies Along the Hubble Sequence. *ARA&A*, 36:189–232.
- Kepler, J. (1619). *Harmonices mundi, Libri V. Lincii, Austriae.* Sumptibus Godofredi Tampachii Bibl. Francof. Excudebat Ioannes Plancus. Anno M. DC. XIX.
- Kim, S., Dopita, M. A., Staveley-Smith, L., and Bessell, M. S. (1999). H I Shells in the Large Magellanic Cloud. *AJ*, 118:2797–2823.
- Kobayashi, C. (2004). GRAPE-SPH chemodynamical simulation of elliptical galaxies - I. Evolution of metallicity gradients. *MNRAS*, 347:740–758.
- Kolesnik, I. and Ogul'Chanskii, I. I. (1990). Supersonic turbulent fragmentation of giant molecular clouds. In Capuzzo-Dolcetta, R., Chiosi, C., and di Fazio, A., editors, *Physical Processes in Fragmentation and Star Formation*, volume 162 of *Astrophysics and Space Science Library*, pages 81–86.
- Kolmogorov, A. N. (1941a). The Local Structure of Turbulence in Incompressible Viscous Fluid for Very Large Reynolds' Numbers. *Akademiia Nauk SSSR Doklady*, 30:301–305 (English transl. in *Proc. Roy. Soc. Lond. A*, 1991).
- Kolmogorov, A. N. (1941b). Dissipation of Energy in the Locally Isotropic Turbulence. *Akademiia Nauk SSSR Doklady*, 31:538–540 (English transl. in *Proc. Roy. Soc. Lond. A*, 1991).
- Korn, A. J., Grundahl, F., Richard, O., Barklem, P. S., Mashonkina, L., Collet, R., Piskunov, N., and Gustafsson, B. (2006). A probable stellar solution to the cosmological lithium discrepancy. *Nature*, 442:657–659.

- Kraichnan, R. H. (1965). Inertial-Range Spectrum of Hydromagnetic Turbulence. *Physics of Fluids*, 8:1385–1387.
- Kroupa, P. (2001). On the variation of the initial mass function. *MNRAS*, 322:231–246.
- Kroupa, P., Tout, C. A., and Gilmore, G. (1993). The distribution of low-mass stars in the Galactic disc. *MNRAS*, 262:545–587.
- Lagrange, J. L. (1788). *Mécanique analytique*. Paris : Desaint, 1788; 512 p. ; in 8.; DCC.4.403.
- Lamb, H. (1879). *A treatise on the mathematical theory of the motion of fluids*. Cambridge University Press, 1879. 258 p.
- Landau, L. D. and Lifshitz, E. M. (1975). *The classical theory of fields*. Course of theoretical physics - Pergamon International Library of Science, Technology, Engineering and Social Studies, Oxford: Pergamon Press, 1975, 4th rev.engl.ed.
- Langer, W. D., Velusamy, T., Kuiper, T. B. H., Levin, S., Olsen, E., and Migenes, V. (1995). Study of Structure and Small-Scale Fragmentation in TMC-1. *ApJ*, 453:293–+.
- Larson, R. B. (1978). A finite-particle scheme for three-dimensional gas dynamics. *Journal of Computational Physics*, 27:397–409.
- Larson, R. B. (1992). Towards understanding the stellar initial mass function. *MNRAS*, 256:641–646.
- Larson, R. B. (1995). Star formation in groups. *MNRAS*, 272:213–220.
- Larson, R. B. (1998). Early star formation and the evolution of the stellar initial mass function in galaxies. *MNRAS*, 301:569–581.
- Lee, L. C. and Jokipii, J. R. (1976). The irregularity spectrum in interstellar space. *ApJ*, 206:735–743.
- Lemaître, G. (1927). Un univers homogène de masse constante et de rayon croissant, rendant compte de la vitesse radiale des nébuleuses extra-galactiques. *Ann. Soc. Sci. Brux. A*, 47:49–59 (English transl. in *MNRAS*, 91, 483–490).
- Lepp, S. and Shull, J. M. (1984). Molecules in the early universe. *ApJ*, 280:465–469.
- Lia, C., Portinari, L., and Carraro, G. (2002a). Erratum: Star formation and chemical evolution in smoothed particle hydrodynamics simulations: a statistical approach. *MNRAS*, 335:864–864.
- Lia, C., Portinari, L., and Carraro, G. (2002b). Star formation and chemical evolution in smoothed particle hydrodynamics simulations: a statistical approach. *MNRAS*, 330:821–836.
- Lipovka, A., Núñez-López, R., and Avila-Reese, V. (2005). The cooling function of HD molecule revisited. *MNRAS*, 361:850–854.
- Lovelace, R. V. E., Salpeter, E. E., Sharp, L. E., and Harris, D. E. (1970). Analysis of Observations of Interplanetary Scintillations. *ApJ*, 159:1047–+.
- Lucy, L. B. (1977). A numerical approach to the testing of the fission hypothesis. *AJ*, 82:1013–1024.
- Mac Low, M.-M. and Ferrara, A. (1999). Starburst-driven Mass Loss from Dwarf Galaxies: Efficiency and Metal Ejection. *ApJ*, 513:142–155.
- Mac Low, M.-M. and Klessen, R. S. (2004). Control of star formation by supersonic turbulence. *Reviews of Modern Physics*, 76:125–194.
- Maio, U., Ciardi, B., Dolag, K., and Tornatore, L. (2008). Cooling in Primordial Structure Formation. In O’Shea, B. W. and Heger, A., editors, *First Stars III*, volume 990 of *American Institute of Physics Conference Series*, pages 33–35.
- Maio, U., Dolag, K., Ciardi, B., and Tornatore, L. (2007). Metal and molecule cooling in simulations of structure formation. *MNRAS*, 379:963–973.
- Maio, U., Dolag, K., Meneghetti, M., Moscardini, L., Yoshida, N., Baccigalupi, C., Bartelmann, M., and Perrotta, F. (2006). Early structure formation in quintessence models and its implications for cosmic reionization from first stars. *MNRAS*, 373:869–878.

- Mandelbrot, B. B. (1982). *The Fractal Geometry of Nature*. The Fractal Geometry of Nature, San Francisco: Freeman, 1982.
- Matsumoto, T., Matsuura, S., Murakami, H., Tanaka, M., Freund, M., Lim, M., Cohen, M., Kawada, M., and Noda, M. (2005). Infrared Telescope in Space Observations of the Near-Infrared Extragalactic Background Light. *ApJ*, 626:31–43.
- Maxwell, J. C. (1873). Molecules. *Nature*, pages 437–441.
- McKellar, A. R. W., Goetz, W., and Ramsay, D. A. (1976). The rotation-vibration spectrum of HD - Wavelength and intensity measurements of the 3-0, 4-0, 5-0, and 6-0 electric dipole bands. *ApJ*, 207:663–670.
- Mestel, L. (1965). Problems of Star Formation I, II. *QJRAS*, 6:265–+.
- Meynet, G., Ekström, S., and Maeder, A. (2006a). The early star generations: the dominant effect of rotation on the CNO yields. *A&A*, 447:623–639.
- Meynet, G., Ekström, S., and Maeder, A. (2006b). The early star generations: the dominant effect of rotation on the CNO yields. *A&A*, 447:623–639.
- Miller, G. E. and Scalo, J. M. (1979). The initial mass function and stellar birthrate in the solar neighborhood. *ApJS*, 41:513–547.
- Millionshtchikov, M. D. (1939). Decay of turbulence in wind tunnels. *Dokl. Akad. Nauk SSSR*, 22:236.
- Misner, C. W., Thorne, K. S., and Wheeler, J. A. (1973). *Gravitation*. San Francisco: W.H. Freeman and Co., 1973.
- Monaghan, J. J. and Lattanzio, J. C. (1985). A refined particle method for astrophysical problems. *A&A*, 149:135–143.
- Mosconi, M. B., Tissera, P. B., Lambas, D. G., and Cora, S. A. (2001). Chemical evolution using smooth particle hydrodynamical cosmological simulations - I. Implementation, tests and first results. *MNRAS*, 325:34–48.
- Mouschovias, T. C. (1976a). Nonhomologous contraction and equilibria of self-gravitating, magnetic interstellar clouds embedded in an intercloud medium: Star formation. I Formulation of the problem and method of solution. *ApJ*, 206:753–767.
- Mouschovias, T. C. (1976b). Nonhomologous contraction and equilibria of self-gravitating, magnetic interstellar clouds embedded in an intercloud medium: Star formation. II - Results. *ApJ*, 207:141–158.
- Mouschovias, T. C. and Spitzer, Jr., L. (1976). Note on the collapse of magnetic interstellar clouds. *ApJ*, 210:326–+.
- Nagao, T., Sasaki, S. S., Maiolino, R., Grady, C., Kashikawa, N., Ly, C., Malkan, M. A., Motohara, K., Murayama, T., Schaerer, D., Shioya, Y., and Taniguchi, Y. (2008). A Photometric Survey for Ly α -He II Dual Emitters: Searching for Population III Stars in High-Redshift Galaxies. *ApJ*, 680:100–109.
- Nakamura, F. and Umemura, M. (2002). The Stellar Initial Mass Function in Primordial Galaxies. *ApJ*, 569:549–557.
- Navarro, J. F., Frenk, C. S., and White, S. D. M. (1997). A Universal Density Profile from Hierarchical Clustering. *ApJ*, 490:493–+.
- Newton, I. (1687). *Philosophiæ Naturalis Principia Mathematica*. Londini, Iussu Societatis Regiæ ac Typis Iosephi Streater. Anno MDCLXXXVII.
- Obukhov, A. M. (1941). On the distribution of energy in the spectrum of turbulent flow. *C.R. Acad. Sci. U.R.S.S.*, 32:19+.
- O’Meara, J. M., Burles, S., Prochaska, J. X., Prochter, G. E., Bernstein, R. A., and Burgess, K. M. (2006). The Deuterium-to-Hydrogen Abundance Ratio toward the QSO SDSS J155810.16-003120.0. *ApJL*, 649:L61–L65.
- Omukai, K. and Palla, F. (2003). Formation of the First Stars by Accretion. *ApJ*, 589:677–687.
- Onsager, L. (1945). The distribution of energy in turbulence. *Phys. Rev.*, 68:286.

- Osterbrock, D. E. (1989). *Astrophysics of gaseous nebulae and active galactic nuclei*. Research supported by the University of California, John Simon Guggenheim Memorial Foundation, University of Minnesota, et al. Mill Valley, CA, University Science Books, 1989, 422 p.
- Padoan, P. (1995). Supersonic turbulent flows and the fragmentation of a cold medium. *MNRAS*, 277:377–388.
- Padoan, P. and Nordlund, Å. (2002). The Stellar Initial Mass Function from Turbulent Fragmentation. *ApJ*, 576:870–879.
- Padovani, P. and Matteucci, F. (1993). Stellar Mass Loss in Elliptical Galaxies and the Fueling of Active Galactic Nuclei. *ApJ*, 416:26–+.
- Park, S., Hughes, J. P., Burrows, D. N., Slane, P. O., Nousek, J. A., and Garmire, G. P. (2003). 0103-72.6: A New Oxygen-rich Supernova Remnant in the Small Magellanic Cloud. *ApJL*, 598:L95–L98.
- Pavlovski, G., Smith, M. D., Mac Low, M.-M., and Rosen, A. (2002). Hydrodynamical simulations of the decay of high-speed molecular turbulence - I. Dense molecular regions. *MNRAS*, 337:477–487.
- Pawlik, A. H., Schaye, J., and van Scherpenzeel, E. (2008). Keeping the Universe ionised: Photo-ionisation heating and the critical star formation rate at redshift $z = 6$. *ArXiv e-prints*, 807.
- Peacock, J. A. (1999). *Cosmological Physics*. Cambridge University Press, 1999. 694 p.
- Peebles, P. J. and Ratra, B. (2003). The cosmological constant and dark energy. *Reviews of Modern Physics*, 75:559–606.
- Peebles, P. J. E. (1974). The Gravitational-Instability Picture and the Nature of the Distribution of Galaxies. *ApJL*, 189:L51+.
- Peebles, P. J. E. (1993). Book Review: Principles of physical cosmology / Princeton U Press, 1993. *Physics Today*, 46:87–+.
- Peebles, P. J. E. and Dicke, R. H. (1968). Origin of the Globular Star Clusters. *ApJ*, 154:891–+.
- Peterson, J. R., Aberth, W. H., Moseley, J. T., and Sheridan, J. R. (1971). Ion-Ion Mutual Neutralization Cross Sections Measured by a Superimposed Beam Technique. II. $O_2^+ + O_2^-$, $O_2^+ + NO_2^-$, and $NO^+ + NO_2^-$. *Phys. Rev. A*, 3:1651–1657.
- Pettini, M. and Bowen, D. V. (2001). A New Measurement of the Primordial Abundance of Deuterium: Toward Convergence with the Baryon Density from the Cosmic Microwave Background? *ApJ*, 560:41–48.
- Pety, J. and Falgarone, E. (2003). Non-Gaussian velocity shears in the environment of low mass dense cores. *A&A*, 412:417–430.
- Planck, M. (1900). Zur Theorie des Gesetzes der Energieverteilung im Normalspektrum. *Verhandl. Dtsch. phys. Ges.*, 2:237.
- Poincaré, H. (1892). *Les méthodes nouvelles de la mécanique céleste*. Paris: Gauthier-Villars, 3 vols. 1892, 1893, 1899.
- Portinari, L., Chiosi, C., and Bressan, A. (1998). Galactic chemical enrichment with new metallicity dependent stellar yields. *A&A*, 334:505–539.
- Press, W. H. and Schechter, P. (1974). Formation of Galaxies and Clusters of Galaxies by Self-Similar Gravitational Condensation. *ApJ*, 187:425–438.
- Ptolemy, C. (150). *Mathematike Syntaxis - Syntaxis Mathematica - Al magiste*. Alexandrian School in Egypt, II century AD (about 150).
- Puy, D., Alecian, G., Le Bourlot, J., Leorat, J., and Pineau Des Forets, G. (1993). Formation of primordial molecules and thermal balance in the early universe. *A&A*, 267:337–346.
- Pynzar, A. V., Shishov, V. I., and Shishova, T. D. (1975). Power spectra of interplanetary scintillations. *Astronomicheskii Zhurnal*, 52:1187–1194.

- Quinn, T., Katz, N., Stadel, J., and Lake, G. (1997). Time stepping N-body simulations. *ArXiv Astrophysics e-prints*.
- Raiteri, C. M., Villata, M., and Navarro, J. F. (1996). Simulations of Galactic chemical evolution. I. O and Fe abundances in a simple collapse model. *A&A*, 315:105–115.
- Rana, N. C. (1991). Chemical evolution of the Galaxy. *ARA&A*, 29:129–162.
- Ratra, B. and Peebles, P. J. E. (1988). Cosmological consequences of a rolling homogeneous scalar field. *Phys. Rev. D*, 37:3406–3427.
- Reddy, N. A., Steidel, C. C., Pettini, M., Adelberger, K. L., Shapley, A. E., Erb, D. K., and Dickinson, M. (2008). Multiwavelength Constraints on the Cosmic Star Formation History from Spectroscopy: the Rest-Frame Ultraviolet, H α , and Infrared Luminosity Functions at Redshifts $1.9 \gtrsim z \lesssim 3.4$. *ApJS*, 175:48–85.
- Reed, D., Gardner, J., Quinn, T., Stadel, J., Fardal, M., Lake, G., and Governato, F. (2003). Evolution of the mass function of dark matter haloes. *MNRAS*, 346:565–572.
- Rickett, B. J. (1977). Interstellar scattering and scintillation of radio waves. *ARA&A*, 15:479–504.
- Rickett, B. J. and Coles, W. A. (2004). Anisotropy and Intermittency in the Turbulent Interstellar Plasma. In *Bulletin of the American Astronomical Society*, volume 36 of *Bulletin of the American Astronomical Society*, pages 1539–+.
- Ricotti, M., Gnedin, N. Y., and Shull, J. M. (2001). Feedback from Galaxy Formation: Production and Photodissociation of Primordial H₂. *ApJ*, 560:580–591.
- Ricotti, M. and Ostriker, J. P. (2004). Reionization, chemical enrichment and seed black holes from the first stars: is Population III important? *MNRAS*, 350:539–551.
- Righi, M., Hernandez-Monteagudo, C., and Sunyaev, R. (2008). Carbon monoxide line emission as a CMB foreground: tomography of the star-forming universe with different spectral resolutions. *ArXiv e-prints*, 805.
- Roberge, W. and Dalgarno, A. (1982). The formation and destruction of HeH⁺ in astrophysical plasmas. *ApJ*, 255:489–496.
- Saitoh, T. R., Daisaka, H., Kokubo, E., Makino, J., Okamoto, T., Tomisaka, K., Wada, K., and Yoshida, N. (2008). Toward First-Principle Simulations of Galaxy Formation: I. How Should We Choose Star-Formation Criteria in High-Resolution Simulations of Disk Galaxies? *Pub. Astron. Soc. Japan*, 60:667–.
- Salpeter, E. E. (1955). The Luminosity Function and Stellar Evolution. *ApJ*, 121:161–+.
- Salvatterra, R. and Ferrara, A. (2006). Where are the sources of the near-infrared background? *MNRAS*, 367:L11–L15.
- Santoro, F. and Shull, J. M. (2006). Critical Metallicity and Fine-Structure Emission of Primordial Gas Enriched by the First Stars. *ApJ*, 643:26–37.
- Sasao, T. (1973). On the Generation of Density Fluctuations Due to Turbulence in Self-Gravitating Media. *Pub. Astron. Soc. Japan*, 25:1–+.
- Saslaw, W. C. and Zipoy, D. (1967). Molecular Hydrogen in Pre-galactic Gas Clouds. *Nature*, 216:976–+.
- Savin, D. W. (2002). Rate Coefficients for D(1s)+H⁺ \rightarrow D⁺+H(1s) Charge Transfer and Some Astrophysical Implications. *ApJ*, 566:599–603.
- Savin, D. W., Krstić, P. S., Haiman, Z., and Stancil, P. C. (2004). Rate Coefficient for H⁺ + H₂(X¹ Σ_g^+ , $\nu = 0$, J = 0) \rightarrow H(1s) + H₂⁺ Charge Transfer and Some Cosmological Implications. *ApJL*, 606:L167–L170.
- Scalo, J. and Elmegreen, B. G. (2004). Interstellar Turbulence II: Implications and Effects. *ARA&A*, 42:275–316.
- Scalo, J. M. (1986). The stellar initial mass function. *Fundamentals of Cosmic Physics*, 11:1–278.
- Scannapieco, C., Tissera, P. B., White, S. D. M., and Springel, V. (2005). Feedback and metal enrichment in cosmological smoothed particle hydrodynamics simulations - I. A model for chemical enrichment. *MNRAS*, 364:552–564.

- Scannapieco, E., Schneider, R., and Ferrara, A. (2003). The Detectability of the First Stars and Their Cluster Enrichment Signatures. *ApJ*, 589:35–52.
- Scheuer, P. A. G. (1968). Amplitude Variations in Pulsed Radio Sources. *Nature*, 218:920–+.
- Schneider, R., Ferrara, A., Ciardi, B., Ferrari, V., and Matarrese, S. (2000). Gravitational wave signals from the collapse of the first stars. *MNRAS*, 317:385–390.
- Schneider, R., Ferrara, A., Salvaterra, R., Omukai, K., and Bromm, V. (2003). Low-mass relics of early star formation. *Nature*, 422:869–871.
- Shapiro, P. R. and Kang, H. (1987). Hydrogen molecules and the radiative cooling of pregalactic shocks. *ApJ*, 318:32–65.
- She, Z.-S. and L ev eque, E. (1994). Universal scaling laws in fully developed turbulence. *Physical Review Letters*, 72:336–339.
- She, Z.-S. and Waymire, E. C. (1995). Quantized Energy Cascade and Log-Poisson Statistics in Fully Developed Turbulence. *Physical Review Letters*, 74:262–265.
- Sheth, R. K., Mo, H. J., and Tormen, G. (2001). Ellipsoidal collapse and an improved model for the number and spatial distribution of dark matter haloes. *MNRAS*, 323:1–12.
- Sheth, R. K. and Tormen, G. (1999). Large-scale bias and the peak background split. *MNRAS*, 308:119–126.
- Shishov, V. I., Smirnova, T. V., Sieber, W., Malofeev, V. M., Potapov, V. A., Stinebring, D., Kramer, M., Jessner, A., and Wielebinski, R. (2003). Measurements of the interstellar turbulent plasma spectrum of PSR B0329+54 using multi-frequency observations of interstellar scintillation. *A&A*, 404:557–567.
- Sigward, F., Ferrara, A., and Scannapieco, E. (2005). Suppression of dwarf galaxy formation by cosmic shocks. *MNRAS*, 358:755–764.
- Silk, J. (1977). On the fragmentation of cosmic gas clouds. III - The initial stellar mass function. *ApJ*, 214:718–724.
- Simon, M. (1997). Clustering of Young Stars in Taurus, Ophiuchus, and the Orion Trapezium. *ApJL*, 482:L81+.
- Smith, M. D., Mac Low, M.-M., and Heitsch, F. (2000). The distribution of shock waves in driven supersonic turbulence. *A&A*, 362:333–341.
- Spangler, S. R. and Gwinn, C. R. (1990). Evidence for an inner scale to the density turbulence in the interstellar medium. *ApJL*, 353:L29–L32.
- Spergel, D. N., Bean, R., Dor e, O., Nolta, M. R., Bennett, C. L., Dunkley, J., Hinshaw, G., Jarosik, N., Komatsu, E., Page, L., Peiris, H. V., Verde, L., Halpern, M., Hill, R. S., Kogut, A., Limon, M., Meyer, S. S., Odegard, N., Tucker, G. S., Weiland, J. L., Wollack, E., and Wright, E. L. (2007). Three-Year Wilkinson Microwave Anisotropy Probe (WMAP) Observations: Implications for Cosmology. *ApJS*, 170:377–408.
- Springel, V. (2005). The cosmological simulation code GADGET-2. *MNRAS*, 364:1105–1134.
- Springel, V. et al. (2005). Simulations of the formation, evolution and clustering of galaxies and quasars. *Nature*, 435:629–636.
- Springel, V. and Hernquist, L. (2003). Cosmological smoothed particle hydrodynamics simulations: a hybrid multiphase model for star formation. *MNRAS*, 339:289–311.
- Springel, V., Yoshida, N., and White, S. D. M. (2001). GADGET: a code for collisionless and gasdynamical cosmological simulations. *New Astronomy*, 6:79–117.
- Stancil, P. C., Lepp, S., and Dalgarno, A. (1998). The Deuterium Chemistry of the Early Universe. *ApJ*, 509:1–10.
- Stibbe, D. T. and Tennyson, J. (1999). Rates for the Electron Impact Dissociation of Molecular Hydrogen. *ApJL*, 513:L147–L150.
- Stinebring, D. R., Smirnova, T. V., Hankins, T. H., Hovis, J. S., Kaspi, V. M., Kempner, J. C., Myers, E., and Nice, D. J. (2000). Five Years of Pulsar Flux Density Monitoring: Refractive Scintillation and the Interstellar Medium. *ApJ*, 539:300–316.

- Sugiyama, N. (1995). Cosmic Background Anisotropies in Cold Dark Matter Cosmology. *ApJS*, 100:281–+.
- Sutherland, R. S. and Dopita, M. A. (1993). Cooling functions for low-density astrophysical plasmas. *ApJS*, 88:253–327.
- Takebe, H., Unno, W., and Hatanaka, T. (1962). On the Condensation of Interstellar Gas, II. The Mass Function in Galactic Clusters. *Pub. Astron. Soc. Japan*, 14:340–+.
- Taylor, G. I. (1921). Diffusion by continuous movements. *Proc. Lond. Math. Soc.*, 20:196+.
- Taylor, G. I. (1935). Statistical theory of turbulence. *Proc. Roy. Soc. Lond. A*, 151:421–478.
- Tegmark, M., Silk, J., Rees, M. J., Blanchard, A., Abel, T., and Palla, F. (1997). How Small Were the First Cosmological Objects? *ApJ*, 474:1–+.
- Thielemann, F.-K., Argast, D., Brachwitz, F., Hix, W. R., Höflich, P., Liebendörfer, M., Martinez-Pinedo, G., Mezzacappa, A., Panov, I., and Rauscher, T. (2003). Nuclear cross sections, nuclear structure and stellar nucleosynthesis. *Nuclear Physics A*, 718:139–146.
- Thielemann, F.-K., Brachwitz, F., Freiburghaus, C., Kolbe, E., Martinez-Pinedo, G., Rauscher, T., Rembges, F., Hix, W. R., Liebendörfer, M., Mezzacappa, A., Kratz, K.-L., Pfeiffer, B., Langanke, K., Nomoto, K., and 3 co-author (2001). Element synthesis in stars. *Progress in Particle and Nuclear Physics*, 46:5–22.
- Thorson, W. R., Choi, J. H., and Knudson, S. K. (1985). Novel theory of the HD dipole moment. I. Theory. *Phys. Rev. A*, 31:22–33.
- Thoul, A. A. and Weinberg, D. H. (1996). Hydrodynamic Simulations of Galaxy Formation. II. Photoionization and the Formation of Low-Mass Galaxies. *ApJ*, 465:608–+.
- Tormen, G., Bouchet, F. R., and White, S. D. M. (1997). The structure and dynamical evolution of dark matter haloes. *MNRAS*, 286:865–884.
- Tornatore, L., Borgani, S., Dolag, K., and Matteucci, F. (2007a). Chemical enrichment of galaxy clusters from hydrodynamical simulations. *MNRAS*, 382:1050–1072.
- Tornatore, L., Ferrara, A., and Schneider, R. (2007b). Population III stars: hidden or disappeared? *MNRAS*, 382:945–950.
- Tumlinson, J., Giroux, M. L., and Shull, J. M. (2001). Probing the First Stars with Hydrogen and Helium Recombination Emission. *ApJL*, 550:L1–L5.
- van Albada, T. S. (1968). Numerical integrations of the N-body problem. *Bulletin of the Astronomical Institutes of the Netherlands*, 19:479–+.
- van den Hoek, L. B. and Groenewegen, M. A. T. (1997). New theoretical yields of intermediate mass stars. *A&A Supp.*, 123:305–328.
- van Dokkum, P. (2007). Evidence of Cosmic Evolution of the Stellar Initial Mass Function. *ArXiv e-prints*, 710.
- Vishniac, E. T. (1983). The dynamic and gravitational instabilities of spherical shocks. *ApJ*, 274:152–167.
- von Kármán, T. (1937). The fundamentals of the statistical theory of turbulence. *J. Aero. Sci.*, 4:131–138.
- von Kármán, T. and T. Howarth, L. (1938). On the Statistical Theory of Isotropic Turbulence. *Proc. Roy. Soc. Lond. A*, 164:192–215.
- Wang, J. G. and Stancil, P. C. (2002). Hydrogen Ion-Molecule Isotopomer Collisions: Charge Transfer and Rearrangement. *Physica Scripta*, T96, 1:72–+.
- Warren, M. S. and Salmon, J. K. (1995). A portable parallel particle program. *Computer Physics Communications*, 87:266–290.
- Weinberg, S. (1972). *Gravitation and Cosmology: Principles and Applications of the General Theory of Relativity*. Gravitation and Cosmology: Principles and Applications of the General Theory of Relativity, by Steven Weinberg, pp. 688. ISBN 0-471-92567-5. Wiley-VCH, July 1972.

- Weizsäcker, C. F. (1951). The Evolution of Galaxies and Stars. *ApJ*, 114:165–+.
- Weizsäcker, C. F. V. (1943). Über die Entstehung des Planetensystems. Mit 2 Abbildungen. *Zeitschrift für Astrophysik*, 22:319–+.
- Weizsäcker, C. F. V. (1948). Das Spektrum der Turbulenz bei großen Reynoldsschen Zahlen. *Zeitschrift für Physik*, 124:614–627.
- Whalen, D., van Veelen, B., O’Shea, B. W., and Norman, M. L. (2008). The Destruction of Cosmological Minihalos by Primordial Supernovae. *ArXiv e-prints*, 801.
- White, S. D. M. (1976). The dynamics of rich clusters of galaxies. *MNRAS*, 177:717–733.
- White, S. D. M. (1978). Simulations of merging galaxies. *MNRAS*, 184:185–203.
- Wilkinson, P. N., Spencer, R. E., and Nelson, R. F. (1988). Interstellar Scattering Towards CYG X-3. In Reid, M. J. and Moran, J. M., editors, *The Impact of VLBI on Astrophysics and Geophysics*, volume 129 of *IAU Symposium*, pages 305–+.
- Woolsey, S. E. and Weaver, T. A. (1995). The Evolution and Explosion of Massive Stars. II. Explosive Hydrodynamics and Nucleosynthesis. *ApJS*, 101:181–+.
- Wyithe, J. S. B. and Cen, R. (2007). The Extended Star Formation History of the First Generation of Stars and the Reionization of Cosmic Hydrogen. *ApJ*, 659:890–907.
- Xie, T., Allen, M., and Langer, W. D. (1995). Turbulent Diffusion and Its Effects on the Chemistry of Molecular Clouds. *ApJ*, 440:674–+.
- Yong, D., Carney, B. W., Aoki, W., McWilliam, A., and Schuster, W. J. (2006). Lithium Abundances in Halo Subgiants. In Kubono, S., Aoki, W., Kajino, T., Motobayashi, T., and Nomoto, K., editors, *AIP Conf. Proc. 847: Origin of Matter and Evolution of Galaxies*, pages 21–24.
- Yoshida, N., Abel, T., Hernquist, L., and Sugiyama, N. (2003a). Simulations of Early Structure Formation: Primordial Gas Clouds. *ApJ*, 592:645–663.
- Yoshida, N., Abel, T., Hernquist, L., and Sugiyama, N. (2003b). Simulations of Early Structure Formation: Primordial Gas Clouds. *ApJ*, 592:645–663.
- Yoshida, N., Oh, S. P., Kitayama, T., and Hernquist, L. (2006a). Early Cosmological HII/HeIII Regions and Their Impact on Second-Generation Star Formation. *ArXiv Astrophysics e-prints*.
- Yoshida, N., Omukai, K., and Hernquist, L. (2007). Formation of Massive Primordial Stars in a Reionized Gas. *ApJL*, 667:L117–L120.
- Yoshida, N., Omukai, K., Hernquist, L., and Abel, T. (2006b). Formation of Primordial Stars in a Λ CDM Universe. *ApJ*, 652:6–25.
- Yoshida, N., Sokasian, A., Hernquist, L., and Springel, V. (2003b). Early Structure Formation and Reionization in a Cosmological Model with a Running Primordial Power Spectrum. *ApJ*, 598:73–85.
- Yoshida, N., Sokasian, A., Hernquist, L., and Springel, V. (2003c). Early Structure Formation and Reionization in a Warm Dark Matter Cosmology. *ApJL*, 591:L1–L4.
- Yoshii, Y. and Sabano, Y. (1980). Fragmentation of Cosmic Gas Clouds due to Thermal Instabilities. *Pub. Astron. Soc. Japan*, 32:229–+.
- Yoshii, Y. and Saio, H. (1985). A fragmentation-coalescence model for the initial stellar mass function. *ApJ*, 295:521–536.
- Zeldovich, Y. B. and Novikov, I. D. (1971). *Relativistic astrophysics. Vol.1: Stars and relativity*. Chicago: University of Chicago Press, 1971.